UNIVERSITÀ
DEGLI STUDI
DI PADOVA

Sede Amministrativa: Università degli Studi di Padova

Dipartimento di Fisica e Astronomia "Galileo Galilei"

SCUOLA DI DOTTORATO DI RICERCA IN: ASTRONOMIA
INDIRIZZO: COMUNE
CICLO: XXVIII

ASTROMETRY AND PHOTOMETRY WITH WIDE-FIELD IMAGERS

Direttore della Scuola: Prof. Giampaolo Piotto

Supervisore: Prof. Giampaolo Piotto
Correlatori: Dr. Luigi Bedin
Dr. Andrea Bellini

Dottorando: Mattia Libralato

Università degli Studi di Padova

Department of Physics and Astronomy
"Galileo Galilei"

Ph.D. Thesis

ASTROMETRY AND PHOTOMETRY WITH WIDE-FIELD IMAGERS

Supervisor: Prof. Giampaolo Piotto

Co-supervisors: Dr. Luigi Bedin
Dr. Andrea Bellini

Ph.D. student: Mattia Libralato

Thesis supervisor: Prof. Giampaolo Piotto
(Dipartimento di Fisica e Astronomia, UNIPD, Padova, Italy)

Thesis co-supervisor: Dr. Luigi Bedin
(INAF-Osservatorio Astronomico di Padova, Padova, Italy)

Thesis co-supervisor: Dr. Andrea Bellini
(Space Telescope Science Institute, Baltimore, MD, USA)

Part of this work has been carried out at the Space Telescope Science Institute (Baltimore, MD, USA) under the STScI 2013 DDRF Spring program *"High-precision astrometry with wide-field detectors"* (PI: Bellini).

Some of the material included in this thesis has been already published in *Astronomy & Astrophysics* and *Monthly Notices of the Royal Astronomical Society.*

Mattia Libralato: *Astrometry and photometry with wide-field imagers*, Ph.D. Thesis, 2016

Final Exam Commitee

Prof. Magali Deleuil
(Aix Marseille Université, CNRS, Laboratoire d'Astrophysique de Marseille, Marseille, France)

Prof. Barbara Lanzoni
(Dipartimento di Fisica e Astronomia, Università degli Studi di Bologna, Bologna, Italy)

Prof. Don Pollacco
(Department of Physics, University of Warwick, Coventry, UK)

Dr. Valérie Van Grootel
(Institut d'Astrophysique et de Géophysique, Liège, Belgium)

I would like to thank my parents without whom everything would not have been possible.

I thank Laura for the help and the patience during my Ph.D. ありがとうございました!

Finally, a special thank also goes to both Padova and overseas groups (in alphabetic order to avoid complaints: Andrea, Giampaolo, Jay, Kunny, Lorenzo, Mimmo, Ranger, Rolly, Sbuffo, Valentina, Valerio) which help made this work possible.

Contents

List of Figures

List of Tables

Abstract

Several projects in astronomy require detectors with a high number of resolution elements on the sky. For this reason, many observatories equipped their telescopes with a particular kind of detectors, the so-called wide-field imagers, that fulfil this requirement. In this thesis we show that, with a careful data analysis based on an accurate point-spread-function (PSF) modelling and geometric-distortion correction, it is possible to obtain high astrometric and photometric accuracy over wide field of views (FoVs). The prescriptions discussed in the thesis can be extended to the most of the detectors that are or will be placed at ground and space observatories.

In the first part of the thesis, we mainly focus on detectors working in the near-infrared (NIR) regime. We want to concentrate on NIR imaging because of the increasing interest of the astronomical community for this wavelength range, which will be the baseline for JWST. In the second part of the thesis we also present a couple of applications to optical wide-field imagers (LBC@LBT and the CCD mounted at the Asiago Schmidt telescope).

We start by investigating the astrometric and photometric performance of the NIR wide-field imager HAWK-I@VLT. We adapt to HAWK-I the techniques originally developed for the *Hubble Space Telescope* (*HST*) imagers to obtain high-precision astrometry and photometry, and then adapted to the ground-based, wide-field imager mounted at the 2.2-m MPI/ESO telescope. We accurately model HAWK-I PSFs and solve for the geometric distortion of the detector. With this careful data reduction, we are able to reach an astrometric accuracy of a few milliarcsec (mas) over the entire FoV of the instrument. Together with the distortion-correction package, we also create astro-photometric catalogues of seven fields (four stellar clusters, two extragalactic fields and one region toward the Galactic centre). Furthermore, to test the reached astrometric accuracy, we compute relative proper motions for stars in two globular clusters (M 22 and M 4) and successfully separate cluster members from background/foreground objects. Proper-motion-selected colour-magnitude diagrams of the globular cluster M 22 allow us to study its multiple stellar populations, finding that the two stellar populations hosted in the sub-giant branches of M 22 have the same radial distribution from the cluster centre out to 9 arcmin, within our uncertainty.

We then move to the wide-field imager VIRCAM@VISTA. Again, we export the tools made for HAWK-I to this imager and solve for the distortion of the detector. The geometric-distortion correction of VIRCAM is quite challenging because the tangential-plane projection effects are not negligible over a FoV larger than 1 deg^2 on the sky. We start by using the 2MASS catalogue as reference frame, and then we auto-calibrate the geometric distortion as done for the HAWK-I detector. This way, we are able to correct the geometric distortion of VIRCAM to an astrometric accuracy of about 8 mas. Finally, we use the 'VISTA Variables in the Vía Láctea' (VVV) data to compute M 22 globular-cluster relative proper motions. VVV observations are not designed to such high-astrometric-accuracy purposes, but, with our tools, we are able to reach a proper-motion precision of $\sim$1.4 mas yr^{-1} and separate cluster and field stars, as well as to measure the motion difference between Galactic bulge and disc stars toward the direction of M 22.

In the last part of the thesis we describe our new project, focused to exploit the data coming from the planet-hunting *K2* mission, the re-designed *Kepler* mission after the problems that occurred to its spacecraft. The analysis of crowded environments using *K2* data can be very complex with classical (aperture-based) photometric approaches. Our method is instead specifically developed to deal with these particular regions (stellar clusters and toward the Galactic cen-

tre) and its key ingredients are PSF astrometry and photometry, high-angular-resolution input catalogues and PSF-based neighbour subtraction.

We first address the problem of the *K2* undersampled PSFs which fine structures, if not properly modelled, can introduce systematic errors that worsen both astrometry and photometry. To this aim, we follow the iterative method made to model *HST* undersampled PSFs. We then use a high-angular-resolution, ground-based catalogue to identify all detectable objects in the field and, for each of them, we measure their flux after we subtract all close-by neighbours. This way, we increase the number of measurable sources in the field and obtain a more reliable estimate of their flux. Most importantly, for variable stars, eclipsing binaries and exoplanet candidates, this method leads to a more reliable value of the true amplitude or eclipse/transit depth of their light curves because we reduce light-dilution effects. This is particularly interesting for exoplanets, as the true radius of the transiting objects would be otherwise under-estimated.

We apply this method to the first *K2* Campaign that covered two open clusters (M 35 and NGC 2158) and extract about 50 000 light curves from only one channel of *K2*. This number is more than two times the total number of sources usually analysed over the entire FoV (76 channels) in a typical *K2* Campaign. For bright stars, we reach a photometric precision of $\sim$30 parts per million, comparable with other works in the literature focused on isolated stars. At the faint end, we measure objects down to 5 magnitudes fainter than in any published work with *K2* data so far, and show that the PSF photometry performs better than aperture photometry in this magnitude regime. The improvement here described is more significant in crowded regions. Within the field of these two clusters we also find more than 2000 variable stars.

All the projects developed during this thesis have also interesting long-term perspectives, since they can be seen as complementary or in preparation to future space-based missions like TESS and PLATO. Candidate exoplanets from *Kepler*/*K2* (but also from the forthcoming TESS) observations can potentially be interesting targets for JWST, and then E-ELT.

Sommario

Diversi progetti in astronomia richiedono rivelatori con un elevato numero di elementi risolutivi in cielo. Per questo motivo, molti osservatori hanno equipaggiato i loro telescopi con un particolare tipo di rivelatori, i cosiddetti rivelatori a grande campo, che soddisfano tale requisito. In questa tesi mostriamo come sia possibile ottenere astrometria e fotometria di elevata accuratezza su grandi campi con un'attenta analisi dei dati basata sul modellare accuratamente le funzioni di sorgenti puntiformi (dall'inglese *point-spread functions*, o PSFs) e sulla correzione della distorsione geometrica. Le metodologie di lavoro discusse in questa tesi possono essere estese alla maggior parte dei rivelatori che sono o verranno collocati in osservatori da terra e da spazio.

Nella prima parte della tesi ci focalizziamo principalmente sui rivelatori che lavorano nel regime del vicino infrarosso. Vogliamo concentrarci su tali camere infrarosse a causa del crescente interesse della comunità astronomica a queste lunghezze d'onda, che saranno alla base di JWST. Tuttavia nella seconda parte della tesi presentiamo anche alcuni esempi di applicazioni con rivelatori a grande campo che lavorano nella parte ottica dello spettro elettromagnetico (la camera LBC montata al telescopio LBT e il rivelatore montato al telescopio Schmidt di Asiago).

Inizialmente esaminiamo le prestazioni astrometriche e fotometriche del rivelatore infrarosso a grande campo HAWK-I montato al VLT. Adattiamo per i dati HAWK-I le tecniche originariamente sviluppate per ottenere astrometria e fotometria di alta precisione con le camere di *Hubble Space Telescope* (*HST*), e successivamente estese alla camera a grande campo posta al telescopio da terra di 2.2 m dell'ESO/MPI. Modelliamo accuratamente le PSFs e correggiamo la distorsione geometrica di HAWK-I. Con questa attenta analisi dei dati, riusciamo a raggiungere un'accuratezza astrometrica di qualche millesimo di arcosecondo (mas) su tutto il campo di vista dello strumento. Oltre alla correzione della distorsione, costruiamo anche cataloghi astrofotometrici di sette campi (quattro ammassi stellari, due campi extragalattici e un campo in direzione del centro Galattico). Inoltre, per testare l'accuratezza astrometrica raggiunta, calcoliamo i moti propri relativi delle stelle in due ammassi globulari (M 22 e M 4) e separiamo con successo i membri di ammasso da quelli di campo. Diagrammi colore-magnitudine decontaminati dalle stelle di campo grazie ai moti propri ci permettono di studiare le popolazioni stellari multiple dell'ammasso M 22, e di trovare che le due popolazioni visibili nei rami delle sub-giganti di M 22 hanno, entro gli errori delle nostre misure, la stessa distribuzione radiale dal centro dell'ammasso fino a 9 arcominuti.

Successivamente ci spostiamo sul rivelatore VIRCAM montato al telescopio VISTA. Adattiamo nuovamente per questa camera i programmi sviluppati per HAWK-I e correggiamo la distorsione geometrica. La correzione della distorsione si è rivelata ardua perché su campi di vista estesi più di un 1 grado quadrato in cielo gli effetti dovuti alla proiezione della sfera celeste sul piano tangente di un'immagine non sono trascurabili. Per questo motivo, usiamo inizialmente come riferimento il catalogo 2MASS e poi auto-calibriamo la distorsione come fatto per HAWK-I. In questo modo siamo in grado di correggere la distorsione di VIRCAM e di raggiungere un'accuratezza astrometrica di circa 8 mas. Infine usiamo i dati provenienti dalle osservazioni di 'VISTA Variables in the Vía Láctea' (VVV) per calcolare i moti propri delle stelle dell'ammasso globulare M 22. Le osservazioni di VVV non sono concepite per conseguire progetti basati su un'elevata accuratezza astrometrica, ma con i nostri strumenti raggiungiamo una precisione nei moti propri dell'ordine di 1.4 mas $yr^{-}1$, separiamo le stelle di campo da quelle di ammasso, ed inoltre misuriamo la differenza tra il moto proprio delle stelle del Bulge e del Disco della nostra

Galassia nella direzione di M 22.

Nell'ultima parte della tesi descriviamo il progetto focalizzato nello sfruttare i dati dal cacciatore di pianeti *K2*, il successore della missione *Kepler*, ridisegnata dopo i vari problemi in cui è incorsa. L'analisi di ambienti ad alta densità stellare usando i dati *K2* può risultare molto complessa con le classiche tecniche fotometriche (basate sulla fotometria di apertura). Il nostro metodo invece è stato specificatamente elaborato per analizzare queste regioni (ammassi stellari e nella direzione del centro Galattico) e i suoi elementi chiave sono astrometria e fotometria di PSF, cataloghi ad alta risoluzione angolare e sottrazione delle stelle vicine tramite l'utilizzo della PSF.

Inizialmente affrontiamo il problema delle PSFs sottocampionate di *K2* le cui strutture su piccola scala, se non correttamente modellate, possono introdurre errori sistematici che peggiorano l'astrometria e la fotometria. Per questo scopo, seguiamo il metodo iterativo progettato per modellare le PSFs sottocampionate di *HST*. Successivamente utilizziamo un catalogo ad alta risoluzione angolare, ottenuto con telescopi da terra, per identificare tutte le sorgenti rilevabili nel campo e, per ciascuna di esse, misuriamo il flusso dopo aver sottratto tutte le stelle vicine. In questo modo aumentiamo il numero di sorgenti analizzabili nel campo e otteniamo una stima più veritiera del loro flusso. In particolare per stelle variabili, binarie ad eclissi ed esopianeti questo metodo permette di ottenere un valore più realistico della vera ampiezza o profondità dell'eclissi/transito della loro curva di luce poiché diminuiamo gli effetti di diluizione della luce. Questo risvolto è particolarmente importante per gli esopianeti perché altrimenti il vero raggio del pianeta verrebbe sottostimato.

Applichiamo questo metodo alla prima campagna osservativa della missione *K2* in cui sono stati osservati due ammassi aperti (M 35 e NGC 2158) ed estraiamo le curve di luce di più di 50 000 oggetti da un solo canale di lettura di una delle camere *K2*. Questo numero è più del doppio del numero di oggetti normalmente analizzati in tutto il campo di vista di *K2* (76 canali) in una data campagna osservativa. Per le stelle brillanti raggiungiamo una precisione fotometrica di circa 30 parti per milione, un valore confrontabile con quanto si può trovare in altri lavori in letteratura su stelle isolate. Inoltre riusciamo ad estendere la nostra analisi a stelle fino a 5 magnitudini più deboli di quanto studiato in lavori già pubblicati, e mostriamo che per questi oggetti deboli la fotometria di PSF è migliore di quella di apertura. Tale miglioramento è maggiori nei campi a più alta densità stellare. Infine troviamo più di 2000 stelle variabili in questi due ammassi.

Tutti i progetti sviluppati in questa tesi hanno anche interessanti prospettive a lungo termine in quanto possono essere visti come complementari o in preparazione a missioni da spazio future come TESS e PLATO. I candidati pianeti trovati con le osservazioni di *Kepler*/*K2* (ma anche dell'imminente TESS) possono potenzialmente essere target interessanti per JWST, e successivamente per E-ELT.

1 Introduction

Stellar astrometry and photometry require different information about the flux of a star. Astrometry needs to know the detailed flux distribution over the pixels, photometry its total amount. For this reason, most of the reduction software have been focused to extract either good photometry or astrometry. However, there is no reason that we cannot obtain both at the same time. In this thesis, we focus our attention on ground- and space-based wide-field imagers and on their data analysis in order to accomplish this goal.

A detector is defined 'wide-field' imager because of the number of the resolution elements[1] on the sky, not because of its field of view (FoV). Indeed, the number of resolution elements of the *Hubble Space Telescope* (*HST*) Wide-Field Channel 3 (WFC3) detector is comparable to that of the wide-field imager (WFI) mounted at the ground-based 2.2-m MPI/ESO telescope. However, *HST*'s FoV does not cover a large portion of sky as the WFI@2.2-m (there is a factor of ∼150 in the total area). In the last decades, the scientific need has stimulated the planning and the construction of larger wide-field detectors to be placed either on ground- or space-based facilities.

We show that, with a careful point-spread-function (PSF) analysis, geometric-distortion and systematic-error corrections we are able to exploit these new facilities and create complete astro-photometric catalogues with high astrometric and photometric precision and accuracy that can also be used as reference frames in very dense fields as, for example, the centre of globular clusters or the Galactic bulge. More interestingly, we can also use these catalogues to exploit the data coming from wide-field, exoplanet-hunting missions in a completely different way than the classical, standard approach (aperture photometry and crude centroid determination).

1.1 Astrometry background

Astrometry can be either absolute or relative. Absolute astrometry provides positions, proper motions and parallaxes in an inertial reference-frame system. Relative astrometry focuses on the relative positioning of stars in different observations.

Absolute astrometry can be obtained by measuring stellar positions with respect to a net of extragalactic sources. Another more accurate but also more complex way to obtain absolute astrometry is to observe fields separated by large angles on the sky and at different year phases to break the relative-parallax degeneracy and measure the absolute parallax. For the latter option, space-based missions are more suitable due to the lack of atmosphere. This is the case of the European Space Agency (ESA) mission Hipparcos (ESA 1997; Perryman et al. 1997; Perryman 2009) and of its successor, the on-going *GAIA* mission (e.g., Perryman et al. 2001, Lindegren et al. 2008).

Relative astrometry does not need wide-angle observations, since it is based in the relative

[1] This value can be estimated as the ratio between the PSF full-width at half maximum and the size of the detector.

positioning of the stars on a pixel grid. Positions measured in such relative way from a given distortion-free exposure can then be linked to the absolute reference frame of the International Reference Frame System (ICRS) by using HIPPARCOS and, in future, *GAIA* catalogues. For example, the absolute positions of the United States Naval Observatory (USNO) CCD Astrograph Catalog (UCAC, Zacharias et al. 2000) and its four releases were obtained this way with the aim to provide an absolute astrometric catalogue with rather-faint stars, increasing the number of reference stars usable to link a given image to the ICRS, otherwise limited to only bright objects. This is only one of the possible synergies between absolute and relative astrometry. Another by-products of this absolute registration are absolute proper motions with a large time baseline.

However, it is not always necessary to perform absolute astrometry. There are several astronomical topics for which a relative measurement of stellar positions can be enough. This is the case, for example, of proper-motion membership probabilities in stellar clusters. Many *HST* projects are based on relative astrometry and, over the last decade, a huge effort has been made to develop tools for several high-precision-demanding investigations with *HST*'s detectors. Most of the work in this thesis started from this effort on *HST* data.

1.2 From *HST* to ground-based, wide-field imagers astrometry

Anderson & King (2000) showed that, with an appropriate PSF modelling, they were able to reach an astrometric precision at the mas level and an accuracy at the sub-mas level with the Wide-Field Planetery Camera 2 (WFPC2) mounted on the *HST*. Accurate PSFs, together with diffraction-limited images, almost-constant PSFs, no gravity effects and absence of atmosphere, make astrometry and photometry on *HST* images much more accurate than those from ground-based observatories. Over the years, Anderson & King ideas were applied to the subsequent generations of *HST*'s cameras, up to the newest WFC3. Several important projects were achieved by using PSFs to extract high-precision astrometry and photometry as, for example, the discovery of multiple stellar populations in globular clusters (Piotto et al. 2015, and references therein), globular-cluster internal kinematics (Bellini et al. 2014), colour-magnitude diagrams down to the Hydrogen-burning limit (Bedin et al. 2001), absolute proper motions (Bedin et al. 2003, Milone et al. 2006, Massari et al. 2013), white-dwarf cooling sequence analysis (e.g., Bedin et al. 2005, 2015; Bellini et al. 2013).

However, the small FoV offered by *HST*'s detectors do not allow us to undertake a series of scientific projects with a reasonable amount of orbits. For example, globular-clusters' tidal tails are very far from their centres where the low number of cluster members forces us to analyse large portion of the sky to achieve an adequate statistics. For this reason, wide-field imagers mounted at the focal plane of ground-based telescopes can be a valid alternative, as well as complementary, to *HST* even if their data is usually plagued by atmospheric effects because of their much larger FoV despite of a worse accuracy.

The large FoV is not the only main advantage of the ground-based detectors with respect to, e.g., *HST*. The other main advantage is the telemetry. Since ground-based facilities can store a huge amount of data, their detectors can have a reasonably-large size and, therefore, number of resolution elements. As result, these imagers do not need to be undersampled to cover a wide FoV on the sky. In particular for astrometry, this benefit (together with the atmospheric turbulence that usually spread the light of the stars over more pixels during the integration time) translates into a less complicated PSF modelling.

Projects like UCAC, or the newest USNO Robotic Astrometric Telescope (URAT), show that astrometry and photometry with ground-based, wide-field imagers can be very useful. The positional accuracy reached by the forth UCAC-catalogue release (UCAC4, Zacharias et al. 2013) is, depending on the magnitude, of the order of 15-100 mas per coordinate; while the typical positional accuracy in the first release of the URAT catalogue (URAT1, Zacharias et al. 2015) is

about 10-30 mas. However, despite their large FoV (1 and 28 deg^2 respectively), the UCAC- and URAT-dedicated detectors were placed at the focus of a 0.2-m Twin Astrograph. Furthermore, UCAC detector also had a low angular resolution. Using larger telescopes, like ESO's 4- and 8-m-class telescopes, and imagers with a higher angular resolution, there can be a non-negligible room for improvement. Moreover, with a specific data reduction similar to that developed for *HST*, it is possible to create catalogues that are accurate both astrometrically and photometrically.

1.2.1 Our expertise in the field

Our work with ground-based, wide-field imagers started with Anderson et al. (2006) in which they applied the techniques successfully developed for *HST* by Anderson & King (2000) to achieve high-precision astrometry and photometry with the wide-field imager WFI mounted at the 2.2-m MPI/ESO telescope. As a test bed, they computed proper motions for the stars in the field of two globular clusters (M 4 and NGC 6397), successfully separating cluster from field stars with observations taken just a few years apart. Besides a careful PSF modelling, Anderson et al. (2006) pointed out two other important concepts that help to achieve high-precision astrometry (and photometry).

The first key ingredient is a geometric-distortion correction. The combined effects of the field distortion, introduced by the optics of the telescope, different path of the photons due to the filters, detectors defects and misalignment on the focal plane, lead to systematic errors in the measured stellar positions that harms the astrometric accuracy reachable with a given detector. This distortion also affects the photometry, even if at a lower level, because it alters the area of the pixel on the sky[2]. By using an auto-calibration method similar to that described by Anderson & King (2003) for the WFPC2@*HST*, Anderson et al. were able to reach an astrometric precision of about 7 mas in each coordinate for well-measured bright stars.

The second requirement is a local-transformation approach. To compute by how much a star has moved from one epoch to another, we could measure its position in the two epochs relative to a set of reference stars which absolute positions are known with high precision and accuracy. However, such net of stars is not always available. Therefore it is typically more convenient to measure the displacement of a given star relative to the bulk motion of a group of stars (e.g., members of a globular cluster initially selected from a colour-magnitude diagram as in Anderson et al. 2006). In addition, the geometric distortion is not stable over time, especially from ground, and it usually varies over large spatial scales. Therefore, to compute stellar proper motions and minimise uncorrected distortion residuals, the reference stars must be spatially close to the target star. This local, relative approach can be very suitable for astrometric (e.g., for proper motions or to register photometric time-series) and photometric (to register the fluxes in two different exposures without including large-scale effects) purposes.

Thanks to the software packages and the techniques made available for the WFI@2.2 m MPI/ESO, new astrometric and photometric scientific investigations were made possible, with astro-photometric catalogues that can be more precise (due to the higher resolution of the imagers) and accurate with respect to the Two Micron All Sky Survey (2MASS, Skrutskie et al. 2006) or UCAC. For example, Yadav et al. (2008) made an astro-photometric and proper-motion catalogue for the open cluster M 67 (recently improved with the same techniques using the wide-field imager mounted at the Asiago Schmidt Telescope by Nardiello et al. 2016). With the same instrument, Bellini et al. (2009a) also made a catalogue for 360 000 stars in the 33×33 arcmin^2 around the globular cluster ω Cen. This catalogue was then used to study the radial distribution of the multiple stellar populations hosted by ω Cen (Bellini et al. 2009b).

[2]But it can be that the true pixel area is not homogeneous across the detector, e.g., the 34$^{\rm th}$ row of the WFPC2@*HST* described in Anderson & King (1999) or the lithographic discontinuity of the WFC3@*HST* in Bellini, Anderson, & Bedin (2011).

1.2.2 The role of this thesis

After these papers and their promising results, the same techniques were exported by Bellini & Bedin (2010) to another ground-based, wide-field imager, the Large Binocular Camera (LBC) of the Large Binocular Telescope (LBT). Again, the careful PSF modelling, geometric-distortion correction and local-transformation approach, allowed Bellini et al. (2010a,b) to study the end of the white-dwarf cooling sequence of M 67, and measure the absolute cluster's motion. More recently, LBC@LBT was used to study ultra-faint dwarf galaxies (Fabrizio et al. 2014) [see also Chapter 4 in this thesis for the improvement made to the LBC@LBT geometric-distortion correction]. It is straightforward to adapt the same methodology to other optical wide-field imagers, as shown in Bellini et al. (2010a,b) for the UH8K@CFHT or for the CCD mounted at the Asiago Schmidt Telescope presented by Nardiello et al. (2015a) [see also Chapter 4 for the geometric-distortion correction we made for this detector].

In this thesis, we extend these techniques (PSF modelling, geometric-distortion correction and local, relative astrometry) to other ground-based, wide-field imagers with the aim of creating astro-photometric and proper-motion catalogues of unprecedented accuracy to be used for different scientific projects. We mainly focus on near-infrared (NIR) detectors, driven by the always-increasing attention of the international community for this wavelength regime. After cornerstone missions like Spitzer (Werner et al. 2004), 2MASS and WISE (Wright et al. 2010), the demand of the astronomical community led to the installation of NIR detectors with higher quality and size at the foci of many telescopes. The next-generation of NIR telescopes will be led by the James Webb Space Telescope (JWST). JWST is the next NASA space mission that should be launched in 2018. With its larger collecting area and new technologies, JWST will increase the number of feasible projects, as well as complete those made by *HST*. Another possible synergy will be with the *GAIA* mission. As for ground-based, wide-field NIR imagers, JWST data will be complementary to that of *GAIA*, especially in crowded environments and toward heavily-absorbed regions of the Galaxy that are out of *GAIA*'s reach. To be ready for when JWST will become operative, we start to work with two NIR wide-field imagers mounted at the foci of two ESO telescopes: HAWK-I@VLT (Chapter 2) and VIRCAM@VISTA (Chapter 3).

We mainly analyse crowded regions like stellar clusters and the Galactic bulge and disc, and release to the community stellar catalogues and geometric-distortion corrections for these detectors. There are different stand-alone projects for which these catalogues are very helpful, but one of the most interesting is the exploitation of the data of wide-field, exoplanet surveys, present and future. It is to this particular context that the second part of this thesis is dedicated.

1.3 Wide-field imagers in the golden-rush of the exoplanet search

After the first discovered exoplanets (Wolszczan & Frail 1992, Mayor & Queloz 1995), the exoplanet search has raised exponentially, stimulating the construction of new telescopes and instruments to be dedicated to this hunting with different techniques, either direct or indirect. With this respect, the most productive projects are those focused on transiting exoplanets using photometry. To date, several dedicated programs were developed, both from ground- and from space-based facilities. Most of them make use of wide-field imagers, due to the need of simultaneously monitoring the largest number of stars possible. Even if ground-based surveys, such as OGLE (Udalski et al. 1992), TrES (Alonso et al. 2004), HAT (Bakos et al. 2004), SuperWASP (Pollacco et al. 2006), XO (McCullough et al. 2005), are still leading to several important discoveries, space-based missions have the obvious advantage of being outside the atmosphere that, together with longer and uninterrupted observations, make them the most interesting.

Without leaving behind the 8-d WFPC2@*HST* photometric campaign of Gilliland et al.

(2000), or the SWEEPS campaign with *HST* Advanced Camera for Surveys (Sahu et al. 2008), one of the first noteworthy photometric, exoplanet-dedicated survey was COROT (COnvection ROtation and planetary Transits, Baglin et al. 2006, Auvergne et al. 2009). This space-based telescope operated from 2007 to 2013 and alternately observed two fields for 6 months at time in the direction of the centre and the anti-centre of the Galaxy.

The breakthrough in the exoplanet discovery was the NASA satellite *Kepler* (Borucki et al. 2010). This mission was developed to determine the frequency of Earth-like planets orbiting Sun-like stars within the habitable zone. *Kepler* observed the same $\sim$110-deg^2 field toward the Lyra and Cygnus constellations (far from the Ecliptic to avoid Sun light entering in the *Kepler* focal plane) for four years, measuring about 150 000 targets. As of January 2016, the number of confirmed exoplanets discovered by this mission[3] is 1042.

In 2012 and 2013, two reaction wheels of the *Kepler* spacecraft failed and the same accurate, stable pointing as in the previous years was not achievable anymore. The workaround that NASA found was to change the observed field and point several fields toward the Ecliptic to use the Sun radiation pressure to balance the spacecraft drift. Hence, in 2014 *Kepler*-2.0, or simply *K2*, started (Howell et al. 2014).

1.3.1 Crowded environments in *K2*

K2 is observing four fields per year. Each field is imaged contiguously for 80 d using the 38 still-working CCDs of *Kepler*. The large variety of observed fields across the Ecliptic, covered during the so-called *K2* Campaigns, offers the opportunity to widen the scientific range of the mission, increasing the number of astrophysical projects doable with *K2* data. For example, in different *K2* Campaigns, several crowded regions, either stellar clusters (mainly open clusters but also a few globular clusters) or regions toward the Galactic centre, have been and will be imaged.

Most of the *K2* data analysis focus on bright, isolated objects. Indeed, the complicated data reduction of undersampled images (as those of *Kepler* and *K2*) in order to obtain high-precision and high-accuracy astrometry and photometry is a hurdle difficult to overcame. Therefore, faint stars and crowded regions are often not searched for transiting exoplanets or are target of other scientific investigations. In this way, only the tip of the iceberg in number of analysable sources has been scratched and, therefore, the potential of *K2* has not been completely exploited yet. In this thesis, we develop a new, independent approach to study these little-considered objects. We show (Chapters 5 and Conclusions) that, by starting from our experience on *HST*'s undersampled images and on ground-based, wide-field detectors (and by using their high-angular-resolution astro-photometric catalogues) we are able to exploit the data coming from *K2* mission, focusing on these crowded environments. Our approach is based on the subtraction of the close-by neighbours before measuring the flux of a given target, in order to better estimate its true flux.

1.3.1.1 Exoplanets in stellar clusters

Our principal targets are stellar clusters, for which the huge amount of *K2* data has the potential to cover a wide range of astrophysical topics. Among the possible applications, the search for exoplanets hosted by cluster stars is one of the most interesting studies. Indeed, open and globular clusters represent an extremely-important test bench for planetary-formation models. By using the *K2* data of these clusters, we have the unique opportunity to study how the environment affects exoplanet formation, evolution and frequency.

Apart from *Kepler*/*K2*, several photometric campaigns have been performed either on globular or open clusters. The main advantage with respect to radial-velocity surveys is that imaging can measure more fainter stars simultaneously, though the transit probability is very low.

[3] http://exoplanetarchive.ipac.caltech.edu/

Four globular clusters have been surveyed so far. With *HST*, Gilliland et al. (2000) observed the core of 47 Tuc for 8 d, with no transit events detected, concluding that metallicity and/or crowding affected the exoplanet formation and evolution in the cluster. More recently, a 33-d extensive ground-based campaign on the outskirts of 47 Tuc, done by Weldrake et al. (2005), resulted in the same null detection. No exoplanets were also found by Weldrake, Sackett, & Bridges (2008) in ω Cen, by Nascimbeni et al. (2012) in NGC 6397 and by Nascimbeni et al. (2014) in M 4. To date (January 2016), only one planet has been found in a globular cluster, the planetary system in M 4 made by a pulsar, a white dwarf and a $\sim$2.5-$M_{\rm Jup}$ exoplanet (Thorsett et al. 1999, Sigurdsson et al. 2003). Among open clusters, many observational campaigns have been carried out, for example those on NGC 2158 (Mochejska et al. 2006), NGC 6791 (Mochejska et al. 2005; Montalto et al. 2007), M 44 (Pepper et al. 2008), M 37 (Hartman et al. 2009). To date, seven candidate (Lovis & Mayor 2007, Sato et al. 2007, Pepper et al. 2008, Meibom et al. 2013) and eight confirmed (Quinn et al. 2012, 2014, Brucalassi et al. 2014, Mann et al. 2015, Malavolta et al. 2016) exoplanets orbiting cluster stars have been found, of which only four candidate and one confirmed exoplanets have been discovered using photometry.

The techniques that we develop and apply to the *K2*-Campaign 0 data set imaging the open clusters M 35 and NGC 2158 (Chapter 5) are a powerful tool to search for exoplanets in these environments. Indeed, we are able to increase the number of analysable stars and decrease the light-dilution effects. The latter benefit is particularly important in the case of stars with transiting exoplanets because a correct knowledge of the stellar flux and of the transit depth translates in a better estimate of the exoplanet radius, otherwise under-estimated in these crowded regions. By carefully handling its data, the 80-d uninterrupted observations of *K2* will confirm or radically change our currently understanding of exoplanets in stellar clusters.

1.3.1.2 Ancillary topics

Exoplanets are not the only interesting objects to study with *K2* data. Indeed, the stellar clusters imaged during the *K2* Campaigns (but also those covered during the *Kepler* main mission, namely NGC 6791, NGC 6811, NGC 6819 and NGC 6866) are an invaluable resource for several astrophysics topics, for example:

- Gyrochronology. As noted for the first time by Skumanich (1972), stellar rotation decreases as stars get old. For low-mass stars, there is a dependency among the surface rotation period, the age and the colour. By measuring colour and rotation period of the stars, we can therefore estimate the stellar age (gyrochronology). From the observational point of view, in young stellar clusters the period versus colour diagram shows a well-defined dichotomy: a diagonal sequence where the period increases with the colour, and a sequence with only fast-rotating stars at all colours. Barnes (2003, 2007) suggested that these two sequences can be associated to two distinct dynamo mechanisms that create the magnetic field of the stars. Several works and projects (e.g., Mamajek & Hillenbrand 2008; Meibom, Mathieu, & Stassun 2009; Meibom et al. 2011, 2015) have been developed on this research field. With over 10 stellar clusters observed and with high photometric precision, *K2* data can be very precious to gyrochronology, in particular to understand more in detail the mechanisms behind this observed dichotomy, as well as to better calibrate the rotation-age-colour relationships.

- Detached eclipsing binaries. *K2* offers the opportunity to discover new eclipsing binaries in stellar clusters. Once these binaries are identified in a colour-magnitude diagram, it is possible to disentangle the two components and put them on a mass-radius diagram. Using systems made by at least one star close to the main-sequence turn-off, age and chemical composition, in particular Helium, can then be derived with an accuracy better than 1% by comparing these measured masses and radii with theoretical tracks (e.g., Brogaard et al. 2011, 2012). If detached eclipsing binaries are members of stellar clusters, the advantage in

studying these objects is that distance, reddening and metallicity dependencies are removed. For example, Brogaard et al. (2012), combining photometry and spectroscopy, measured masses and radii of the components of two binary systems members of NGC 6791 with an accuracy better than 1%, and estimated the cluster age (∼8.3 Gyr) and its Helium content ($Y \sim 0.30 \pm 0.01$). Last, this method can be very useful for globular clusters. Indeed, many globular clusters host multiple stellar populations with different Helium abundances (e.g., ω Cen, where its blue main sequence reaches a value of Y∼0.39, King et al. 2012). In *K2* Campaign 2, the globular cluster M 4 has been observed. By analysing eclipsing binaries belonging to each stellar population, we can independently determine the Helium abundance of M 4 populations (that have ΔY∼0.02, Nardiello et al. 2015b, and reference therein).

- Asteroseismology. Even if the *K2* photometric precision is worsen by the larger spacecraft pointing jitter, the various fields observed in every Campaign allow us to study the stellar oscillations and therefore the stellar interior and parameters (like age, mass and radius) for different populations (e.g., young and old stars, cluster and field stars). Another interesting (but not easy) way to use asteroseismology is to identify cluster members, as done by Stello et al. (2011) with *Kepler* data for NGC 6791, NGC 6811 and NGC 6819.

Besides stellar clusters, Galactic-bulge fields are additional crowded regions for which the methodology described in this thesis will be perfectly suitable. The Galactic centre will be observed during *K2* Campaigns 9 and 11 (see Conclusions).

Another extension of our work comes from the fact that, in *Kepler*/*K2*, 'crowding' is a relative concept. Indeed even a star in a rather-sparse field could have close-by neighbours within a few arcsec which light contamination can prevent a correct target-flux estimate[4]. The procedures described in Chapter 5 can also be applied to this particular case, and therefore be useful to extract high-precision photometry over the entire *K2* FoV of a given Campaign.

1.3.1.3 Extension to future space missions

Finally, it is worth to mention that all the efforts made for *Kepler*/*K2* can be seen in preparation to the next space-based projects that will search for exoplanets: TESS (Ricker et al. 2014) and PLATO (Rauer et al. 2014). These missions have many characteristics similar to those of *Kepler* and *K2* (see Conclusions), and their data can be exploited by using techniques exported from the work described in this thesis.

Bibliography

Alonso R., et al., 2004, ApJ, 613, L153

Anderson J., King I. R., 1999, PASP, 111, 1095

Anderson, J., & King, I. R. 2000, PASP, 112, 1360

Anderson, J., & King, I. R. 2003, PASP, 115, 113

Anderson J., Bedin L. R., Piotto G., Yadav R. S., Bellini A., 2006, A&A, 454, 1029

Auvergne M., et al., 2009, A&A, 506, 411

Baglin A., et al., 2006, cosp, 36, 3749

[4]With the typical angular resolution and full-width at half maximum on the UVIS/WFC3@*HST*, two stars separated by 4 arcsec (100 UVIS/WFC3@*HST* pixels) on the sky are not hard to measure with aperture photometry. This is not the case for *Kepler*/*K2* where, with a pixel scale of 4 arcsec pixel^{-1} and a full-width at half maximum of ∼1.5 *Kepler* pixels, the two stars would fall within the same *Kepler* pixel.

Bakos, G., Noyes, R. W., Kovács, G., et al. 2004, PASP, 116, 266

Barnes S. A., 2003, ApJ, 586, 464

Barnes S. A., 2007, ApJ, 669, 1167

Bedin L. R., Anderson J., King I. R., Piotto G., 2001, ApJ, 560, L75

Bedin L. R., Piotto G., King I. R., Anderson J., 2003, AJ, 126, 247

Bedin L. R., Salaris M., Piotto G., King I. R., Anderson J., Cassisi S., Momany Y., 2005, ApJ, 624, L45

Bedin L. R., Salaris M., Anderson J., Cassisi S., Milone A. P., Piotto G., King I. R., Bergeron P., 2015, MNRAS, 448, 1779

Bellini A., et al., 2009a, A&A, 493, 959

Bellini A., Piotto G., Bedin L. R., King I. R., Anderson J., Milone A. P., Momany Y., 2009b, A&A, 507, 1393

Bellini A., et al., 2010a, A&A, 513, A50

Bellini A., Bedin L. R., Pichardo B., Moreno E., Allen C., Piotto G., Anderson J., 2010b, A&A, 513, A51

Bellini A., Bedin L. R., 2010, A&A, 517, A34

Bellini A., Anderson J., Bedin L. R., 2011, PASP, 123, 622

Bellini A., Anderson J., Salaris M., Cassisi S., Bedin L. R., Piotto G., Bergeron P., 2013, ApJ, 769, L32

Bellini A., et al., 2014, ApJ, 797, 115

Borucki W. J., et al., 2010, Sci, 327, 977

Brogaard K., Bruntt H., Grundahl F., Clausen J. V., Frandsen S., Vandenberg D. A., Bedin L. R., 2011, A&A, 525, A2

Brogaard K., et al., 2012, A&A, 543, A106

Brucalassi A., et al., 2014, A&A, 561, L9

ESA, 1997, ESASP, 1200,

Fabrizio M., et al., 2014, A&A, 570, A61

Gilliland R. L., et al., 2000, ApJ, 545, L47

Hartman J. D., et al., 2009, ApJ, 695, 336

Howell S. B., et al., 2014, PASP, 126, 398

King I. R., et al., 2012, AJ, 144, 5

Lindegren L., et al., 2008, IAUS, 248, 217

Lovis C., Mayor M., 2007, A&A, 472, 657

Malavolta L., et al., 2016, A&A, accepted for publication on 2016 January 26

Mamajek E. E., Hillenbrand L. A., 2008, ApJ, 687, 1264

Mann A. W., et al., 2015, arXiv, arXiv:1512.00483

Massari D., Bellini A., Ferraro F. R., van der Marel R. P., Anderson J., Dalessandro E., Lanzoni B., 2013, ApJ, 779, 81

Mayor M., Queloz D., 1995, Natur, 378, 355

McCullough, P. R., Stys, J. E., Valenti, J. A., et al. 2005, PASP, 117, 783

Meibom S., Mathieu R. D., Stassun K. G., 2009, ApJ, 695, 679

Meibom S., et al., 2011, ApJ, 733, L9

Meibom S., et al., 2013, Nature, 499, 55

Meibom S., Barnes S. A., Platais I., Gilliland R. L., Latham D. W., Mathieu R. D., 2015, Nature, 517, 589

Milone A. P., Villanova S., Bedin L. R., Piotto G., Carraro G., Anderson J., King I. R., Zaggia S., 2006, A&A, 456, 517

Mochejska B. J., et al., 2005, AJ, 129, 2856

Mochejska B. J., et al., 2006, AJ, 131, 1090

Montalto M., et al., 2007, A&A, 470, 1137

Nardiello D., et al., 2015a, MNRAS, 447, 3536

Nardiello D., Milone A. P., Piotto G., Marino A. F., Bellini A., Cassisi S., 2015b, A&A, 573, A70

Nardiello D., Libralato M., Bedin L. R., Piotto G., Ochner P., Cunial A., Borsato L., Granata V., 2016, MNRAS, 455, 2337

Nascimbeni V., Bedin L. R., Piotto G., De Marchi F., Rich R. M., 2012, A&A, 541, A144

Nascimbeni V., et al., 2014, MNRAS, 442, 2381

Pepper, J., Stanek, K. Z., Pogge, R. W., et al. 2008, AJ, 135, 907

Perryman M. A. C., et al., 1997, A&A, 323, L49

Perryman M. A. C., et al., 2001, A&A, 369, 339

Perryman M., 2009, aaat.book

Piotto G., et al., 2015, AJ, 149, 91

Pollacco, D. L., Skillen, I., Collier Cameron, A., et al. 2006, PASP, 118, 1407

Quinn S. N., et al., 2012, ApJ, 756, L33

Quinn S. N., et al., 2014, ApJ, 787, 27

Rauer H., et al., 2014, ExA, 38, 249

Ricker G. R., et al., 2014, SPIE, 9143, 914320

Sahu, K. C., Casertano, S., Valenti, J., et al. 2008, Extreme Solar Systems, 398, 93

Sato B., et al., 2007, ApJ, 661, 527

Sigurdsson S., Richer H. B., Hansen B. M., Stairs I. H., Thorsett S. E., 2003, Sci, 301, 193

Skrutskie, M. F., Cutri, R. M., Stiening, R., et al. 2006, AJ, 131, 1163

Skumanich A., 1972, ApJ, 171, 565

Stello D., et al., 2011, ApJ, 739, 13

Thorsett S. E., Arzoumanian Z., Camilo F., Lyne A. G., 1999, ApJ, 523, 763

Udalski, A., Szymanski, M., Kaluzny, J., Kubiak, M., & Mateo, M. 1992, ACTAA, 42, 253

Weldrake D. T. F., Sackett P. D., Bridges T. J., Freeman K. C., 2005, ApJ, 620, 1043

Weldrake D. T. F., Sackett P. D., Bridges T. J., 2008, ApJ, 674, 1117

Werner M. W., et al., 2004, ApJS, 154, 1

Wolszczan A., Frail D. A., 1992, Natur, 355, 145

Wright E. L., et al., 2010, AJ, 140, 1868-1881

Yadav R. K. S., et al., 2008, A&A, 484, 609

Zacharias N., et al., 2000, AJ, 120, 2131

Zacharias N., Finch C. T., Girard T. M., Henden A., Bartlett J. L., Monet D. G., Zacharias M. I., 2013, AJ, 145, 44

Zacharias N., et al., 2015, AJ, 150, 101

2 High-precision astrometry with HAWK-I

High-precision astrometry requires accurate point-spread function modelling and accurate geometric-distortion corrections. In this Chapter we show that it is possible to achieve both requirements. For the former, we use the same techniques developed for the *Hubble Space Telescope* and then successfully applied to wide-field, ground-based imaging by Anderson et al. (2006). For the latter, we show that, by performing an auto-calibration, we are able to reach an astrometric accuracy of a few mas over the entire field of view for the near-infrared imager HAWK-I@VLT. Here and in the following Chapters we show how deep, complete and high-angular-resolution catalogues obtained this way with such detectors can also be used to exploit the data coming from wide-field, space-based surveys. The material discussed in this Chapter has been published in Astronomy and Astrophysics (A&A)[1].

2.1 Introduction

Multiple fields within astronomy are driving the execution of larger and yet larger surveys of the sky. Over the last two decades, this scientific need has stimulated the construction of instruments equipped with mosaics of large-format digital detectors for wide-field imaging at both the optical and near-infrared (NIR) wavelengths. The most recent generation of these wide-field imagers now competes with the older technology of Schmidt telescope and photographic plates in terms of number of resolution elements on sky but does so with order-of-magnitude greater sensitivity and efficiency.

A list of some widely-used wide-field imagers was given by Anderson et al. (2006, hereafter Paper I). Since then, however, many wide-field imagers have been upgraded or decommissioned, and additional new wide-field imagers have begun their operations. In the top-half of Table 2.1, we provide a brief list of the major operative wide-field imagers on 3 m+ telescopes (we also included the WFI@2.2 m MPI/ESO as reference).

In addition, two wide-field imagers mounted on 1 m telescopes should be mentioned. The LaSilla-QUEST Variability survey is a project that uses the ESO 1.0-m Schmidt Telescope at the La Silla Observatory of the European Southern Observatory in Chile with the new large area QUEST camera. It is a mosaic of 112 600×2400 pixels CCDs covering a field of view of about 4.°6×3.°6. The camera, commissioned in early 2009 has been built at the Yale and Indiana University. La Silla-QUEST survey is expected to cover ∼1000 square degrees per night repeated with a 2-day cadence (Hadjiyska et al. 2012).

The Panoramic Survey Telescope and Rapid Response System (Pan-STARRS) also is of great interest for the astronomical community. The Pan-STARRS survey will cover the sky using wide-

[1]Libralato et al. (2014, A&A, 563, A80) - Received 2013 June 11 / Accepted 2013 December 18.

Table 2.1. List of the major operative wide-field imagers on 3 m + telescopes.

Name	Telescope	Detectors	Pixel Scale [″/pixel]	FoV
		OPTICAL REGIME		
WFI	2.2 m MPI/ESO	8×(2048×4096)	0.238	34′×33′
Prime Focus Camera	William Herschel Telescope	2×(2048×4100)	0.24	16.′2×16.′2
LBC (blue and red)	LBT	4×(2048×4608)	0.23	23′×23′
Suprime-Cam	Subaru Telescope	10×(2048×4096)	0.202	34′×27′
MOSA	KPNO Mayall 4 m	8×(2048×4096)	0.26	36′×36′
LAICA	Calar Alto 3.5 m Telescope	4×(4096×4096)	0.225	44.′36×44.′36
MegaCam	CFHT	36×(2048×4612)	0.187	57.′6×56.′4
OmegaCam	VST	32×(2048×4102)	0.21	60′×60′
DECam	CTIO Blanco 4 m	62×(2048×4096) + 12×(2048×2048)	0.27	132′×132′
		NIR REGIME		
GSAOI	Gemini	4×(2048×2048)	0.02	1.′42×1.′42
HAWK-I	VLT	4×(2048×2048)	0.106	7.′5×7.′5
ISPI	CTIO Blanco 4 m	1×(2048×2048)	0.3	10.′25×10.′25
FourStar	Magellan	4×(2048×2048)	0.159	10.′8×10.′8
WFCAM	UKIRT	4×(2048×2048)	0.4	12.′6×12.′6
Omega2000	Calar Alto 3.5 m Telescope	4×(2048×2048)	0.45	15.′4×15.′4
WIRCAM	CFHT	4×(2048×2048)	0.3	20.′5×20.′5
NEWFIRM	CTIO Blanco 4 m	4×(2048×2048)	0.4	27.′6×27.′6
VIRCAM	VISTA	16×(2048×2048)	0.339	35.′4×35.′4

Notes. The WFI@2.2 m MPI/ESO has been included as reference.

field facilities and provide astrometric and photometric data for all observed objects. The first Pan-STARRS telescope, PS1, is located at the summit of Haleakala on Maui, Hawaii and began full time science observations on May 13, 2010 (Kaiser et al. 2010). With its 1.8 m primary mirror, it covers a FoV of ∼7 square degrees.

Among wide-field imagers planned for the future, the LSST[2] (Large Synoptic Survey Telescope) represents the most significant step forward for wide-field imagers in modern astrophysics. It will be a 8.4 m wide-field ground-based telescope with a FoV of about 9.6 square degrees. With its 189 4k×4k CCDs, it will observe over 20 000 square degrees of the southern sky in six optical bands. Construction operations should begin in 2014; the survey will be taken in 2021.

While a great number of papers have presented photometry obtained with these facilities over the last decade, their astrometric potential has remained largely unexploited. Our team is committed in pushing the astrometric capabilities of wide-field imagers to their limits. Therefore, we have begun to publish on A&A a series of papers on *Ground-based astrometry with wide field imagers*. In Paper I, we developed and applied our tools to data collected with the WFI@2.2 m MPI/ESO telescope. The techniques used in *Paper II* (Yadav et al. 2008) and *Paper III* (Bellini et al. 2009) produced astro-photometric catalogues and proper motions of the open cluster M 67 and of the globular cluster NGC 5139, respectively. In *Paper IV* (Bellini & Bedin 2010), we applied the technique to the wide-field camera on the blue focus of the LBC@LBT 2×8.4 m.

In this Chapter, we turn our attention to wide-field imagers equipped with NIR detectors. Indeed, the pioneering work of 2MASS has shown the great potential of these instruments (Skrutskie et al. 2006). The number and the quality of NIR detectors has improved considerably since then. New generations of 2k×2k arrays are now mounted at the foci of various telescopes (bottom-half of Table 2.1).

These wide-field imagers enable wide surveys, such as the VISTA Variables in the Vía Láctea (VVV, Minniti et al. 2010). The VVV is monitoring the Bulge and the Disc of the Galaxy. The survey will map 562 square degrees over 5 years (2010-2014) and give NIR photometry in Z, Y, J, H, and K_S bands. The first data set of the VVV project has already been released to the community (Saito et al. 2012). It contains 348 individual pointings of the Bulge and the Disc,

[2]http://www.lsst.org/lsst/

taken in 2010 with $\sim 10^8$ stars observed in all filters. Typically, the declared astrometric precision vary from $\sim$25 mas for a star with K_S=15, to $\sim$175 mas for a star with K_S=18 mag.

Ground-based telescopes are not alone in focusing their attention on this kind of detector. The James Webb Space Telescope (JWST) will be a 6.5-meter space telescope optimised for the infrared regime. It will orbit around the Earth's second Lagrange point (L2), and it will provide imaging and spectroscopic data. The wide-field imager, NIRCam, will be made up by a short- (0.6 – 2.3 μm) and a long-wavelength (2.4 – 5.0 μm) channel with a FoV of $2\farcm2 \times 4\farcm4$ each.

In this Chapter, we explore the astrometric performance of the HAWK-I@VLT facility and provide astrometric catalogues (together with stacked images) of seven dense stellar fields along with the tools required to correct any observed field for geometric distortion. We adopt the UCAC 4 catalogue (Zacharias et al. 2013) as a reference frame to determine the linear terms of the distortion and to put all the objects in on the International Celestial Reference System but at the epoch of our observations.

The Chapter is organised as follows: In Sect 2.2, we briefly describe the instrument. Section 2.3 presents the observations. Section 2.4 describes the tools developed to extract the position and flux of the sources. In Sect. 2.5, we derive our geometric-distortion solution. In Sect. 2.6, we discuss the periodic feature of the residual highlighted during the geometric-distortion correction and give a possible explanation. Sections 2.7 and 2.8 describe how we removed the point-spread function (PSF) artefacts from the catalogues and the photometric calibration, respectively. Section 2.9 shows some possible applications of our calibrations. Finally, we describe the catalogues that we release in Sect. 2.10.

2.2 HAWK-I@VLT

An exhaustive description of HAWK-I is given in Kissler-Patig et al. (2008). Here, we only provide a brief summary. The HAWK-I focal plane is equipped with a mosaic of four 2048×2048 pixels Rockwell HgCdTe Molecular Beam Epitaxy HAWAII-2RG arrays. The pixel scale (as described in Kissler-Patig et al. 2008) is about 106 mas pixel^{-1}, resulting in a total FoV of about $7\farcm5 \times 7\farcm5$ (with gaps of $\sim 15''$ between the detectors). A sketched outline of the HAWK-I FoV layout is shown in Fig. 2.1. The detectors and the filter wheel unit are connected to the second stage of the Closed Cycle Cooler and operated at a temperature close to 75–80 K. The remaining parts of the instrument are cooled to a temperature below 140 K. The acquisition system is based on the IRACE system (Infrared Array Control Electronics) developed at ESO. HAWK-I is designed to work with a ground-layer adaptive optics module (GRAAL) as part of the Adaptive Optics Facility (Arsenault et al. 2006) for the VLT (scheduled to be installed in 2016). HAWK-I broad band filters follow the Mauna Kea Observatory specification.

2.3 Observations

In Table 2.2 we provide a detailed list of the observations. All of the HAWK-I images used here were collected during the instrument commissioning, when several fields were observed with the aim of determining an average optical geometric-distortion solution for HAWK-I and for monitoring its stability in the short- and mid-term.

To this end, the fields were observed with an observing strategy that would enable a self-calibration of the distortion. Briefly, the strategy consists of observing a given patch of sky in as many different parts of the detectors as possible. Each observing block (OB) is organised in a run of 25 consecutive images. The exposure time for each image was the integration time (DIT in s) times the number of individual integrations (NDIT). Figure 2.2 shows the outline of the adopted dither-pattern strategy[3].

[3]Note that this strategy had been modified for some fields. We specify these changes, when necessary, in the following subsections.

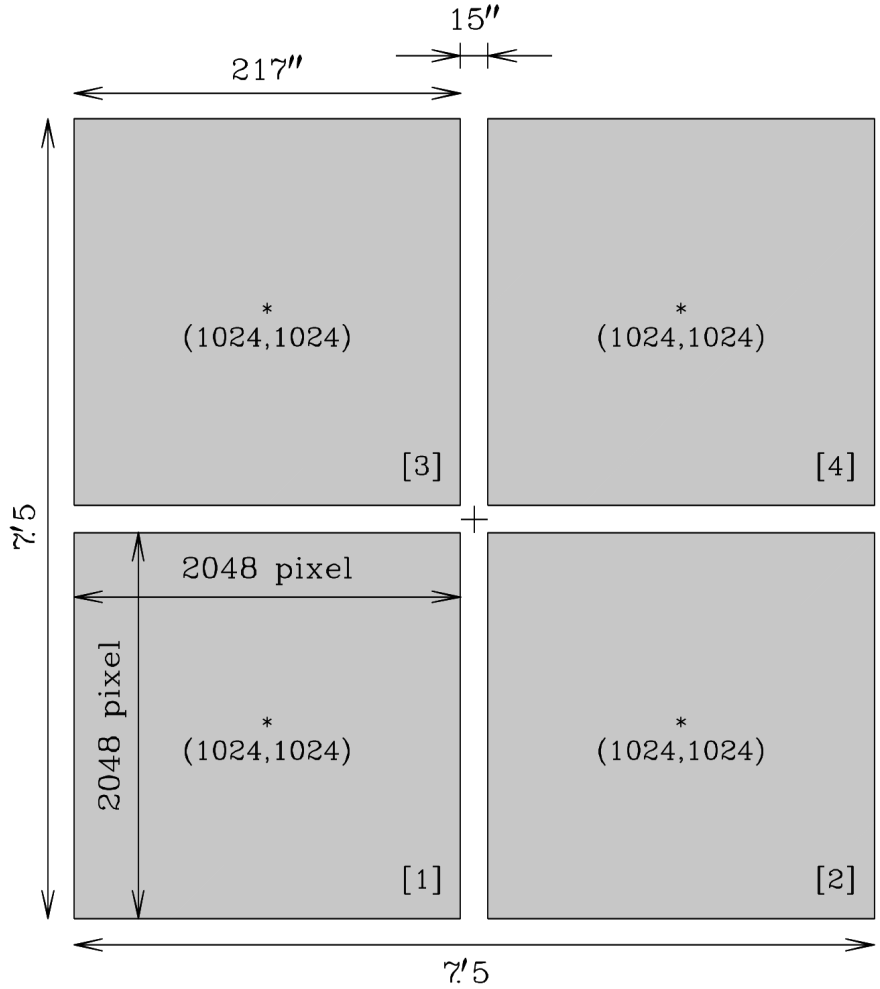

Figure 2.1. HAWK-I layout. The labels give the dimensions in arcsec and arcmin (and in pixels) of the four detectors and of the gaps. Numbers in square brackets label the chip denomination used in this Chapter (note that the choice is different from that of Fig. 9 of Kissler-Patig et al. 2008). In each chip, we indicate the coordinate of the chip centre. This is also the reference position that we used while computing the polynomial correction described in Sect. 2.5.1. The black cross in the middle shows the centre of the field of view in a single exposure that we used in Fig. 2.2.

Important by-products of this effort are *astrometric standard fields* (i.e., catalogues of distortion-free positions of stars), which in principle could be pointed by HAWK-I anytime in the future to efficiently assess whether the distortion has varied and by how much. Furthermore, these astrometric standard fields might serve to calibrate the geometric distortions of many other cameras on other telescopes (including those equipped with AO, MCAO, or those space-based). However, the utility of our fields deteriorate over time since a proper motion estimate for stars in our catalogues is only provided for those stars that are in common with UCAC 4 catalogue. We make these astrometric standard fields available to the community.

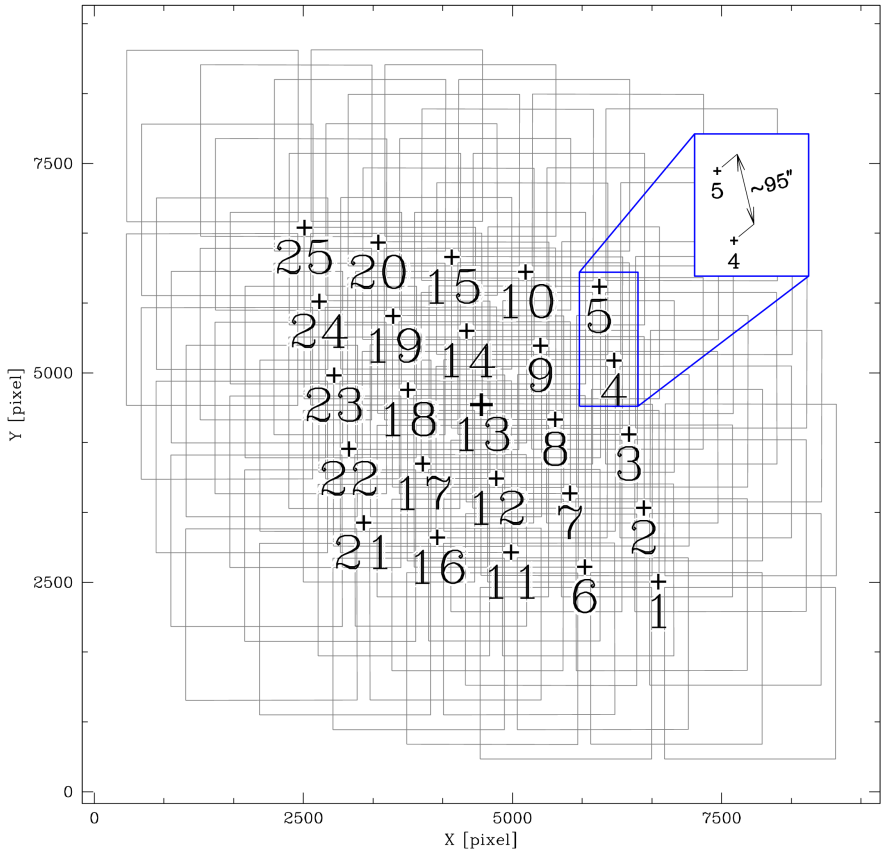

Figure 2.2. Outline of the relative positions of pointings in our adopted dither-pattern strategy. The 25 images are organised in a 5×5 array, where the centre of the field falls in the central position 13. The other pointings are taken in a way that the gaps between the four detectors never cover the same point of sky more than once. The 25 images were designed for astrometric purposes allowing stars in frame 13 to be imaged in as many different locations of the detectors as possible. This enables us to self-calibrate the geometric distortion. The zoom-in in the blue panel shows an example of the adopted dither between two pointings. As described in Table 2.2, the shift step can change from field to field.

2.3.1 The Baade's Window astrometric field

The first selected astrometric field is located in Baade's Window. Our field is centred on coordinates $(\alpha, \delta)_{\mathrm{J2000.0}} \sim (18^{\mathrm{h}}03^{\mathrm{m}}10\overset{\mathrm{s}}{.}4, -29°56'48\overset{''}{.}4)$. Most of this field has a smooth, uniform distribution of Galactic Bulge stars.

Stars just below saturation in a 60 s K_{S} exposure are typically separated by a few arcsec, so that there are many of them in each field. In general, however, they are sufficiently isolated to allow us to compute accurate positions. The choice of a cumulative integration time of 60 s was driven by two considerations. First, we wanted to have the upper main sequence in a colour-magnitude diagram (CMD) of all chosen targets to be optimally exposed with low-luminosity red-giant-branch (RGB) stars still below the saturation threshold. Second, the large-scale semi-periodic and correlated atmospheric noise (with estimated scale length at ∼3-5′) noted by Platais et al. (2002) and Platais, Wyse, & Zacharias (2006) essentially disappears at exposures exceeding 30 s. Thus, 60 s was a good compromise of integration time.

Table 2.2. List of the HAWK-I@VLT data set used in this Chapter. N_{dither} is the number of dithered images per observing block. "Step" is the dither spacing (shift in arcsec from one exposure to the next one). The integration time (DIT) times the number of individual integrations (NDIT) gives the exposure time. σ(Radial residual) gives an assessment of the astrometric accuracy reached (see Sect. 2.5.5 for the full description).

Filter	N_{dither}	Step (arcsec)	Exposure Time (NDIT×DIT)	Image-quality (arcsec)	Airmass (sec z)	σ(Radial residual) (mas)
			***Commissioning 1**, August 3-6, 2007*			
			Bulge — Baade's window (#1)			
J	25	95	(6×10 s)	0.56-1.07	1.038-1.085	4.5
H	25	95	(6×10 s)	0.40-0.76	1.081-1.149	4.3
K_S	25	95	(6×10 s)	0.25-0.45	1.042-1.091	2.8
			Bulge — Baade's window (Rotated by 135°) (#2)			
K_S	25	95	(6×10 s)	0.49-0.85	1.015-1.044	5.6
			NGC 6121 (M 4)			
J	4×25	95	(6×10 s)	0.36-1.04	1.010-1.540	6.5
K_S	5	140	(6×10 s)	0.40-0.51	1.050-1.056	3.8
			NGC 6822			
J	9	190	(12×10 s)	0.61-0.83	1.028-1.049	5.3
K_S	9	190	(12×10 s)	0.43-0.75	1.050-1.082	4.8
			***Commissioning 2**, October 14-19, 2007*			
			NGC 6656 (M 22)			
K_S	25	47.5	(6×10 s)	0.28-0.41	1.252-1.420	3.1
			NGC 6388			
J	25	95	(6×10 s)	0.64-0.94	1.287-1.428	9.7
K_S	25	95	(6×10 s)	0.50-0.75	1.436-1.637	12.2
			JWST calibration field (LMC)			
J	25	95	(6×10 s)	0.51-0.65	1.408-1.412	5.3
K_S	24	95	(6×10 s)	0.45-0.60	1.411-1.429	4.8
			***Commissioning 3**, November 28-30, 2007*			
			NGC 104 (47 Tuc)			
J	25	47.5	(6×10 s)	0.51-0.82	1.475-1.479	7.1
K_S	23	47.5	(6×10 s)	0.54-1.01	1.475-1.483	15.0

According to the formula developed by Lindegren (1980) and Han (1989), a standard deviation due to atmospheric noise on the order of 15 mas is expected over the angular extent of HAWK-I FoV. This certainly is an upper limit of the actual standard deviation because the seeing conditions of our NIR observations were 2-3 times better than those considered by the aforementioned authors for visual wavelengths. The images were also taken close to the zenith in an effort to minimise differential refraction effects, which plague ground-based images (and consequently affect the estimate of the low-order terms of the distortion solution).

The Baade's Window field is the main field we use to derive the geometric-distortion solution that is tested for stability –or refined– with the other fields. In Sect. 2.5, we derive the geometric-distortion solution in this field for each of the three available filters, J, H and K_S, using 25 images dithered with a step of about 95″. In addition to this, we also collected 25 K_S images of the same field but with the de-rotator at a position of 135° clockwise. We used this field to perform a check of the distortion with different angles (see Sect. 2.5.8).

In Fig. 2.3, we show a summary of one of these observing runs in filter K_S from left to right: the overlap of the different pointings, the stacked image, a zoom-in of the region actually used to calibrate the geometric distortion (the region highlighted in green), and a further zoom-in at a resolution able to reveal individual pixels (region indicated in red in the other panels).

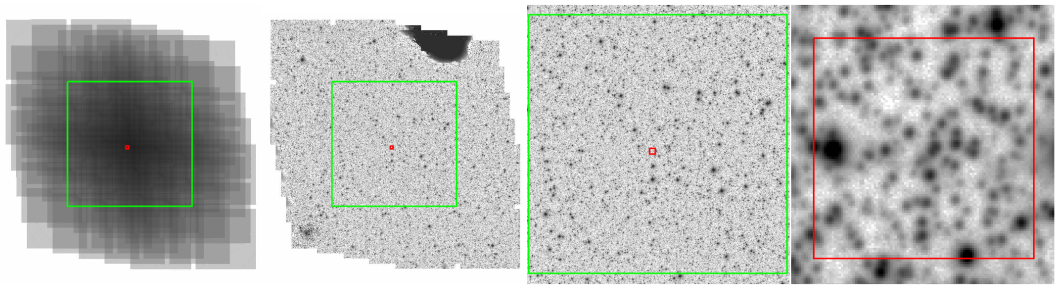

Figure 2.3. From left to right. First panel: a depth-of-coverage map of 25 K_S HAWK-I's images collected in Baade's window during the run of August 3-6, 2007. The grey-scale goes linearly from 1 to 25. The green box is the $7\farcm5 \times 7\farcm5$ patch of sky within which there are always at least five images. Second panel: resulting stack of the 25 images. The dark spot on the top-right is the signature left by the "shadow" of the probe, which pick-up the star used for the simultaneous Active Optic correction of the VLT/UT4's primary mirror. On the bottom-left, there is the globular cluster NGC 6522. Note that neither the dark spot nor NGC 6522 are inside the region enclosed by the green box. Third panel: focus on the green region that shows that the distribution of stars in this field is remarkably homogeneous. Fourth panel: zoom-in of a representative sub-set of the field (indicated by the $10'' \times 10''$ red box in all panels), which is able to show a better resolved image.

2.3.2 The star-cluster astrometric fields

The tangential internal motions of Bulge stars is on average 100 km s^{-1}, and assuming an average distance of 8 kpc, this yields a proper motion dispersion of $\sim$3 mas yr^{-1} (see, for example, Bedin et al. 2003). In just a few years, proper motions this large can mask out systematic distortion trends that have amplitudes below the 3-mas-yr^{-1} level (such as those discussed in Sect. 2.5.2). It is therefore important in some applications to have more stable astrometric fields.

For this reason, we also observed four globular clusters. Stars gravitationally bound in globular clusters have an internal velocity dispersion $\lesssim$20 km s^{-1} in their cores and are even smaller in their outskirts. Although the systemic motion of star clusters is usually different to (and larger than) the Galactic field dispersion, their common rest-frame motions are generally more than 10 times smaller than the internal motions of Bulge stars, so clusters members can be expected to serve as astrometric standards with much smaller internal proper motions.

2.3.2.1 NGC 6656 (M 22)

The second field was centred on the globular cluster NGC 6656 (M 22). At a distance of about 3.2 kpc, M 22 $(\alpha, \delta)_{\rm J2000.0} = (18^{\rm h}36^{\rm m}23\fs94, -23^\circ54'17\farcs1$, Harris 1996, 2010 edition) is one of the closest globular clusters to the Sun.

These data were impacted by an internal reflection of the Moon in the optics, causing an abnormally-high sky value on the rightmost 300 pixels of the detector. In spite of this, the exquisite image quality of these data makes them among the best in our database. We used this field to test the solution of the geometric distortion (see Sect. 2.5.7 for detail).

2.3.2.2 NGC 6121 (M 4)

The third field is centred on globular cluster NGC 6121 (M 4), $(\alpha, \delta)_{\rm J2000.0} = (16^{\rm h}23^{\rm m}35\fs22,$ $-26^\circ31'32\farcs7$, Harris 1996, 2010 edition). It is the closest globular cluster to the Sun, and its rich star field has a small angular distance from the Galactic Bulge.

The observing strategy for the J-filter is similar to that described before. Each OB is organised in a run of 25 consecutive exposures and the the same block was repeated four times in four different nights, shifting the grid by few arcsec each time.

This field was also observed in the K_S-filter but with a dither pattern completely different from the others. There are only five exposures dithered with steps of $100''$, which are taken with the purpose of estimating stars' colour.

2.3.2.3 NGC 6388

NGC 6388 is a globular cluster located in the Galactic Bulge at $(\alpha, \delta)_{J2000.0} = (17^h36^m17^s.23, -44^o44'07''.8$, Harris 1996, 2010 edition). Some exposures of this field show the same dark spot due to the probe as in the Baade's window (see Fig. 2.3).

2.3.2.4 NGC 104 (47 Tuc)

The last globular cluster observed during the HAWK-I commissioning is NGC 104 (47 Tuc), $(\alpha, \delta)_{J2000.0} = (00^h22^m05^s.67, -72°04'52''.6$, Harris 1996, 2010 edition). Two of the 25 pointings of the K_S-filter data were not usable.

2.3.3 The Extra-Galactic astrometric fields

Extra-galactic fields are more stable than Galactic fields, since their internal proper motions are negligible compared to foreground stars, even with a 10-yr time baseline. The downside of such extra-galactic fields is the need to increase the integration time to compensate for the faintness of the targets.

2.3.3.1 NGC 6822

The first extra-galactic field is centred on the Local Group dwarf irregular galaxy NGC 6822 at a distance of ∼500 kpc (Madore et al. 2009).

For this galaxy, we took fewer pointings (9 in a 3×3 array) but with a longer integration time. Adopting the same numbers as in Fig. 2.2, we only used dithers labelled 1, 3, 5, 11, 13, 15, 21, 23, and 25. The integration time was 120 s with NDIT=12 and DIT=10 s.

2.3.3.2 An astrometric field for JWST in LMC

In 2005, a field near the centre of the Large Magellanic Cloud (LMC) was selected as reference field to solve for the geometric distortion and to eventually help calibrate the relative positions of JWST's instruments in the focal plane. This field is in the JWST continuous viewing zone and it can be observed whenever necessary. In 2006, it was observed with the Advanced Camera for Surveys (ACS) Wide Field Channel (WFC) to create a reference catalogue in F606W.

The field is centred at $(\alpha, \delta)_{J2000.0} = (5^h21^m55^s.87, -69°29'47''.05)$. The distortion-corrected star catalogue we provide can be used as distortion-free frame to compute the geometric distortion of the JWST's detectors when the time comes. We adopted the same observing strategy as above with 25 images organised in a 5×5 array. Unfortunately, one of the pointings in the K_S-filter data set was not usable.

2.4 PSF-modelling, fluxes and positioning

In our reductions, we used the custom-made software tools. It is essentially the same software used throughout this thesis. We started from a raw multi-extension FITS image. Each multi-extension FITS image stores all four chips in a data-cube. We kept this FITS format up to the sky-subtraction phase.

First, we performed a standard flat-field correction[4] on all the images. In the master flat fields, we built a bad-pixel mask by flagging all the outliers respect to the average counts. We used the bad-pixel-mask table to flag warm/cold/dead pixels in each exposure. Cosmic rays were corrected by taking the average value of the surrounding pixels if they were not inside a star's region[5]; bad columns were replaced by the average between the previous and following columns.

Digital saturation in our images starts at 32 768 counts. To be safe, we adopted a saturation limit of 30 000 counts to minimise deviations from linearity close to the saturation regime (accordingly to Kissler-Patig et al. 2008) and flat-field effects. Each pixel for which the counts exceed the saturation limit was flagged and not used.

Finally, we subtracted the sky from the images, computing the median sky value in a 10×10 grid and then subtracting the sky according to the table (bi-linear interpolation was used to compute the sky value in a given location). After the sky subtraction, we split each multi-extension FITS file in four different FITS files, one per chip. The next step was to compute the PSF models.

HAWK-I's PSF is always well sampled, even in the best-seeing condition. To compute PSF models, we developed the software IMG2PSF_HAWKI in which our PSF models are completely empirical. This is derived from the WFI@2.2m reduction package (Paper I). They are represented by an array of 201×201 grid points, which super-sample PSF pixels by a factor of 4 with respect to the image pixels. The fraction of flux contained in the central pixel of a star is given by the central PSF pixel. A bi-cubic spline is used to interpolate the value of the PSF in between the grid points. The value of a given pixel $P_{i,j}$ in the vicinity of a star of total flux z_* that is located at position (x_*, y_*) is:

$$P_{i,j} = z_* \cdot \psi(i - x_*, i - y_*) + s_* \ ,$$

where $\psi(\Delta x, \Delta y)$ is the instrumental PSF, or specifically, the fraction of light (per unit pixel area) that falls on the detector at a point offset $(\Delta x, \Delta y) = (i - x_*, j - y_*)$ from the star's centre, and s_* is the local sky background value. For each star, we have an array of pixels that we can fit to solve for the triplet of parameters: x_*, y_*, and z_*. The local sky s_* is calculated as the 2.5σ-clipped median of the counts in the annulus between 16 and 20 pixels from the location where the star's centre falls. The previous equation can be inverted (with an estimate of the position and flux for a star) to solve for the PSF:

$$\psi(\Delta x, \Delta y) = \frac{P_{i,j} - s_*}{z_*} \ .$$

This equation uses each pixel in a star's image to provide an estimate of the 2-dimensional PSF at the location of that pixel, $(\Delta x, \Delta y)$. By combining the array of sampling from many stars, we can construct a reliable PSF model. As opposed to the pioneering work of Stetson and his DAOPHOT code (Stetson 1987) that combines an empiric and semi-analytic PSF model, we created a fully-empirical PSF model, as described in Paper I.

The software IMG2PSF_HAWKI iterates to improve both the PSF model and stellar parameters. The starting point is given by simple centroid positions and aperture-based fluxes. A description of the software is given in detail in Paper I.

To model the PSFs in both the core and the wings, we use only stars with a high S/N (signal-to-noise ratio). This is done by creating a list of stars that have a flux of at least 5000 counts above the local sky (i.e., S/N>60-70 in the central pixel) and also have no brighter neighbours within 15 pixels. We need at least 50 such stars for each PSF model, so that we can iteratively reject stars that may be compromised by nearby neighbours, cosmic rays, or detector defects (e.g., bleeding columns).

[4]The correction was performed using a single master flat field for each of the 3 filters. We did not use a flat field tailored to each epoch because some of them were not collected.

[5]Cosmic rays close to the star's centre increase the apparent flux and shift the centre of the star, resulting in a large QFIT value (see Sect. 2.4.1 for detail).

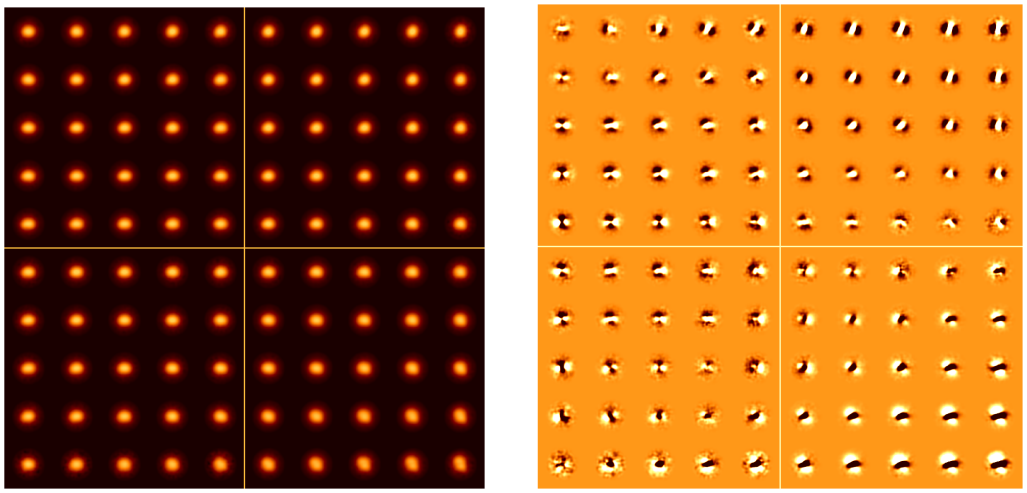

Figure 2.4. Left: 10×10 PSFs for the whole HAWK-I detector (5×5 PSFs per chip). Right: spatial variation of the PSFs. To each local PSF, we subtracted a single average PSF for the whole detector. A darker colour means less flux than the average PSF, and a lighter colour means more flux.

Determining both a good model for the PSF and determining stellar positions and fluxes requires an iterative solution, so the software iterates this process several times until convergence is reached with both good PSF models and stellar parameters that fit well. The result is a 5×5 grid of PSF models for each chip, which are bi-linearly interpolated to provide a model PSF at any pixel position.

With an array of PSF models, we are able to measure stars' positions and fluxes for all the stars in the image by using a software analogue to that described in Paper I. As an input, we need to give the faintest level above the sky for a star to be found and determine how close this star can be to brighter neighbours. The program finds and measures all stars that fit these criteria. The final catalogues (one for each chip) contain positions, instrumental magnitudes, and another quantity called quality-of-PSF-fit (QFIT, which represents the fractional error in the PSF-model fit to the star). For each pixel of a star within the fitting radius (2.5 pixels), the QFIT is defined as the sum of the absolute value of the difference between the pixel values $P_{i,j}$ (sky subtracted) and what the local PSF model predicts at that location $\psi(i-x_*, j-y_*)$, normalised with respect to the sky-subtracted $P_{i,j}$:

$$\mathsf{QFIT} = \sum_{i,j} \left| \frac{(\mathrm{P}_{i,j} - \mathrm{sky}) - z_* \cdot \psi(i-x_*, j-y_*)}{\mathrm{P}_{i,j} - \mathrm{sky}} \right|,$$

where (x_*, y_*) is the star's centre. The QFIT is close to zero for well-measured stars and close to unity for ones that are badly-measured (or not star-like). Typically we found QFIT $\lesssim 0.05$ for well-measured stars in our images. Saturated stars are also measured in our pipeline. For these, stars we only fitted the PSF on the wings of the stars using unsaturated pixels. In this way, we are able to measure a flux and a position for saturated stars, even if they are less accurate (high QFIT) than for unsaturated stars.

2.4.1 PSF spatial variability

As in the case of the WFI@2.2 m (Paper I), the PSF shape for the HAWK-I@VLT detector is different from one chip to the other and from side to side within the same chip. To fully take

this spatial variation into account, we decided to solve for an array of 25 PSFs per chip (5 across and 5 high). A bi-linear interpolation is used to derive the proper PSF model in each location of the detector (see Paper I). The left-hand panel of Fig. 2.4 shows these 5×5 PSFs for the whole HAWK-I detector. At a first glance, we can already see that the PSFs' shape and orientation vary across the detector (especially close to the edge). To better quantify the size of these variations, we built a single, average PSF for the whole detector, and we subtracted it to each of the local PSFs. The result is shown on the right-hand panel of the Fig. 2.4. The actual spatial variation of the PSF is indeed large, even between two adjacent PSFs. The darker colour of Fig. 2.4 means less flux than the average PSF, while a lighter one means more flux. The maximum variation of the local PSF with respect to the average one is 0.02%.

In sparse fields (or short exposures), there might not be enough bright and isolated stars to build the full $5 \times 5 \times 4 = 100$ set of PSFs. We customised the software to allow for different PSF-array solutions: (1) one PSF per chip; (2) four PSFs per chip (at the corners); (3) six PSFs per chip, (4) nine PSFs per chip; and (5) the full 5×5 array. The user can choose to include fainter and more crowded stars to model the PSF to increase the statistics of each PSF model. According to the crowding of the field of interest and the image quality, the user must determine the best compromise between how finely to model the PSF's spatial variability and the need to have an adequate number of stars to model each PSF. Choosing the best solution is a delicate matter. To obtain the best results, we investigated for every single exposure whether it was better to have more or less PSFs by analysing the trend of the QFIT across the image: better PSF models provide smaller QFIT values.

The left-hand panel of Fig. 2.5 shows QFIT values as a function of the instrumental magnitude for chip[1] of exposure HAWKI.2007-08-03T01:41:29.785.fits. This is an image in the field of M 4 taken through J filter. The instrumental magnitude is defined as $-2.5 \times \log(\sum \text{counts})$, where $\sum$counts is the sum of the total counts under the fitted PSF. The red line in the figure indicates when stars start to be saturated[6].

For well-exposed stars (e.g., with instrumental magnitude J between -14 and -10), QFIT values are typically below 0.05 and increase for fainter or saturated stars. However, there are a few sources with anomalously high QFIT in this interval. To find out what kind of outliers these sources are, we selected two of them (highlighted in yellow in Fig. 2.5). Their location on the image is shown in the middle panels of Fig. 2.5 in yellow. Blue circles mark all stars for which we were able to measure a position and a flux. White pixels are those flagged using the bad-pixel mask. We did not find stars too close to these bad pixels. Bottom-right panels in the figure show the corresponding subtracted images. We can see that our PSF-fitting procedure is able to leave very small residuals in the subtracted image, except for saturated stars. The first of the two high-QFIT stars we selected (see left-hand panel) is in close proximity of a saturated star; it has been poorly measured because of the light contamination from the neighbouring star, and therefore has a large QFIT value. The second star has a cosmic ray event close to its centre, increasing its total apparent flux and shifting its centre on the image. This star has been over-subtracted (see bottom-right panel), resulting again in a larger QFIT value.

To better quantify how our PSF models adequately represent star profiles across the detector, we perform the following test. A total of 100 exposures in the field of M 4 were taken between August 3 and 5, 2007 in four runs of 25 images each. We used here only the first 25 images taken consecutively on August 3, 2007 during a time span of about 34 minutes. We derived an array of 5×5 PSFs for each chip of these images. Then, we selected all the k bright, unsaturated stars (instrumental magnitude $J < -10$), which have no brighter neighbours within 10 pixels, and we measured positions and fluxes for them using our 5×5 PSF arrays. Usually, there are over 1000 such stars per chip in our exposures, uniformly distributed over the detector.

If our PSFs are well characterised, we should be able to obtain subtracted images where

[6]The maximum central pixel value of the PSFs for this exposure is 0.058 (i.e., 5.8% of the star's flux falls within its central pixel). We set saturation to take place at 30 000 counts, which means at instrumental magnitude $-2.5 \times \log(30000/0.058) \simeq -14.28$.

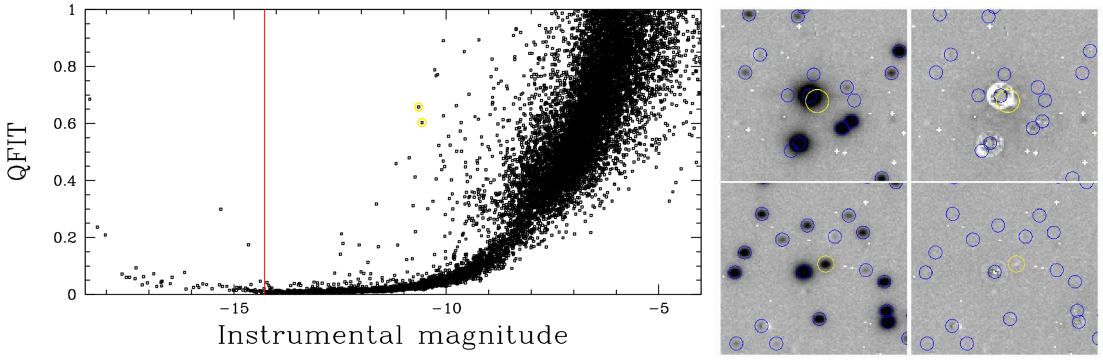

Figure 2.5. Left: QFIT parameter as a function of the instrumental magnitude J for chip[1] of exposure HAWKI.2007-08-03T01:41:29.785.fits. In yellow, we highlighted two sources with anomalously high QFIT. The red line shows the saturation limit. Middle: location of the two sources (in yellow) on the image. Blue circles mark all stars for which we were able to measure a position and a flux. White pixels are those flagged according to the bad-pixel mask. We do not find stars too close to these bad pixels. Right: the corresponding subtracted images. The first of the two high-QFIT stars (top panels) we selected is in close proximity to a saturated star; it has been poorly measured and therefore has a large QFIT value. The second star (bottom panels) has a cosmic ray event close to its centre, increasing its total apparent flux and shifting its centre on the image. This star has been over-subtracted, resulting again in a larger QFIT value.

removed stars leave nearly no flux residuals. Therefore, the size of these residuals tell us how much our PSF models differ from real star profiles.

We extracted 11×11 pixel rasters around each star k (i.e., $\pm$ 5 pixels from its centre) in each exposure for a total of 121 $\mathrm{P}_{i,j}$ pixel values per star. We subtracted the local sky value to all of them, which is computed as the 2σ-clipped median value of the counts in an annulus between 8 and 12 from the star's centre. This is the net star's flux at any given location on the raster. The fractional star's flux is obtained by dividing these values by the total star's flux z. Besides Poisson errors, these values should reflect what our PSF models predict for those pixels ($\psi_{i,j}$), so that we should always have in principle:

$$\frac{\mathrm{P}^k_{i,j} - \mathrm{sky}^k}{z^k} - \psi^k_{i,j} = 0.$$

Deviations of these values from zero tell us how much our PSFs over- or underestimate the true star's profile. Results of this test are reported in Fig. 2.6 for chip[1]. We divided the 2048×2048 pixels of the chip into 5×5 sub-regions with one for each PSF we built. Within each area, we computed the 3σ-median values of the residuals for each pixel of the raster. Pixel values are colour-coded as shown on top of Fig. 2.6. From the Fig. 2.6, we can easily see that PSF residuals are in general smaller than 0.05% even in the central pixel (where Poisson noise is most effective). This proves that our spatial-dependent PSF models are able to adequately represent a star profile at any given location of the chip.

2.4.2 PSF time variability

Ground-based telescopes suffer from varying seeing and airmass conditions, telescope flexures, and changes in focus. These are all effects that may severely alter the shape of the PSF. Figure 2.7 illustrates how much the seeing can actually affect the PSFs. In the figure, we show the first 25 exposures of M 4 that were consecutively taken on August 3, 2007. The total time baseline

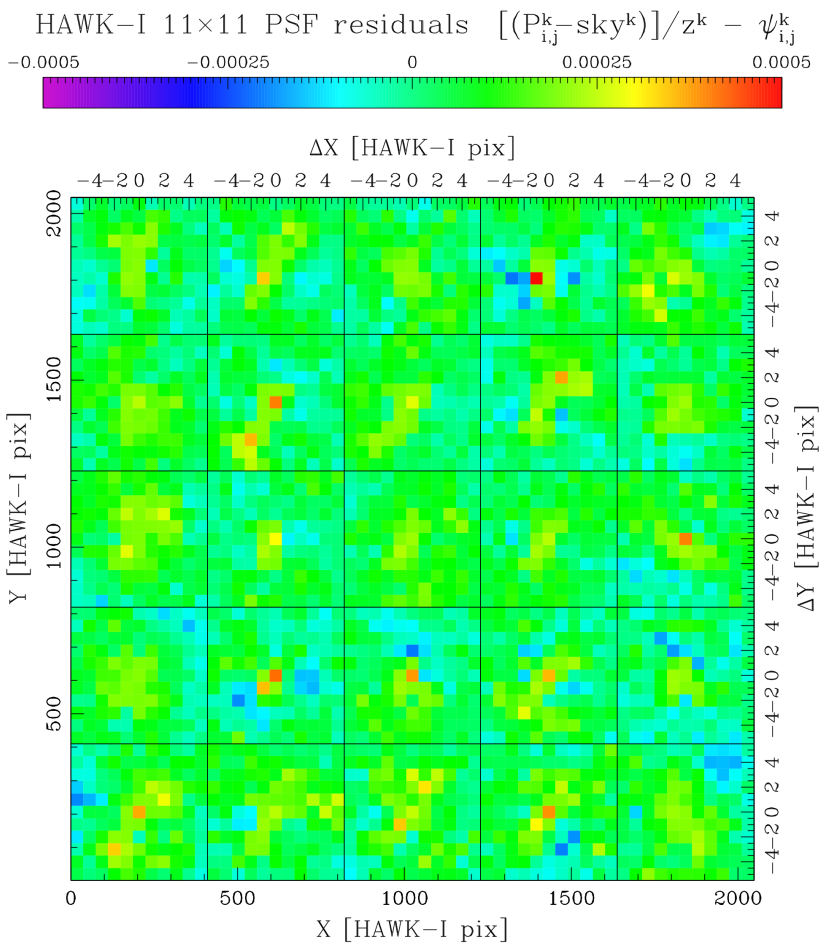

Figure 2.6. PSF spatial variability for chip[1]. Pixel values are colour-coded as shown on top.

is 34 minutes. For each of our PSF models, we considered the value of its central pixel as a function of the exposure sequence, starting from the first exposure. On average, chip[4] PSFs are sharper, while chip[2] stars have the least amount of flux in their central pixels. As a reference, we highlight a central PSF value of 0.05 (i.e., 5% of the total star's flux in its centre pixel) in blue. Within the same exposures, central PSF values can range from 0.03 to 0.07 (see also Fig. 2.4 for the PSF to PSF variation).

In a time span as short as half an hour, we can already see some interesting PSF time-variability effects. First of all, central PSF values vary in an inhomogeneous way across the detector. For instance, there are specific locations on the detector (e.g., the top PSFs of chip[4]) where central PSF values can change by up to 40%. On the other hand, central PSF values are more stable in different locations (e.g., the bottom PSFs of chip[2]).

Moreover, while for some PSFs (e.g., the one labelled as 4-(1,5) on chip[4]), we have a general decrease of the central values, for other PSFs (e.g., 1-(2,1) on chip[1]), we have a decrease of the central values during the first 15 minutes, followed by an increase afterwards. [Note that no focus adjustments have been made during this 34 minutes.]

Figure 2.7 clearly shows that there are large variations in the PSF shape even from one exposure to the other, and this variation is not constant across the field. *HST*'s PSFs are very

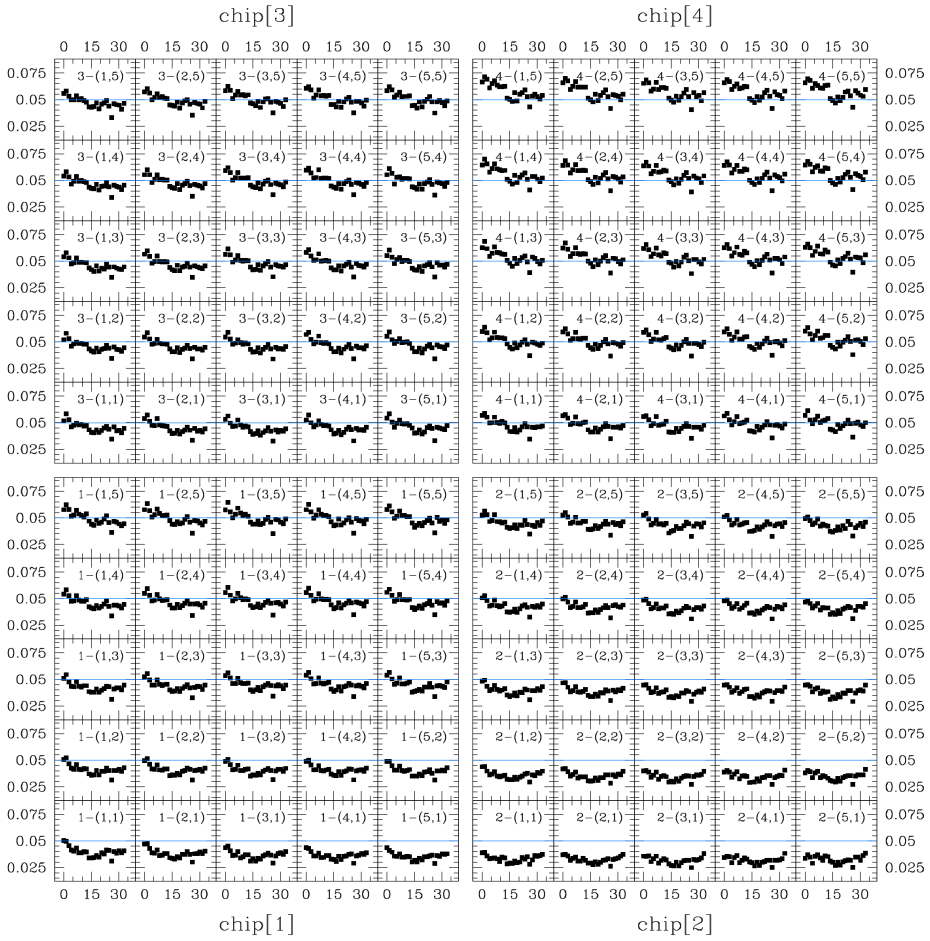

Figure 2.7. Central PSF values as function of the exposure sequence. We highlighted the central PSF value of 0.05 in blue.

stable over time with variations on the order of at most a few percent, mostly due to the so-called telescope breathing[7]. For *HST*, one spatially-constant perturbation PSF for is generally enough to take into account this effect (e.g., ACS/WFC PSFs, Anderson & King 2006). To achieve high-precision astrometry and photometry with the HAWK-I camera, we have to derive a specific set of PSFs for each individual exposure.

To further infer the effects of time variation on our PSF models, we performed the following additional analysis using the 100 images in the field of M 4. As already mentioned, these images were taken in blocks of 25 consecutive exposures in four different runs, spanning three nights. Because each observing run lasted about 30 minutes, we can safely assume that focus variations have played a little role in changing the shape of PSFs, if compared to airmass and seeing variations. Seeing should actually be the most important factor in changing the PSF shape from one exposure to the next one. We focused on the centremost four PSFs, namely: 1-(5,5); 2-(1,5); 3-(5,1); and 4-(1,1), following labels of Fig. 2.7. In Fig. 2.8, we plot the central value of these PSFs as a function of the image quality (i.e., the average stars' FWHM as measured directly on

[7] *HST* focus is known to experience variations on the orbital time scale, which are attributed to thermal contraction/expansion of the *HST* optical telescope assembly as the the telescope warms up during its orbital day and cools down during orbital night.

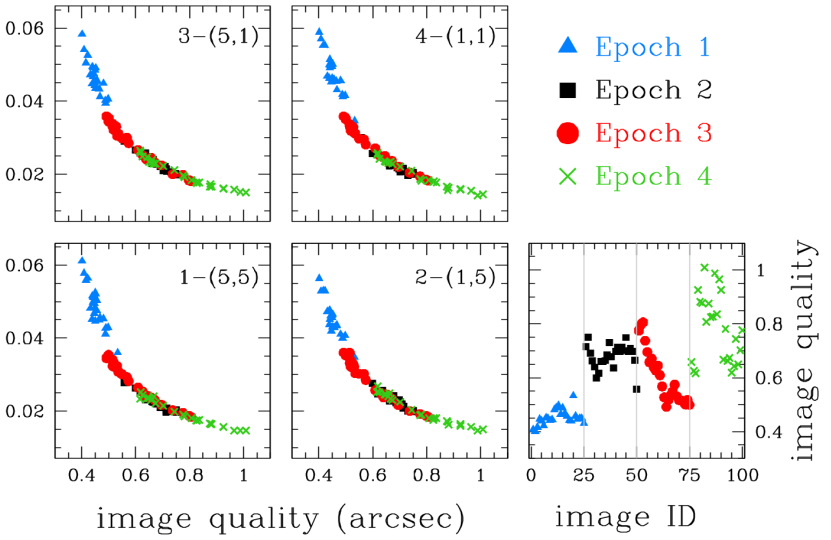

Figure 2.8. The central PSF value of these PSFs as a function of the image quality.

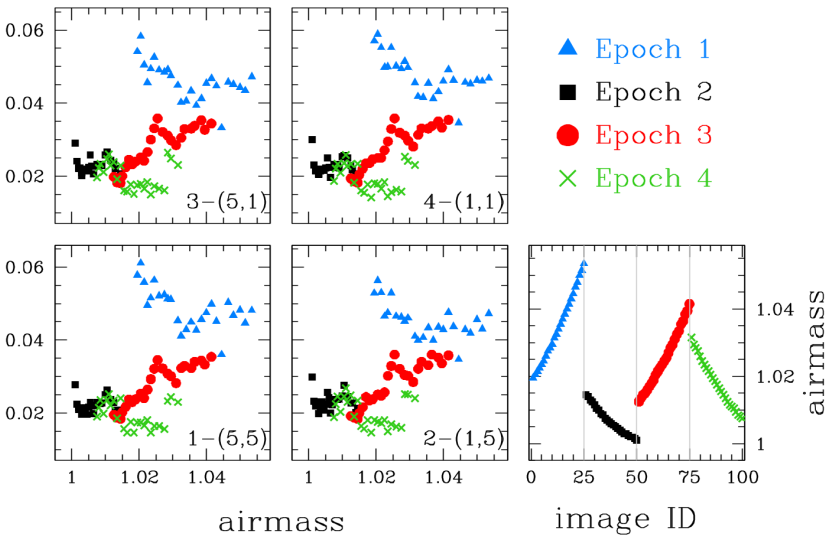

Figure 2.9. Same as Fig. 2.8 but for airmass variations.

the exposures). Different observing runs are marked with different colours and symbols. On the bottom-right panel of the figure, we plot the variation in the image quality during the four runs. Here, we want to emphasise that these variations occurred within 30 minutes within the same run. As we expected, there is a strong correlation between our PSF shapes and image quality. The correlation between PSF shapes and airmass is shown in Fig. 2.9. Airmass variations seem to play a secondary role in changing PSF shape with respect to image quality.

2.5 Geometric distortion correction

In this section, we present a geometric-distortion solution for the HAWK-I in three broad band filters (J, H, and K_S) derived using exposures of the Baade's Window field. No astrometric reference data is available for the Baade's Window field, so we iteratively constructed our own.

Adopting the observing strategy described in Sect. 2.3, the systematic errors in the measure of stars' positions from one exposure to the other have a random amplitude and the stars' averaged positions provide a better approximation of their true positions in the distortion-free master frame.

To build the master frame, we cross-identified the star catalogues from each individual HAWK-I chip. Conformal transformations (four-parameter linear transformations, which include rigid shifts in the two coordinates, one rotation, and one change of scale, so the shape is preserved) were used to bring the stars' positions, as measured in each image, into the reference system of the master frame. We considered only well-measured, unsaturated objects with a stellar profile and measured in at least three different images.

Our geometric-distortion solution for HAWK-I is made up of five parts: (1) a linear transformation to put the four chips into a convenient master frame (Hereafter, we refer to the transformation from chip k of the coordinate system of image j to the master system $T_{j,k}$.), (2) two fifth-order polynomials to deal with the general optical distortion (hereafter, the "P" correction), (3) an analytic correction for a periodic feature along the x-axis, as related to the detector read-out amplifiers (the "S" correction), (4) a fine-tuning to correct second-order effects on the x-residuals of the S correction (the "FS" correction), and (5) a table of residuals that accounts for both chip-related anomalies and a fine-structure introduced by the filter (the "TP" correction).

The final correction is better than ∼0.027 pixel (∼2.8 mas) in each coordinate. We provide the solution in two different forms: a FORTRAN subroutine and a set of FITS files for each filter/chip/coordinate. Since focus, flexures, and general conditions of the optics and telescope instrumentation change during the observations (within the same night and even between consecutive exposures), we derive an *average* distortion correction.

Here, we describe our correction procedure for filter K_S. The procedure for filters J and H is identical, and the results are presented in the Sect. 2.5.6.

2.5.1 Polynomial correction (P)

We followed the method given in Anderson & King (2003) for the Wide-Field Planetary Camera 2 (WFPC2). This method was subsequently used to derive the distortion correction for the ACS High Resolution Channel (Anderson & King 2004) and for the Wide Field Camera 3 (WFC3) Ultraviolet-Visual (UVIS) channel (Bellini & Bedin 2009; Bellini, Anderson, & Bedin 2011). The same strategy was also used by two of us to calibrate the blue prime-focus camera at the LBT (Paper IV). We treated each chip independently, and we solved the 5^{th}-order polynomial that provided the most correction. We chose pixel (1024,1024) in each chip as a reference position and solved for the distortion with respect to it.

The polynomial correction is performed as follows:

- In each of the list of unsaturated stars found in each chip of each exposure (4×25 lists), we first selected stars with an instrumental magnitude brighter than $K_S \simeq -11$ and with a QFIT lower than 0.05, to ensure that the master list would be free from poorly measured stars, which would harm the distortion solution.

- We computed the linear transformation ($T_{j,k}$) between stars in each chip of each exposure and the current master frame.

- Each star in the master frame was conformally transformed in the raw-coordinate system of each chip/image ($T_{j,k}^{-1}$) and cross-identified with the closest source. Each such cross-identification generates a pair of positional residuals (δx,δy), which correspond to the difference between the observed position and the transformed reference-frame position.

- These positional residuals were distilled into a look-up table made up of 12×12 elements of 170.7×170.7 pixels each. This setup proved to be the best compromise between the need of an adequate number of grid points to model the polynomial part of the distortion solution and an adequate sampling of each grid element. We found about 19 000 pairs of residuals in each chip with a median number of 135 pairs per cell (the number varied between 30, which occurred in a corner grid element, and 170, which was near the chips' centre).

- We performed a linear least-square fit of the average positional residual of each of the 144 cells to obtain the coefficients for the two fifth-order polynomials in each chip (see Paper IV for a detailed description).

- We applied this P correction to all stars' positions.

- Finally, we iterated the entire process, deriving a new and improved combination of a master frame and distortion solution. The residuals improved with each iteration.

The iterative process was halted when the polynomial coefficients from one iteration to the next differed by less than 0.01%.

The final P correction reduced the average distortion residuals (from the centre of the detector to the corner) from ∼2.1 pixels down to ∼0.2 pixel. By applying the P correction, the accuracy of our distortion solution (defined as $68.27^{\rm th}$ percentile of the σ(Radial residual), see Sect. 2.5.5 for detail) improves from ∼0.336 to ∼0.043 pixel per coordinate for a well-exposed star, which translates from ∼35.6 mas to ∼4.5 mas. In Fig. 2.10, we show the HAWK-I distortion map before and after our P correction. Although the aim of our work is not to analyse what makes the distortion happen, the distortion pattern before the correction appears to be primarily a radial distortion in the focal plane with some vignetting at the edges plus some shift-rotation-shear in the detector positioning.

2.5.2 Average periodic "step" correction (S)

Our P correction reveals a high-frequency, smaller-amplitude effect, which is a periodic pattern in the x-positional residuals as a function of the x positions in all HAWK-I chips. This effect is clearly shown in the distortion map after the P correction is applied (δx versus X panels in Fig. 2.10). For every 128 columns, stars' positions have positive residuals (about 0.075 HAWK-I pixel) in the first 64 pixels and negative residuals (about 0.045 HAWK-I pixel) in the second 64 pixels (see panels (a) of Fig. 2.11). At first glance, this residual pattern has the appearance of being caused by irregularities in the pixel grid of the detectors. However, a detailed analysis (see Sect. 2.6) leads us to conclude that it is instead a pattern caused by a "periodic lag" in the readout process, which is offset in opposite directions in alternating 64 pixel sections of the detector addressed by each of the 32 read-out amplifiers.

We adopted an iterative procedure to empirically correct for this periodic pattern that shows up only along the x axis. We started with the master frame made by using catalogues corrected with our P correction. We then transformed the position of each star (i) from the master frame back into the raw coordinate system of each chip (k) of each image (j). We determined the quantity:

$$\delta x_i = x_i^{\rm raw} - x_{i,j}^{\rm P^{-1}(T_{j,k}^{-1})},$$

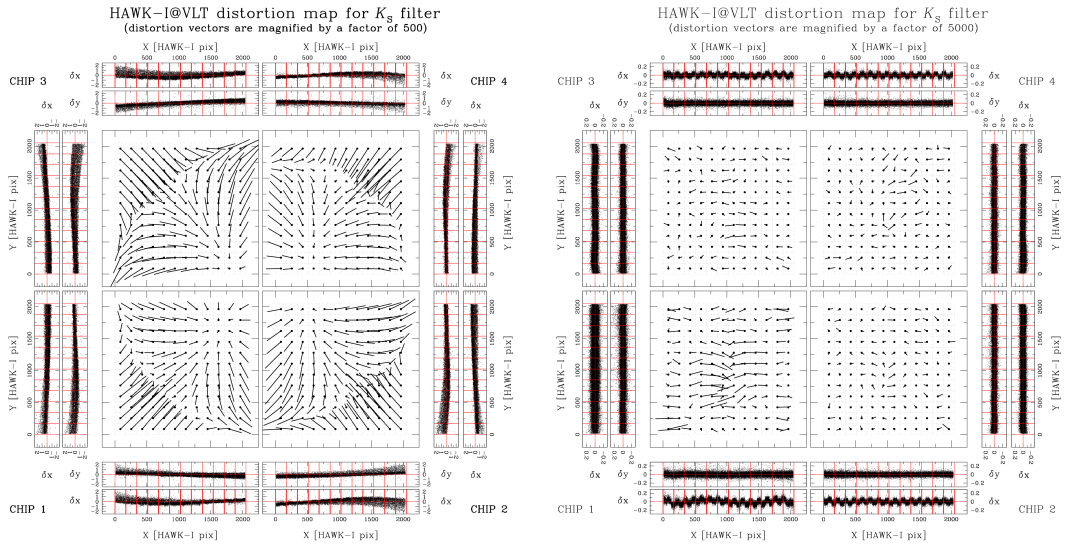

Figure 2.10. Left: residual trends for the four chips when we use uncorrected stars' positions. The size of the residual vectors is magnified by a factor of 500. For each chip, we also plot the single residual trends along X and Y axes. Units are expressed in HAWK-I raw pixel. Right: residuals after our polynomial correction is applied. The size of the residual vectors is now magnified by a factor 5000.

where $x_i^{\rm raw}$ are the raw x-coordinates, and $x_{i,j}^{{\rm P}^{-1}({\rm T}_{j,k}^{-1})}$ are the x-coordinates on the master frame transformed to the raw coordinate system and corrected with the inverse P correction. We assumed that the periodic trend had a constant amplitude across the detector. Panels (a) in Fig 2.11 show δx vs $x^{\rm raw}$ for each chip (from 1 to 4) and δx versus $x^{\rm raw}$ modulus 128, in which we collect together all the residuals (panel 5) before applying the S correction.

To model the trend in the residuals, we used a square-wave function (panel (5a) of Fig. 2.11). The amplitude of this function is defined as the 3σ-clipped median value of the residuals between pixels 2.8–62.2 and 66.8–126.2. To model the average periodicity between $62.2 \leq x^{\rm raw} \leq 66.8$ pixels, we fitted the data points with a straight line using by linear least squares.

We corrected the stars' positions by applying 75% of the S correction (to encourage smooth convergence) and the P correction. We computed an improved master frame and calculated new, generally smaller, residuals. New square-wave-function amplitudes were derived and added to the previous corrections to improve the S correction. The procedure was iterated until the observed average periodicity residuals had an amplitude smaller than 10^{-4} pixel.

Combining the two corrections (S+P, applied in this order to the raw coordinates), we are able to reduce the $68.27^{\rm th}$ percentile of the σ(Radial residual) down to $\sim$4.0 mas (0.038 pixel).

2.5.3 Fine-tuned correction of the residual periodicity (FS)

In panels (b) of Fig. 2.11, we show the residual trend after the S+P correction is applied. Looking at panels (1–4b), it is obvious that the amplitude of the δx periodicity pattern is not constant from chip to chip. In addition to this, there is still a polynomial residual that needs to be removed. For this reason, we applied a fine-tuned residual correction as follows.

We first computed a master frame by applying the S+P correction to the raw positions of each chip/exposure. We then determined the residuals as the difference between the raw x-coordinates corrected with the S correction and $x_{i,j}^{{\rm P}^{-1}({\rm T}_{j,k}^{-1})}$. Next, we divided each chip into 32

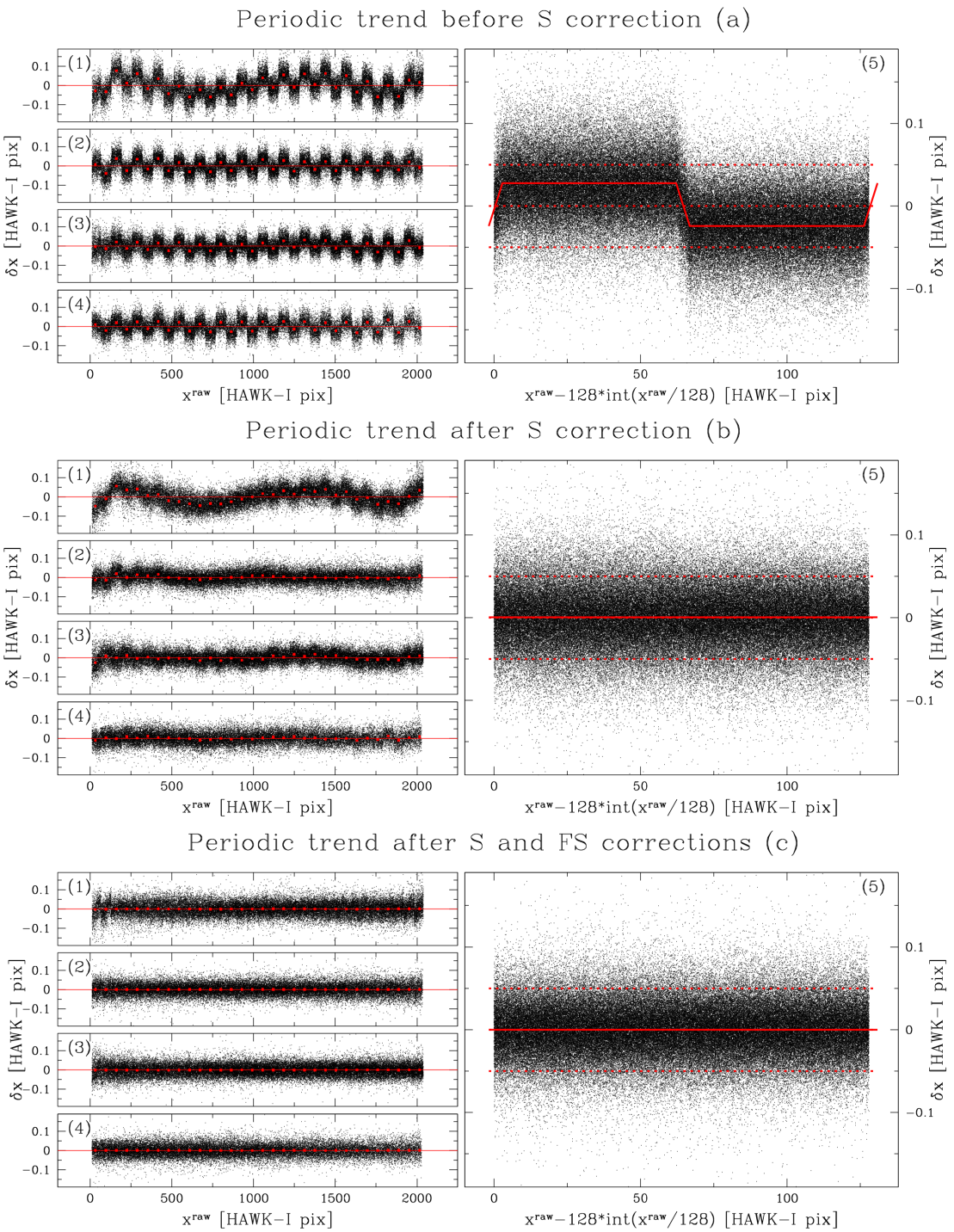

Figure 2.11. Top: δx as a function of X in units of HAWK-I pixels before S correction. Middle: as above but after S correction. Bottom: same as above but after S and FS corrections. In the left-hand panels (from 1 to 4), we took 32 bins of 64 pixels each and computed the median of residuals in each bin (red squares). In the right-hand panels (5), we show the periodogram with a period of 128 columns containing all the points plotted in the left-hand panels. The red dashed lines show +0.05, 0, and −0.05 HAWK-I pixel.

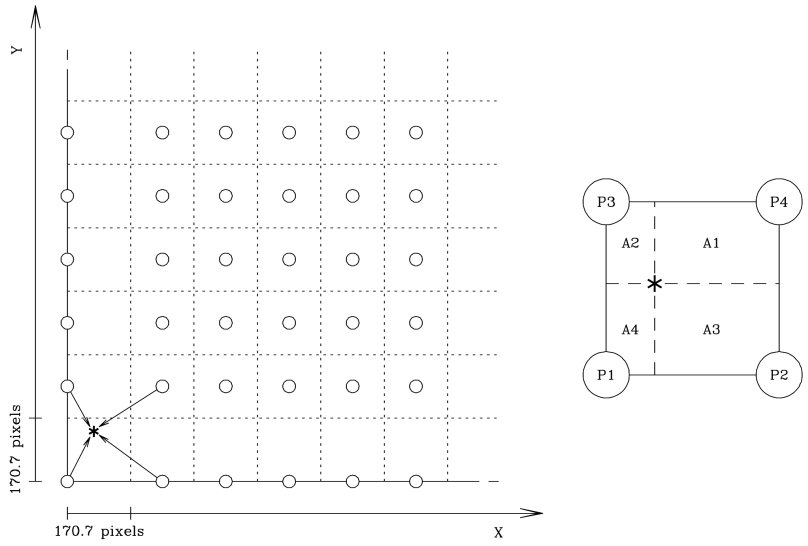

Figure 2.12. Left: example of cell and grid-point locations on the bottom-left area of chip[1]. Dotted lines mark the 170.7×170.7 pixels square elements inside which we computed the median value of the distortion residual to use as grid point (empty circles) in the look-up table. For a given star (marked with an $*$), we used the four surrounding closest grid point to perform the bi-linear interpolation (sketched with the arrows) and evaluate the residual geometric distortion in that location of the detector. Right: bi-linear interpolation outline. Each grid point $\mathrm{P}_1, \ldots, \mathrm{P}_4$ is weighted by the corresponding area $\mathrm{A}_1, \ldots, \mathrm{A}_4$ to associate the correction in $*$.

bins of 64 pixels each along the x axis, computed the 3σ-clipped average value of the residuals, and subtracted the 75% of it from the δx residuals in each bin. Then, we iterated the procedure until the difference between the 3σ-clipped average value of the residuals in all bins of all chips from one iteration to the next one was smaller than 10^{-3} pixel. In panels (c-1) to (c-4) of Fig. 2.11, we show the residual trends for all chips after our S+FS+P corrections are applied.

This approach was able to provide an accuracy (68.27^{th} percentile of the σ(Radial residual)) down to $\sim$0.035 pixel ($\sim$3.7 mas).

2.5.4 Table of residual geometric-distortion correction (TP)

The final step of our distortion-solution model consists of four look-up tables (one for each chip) to minimise all the remaining detectable systematic residuals that were left. We constrained the look-up tables using the same procedure that Bellini, Anderson, & Bedin (2011) used to derive the distortion correction for the WFC3/UVIS camera.

First, we corrected all stars' positions by applying the S, FS, and P corrections (in this order). We then built a new master frame and computed the residuals, as described in Sect. 2.5.1. We subdivided again each chip into 12×12 square elements. We used the stars' residuals within each cell to compute a 3σ-clipped median positional residuals and assigned these values to the corresponding grid points (open circles in Fig 2.12). When a cell adjoins detector edges, the grid point is displaced to the edge of the cell, as shown. For the grid point on the edges, the value of the median only at the first iteration is computed at the centre and shifted to the edge. Then, we iteratively found the value that the grid-point element on the edge should have to remove the systematic errors. We built a look-up table correction for any given location of the chip, using a bi-linear interpolation among the surrounding four grid points. Figure 2.12 shows an example

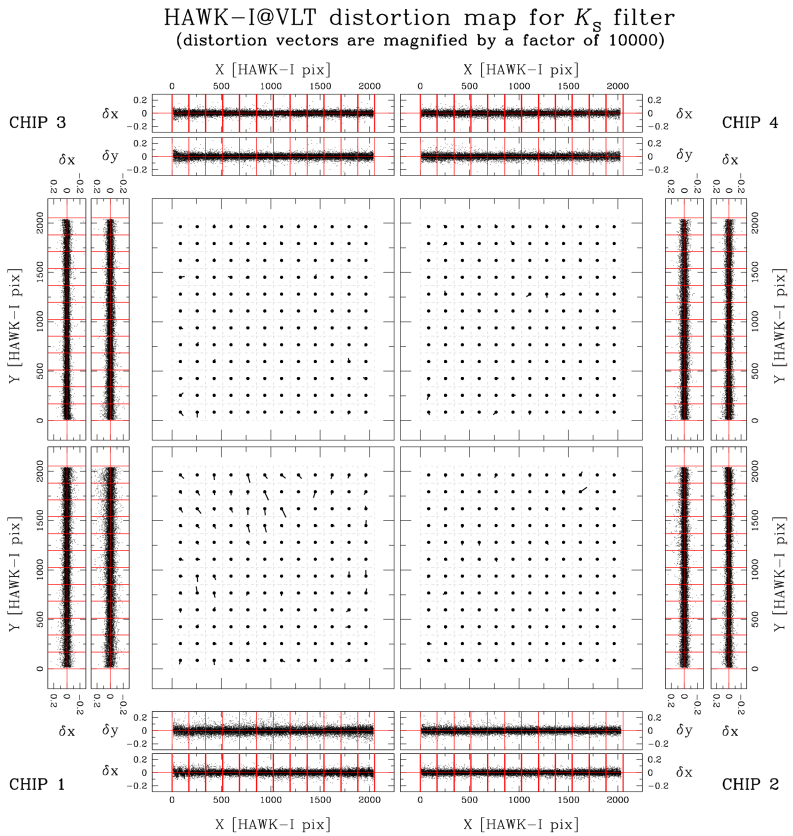

Figure 2.13. As Fig. 2.10 but after we have applied all the distortion corrections. The size of the residual vectors are now magnified by a factor 10000.

of the geometry adopted for the look-up table and of the bi-linear interpolation.

We corrected stars' positions using only 75% of the recommended grid-point values, computed an improved master frame, and calculated new (generally smaller) residuals. We calculated new grid-point values and added them to the previous values. The procedure was iterated until the bi-linear interpolation offered negligible improvement of the positional residuals rms from one iteration to the next.

2.5.5 Accuracy of the geometric-distortion correction

In Fig. 2.13, we show the final HAWK-I distortion map after we applied our full distortion solution (S+FS+TP+P). To have a reliable assessment of the errors in the distortion correction, we computed the rms of the position residuals of each star (i) observed in each chip (k) of the image (j), which have been distortion corrected and conformally transformed into the master-frame reference system ($x_{i,j,k}^{T_{j,k}}, y_{i,j,k}^{T_{j,k}}$). The difference between these positions and the distortion-free positions ($X_i^{\rm master}, Y_i^{\rm master}$) directly quantifies how close we are to reach the ideal distortion-free system. We defined the σ(Radial residual) as:

$$\sigma(\text{Radial residual})_{i,j} = \sqrt{\frac{(x_{i,j,k}^{T_{j,k}} - X_i^{\rm master})^2 + (y_{i,j,k}^{T_{j,k}} - Y_i^{\rm master})^2}{2}} \ .$$

In Fig. 2.14, we show the size of these σ(Radial residual) versus instrumental K_S magnitude after each step of our solution. To test the accuracy of the geometric-distortion solution, we only used unsaturated stars with an instrumental magnitude $K_S \leq -12.4$ (red dashed line) in the master list, which is observed in at least 3 images and with a QFIT ≤ 0.05. Faint stars have larger residuals due to an increasing contribution of random errors. The 3σ-clipped $68.27^{\rm th}$-percentile value of these residuals is shown on the right of each panel. The 3σ clipping rule excludes outliers, which can bias the percentile value. These outliers can have different explanations. For example, most of the outliers for the Bulge field are close to the edge of the FoV, where the distortion solution is less constrained. In the case of NGC 6656, most of these outliers are close to the centre of the cluster (crowding effects) or are located in the region affected by the internal reflection of the Moon in the optics. Hereafter, we refer in the text with $\sigma_{\rm perc}$ to the 3σ-clipped $68.27^{\rm th}$-percentile value of the σ(Radial residual). The distributions of the rms is very non-Gaussian and the $68.27^{\rm th}$-percentile is an arbitrary choice to represent the errors. Although it is not absolutely correct mathematically, it gives a good indications of where an outlier will lie.

In the bottom panel, we plot the σ(Radial residual) obtained using more-general 6-parameter linear transformations to compute the master-frame average positions. These transformations also include other two terms that represent the deviation from the orthogonality between the two axes and the change of relative scale between the two axes (the shape is not preserved anymore). When general linear transformations are applied, most of the residuals introduced by variations in the telescope+optics system and differential atmospheric refraction are removed, and $\sigma_{\rm perc}$ further reduces to 0.027 pixel ($\sim$2.8 mas).

2.5.6 Geometric-distortion correction for *J* and *H* filters

Each HAWK-I filter constitutes a different optical element, which could slightly change the optical path and introduce changes in the distortion. To test the filter-dependency of our K_S-based distortion solution, we corrected the positions measured on each J- and H-filter images of Baade's Window field with our K_s-filter-derived distortion solution and studied the residuals. We found σ(Radial residual) significantly larger than those obtained for the K_s-band images. We also tried to apply the K_s-filter distortion solution plus an ad-hoc table of residual (TP correction) for each filter without significant improvements. For these reasons, we decided to independently solve for the distortion for the J and H images.

We built the J-filter master frame using only stars with an instrumental magnitude brighter than $J \simeq -11.5$ and with a QFIT ≤ 0.05. For the H-filter, we built the master frame using only stars with $H \simeq -12.5$ and, again, QFIT ≤ 0.05. We adopted these selection criteria to sample each chip with an adequate number of stars (at least 12 000 and 19 000 stars for the J- and H-filter, respectively). The distortion corrections were performed as described in the previous sections.

As shown in Table 2.2, the image quality of the J-filter Bulge images changed dramatically during the night of the observation, reaching 1.07 arcsec. We initially used all J-filter images to compute the distortion correction and obtained a $\sigma_{\rm perc}$ (using general transformations) of $\sim$6.8 mas. We then only considered those exposures with an image quality better than FWHM=0.80 arcsec and re-derived the distortion correction (57 out of 100 catalogues were excluded this way).

In Fig. 2.15, we show that the σ(Radial residual) before and after applying the distortion correction for the J and H images. The $\sigma_{\rm perc}$ for well-measured unsaturated stars is shown on the right of each panel. Using general linear transformations, we obtained σ(Radial residual) of $\sim$4.5 mas and $\sim$4.3 mas for J and H filter, respectively.

On the left-hand panel in Fig. 2.16, we compare the residual trends obtained by applying the K_S-filter correction to J-filter Bulge images (blue vectors) to the residual trends obtained by applying the J-filter correction instead (red vectors). In the right-hand panel, we show the same comparison for the H-filter case. A clear residual trend (up to 0.1 pixel) of is present when a

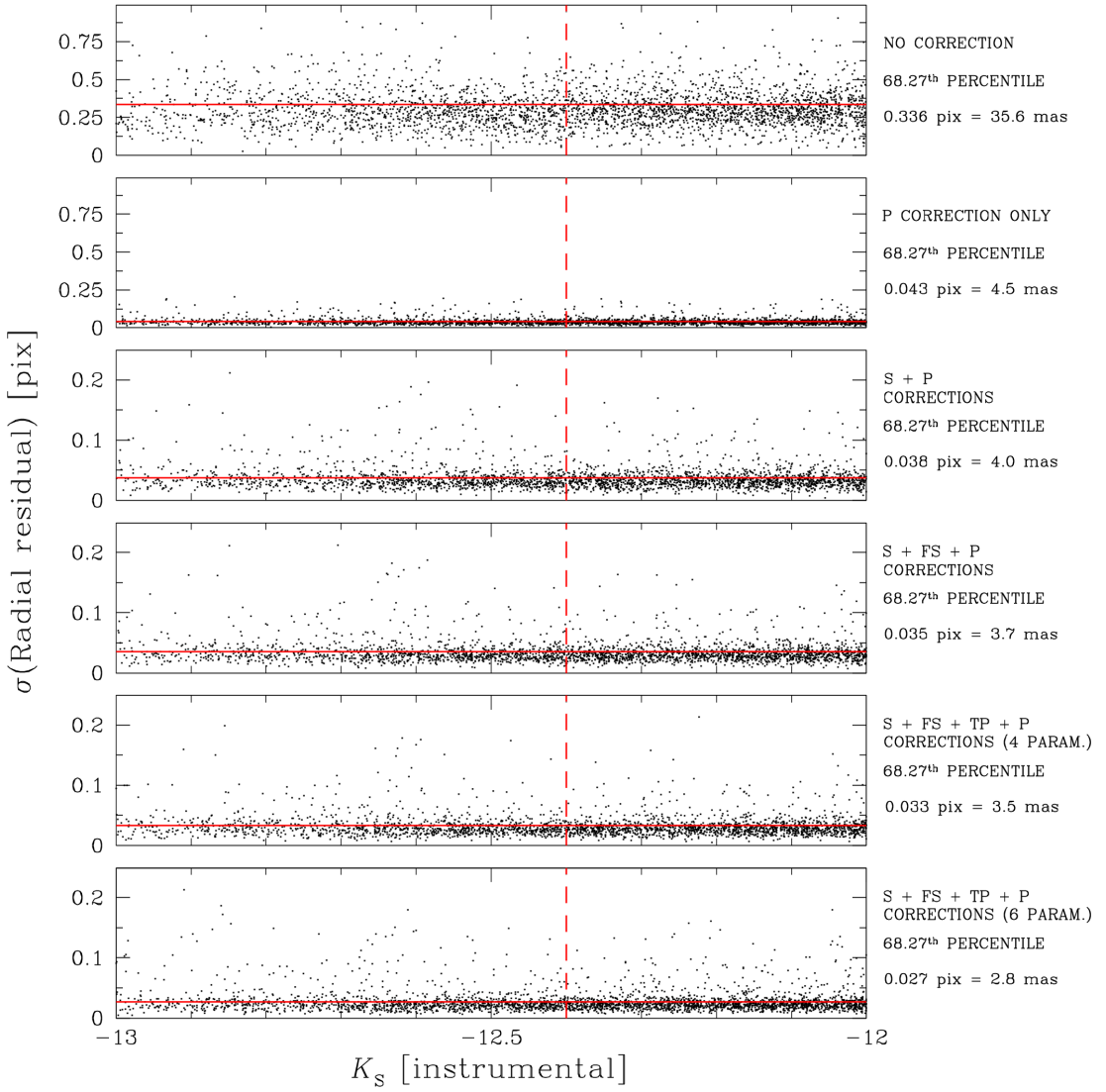

Figure 2.14. σ(Radial residual) versus instrumental K_S magnitude after each step of our solution. The red solid horizontal line shows the σ_{perc}; the red dashed vertical line indicates the magnitude cut-off $K_S = -12.4$.

correction made for a different filter is applied to a given data set of images. The optical system performances are different at different wavelengths, so it is not surprising that the K_S solution is not completely suitable for the J- and H-filter data. The filter also introduces an additional optical element that leads to a different distortion on the focal plane. Both σ(Radial residual) and distortion maps tell us that an auto-calibration for the distortion correction in each filter is required for high-precision astrometry.

2.5.7 Stability of the correction

Different factors (e.g., the contribution given by light-path deviations caused by filters, alignment errors of the detector on the focal plane) change the HAWK-I distortion over time. To explore

the stability of our derived distortion solution over time, we observed the astrometric precision obtained by applying our distortion correction to images taken several months apart.

We applied our distortion solution to images of NGC 6656 (M 22) taken during the second commissioning. The $\sigma_{\rm perc}$ (computed as described in Sect. 2.5.5) was found to be $\sim$3.5 mas for well-measured unsaturated stars. To estimate the stability of the distortion correction over the 3-month time baseline between the first and second commissioning, we derived an independent distortion solution from the second commissioning run images and compared the results. We adopted the same auto-calibration method described above. In this way, we were able to reduce the 1-D rms down to $\sim$3.1 mas. In Fig. 2.17, we show the comparison between the σ(Radial residual) after we applied the Bulge-based distortion correction (bottom) and the newly made NGC 6656-based correction (top). The difference between these distortion solutions is only 0.003 pixel. Therefore, our Bulge distortion correction should be stable at a 3-mas level on a 3-month scale for general uses. In Fig. 2.18, we show the distortion-map comparison. There are systematic trends when the $K_{\rm S}$-filter Bulge solution is applied to this data set. Nevertheless, for high-precision astrometry, we suggest auto-calibrating the distortion correction for each data set, as it is continuously evolving.

We note that the positions of the nodes of the periodic trend did not change over this trim baseline, adding support to our conclusion that this periodic residual is linked to the *detector's* properties and is not a function of the telescope, epoch, filter, or image quality (see Sect. 2.6).

2.5.8 An external check

As done in the previous section for the case of NGC 6656, we apply the distortion correction obtained by self-calibration of Bulge images (hereafter, Bulge#1) to a different data set, which is collected for the same field, but with the de-rotator at a different position angle at $\sim$135° (hereafter, Bulge#2). In this case, we obtained a $\sigma_{\rm perc}$ of $\sim$5.8 mas, which is significantly larger than that obtained in Sect. 2.5.5 for Bulge#1 ($\sigma_{\rm perc}\sim$2.8 mas). This may give the impression that the distortion solution obtained for Bulge#1 is not suitable for the rotated images of Bulge#2. However, self-calibration of these rotated images gives us a $\sigma_{\rm perc}$ of $\sim$5.6 mas, indicating only a marginal improvement. The lower accuracy of the distortion solution of Bulge#2 must be ascribed to the intrinsic lower quality of this data set (worse average seeing, higher airmass, worse weather conditions, guiding, and instrument+telescope conditions). The distortion maps obtained applying the two solutions to the same data set (Fig. 2.19) highlight different trends (even if the residuals are lower than 0.05 pixel), in the upper-right corner of chip[4], which recommends again the auto-calibration for the distortion solution of each data set for high-accuracy astrometry.

Nevertheless, even if rotated Bulge#2 images were taken under worse conditions, the value of their $\sigma_{\rm perc}\sim$5.6 mas allows us to make an important external check of our solution down to this level. The astrometric quantity $\sigma_{\rm perc}$ tells us how accurately we can expect to register the *relative* position of a star among different dithered images. However, these are internal estimates of the error, and do not account for all of the sources of systematic errors. For a better estimate of the uncertainty on the relative position of stars, we compared the two calibrated master frames of Bulge#1 and Bulge#2 and measured how much the two frames deviate from each other. We know the linear terms could be different due to change in the thermal- or flexure-induced focal lengths, differential atmospheric refraction, etc. For this reason, we transformed the two master frames of Bulge#1 and Bulge#2 using general linear transformations and measured the amount of residuals in the non-linear part of the distortion. For this test, we only used those regions of both master frames where stars were measured in at least 10 images (out of 25). In Fig. 2.20, we show the residual trend of bright, unsaturated stars between the 2 frames. The 68.27$^{\rm th}$ percentile of the ΔX distribution is about 10.7 mas, while that of ΔY is about 9.4 mas. Thus, the non-linear terms of our distortion solution can be transferred between observing runs at the 10 mas level.

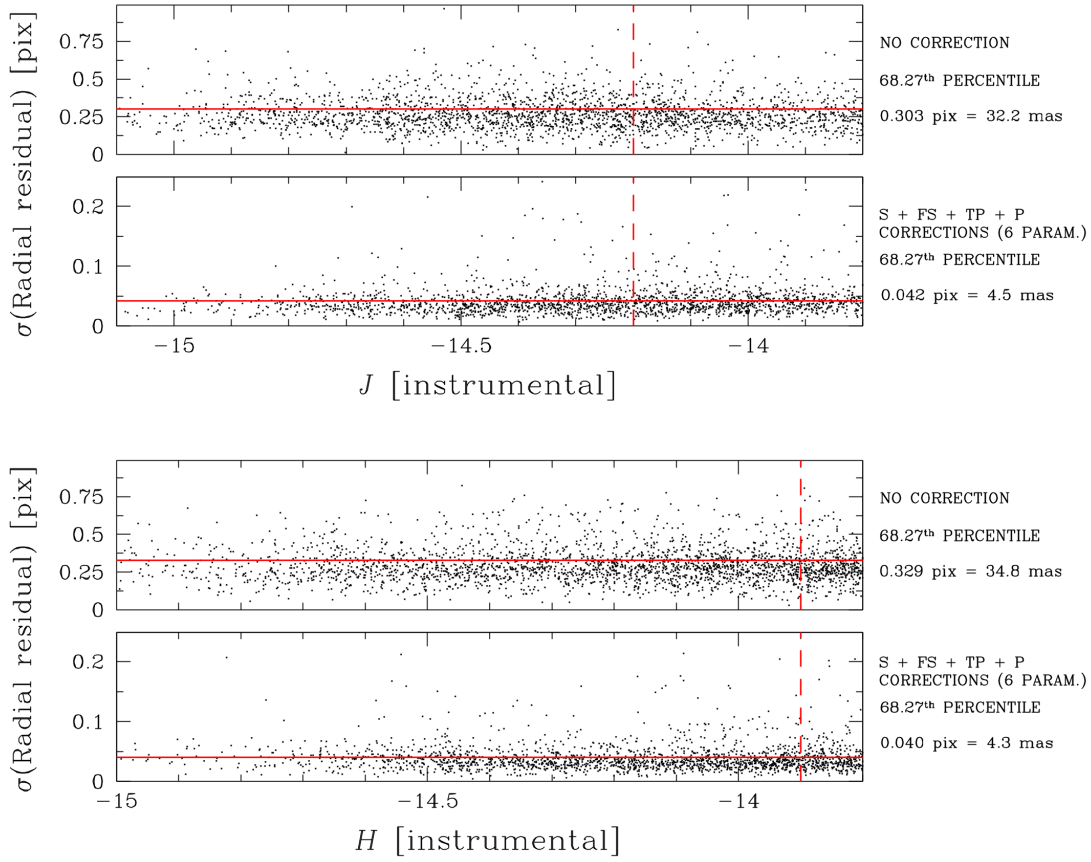

Figure 2.15. In each half of the figure, we show the σ(Radial residual) versus instrumental magnitude before and after we applied our distortion correction for the J (top) and H (bottom). The red lines have the same meaning as in Fig. 2.14 but the red dashed vertical lines are set at $J = -14.2$ (top) and $H = -13.9$ (bottom), respectively.

2.5.9 Description of the geometric-distortion-correction subroutines, 2-D maps and size of the corrections

We release on VizieR on-line database[8] FORTRAN routines to correct the geometric distortion, using the solution computed for the Bulge#1 field (Sect. 2.5.1, 2.5.2, 2.5.3 and 2.5.4). There are three different routines with one for each filter (J, H, K_S). They require x^{raw} and y^{raw} coordinates and the chip number. In output, the codes produce x^{corr} and x^{corr} corrected coordinates. Both raw and corrected coordinates are in the single-chip reference frame ($1 \leq x^{raw/corr}, y^{raw/corr} \leq 2048$).

In Table 2.3, 2.4, and 2.5, we show the minimum and maximum values of each correction in both coordinates for all chips. The largest correction is applied with the P corrections, which decrease from the corner to the centre of the detector. The S and FS corrections are only applied to the x-coordinates. Figure 2.21 demonstrates there is no δy periodic pattern, so an FS correction along this axis is not necessary. The residual distortion is corrected with the TP correction. While the S correction is the same for all chips and has only two values, the FS

[8] http://cdsarc.u-strasbg.fr/viz-bin/qcat?J/A+A/563/A80

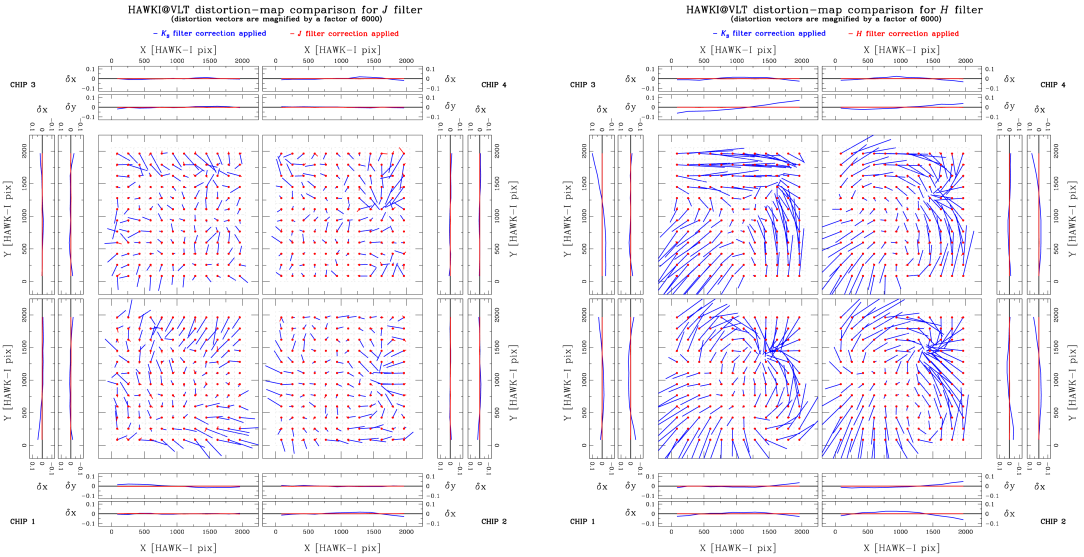

Figure 2.16. Left: J-filter distortion map comparison. In blue, we plot the vectors when the K_S-filter correction is applied; in red, we show when the J-filter correction is used. We plot the single residual trends along X and Y axes with the same colours, but we do not plot the single stars to not create confusion in the plot. Right: the same but for the H filter. The size of the residual vectors is magnified by a factor 6000.

correction changes from chip to chip and varies across the same chip.

In addition to these codes, we release our distortion solution as FITS images (one per each coordinate/chip/filter) to make the distortion solutions also available for other program languages. Bi-linear interpolation must be used to compute the amount of the distortion correction in inter-pixel locations. In Fig. 2.22, we show a 2-D map of the correction for each chip/filter. In the four left-hand boxes of each row, we plot the correction of each chip for the x-coordinates in the right-hand boxes for the y-coordinates. The polynomial correction creates the radial pattern that changes from the corner to the centre in all chips. The S correction is visible only in the left-hand boxes (x-coordinate corrections) and creates a striped pattern.

Another important correction that we are going to release (as FITS images) is the correction for the pixel area variation across the detector. This is a useful tool for improving HAWK-I photometry. On average the size of the pixel area varies up to 0.7% across the detector. This value is reached at a point close to the edge and to the centre of the detector. We only applied the polynomial correction, since it gives the maximum correction. Note that the corrections of the periodic-lag effect should not be included in the pixel area correction. The periodic lag is due to charges left in the amplifiers, so the area of the pixel itself is not modified on sky. This is different to what happens with the optics+filters distortion. In Fig. 2.23, we show three maps of the correction with one for each HAWK-I filter.

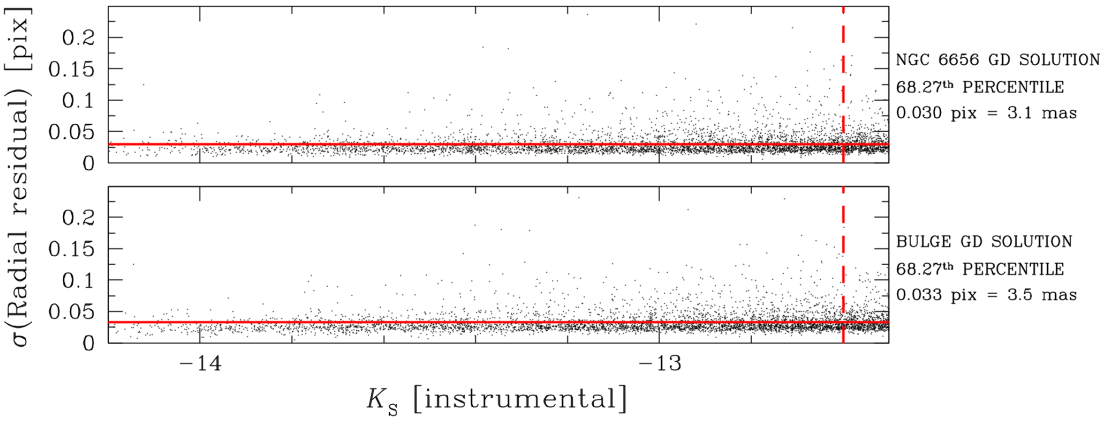

Figure 2.17. Comparison of NGC 6656 σ(Radial residual) after application of the Bulge-based (bottom) and the NGC 6656-based (top) correction. The red solid horizontal line shows the 3σ-clipped value of the σ(Radial residual); the red dashed vertical line indicates the magnitude limit $K_S = -12.6$.

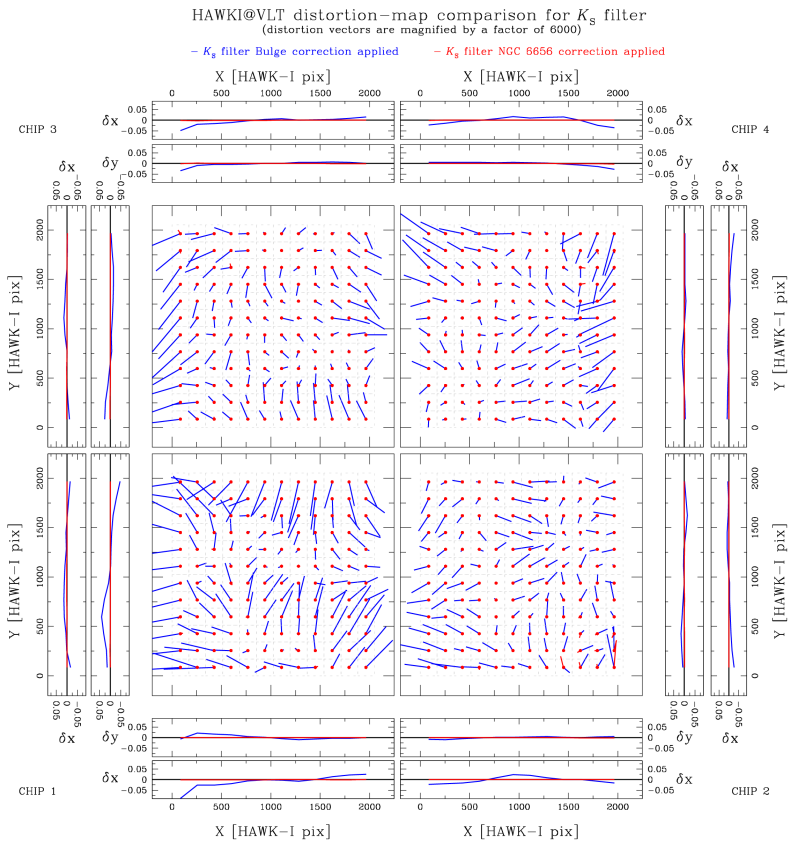

Figure 2.18. As in Fig. 2.16 but for the NGC 6656 case. In blue, we plot the vectors when the Bulge correction is applied, and in red, we show when the NGC 6656-made solution is applied. The size of the residual vectors is magnified by a factor 6000.

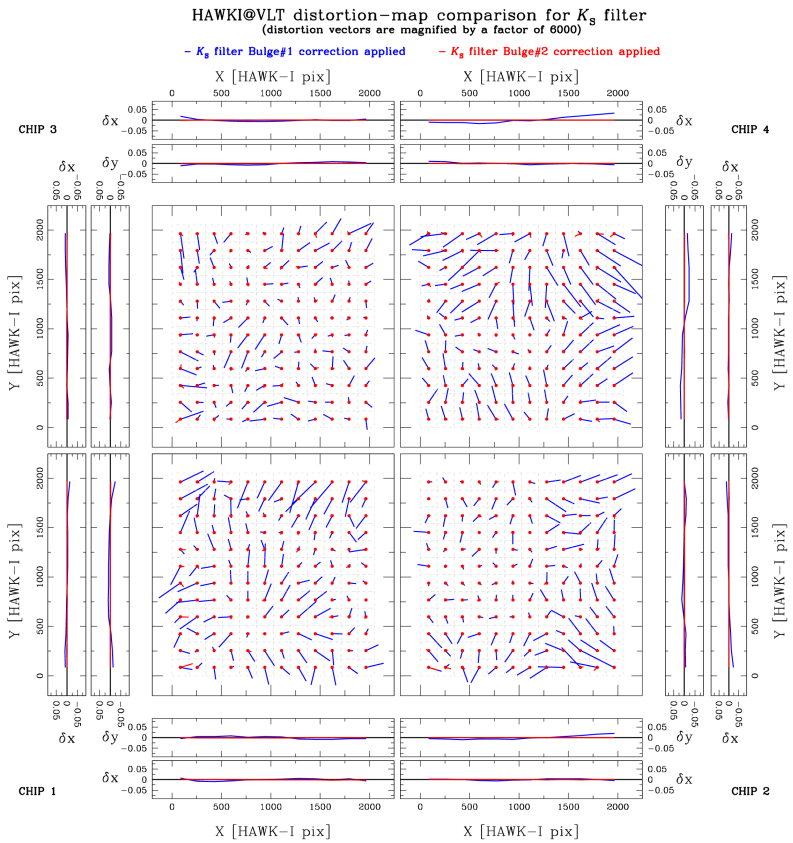

Figure 2.19. As in Fig. 2.16 but for the Bulge#2 case.

2.6 A possible explanation of the periodicity

In Sect. 2.5.2, we have corrected for the periodic trend observed in the δx positions. At first, this component might suggest the presence of some irregularities in the pixel grid, due to manufacturing defects, such as an imperfect alignment in the placement of the lithographic stencils that established the pixel boundaries on the detector. Examples include, the well-known $34^{\rm th}$-row error found by Anderson & King (1999) in the case of the CCDs of the WFPC2 of the *Hubble Space Telescope* (*HST*), or, for a more recent example, the pattern observed on the detectors of the *HST*'s WFC3/UVIS channel (see Bellini, Anderson, & Bedin 2011 for details). If the square wave that we see here in the HAWK-I δx residuals (from a-1 to a-4 panels of Fig. 2.11) is due to a geometric effect, then the variation in pixel spacing would cause periodic features in the flat fields, since wider pixels collect more light when the detector is illuminated by a flat surface brightness. In this case, the observed δx-residual trend would imply that the $64^{\rm th}$ and the $65^{\rm th}$ pixels in each row would be physically smaller than the $128^{\rm th}$ and the $129^{\rm th}$ pixels.

To verify this hypothesis, we computed the local flat ratio as described in Bellini, Anderson, & Bedin (2011). We took the ratio of the pixel values over the median of the 32-pixel values on either side along X direction (independently for each of the amplifiers). We computed the median value of this ratio for all pixels within $400 < y^{\rm raw} < 1900$ in each column. We did this for each column between $100 < x^{\rm raw} < 1900$ pixels. We chose this particular area to avoid some artefacts in the flat field near the edge of each chip. We then plotted the local flat ratio as a function of the 128-column pattern. The plot for chip[3] of the $K_{\rm S}$-filter flat field is shown in

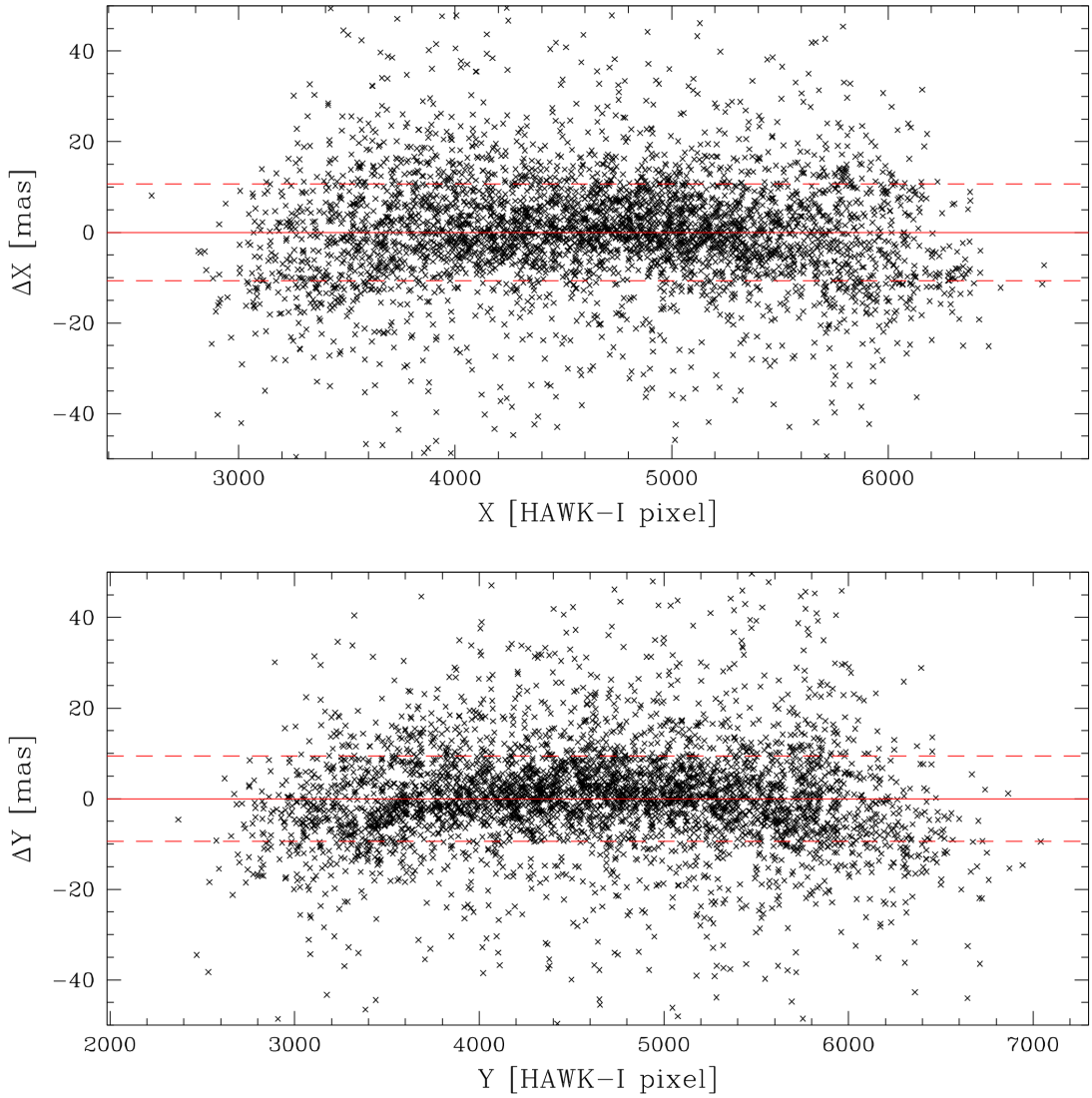

Figure 2.20. Top: Δx versus X between the two Bulge fields. We plotted only bright unsaturated stars. Bottom: as on top but with Δy versus Y. The red solid line is set at 0 mas, while the dashed lines are set at ±10.7 mas on the top and ±9.4 mas on the bottom.

Fig. 2.24 as example. The variation of the flat ratio of all chips in the vicinity of the columns 1, 64, and 128 is lower than 0.25%, thus suggesting an uniform pixel grid.

Another possible explanation of this effect can be ascribed to the readout process of the Rockwell detectors. The Rockwell HgCdTe detectors are designed to have three output modes. It can use 1, 4 or 32 amplifiers. The HAWK-I detector is set up to use all 32 amplifiers, and it takes 1.3 s to read out the entire chip. In the 32-amp mode, the chip is divided into 32 64-pixel-wide strips, each fed into a different amplifier. The adopted operating mode performs the read-out from left-to-right in even amplifiers and from right-to-left in odd amplifiers.

An apparent shift of the stars' position along the x axis may happen if there is a "periodic lag" during the read out, since the amplifier reads the pixels in sequence. This effect is very similar

Table 2.3. Size of the J corrections. All the values are given in pixel.

Chip	X-axis		Y-axis		X-axis		X-axis		X-axis		Y-axis	
	Min	Max	Min	Max	Min	Max	Min	Max	Min	Max	Min	Max
	P Correction				S Correction		FS Correction		TP Correction			
1	−2.4974	0.0001	−3.4467	0.7815	−0.0354	0.0294	−0.0922	0.0828	−0.3698	0.1842	−0.0638	0.1439
2	−0.2483	2.7147	−3.7959	0.8621	−0.0354	0.0294	−0.0221	0.0391	−0.0903	0.0602	−0.0847	0.0694
3	−2.2199	0.0001	−0.9715	3.2343	−0.0354	0.0294	−0.0197	0.0288	−0.0784	0.0979	−0.0713	0.0974
4	−0.2678	2.8462	−0.7153	3.8896	−0.0354	0.0294	−0.0323	0.0266	−0.0929	0.1281	−0.0803	0.0751

Table 2.4. As in Table 2.3 but for the H corrections (in pixel).

Chip	X-axis		Y-axis		X-axis		X-axis		X-axis		Y-axis	
	Min	Max	Min	Max	Min	Max	Min	Max	Min	Max	Min	Max
	P Correction				S Correction		FS Correction		TP Correction			
1	−2.2681	0.0001	−2.7934	0.6161	−0.0307	0.0308	−0.0365	0.0547	−0.0833	0.0643	−0.0543	0.0505
2	−0.0449	2.6406	−4.0058	0.9549	−0.0307	0.0308	−0.0188	0.0245	−0.0575	0.0497	−0.0473	0.0506
3	−2.2937	0.0001	−1.3461	3.4982	−0.0307	0.0308	−0.0328	0.0257	−0.0768	0.0920	−0.0439	0.0624
4	−0.3316	2.8668	−0.4570	3.5777	−0.0307	0.0308	−0.0298	0.0395	−0.1149	0.1084	−0.0507	0.0538

Table 2.5. As in Table 2.3 but for the K_S corrections (in pixel).

Chip	X-axis		Y-axis		X-axis		X-axis		X-axis		Y-axis	
	Min	Max	Min	Max	Min	Max	Min	Max	Min	Max	Min	Max
	P Correction				S Correction		FS Correction		TP Correction			
1	−2.3696	0.1417	−3.4477	0.7932	−0.0245	0.0275	−0.0661	0.0678	−0.2406	0.1095	−0.0763	0.0632
2	−0.1348	2.7460	−3.7555	0.8715	−0.0245	0.0275	−0.0146	0.0256	−0.0636	0.0557	−0.0340	0.0403
3	−2.1681	0.0001	−1.0793	3.3528	−0.0245	0.0275	−0.0272	0.0212	−0.0797	0.0799	−0.0419	0.0320
4	−0.1457	2.8005	−0.5338	3.4126	−0.0245	0.0275	−0.0152	0.0144	−0.0836	0.0532	−0.0573	0.0375

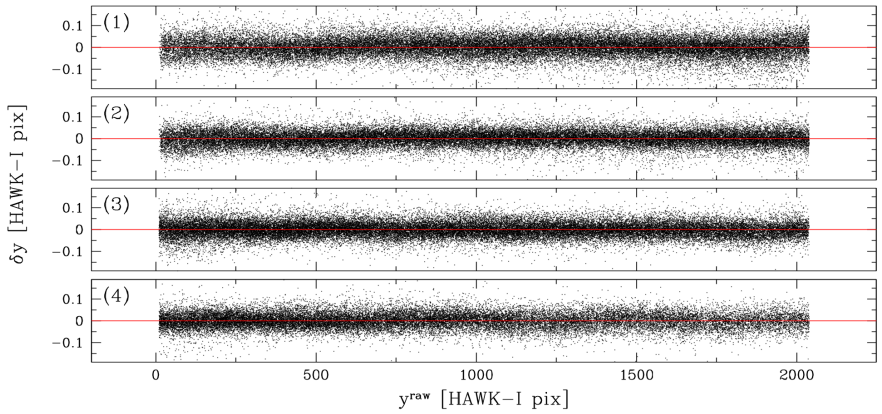

Figure 2.21. δy as function of Y in units of HAWK-I pixels for all chips. The red lines is set at 0 HAWK-I pixel.

to the "bias shift" observed in ACS/WFC of the *HST* after part of the electronics, in particular the new amplifiers, has been replaced during service mission 4 (Golimowski et al. 2012). As for ACS, the readout electronics of HAWK-I's detectors take a while to settle to a new value when the charge of another pixel is loaded. Without waiting an infinite amount of time to settle down,

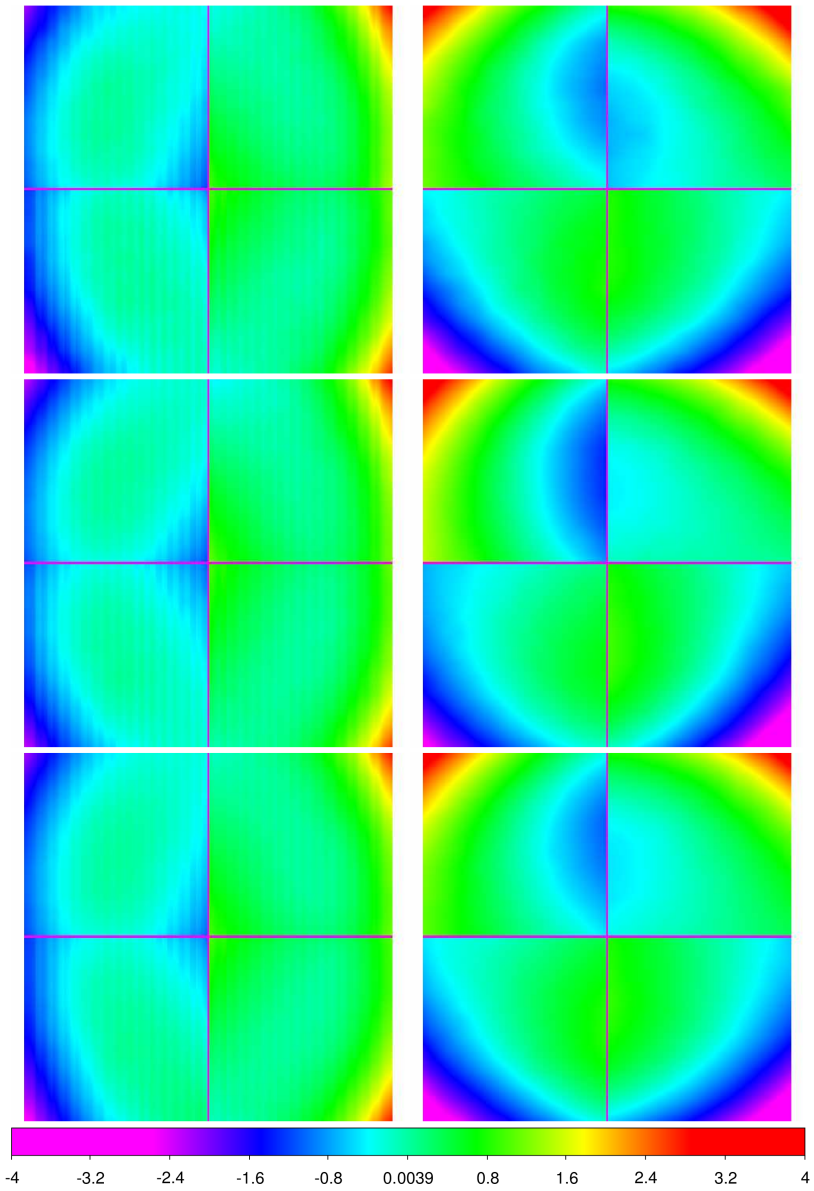

Figure 2.22. Maps of the corrections. From top to bottom, J-, H-, and K_S-filter corrections. For each filter, the four chips on the left show the X-correction, while the four chips on the right show the Y-correction. A linear scale is used. Red means positive corrections; purple are negative corrections. The values in the colour bar are expressed in pixels. For the J filter, the x-corrections varies between -2.95 and 2.96 pixels across the whole detector, while the y-corrections between -3.88 and 3.95 pixels. For the H filter, the minimum and maximum corrections for the x-coordinate are -2.40 and 2.99 pixels, while the corrections for the y-coordinate are -4.00 and 3.59 pixels. The minimum and maximum x-corrections for the K_S-filter solution are -2.67 and 2.85 pixels; for y-corrections, the minimum and maximum are -3.77 and 3.42 pixels.

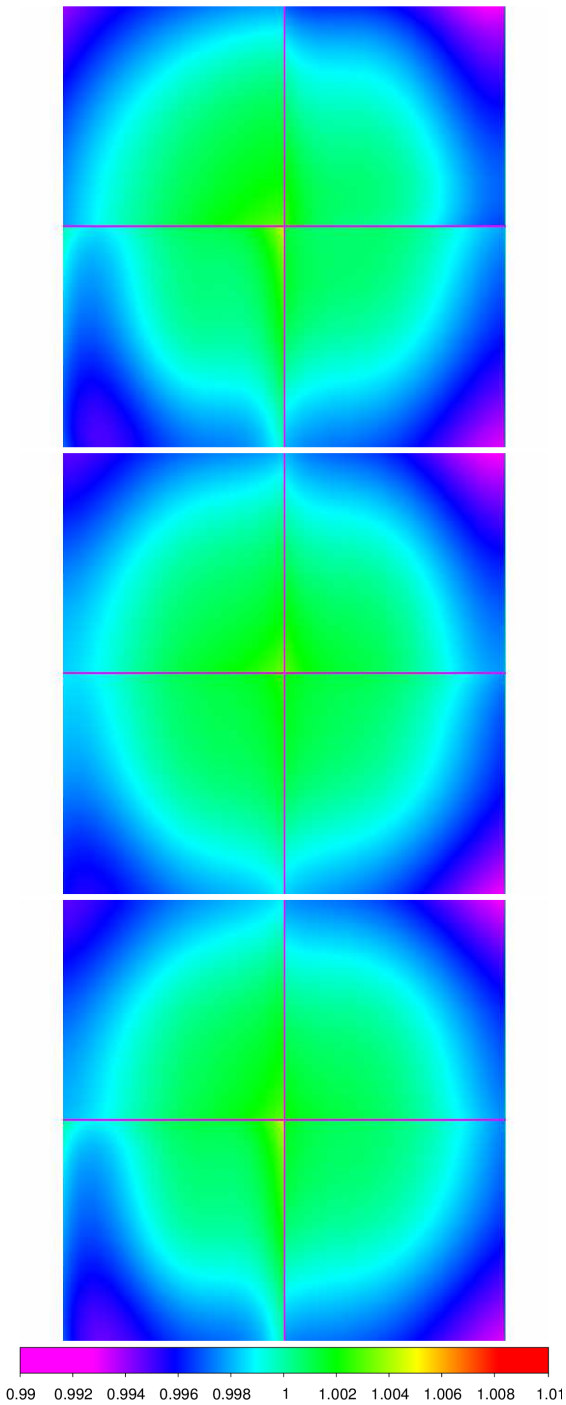

Figure 2.23. Maps of the pixel-area corrections. From top to bottom, J-, H-, and K_S-filter corrections. The values in the colour bar represent the corrected area of the pixels. Before the correction, all pixels have an area of 1 pixel^2. The scale in the images is linear.

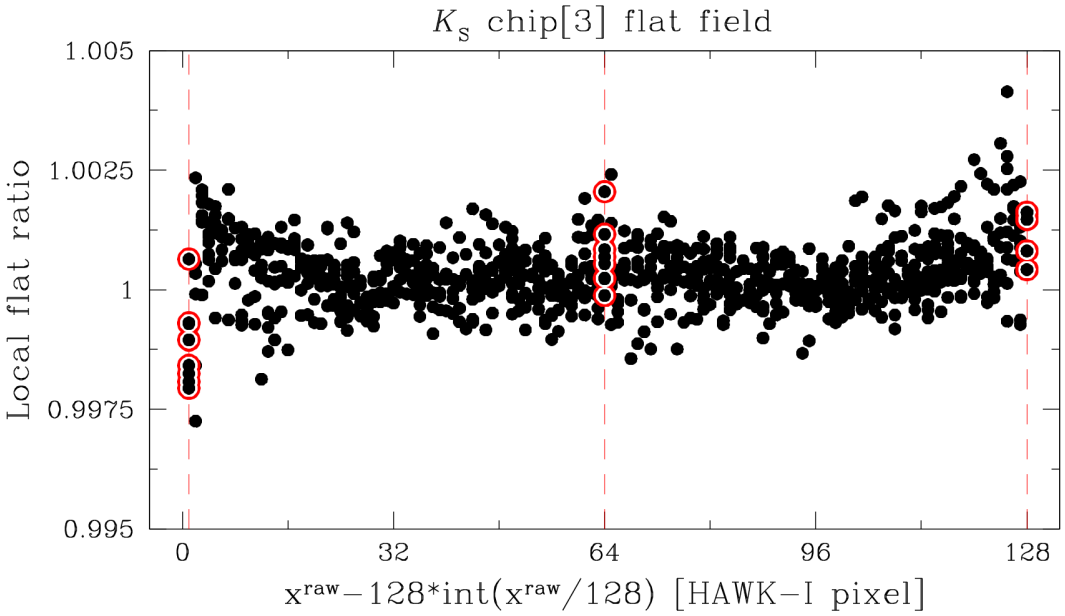

Figure 2.24. Local flat ratio of K_S chip[3] flat field. Dashed red lines mark the boundaries of the possible discontinuities. There are not significant local flat ratio variations at the 1^{st}, 64^{th}, and 128^{th} columns (highlighted by red open circles).

there is some imprint left from the previous pixel. Although HAWK-I's NIR-detectors are very different from the ACS/WFC CCDs, a similar effect, or, an inertia of discharging the capacitors to reset to a new value, could cause the observed periodicity. Furthermore, each amplifier in the 32-amp mode reads 64 pixels, and 64 pixels is the observed periodicity of the effect that we found. This suggests that the cause of the periodic trend we see in the distortion could be related to the amplifiers' setup.

2.7 Weeding out spurious objects

We applied our Bulge-based distortion correction, derived as in Sect. 2.5, to the entire data set with the exceptions of the Bulge#2 and NGC 6656 fields, where we applied the distortion correction computed from their own exposures. We also produced stacked images to have a visible reference for our catalogues.

While analysing the catalogues and inspecting the stacked images, we noted the presence of some faint, spurious objects identified as stars and close to brighter stars. Many of these objects were found to be in fact PSF artefacts and are not real stars. These artefacts are called "PSF bumps". These bumps can easily mimic faint, real stars in the proximity of much brighter stars. Normally, PSF bumps are located at the same radial distance from the PSF centre and have about the same brightness level. Because of these two characteristics, PSF bumps can be removed. Therefore, we introduced a flag to purge the catalogues from these detections. This flag may necessary exclude a few real stars, but faint stars close to a bright one could not be well measured anyway.

To flag these spurious objects, we followed the same approach as described in Sect. 6.1 of Anderson et al. (2008). We first selected all stars fainter than a specific instrumental magnitude (e.g. for 47 Tuc, shown in Fig. 2.25, we chose $J \geq -10$) and with a QFIT ≥ 0.4. For each of such

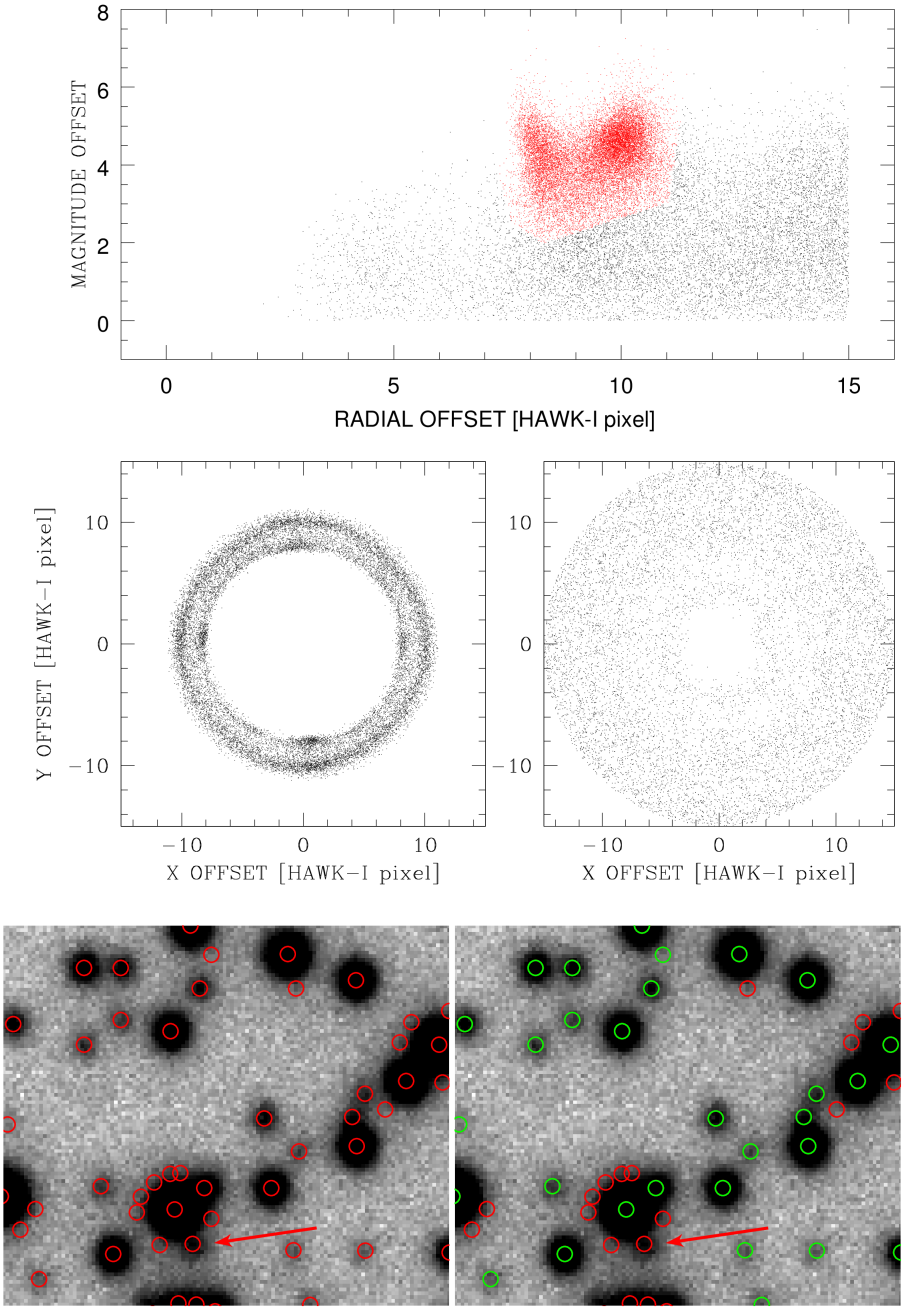

Figure 2.25. Example of the weeding process for the 47 Tuc catalogue. Top: magnitude offset versus radial offset for sources found around bright stars. We plotted the spurious objects that have been rejected in red. Middle: Y versus X separation of the rejected (left) and accepted (right) detections from the corresponding bright stars. Bottom: on the left, we show all the objects (red circles) in a ∼100×100 pixels region in the 47 Tuc catalogue, and on the right, we highlight the detections that have been accepted (green circles). As described in the text, a faint star near the bright one pointed by the red arrow on the bottom has been flagged even if it was not an artefact.

Table 2.6. List of the HAWK-I filter zero-points, rms, number of stars used, and zero-point formal uncertainties ($\frac{\sigma}{\sqrt{N-1}}$) to which 2MASS error of the stars used to calibrate should be added in quadrature. The values listed in columns from (3) to (6) are those obtained in the 2MASS system, and from (7) to (10) in the MKO system.

		2MASS				MKO			
Field	**Filter**	**Zero-point**	σ	N	$\frac{\sigma}{\sqrt{N-1}}$	**Zero-point**	σ	N	$\frac{\sigma}{\sqrt{N-1}}$
Bulge (Baade's window #1)	J	−28.31	0.07	995	0.01	−28.25	0.07	966	0.01
	H	−28.60	0.05	57	0.01	−28.57	0.05	37	0.01
	K_S	−28.01	0.09	543	0.01	−27.98	0.09	543	0.01
Bulge (Baade's window #2)	K_S	−27.77	0.09	543	0.01	−27.75	0.09	542	0.01
NGC 6121 (M 4)	J	−28.76	0.06	298	0.01	−28.71	0.06	298	0.01
	K_S	−28.69	0.09	86	0.01	−28.67	0.09	86	0.01
NGC 6822	J	−28.40	0.04	28	0.01	−28.36	0.04	28	0.01
	K_S	−27.59	0.07	26	0.01	−27.57	0.07	26	0.01
NGC 6656 (M 22)	K_S	−27.95	0.15	83	0.02	−27.93	0.15	81	0.02
NGC 6388	J	−28.46	0.06	289	0.01	−28.41	0.06	286	0.01
	K_S	−27.73	0.05	229	0.01	−27.72	0.05	229	0.01
JWST calibration field (LMC)	J	−28.78	0.07	233	0.01	−28.74	0.07	226	0.01
	K_S	−27.84	0.09	122	0.01	−27.82	0.09	123	0.01
NGC 104 (47 Tuc)	J	−28.26	0.05	80	0.01	−28.22	0.05	80	0.01
	K_S	−27.71	0.05	128	0.01	−27.69	0.05	128	0.01

objects, we computed the magnitude difference and the distance from the closest bright star (e.g. $J \leq -11$ for the case of 47 Tuc) out to 15 pixels. We then plotted those magnitude differences as a function of the radial distance (top panel of Fig. 2.25). Different clumps show up on the plot. We drew-by-hand a region around them that encloses most of these spurious objects (in red). In this way, we built a mask (one for each filter/field) used to purge PSF artefacts.

The selection we made is a compromise between missing faint objects near bright stars and including artefacts in the catalogue. In the bottom panel of Fig. 2.25, the red circles show all the detected objects in the 47 Tuc catalogue. In the bottom-right panel of Fig. 2.25, the green circles highlights the objects that have been finally accepted as real stars. The bright star close to the bottom of the figure has a faint neighbour (pointed by the arrow) that clearly is not an artefact but has been unfortunately flagged-out by our mask. These flagged stars represent only a very small fraction with respect to the total number of PSF artefacts removed by our procedure.

In each final catalogue, we added a column for each filter called F_{weed}. The flag F_{weed} is equal to 0 for those objects rejected by our mask. The only exception is the K_S-filter catalogue of Bulge#1, for which the purging was not possible because of the too-high number of objects in the catalogue that did not allow us to build a reliable mask for the PSF artefacts.

2.8 Photometric calibration

In this section, we provide two calibrations of the zero-points. The first calibration was performed using the 2MASS photometric system (Skrutskie et al. 2006) and the second calibration using the native system of the HAWK-I filters.

2.8.1 2MASS system

The first photometric calibration was performed using the 2MASS catalogue. Since 2MASS is a shallow survey, we only got a small overlap between unsaturated stars in HAWK-I images and 2MASS data covering a very narrow magnitude range near the faint limit of 2MASS. Therefore,

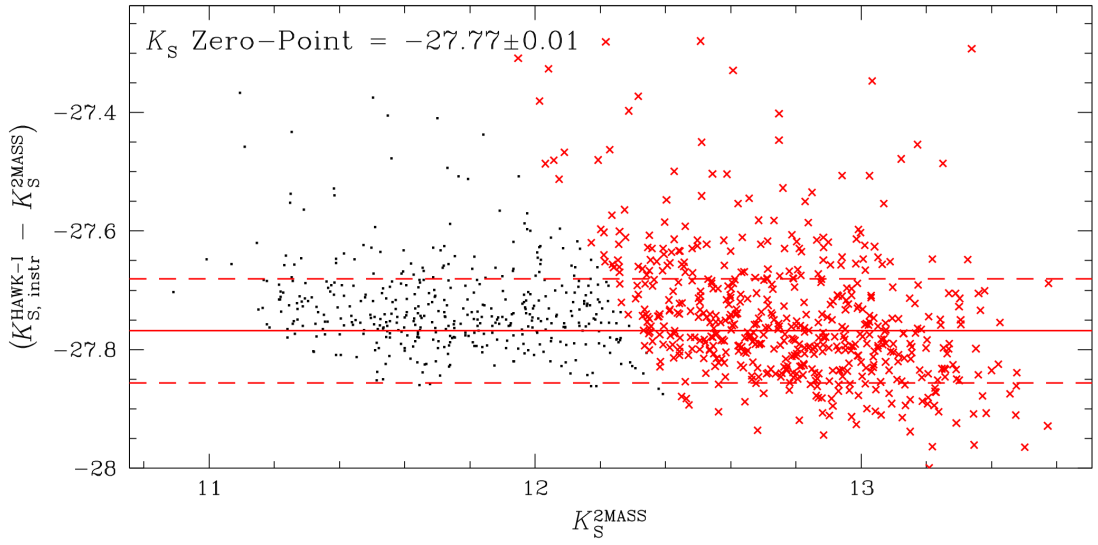

Figure 2.26. Magnitude difference between HAWK-I and 2MASS as function of the 2MASS magnitude. The black dots represent all the stars matched between HAWK-I and 2MASS with good photometry. Red crosses show stars from the saturation limit ($K_S = -15.46$) to two magnitudes fainter. The red solid line is the zero-point (median of the magnitude difference of the red crosses); the dashed line are set at a zero-point $\pm 1\sigma$ (defined as the 68.27^{th} percentile of the distribution around the median). The label on the top left corner gives the zero-point $\pm\sigma/\sqrt{N-1}$, where N is the number of stars used to compute the zero-point.

we can apply a single zero-point calibration only. We selected well-measured bright unsaturated stars within two magnitudes from saturation in our catalogues to calculate these photometric zero-points. In Fig. 2.26, we show the case of the Bulge#2 catalogue, as an example. For the Bulge#1 K_S-filter, we first registered the zero-point to that of the Bulge#2, and then used the Bulge#2 zero-point due the low number of unsaturated stars in common with 2MASS.

In Table 2.6, we list the zero-points, their rms (σ), the number of stars used to compute the zero-points (N) and $\sigma/\sqrt{N-1}$ (formal error values) for all fields. These are estimates of the zero-point uncertainties and not the errors because the 2MASS errors are not added in quadrature. Note that we only provide one zero-point for each filter/field and not one for each chip/filter/field. We registered all chips in the flat-fielding phase to the common reference system of chip[1], and while building the master frame, we iteratively registered the zero-point of all chips to that of the chip[1].

As clearly visible in Fig. 2.26, this calibration is not perfect, but there is a more conceptual limitation of this calibration. The filters of HAWK-I are in the Mauna Kea Observatory (hereafter, MKO) photometric system, which have pass-bands slightly different from the 2MASS pass-bands and are likely to contain a colour term.

2.8.2 MKO system

Determining the zero-points in the native MKO photometric system would be a more rigorous zero-point calibration. Therefore, we transformed the 2MASS magnitudes into the MKO system using the transformations described in the "2MASS Second Incremental Release" website[9] for

[9]http://www.ipac.caltech.edu/2mass/releases/allsky/doc/sec6_4b.html

2MASS stars in common with our catalogues:

$$(K_{\rm S})_{\rm 2MASS} = (K)_{\rm MKO} + (0.002 \pm 0.004) + (0.026 \pm 0.006)(J-K)_{\rm MKO} \ ,$$
$$(J-H)_{\rm 2MASS} = (1.156 \pm 0.015)(J-H)_{\rm MKO} + (-0.038 \pm 0.006) \ ,$$
$$(J-K_{\rm S})_{\rm 2MASS} = (1.037 \pm 0.009)(J-K)_{\rm MKO} + (-0.001 \pm 0.006) \ ,$$
$$(H-K_{\rm S})_{\rm 2MASS} = (0.869 \pm 0.021)(H-K)_{\rm MKO} + (0.016 \pm 0.005) \ .$$

We used only 2MASS stars that, once transformed in the MKO system, were in the colour range $-0.2<(J-K)_{\rm MKO}<1.2$. We then registered the zero-points as described in the previous section. We found an average difference between the MKO and 2MASS zero-points of 0.05, 0.03, and 0.02 mag in J-, H-, and $K_{\rm S}$-filter, respectively. For the $K_{\rm S}$ filter in NGC 6121 catalogue, we did not have enough stars to compute the zero-point in the colour range in which the transformations are valid, so we added the average $K_{\rm S}$-filter offset (0.02 mag) between the two systems to the 2MASS-based zero-point. In Table 2.6, we also list the MKO zero-points (with their σ, N, and $\sigma/\sqrt{N-1}$).

2.9 Applications: NGC 6656 and NGC 6121

Figure 2.27 shows a full set of CMDs with one for each field. For the HAWK-I data used in this section, the photometric zero-points are those obtained in the 2MASS system (Sect. 2.8.1). We chose two possible targets among the observed fields to illustrate what can be done with HAWK-I. The two close globular clusters NGC 6656 and NGC 6121 have high proper motions relative to the Galactic field. In the ESO archive, we found WFI@2.2 m MPI/ESO exposures of the same fields taken ∼8 years before our HAWK-I observations. These exposures allow us to obtain a nearly-perfect separation between cluster and field stars, as we will show in the following subsections.

2.9.1 WFI data set: photometric calibration and differential reddening correction

We downloaded multi-epoch images of NGC 6656 from the ESO archive (data set 163.O-0741(C), PI: Renzini), taken between May 13 and 15 1999 in B, V, and I filters with the WFI@2.2 m MPI/ESO. These images were not taken for astrometric purposes and only have small dithers, thus preventing us from randomising the distortion-error residuals. Photometry and astrometry were extracted with the procedures and codes described in Paper I. Photometric measurements also were corrected for "sky concentration" effects (light contamination caused by internal reflections of light in the optics, causing a redistribution of light in the focal plane) using recipes in Paper III. The WFI photometry was calibrated matching our catalogues with the online secondary-standard stars catalogue of Stetson (Stetson 2000, 2005) using well-measured, bright stars, and least-square fitting. We found that a linear relation between our instrumental magnitudes and Stetson standard magnitudes was adequate to register our photometry. The calibration equations are shown in Fig. 2.28 in the left-hand panels.

As for NGC 6656, we downloaded the NGC 6121 images from the ESO archive taken with the WFI@2.2 m MPI/ESO between August 16 and 18 1999, in B, V, and Rc filters. We performed the photometric calibration as described above. The corresponding calibration fit and equations are shown in Fig. 2.28 in the right-hand panels.

In the following subsections, we explore some applications in which the photometry has been corrected for differential reddening. We performed a differential reddening correction following the iterative procedure described in Milone et al. (2012). As described in detail by Milone et al., the correction to apply to a given star is measured from the differential reddening of the

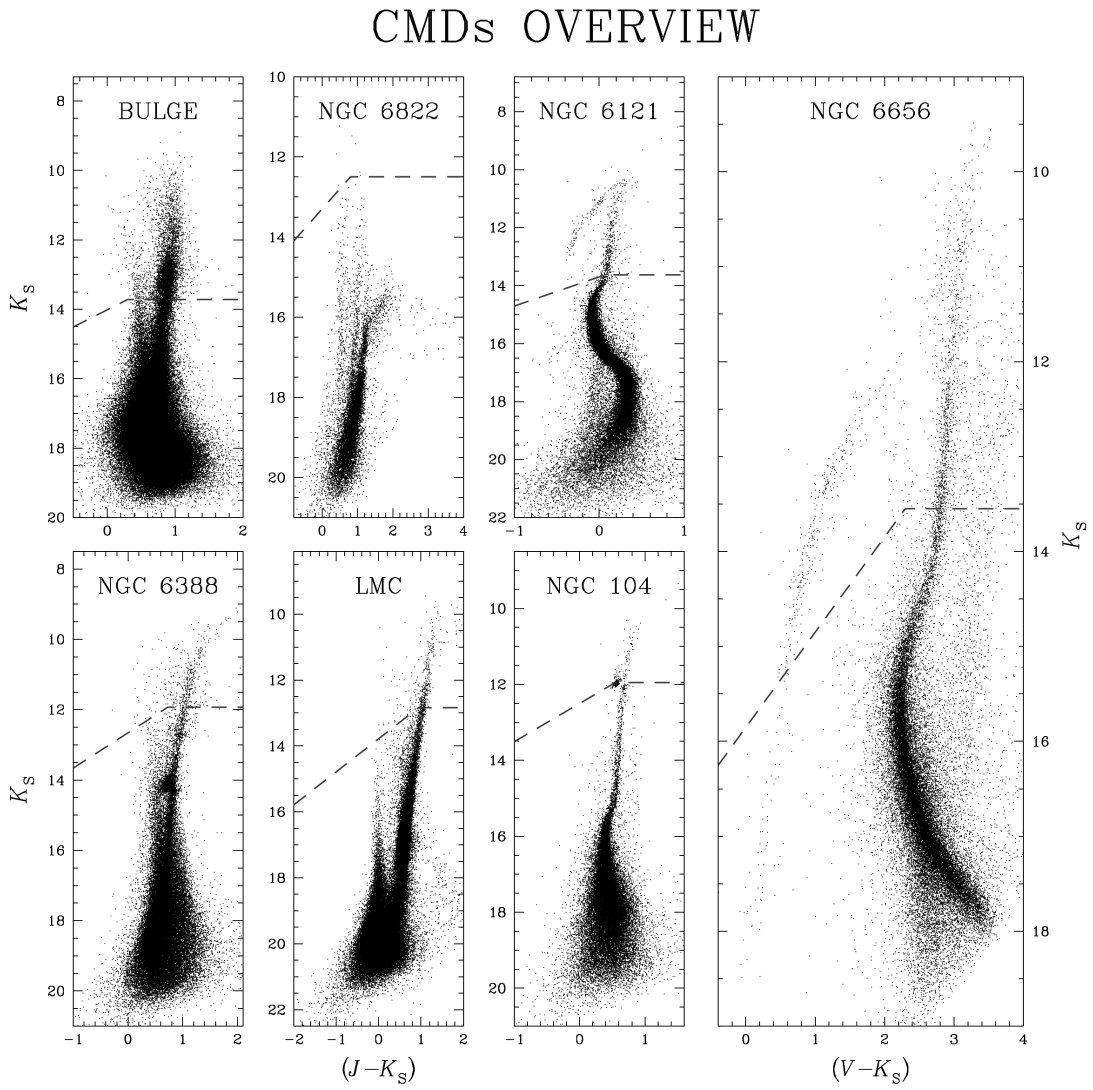

Figure 2.27. Full set of CMDs of the fields used in this Chapter. The dotted grey lines set the saturation threshold in K_S filter.

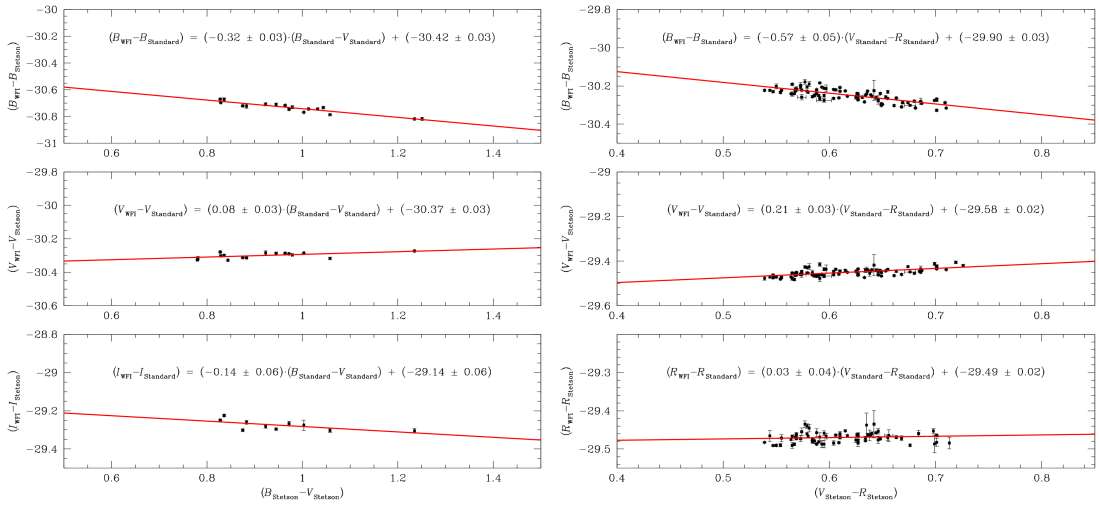

Figure 2.28. Left: calibration fits and equations for B, V, and I filters for NGC 6656. Right: same as on the left but for B, V, and Rc filters for NGC 6121.

selected reference stars that are spatially close to the target. The number of stars to use should be a compromise between the need to have an adequate number of reference stars to compute the correction and the need for spatial resolution. We chose the nearest 45 reference stars from the faint part of the RGB to the brighter part of the main sequence (MS) to compute the correction. In Fig. 2.29, we present an example to demonstrate how the CMDs change by taking the differential reddening into account and correcting for it. We show a zoom-in of the NGC 6121 K_S versus $(J - K_S)$ CMD before (left-hand panel) and after (right-hand panel) the correction. Around the MS turn-off (K_S∼15), the sequence narrowed from $\Delta(J - K_S)$∼0.08 to ∼0.03 mag. Hereafter, all CMDs for both NGC 6656 and NGC 6121 are corrected for differential reddening.

2.9.2 NGC 6656 proper motion

To compute proper motions, we followed the method described in Paper I, to which we refer for the detailed description of the procedure. For the WFI images, we only used those chips that overlap with the HAWK-I field and with an exposure time of ∼239 s for a total of 19 first-epoch catalogues that include B, V, and I filters. With the 100 catalogues for the second epoch (HAWK-I) in K_S band, we computed the displacements for each star. As described in Paper I, the local transformations used to transform the star's position in the 1st epoch system into that of the 2nd epoch minimise the effects of the residual geometric distortion.

In Fig. 2.30, we show our derived proper motions for NGC 6656. We show only stars with well-measured proper motions. In the left-hand panels of Fig. 2.30, we show the entire sample of stars; the middle panels display likely cluster members. The right-hand panels show predominantly field stars. In the middle vector-point diagram (VPD), we drew a circle around the cluster's motion centroid of radius 4 mas yr^{-1} to select proper-motion-based cluster members. The chosen radius is a compromise between missing cluster members with larger proper motions and including field stars that have velocities equal to the cluster's mean proper motion. This example demonstrates the ability of our astrometric techniques to separate field and cluster stars. To enclose most of the field stars, we drew an ellipse centred at (−11.8,1.2) mas yr^{-1} in the right-hand VPD with major and minor axes of 12.5 and 14.8 mas yr^{-1}, respectively.

We analysed the impact of the differential chromatic effects in our astrometry for this cluster

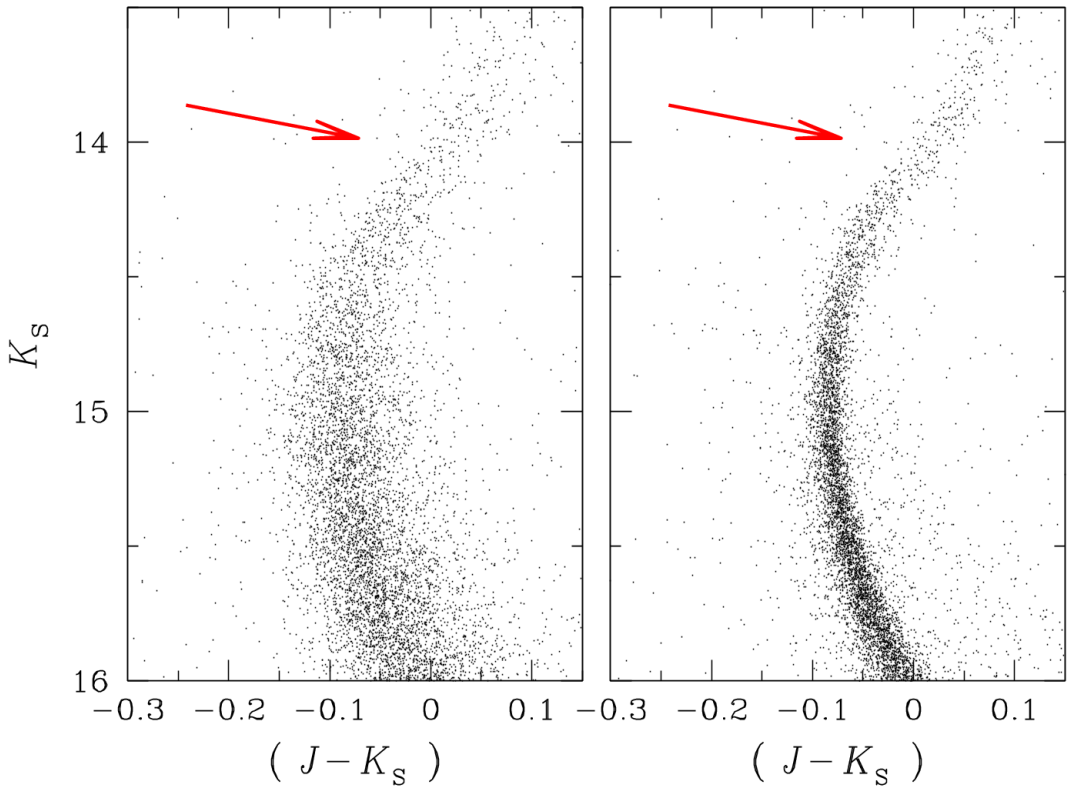

Figure 2.29. Zoom-in of the K_S versus $(J-K_S)$ CMD of NGC 6121. We show the CMDs before and after the differential reddening correction is applied (left- and right-hand panels respectively). The red arrow indicates the reddening direction.

as done by Anderson et al. (2006). Using unsaturated stars and with a colour baseline of about 3 mag, the effects seem to be negligible (less than 1 mas/yr in each direction) within the airmass range of our data set. Thus we assumed to be negligible and did not correct it.

2.9.2.1 The radial distribution of NGC 6656 SGB stars

The sub-giant branch (SGB) based on HAWK-I data remains broadened even after the differential reddening correction. This is not surprising since NGC 6656 is known to have a split SGB (Piotto et al. 2012). The large FoV of our data set allowed us to study the behaviour of the radial trend of the ratio $\hat{p}_{fSGB} = N_{fSGB}/(N_{fSGB} + N_{bSGB})$, where N_{bSGB} and N_{fSGB} are the number of stars belonging to the bright (bSGB) and the faint SGB (fSGB), respectively. First of all, we computed this ratio for SGB stars between 1.5 and 3.0 arcmin from the centre of the cluster (we adopted the centre given by Harris 1996, 2010 edition), and between 3.0 and 9.0 arcmin (close to the edge of the FoV). We chose these two radial bins to have about the same number of SGB stars in both samples. Since the innermost region (within $1\farcm5$ from the centre) of the cluster is too crowded to be analysed with the HAWK-I data, we also used the data set of Piotto et al. (2012) to have a third, inner point.

To compute the $N_{fSGB}/(N_{fSGB} + N_{bSGB})$ ratio, we rectified the SGBs using an approach similar to that described in Milone et al. (2009). In this analysis, we used only cluster members

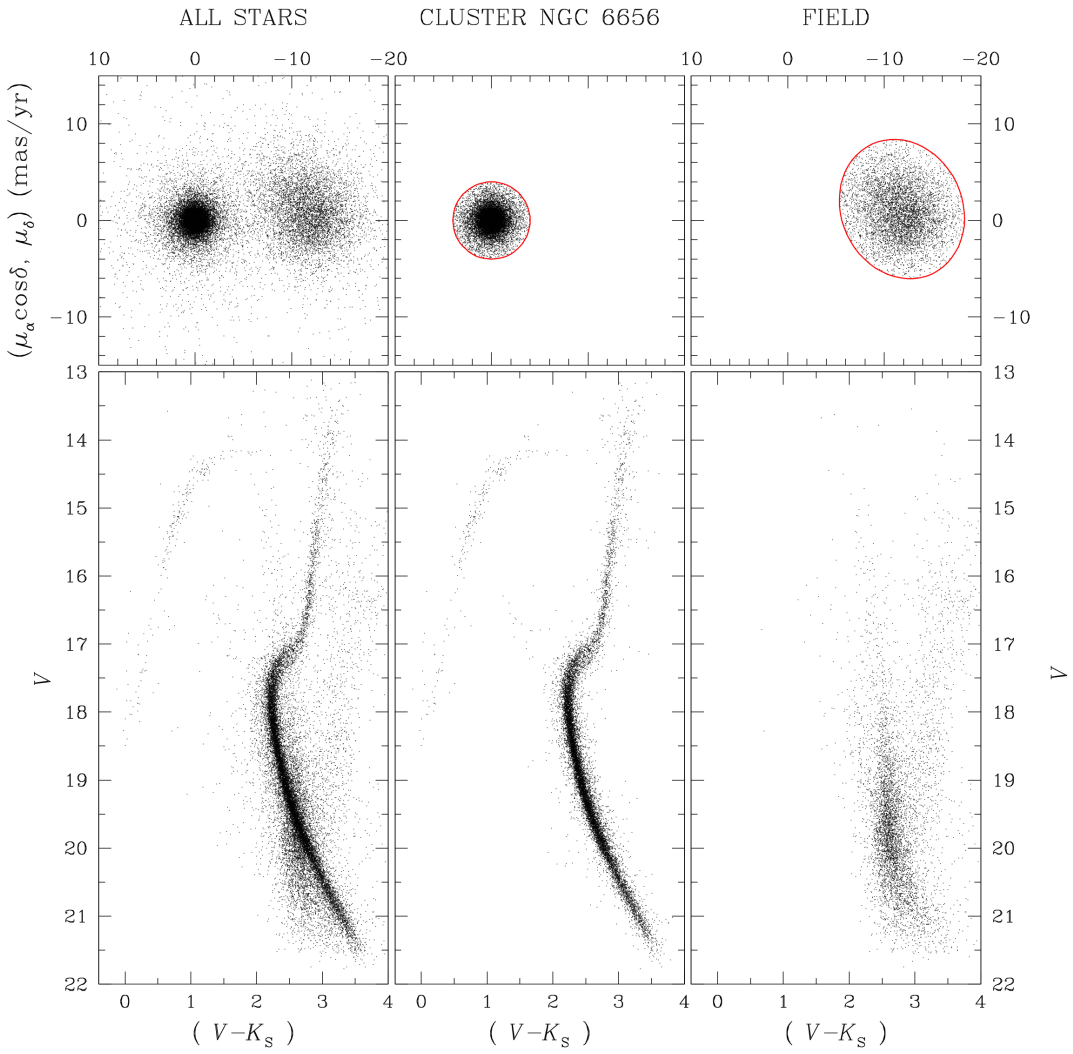

Figure 2.30. Top panels: proper motion vector-point diagram with a ∼8-yr time baseline between HAWK-I and WFI data. The (0,0) location in VPD is the mean motion of cluster stars candidates. Bottom panels: V versus $(V - K_S)$ CMD. Left: the entire sample. Centre: Stars in VPD with proper motion within 4 mas yr^{-1} around the cluster mean. Right: Probable background/foreground field stars in the area of NGC 6656 studied in this section. The ellipse that encloses most of the field stars is centred at (−11.8,1.2) mas yr^{-1} with major and minor axes of 12.5 and 14.8 mas yr^{-1}, respectively.

with good photometry. The results are shown in Fig. 2.31. We started by using HAWK-I data only. As described by Milone et al., we need four points (P1b, P1f, P2b, and P2f in Fig. 2.31) to rectify the SGBs. Once selected these points, we transformed the CMD into a new reference system in which the points P1b, P1f, P2b, and P2f have coordinates (0,0), (1,0), (0,1), and (1,1), respectively. We drew by hand a line to separate the two sequences. We derived a fiducial line for each SGB by dividing it into bins of 0.12 'Ordinate' value and fitting the 3.5σ-clipped

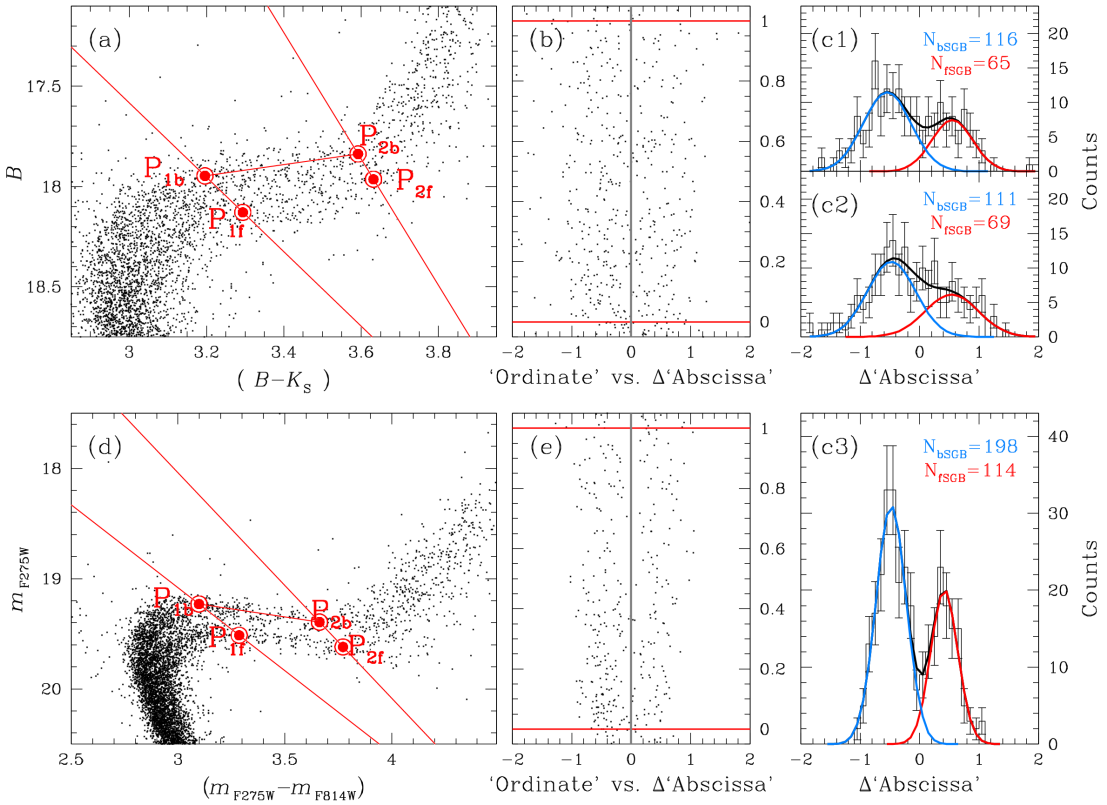

Figure 2.31. (a): SGB zoom-in on B versus $(B - K_S)$ CMD of NGC 6656. The four points (and the two straight lines) used to perform the linear transformation are plotted in red. (b): Rectified SGB. The red horizontal lines are set at 'Ordinate' 0 and 1; the grey solid line is set at Δ'Abscissa'=0. (c1): Dual-Gaussian fit in black; individual Gaussian in blue and red are used for bright and faint SGB respectively, for the SGB-star sample between 1.5 and 3.0 arcmin from the cluster centre. (c2): As for $(c1)$ but in the range 3.0-9.0 arcmin. (c3, e, d): Same as in panels (a, b, c1, c2) but for the *HST* data in the $m_{\rm F275W}$ versus $(m_{\rm F275W} - m_{\rm F814W})$ plane.

median 'Abscissa' and 'Ordinate' for each of them with a spline. We rectified the two sequences using the average of the two fiducials. The rectification was performed by subtracting, from the 'Abscissa' of each star, the 'Abscissa' of the fiducial line at the same 'Ordinate' level (panel (b)). In panels (c1) and (c2), we show the resulting final Δ'Abscissa' histogram (between Δ'Abscissa' −0.19 and +0.19 and 'Ordinate' 0 and 1) for stars between 1.5 and 3.0 arcmin (c1) and between 3.0 ad 9.0 arcmin (c2) from the cluster centre. The individual Gaussians for the bright and the faint SGB are shown in blue and red, where the sum of the two in black. After this complicated procedure, we were finally able to estimate the fraction of stars belonging to the fSGB and bSGB. We used binomial statistics to estimate the error σ associated with the fraction of stars. We defined $\sigma_{\hat{p}_{\rm fSGB}} = \sqrt{\hat{p}_{\rm fSGB}(1 - \hat{p}_{\rm fSGB})/(N_{\rm fSGB} + N_{\rm bSGB})}$.

As noted by Piotto et al. (2012), points P1b-P2b and P1f-P2f define a mass interval for stars in the two SGB segments. If we want to calculate the absolute value of the ratio $\hat{\rm p}_{\rm fSGB}$, we need to make sure that the same mass interval is selected in the two SGBs and at all radial distances. Due to the lack of appropriate isochrones for the HAWK-I data, this was not feasible. Still, we can estimate the radial trend of $\hat{\rm p}_{\rm fSGB}$ by taking advantage of both *HST* (for the inner region)

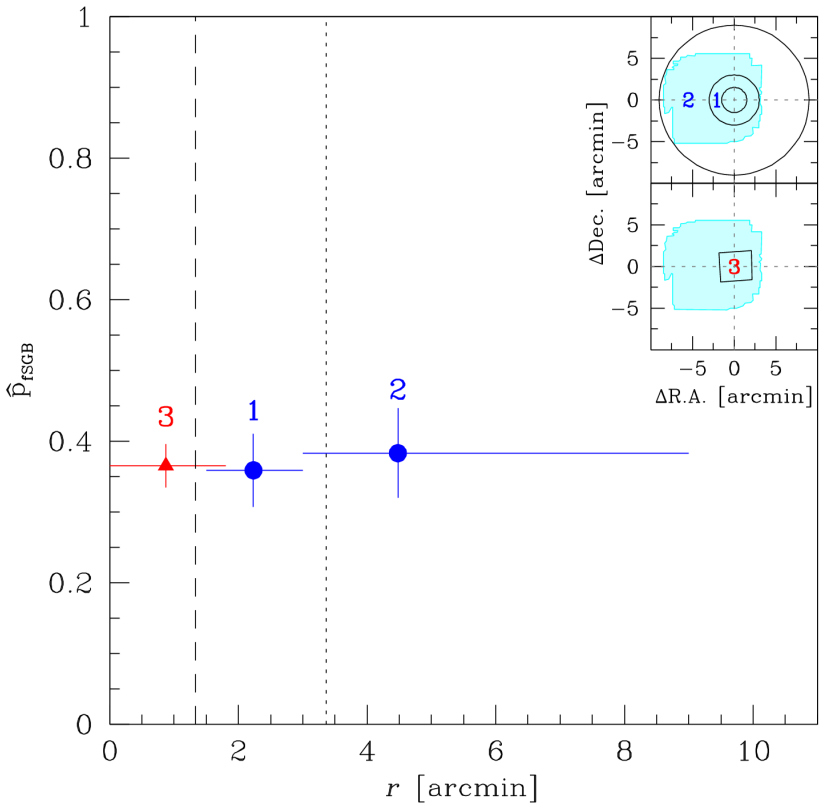

Figure 2.32. Radial trend of $\hat{p}_{fSGB}$. The numbers 1, 2, and 3 correspond to panels (c) in Fig. 2.31. The points are placed at the average distance of the SGB stars used to compute the ratio in each radial bin. In blue, we plotted the ratios obtained with the HAWK-I data set; in red, we show the ratio obtained with the *HST* data set. The vertical error bars are computed as described in the text. The horizontal error bars cover the radial intervals. The two vertical lines indicate the core radius and half-light radius (1.′33 and 3.′36 respectively; from Harris 1996, 2010 edition). In the top-right panels, the cyan region highlights the HAWK-I field. The cluster centre is set at (0,0). The three circles have radius 1.5, 3.0, and 9.0 arcmin. The black parallelogram represents the field covered by the *HST* data. The regions used to compute the ratios are labelled with the numbers 1, 2, and 3, respectively.

and HAWK-I (for the outer region) data by making sure that we use the same mass interval for the bSGB (and the same mass interval for the fSGB) in both data sets.

For this reason, we cross-correlated our HAWK-I catalogue with that of Piotto et al. (2012). First, we selected the sample of SGBs stars in the B versus $(B - K_S)$ CMD between the P1b, P1f, P2b, and P2f points of panel (a) in Fig. 2.31. In the m_{F275W} versus $(m_{F275W} - m_{F814W})$ CMD, we selected the same stars. In this CMD, we fixed four points that enclose these stars, used them to rectify the SGBs, and then calculated the ratio by following the same procedure as described for HAWK-I data (panels (c3), (d), and (e) in Fig. 2.31). We emphasise that these intervals are not the same as the ones used in Piotto et al. (2012), but we used approximately (within the uncertainties due to difficulty to select the limiting points) the same mass intervals in calculating the three SGB population ratios.

The trend of the $\hat{p}_{fSGB}$ ratio is shown in Fig. 2.32. To give a more reliable estimate of the error

bars, we also included the histogram binning uncertainty (We computed the ratio varying the starting point/bin width in the histogram and estimate the σ of these values.) and quadratically added them to $\sigma_{\hat{p}_{\rm fSGB}}$. In any case, these error bars still represent an underestimate of the total error because other sources of uncertainty should to be taken in account (e.g., the uncertainty in the location of the limiting points of the selected SGB segments). The error bars are larger for the two HAWK-I points because of the smaller number of objects in the sample.

Our conclusion is that the radial trend of the two SGB populations within the error bars is flat.

2.9.3 NGC 6121 proper motion

As before, we chose all WFI images with an exposure time of about 180 s and only used the chips overlapping HAWK-I data. In this way, we had 36 catalogues for the first epoch. For the second HAWK-I epoch, we had 400 catalogues (100 images $\times$ 4 chips). Using local transformations, we iteratively computed the star's displacements.

The resulting CMD and VPD are shown in Fig. 2.33. We only show here the best-measured stars. Unfortunately, the stars fainter than $J \sim 18.5$ in the NIR catalogues were not detectable in the optical-band WFI images. Even though the lower part of the CMD is poorly sampled (near the MS kink at $K_{\rm S}{\sim}17.5$), the separation between cluster and field objects is still good. Cluster members are those within 4 mas yr^{-1} of the cluster mean motion, while we drew an ellipse centred at (9.5,14.0) mas yr^{-1} with major and minor axes of 17.6 and 14.3 mas yr^{-1} for field stars (right-hand VPD), respectively.

Unlike NGC 6656, we did not estimate the differential chromatic refraction effects, since the colour baseline is not large enough to study the effect using only unsaturated stars. Saturated stars' proper motions are less precise, and we could confuse differential chromatic refraction with systematic trends in saturated stars' proper motions.

2.9.4 Cluster membership probability

For the two globular clusters with new proper motions, NGC 6656 and NGC 6121, we calculated cluster membership probability, P_μ, for each star. Recently, these two clusters have been analysed by Zloczewski et al. (2012) but, instead of giving membership probabilities, these authors simply divided all stars with measured proper motions into field stars, possible cluster members, and likely cluster members. This approach can be justified on the grounds of a clear separation between field and cluster in the VPD (Fig. 2.30, 2.33). However, a more rigorous cluster membership calculation technique would help to better characterise each star's membership probability. We selected a well-tested local sample method (e.g., van Altena 2013, Chapter 25). In this method, a limited subset of stars is selected for each target star with properties close to those of a target. Then, a cluster membership probability, P_μ of a star is calculated using the density functions defined by the local sample. This approach delivers more accurate membership probabilities over the entire range of magnitudes. In the case of globular clusters, the potential bias in P_μ at various magnitudes is less significant because the cluster stars dominate a relatively small number of field stars. In the presence of a highly varying precision of calculated proper motions (ranging from 0.2 to 5.5 mas yr^{-1} for NGC 6656 and NGC 6121), however, using an aggregate density function for a cluster and field can produce unreliable membership probabilities for low-precision proper motions. This is due to a significant widening of cluster's density function at the low-precision end of proper motions. Therefore, we adopted the mean error σ_μ of proper motions as a single parameter allowing us to find a local sample, which is similar to what was applied to the catalogue of proper motions in ω Cen (Paper III). There are a few differences from the study of ω Cen. First, we used a fixed window in the error distributions with the total width not exceeding 0.75 mas yr^{-1} so that a target star is located in the middle of this window. The total number of stars in local sample never exceeds 3000, hence the window size for

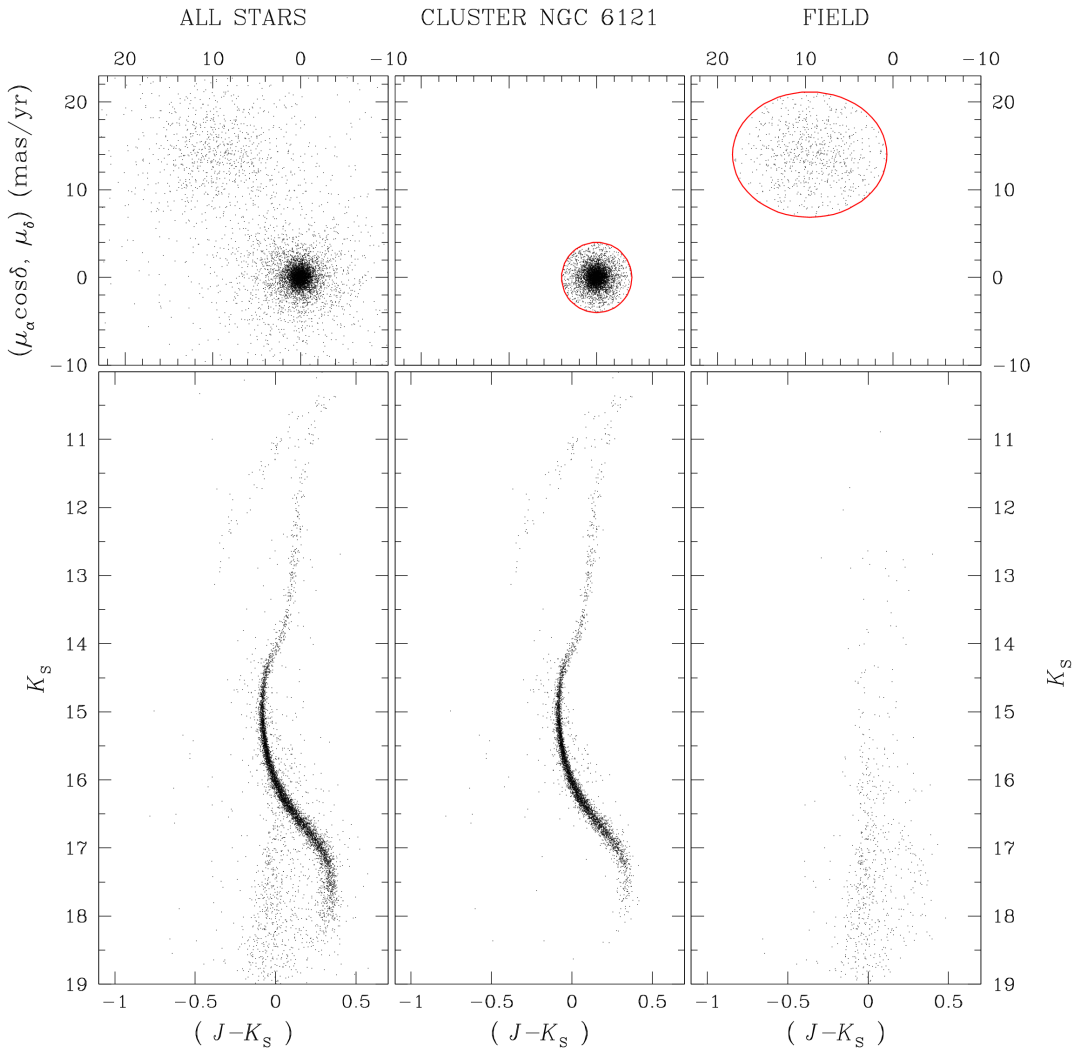

Figure 2.33. Same as Fig. 2.30 but for NGC 6121. The radius of the circle centred on the origin of the VPD is 4 mas yr^{-1}, while the ellipse in the right-hand VPD defining probable field stars is centred at (9.5,14.0) mas yr^{-1} with major and minor axes of 17.6 and 14.3 mas yr^{-1}, respectively. The ellipse mainly encloses stars in the outer part of the Bulge.

well-measured proper motions, which dominate the catalogue, can be as small as 0.1 mas yr^{-1}. At the extreme values of proper-motion errors, the window size is fixed and the placement of a target may no longer be in the middle of this window. Second, we used a modified mean $\sigma_\mu = \sqrt{(\mu_\alpha \cos\delta)^2 + \mu_\delta^2}/\sqrt{2}$. Third, the Gaussian width of a cluster density function was interpolated by using an empirical relationship: $\sigma_c = (0.04 \times (K_s - 12) + 1) \times \sigma_\mu$, where K_S is the measured near-infrared magnitude of a target star. In addition, σ_c was never let to be lower than 0.7 mas yr^{-1}.

While the cluster density function is always a 2-D Gaussian, it is often convenient to use a flat sloping density function for the field-star distribution in the VPD. This is related to the

binning of VPD. The adopted size of a binning area, centred on the cluster, is $5\sigma_c \times 5\sigma_c$ which formally should contain all cluster members. If a star's σ_μ<2 mas yr^{-1}, then it also means that the binning area never reaches the centre of a field-star centroid in the VPD for both globular clusters. In the regime of high proper motion errors ($>$ 3 mas yr^{-1}), the distribution of field stars is so diffuse that a significant portion of its wings falls outside the VPD area covered by proper motions. The few free parameters of both cluster and field density distributions, Φ_c and Φ_f, are calculated according to Kozhurina-Platais et al. (1995) but the resulting cluster membership probability P_μ is defined by Eq. 25.8 from van Altena (2013).

We note that likely clusters stars have P_μ >75%, but almost certain field stars have P_μ <1%. The stars with intermediate membership probabilities are more likely to be cluster members than field stars. This follows from the fact that the respective centroids in the VPD have a significant separation and that there is a relatively small fraction of field stars among all stars with measured proper motions, namely ∼24% for NGC 6656 and ∼9% for NGC 6121. This should be considered when examining the astrometric cluster membership of rare stars, such as variables, blue stragglers, and horizontal-branch stars.

2.9.4.1 Membership of variables in NGC 6656

Kaluzny & Thompson (2001) published a catalogue of 36 variable stars in the central field of NGC 6656. We cross-identified these sources in our catalogue and found 27 stars in our proper motion catalogue. In Table 2.7, we report the membership probability for these stars (ID_{KT} are Kaluzny & Thompson labels; ID_{ML} are the identification labels in our catalogue.). In Fig. 2.34, we show V versus $(V - K_S)$ CMD (bottom-left panel), V versus P_μ (bottom-right panel) and the VPD (top panel) for all stars in our sample with a membership probability measure. We set two thresholds in P_μ ($P_\mu = 2\%$ and $P_\mu = 75\%$) and divided our catalogue in three samples: likely-field stars with $P_\mu < 2\%$, dubious membership stars with $2\% \leq P_\mu < 75\%$ and likely cluster members with $P_\mu \geq 75\%$. Eleven stars have $P_\mu < 2\%$ (green triangles); two stars have $2\% \leq P_\mu < 75\%$ (yellow squares), and the remaining 14 stars have $P_\mu \geq 75\%$ (azure circles). The two variable stars with $2\% \leq P_\mu < 75\%$, namely M22_V37 and M22_V14, are saturated horizontal-branch stars for which the motion is generally consistent with the cluster's mean motion. As we stated in Sect. 2.9.4, they should be considered likely cluster members although their formal membership probabilities are below 75%. Note that not all the saturated stars could have well-measured proper motion due to the less-accurate PSF-fitting process and less-constrained positions (QFIT could be higher than 0.1). Saturated stars (while they will have less precise astrometry) are of intrinsic interest, since they are the best candidates for follow-up spectroscopy if identified as cluster members. Nonetheless, caution must be taken in interpreting their astrometry.

2.9.4.2 Membership of variables in NGC 6121

We can similarly use our proper motion data to assign membership probabilities to candidate variable star members of NGC 6121. Shokin & Samus (1996) catalogued 53 NGC 6121 variable stars from the literature and provided equatorial coordinates. We cross-checked our proper motion catalogue with that provided by the authors, and we found 42 sources in common. Figure 2.35 shows these variable stars in J versus $(B - J)$ CMD and VPD. As for NGC 6656, we set two thresholds at $P_\mu = 2\%$ and $P_\mu = 75\%$, dividing our catalogue in three samples. The membership probabilities are listed in Table 2.8 (ID_S and ID_{ML} are the labels in Shokin & Samus 1996 and in this Chapter, respectively.). All cross-identified variable stars are saturated in our proper motion catalogue. Five stars (V6, V7, V11, V19, and V31) have $2\% \leq P_\mu < 75\%$. For these stars, the same considerations we made for M22_V37 and M22_V14 should be applied. All the known variable stars in NGC 6121 seem to be horizontal-branch stars. As field contamination is small in that portion of the CMD, their membership is strengthened considering that these are poorly-measured saturated stars.

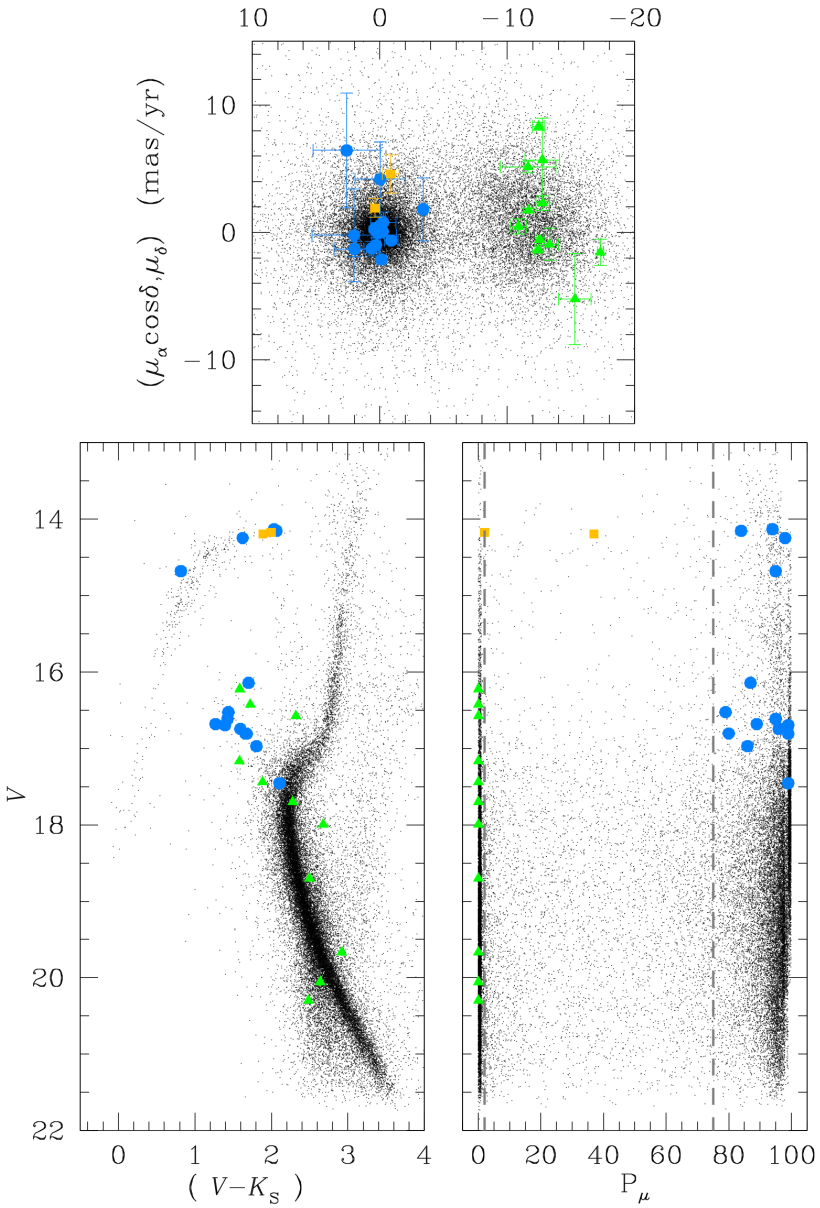

Figure 2.34. Bottom-left: NGC 6656 V versus $(V - K_S)$ CMD for all stars in our catalogue (black dots) that have a membership probability measure. We plotted variable stars from Kaluzny & Thompson (2001) with green triangles that are cross-identified in our catalogue with $P_\mu < 2\%$; yellow squares represent the star with $2\% \leq P_\mu < 75\%$. The azure circles are those stars with $P_\mu \geq 75\%$. Bottom-right: V versus P_μ. Top: VPD. We also drew proper motion error bars for matched variable stars.

Table 2.7. Membership probability for the NGC 6656 variable star catalogue of Kaluzny & Thompson (2001).

ID_{KT}	ID_{ML}	P_μ	ID_{KT}	ID_{ML}	P_μ
Members					
M22_V02	45566	99	M22_V29	161746	96
M22_V04	56333	99	M22_V33	181768	86
M22_V10	93320	89	M22_V34	181631	80
M22_V16	104996	98	M22_V36	185551	84
M22_V20	131248	99	M22_V45	155768	79
M22_V23	144995	95	M22_V51	77720	95
M22_V28	155692	87	M22_V55	148685	94
Probably Members					
M22_V14	102946	2	M22_V37	193535	37
Non Members					
M22_V03	47877	0	M22_V18	113038	0
M22_V05	57746	0	M22_V42	79935	0
M22_V07	68695	0	M22_V46	157407	0
M22_V08	74698	0	M22_V48	183116	0
M22_V12	101344	0	M22_V54	138212	0
M22_V15	106319	0			

Notes. ID_{KT} is the ID used in Kaluzny & Thompson (2001), ID_{ML} is that in our catalogue.

Table 2.8. Membership probability for the NGC 6121 variable star catalogue of Shokin & Samus (1996).

ID_S	ID_{ML}	P_μ	ID_S	ID_{ML}	P_μ
Members					
V1	176589	99	V28	30831	99
V2	173396	98	V30	16737	99
V5	164050	97	V36 (NE)	167082	91
V8	148455	87	V36 (SW)	167583	96
V9	146061	92	V37	125921	94
V10	136435	93	V38	119757	98
V12	129429	98	V39	111350	99
V14	127336	91	V41	87105	99
V15	123997	99	A381	98514	95
V16	121622	78	A382	96072	99
V18	111157	95	A505	98523	85
V20	107627	98	A519	112683	99
V22	100193	93	L1610	142443	87
V24	94766	91	L1717	115979	96
V25	87432	97	L2630	155330	98
V26	76423	86	L3602	60119	99
V27	68948	97	L3732	97216	85
Probably Members					
V6	149664	39	V19	109197	20
V7	149106	6	V31	14721	71
V11	133287	41			
Non Members					
V17	114412	0	A246	174902	0
V23	98450	0			

Notes. ID_S is the ID used in Shokin & Samus (1996), ID_{ML} is that in our catalogue.

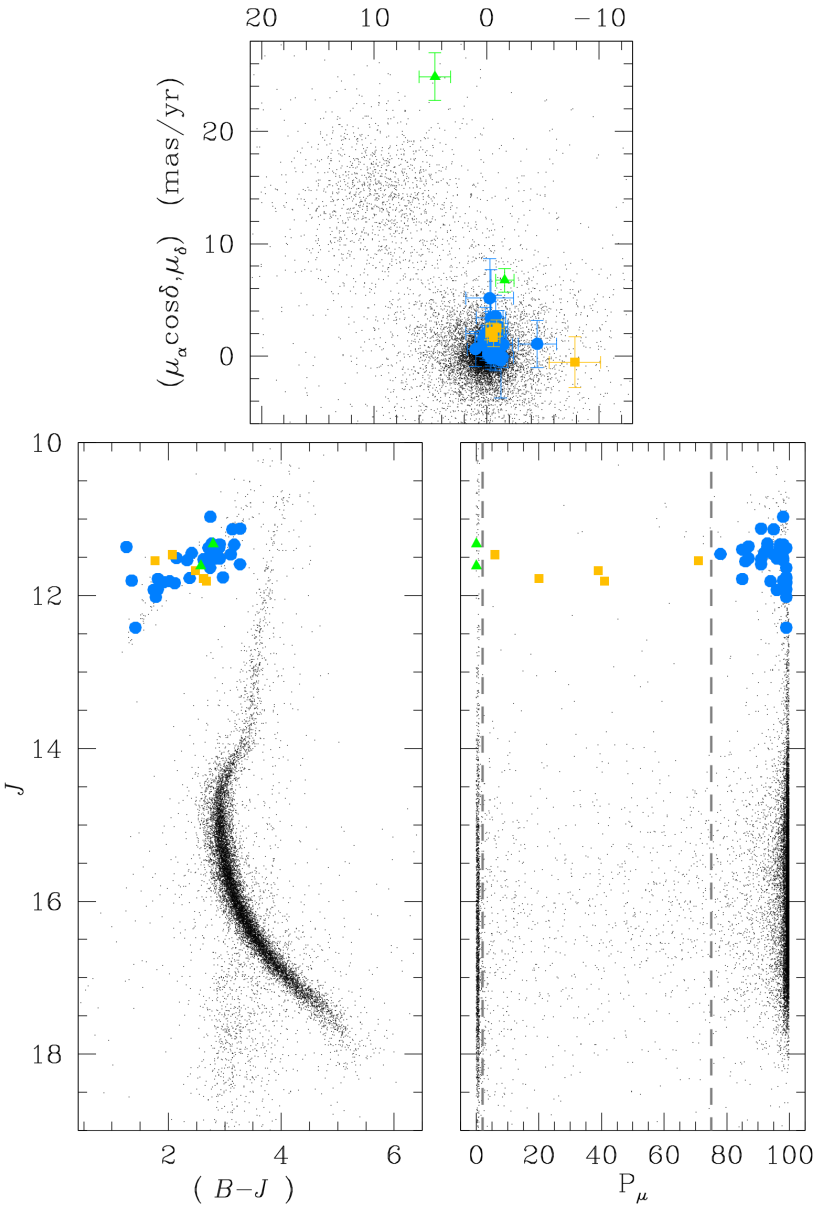

Figure 2.35. Bottom-left: NGC 6121 J versus $(B - J_S)$ CMD for all stars with a membership probability measure. As in Fig. 2.34, all stars are shown with black dots. We used azure circles, yellow squares, and green triangles to highlight cross-identified stars in Shokin & Samus (1996) with $P_\mu \geq 75\%$, $2\% \leq P_\mu < 75\%$, and $P_\mu < 2\%$, respectively. Bottom-right: J versus P_μ. Top: VPD. We show proper motion error bars for Shokin & Samus variable stars. Star V17 ($P_\mu = 0\%$) is not shown because it lies outside the VPD.

2.10 Catalogues

We constructed eight different catalogues for our seven fields. We split the Baade's Window field into two different catalogues (Bulge#1 and the rotated Bulge#2). These catalogues are electronically available in the VizieR on-line database[10].

We also converted pixel-based coordinates into equatorial coordinates using the UCAC 4 catalogue as reference. We only used bright, unsaturated stars to compute the coefficients of the 6-parameter linear transformation between HAWK-I and UCAC 4 frames. The choice of using 6-parameter linear transformations (see Sect. 2.5.5 for a description of these transformations) to transform star positions in our catalogues into the UCAC 4 reference system allows us to solve not only for shift, orientation, and scale, but it also minimises most of the telescope+optics-system residuals, as well as most of the atmospheric refraction effects. Furthermore, linking our catalogues to the UCAC 4 catalogue, we did not only provide the equatorial coordinates for all stars but we determined the linear terms of our distortion. The equatorial coordinates are truly our best calibrated coordinates.

The first eight columns are the same in all catalogues. Column (1) contains the ID of the star; columns (2) and (3) give J2000.0 equatorial coordinates in decimal degrees. Note that positions are given at the epoch of HAWK-I observations because of proper motion. Columns (4) and (5) contain the pixel coordinates x and y of the distortion-corrected reference frame. Columns (6) and (7) contain the corresponding positional rms; column (8) gives the number of images where the star was found.

Columns (9) and the following columns contain the photometric data and proper motions when present. Values are flagged to -1 when their measures are not available with the only exception of the proper motions and their errors, for which we set to 99. Table 2.9 lists all columns contained in the Bulge#1 catalogue. Tables 2.10 to 2.13 only contain those columns that are not in common. In the following subsections, we describe more in detail the remaining columns (9+) of each catalogue.

Baade's Window (Bulge#1). Columns (9) to (23) contain the photometric data: i.e., J, H, K_S (both with 2MASS- and MKO-based zero-points added) , their errors, the number of images used to compute the magnitude of the star in the master frame, and the QFIT in this order. Columns (24) and (25) contain a flag to weed out PSF artefacts from the J and H filter (see Sect. 2.7). All stars in this catalogue have a measure of the magnitude in K_S filter.

NGC 6822, NGC 6388, LMC, and 47 Tuc. Columns (9) to (18) contain the J and K_S photometric data; columns (19) and (20) contain the weed-out flags (see Table 2.10). In the NGC 6822, LMC, and 47 Tuc catalogues, all stars have a J-magnitude measurement, and NGC 6388 has a K_S-magnitude measurement.

Baade's Windows rotated by 135° (Bulge#2). Columns (9) to (14) contain K_S magnitudes, errors, the number of stars used to compute the average magnitudes, QFIT and the weed-out flag values, respectively (Table 2.11).

NGC 6656. Columns (9) to (26) contain the photometric data in K_S, B, V, and I band. Finally, Columns (27) to (31) contain the proper motion data: $\mu_\alpha \cos\delta$ (27), $\sigma_{\mu_\alpha \cos\delta}$ (28), μ_δ (29), σ_{μ_δ} (30), and the number of pairs of images in which a given star's proper motion was measured (31). Finally, column (32) contains the membership probability (Table 2.12). Stars measured in only one exposure in either B, V, or I filters have photometric rms values of 9.9. As for Bulge#1, all stars have a measure of the magnitude in K_S filter.

[10] http://cdsarc.u-strasbg.fr/viz-bin/qcat?J/A+A/563/A80

NGC 6121. Columns (9) to (32) contain the photometric data in J, K_S, B, V, and Rc bands. Columns (33) to (37) contain the proper motion data and column (38) is the membership probability (Table 2.13). As in the NGC 6656 catalogue, a rms equal to 9.9 is used for those stars measured in only 1 exposure in K_S, B, V, or Rc filter. In this catalogue, all stars have a J-magnitude measurement.

2.11 Conclusions

We derived an accurate distortion solution in three broad band filters for the HAWK-I detector and release the tools to correct the geometric distortion with our solution. We also produced astro-photometric catalogues of seven stellar fields. We release catalogues with astrometric positions, photometry, proper motions, and membership probabilities of NGC 6121 (M 4) and NGC 6656 (M22), while the remaining fields (the Baade's window, NGC 6822, NGC 6388, NGC 104, and the James Webb Space Telescope calibration field) studied in the present Chapter only contains astrometry and photometry. These catalogues are useful for selecting spectroscopic targets, and can serve as distortion-free frames with respect to which one can solve for the geometric distortion of present/future imagers. The astronomical community has started to focus its attention on wide-field cameras equipped with NIR detectors, and the quantity and quality of NIR devices have improved considerably. This is a first effort to develop the expertise with these detectors to fully exploit the data coming from large-field NIR surveys, such as the VVV survey taken with VIRCAM@VISTA. Finally, an additional goal of this Chapter is to get ready for the upcoming James Webb Space Telescope, whose imagers define the state-of-the-art in astrometry, in particular in crowded environments not reachable by GAIA.

We analysed both photometric and astrometric performance of the NIR mosaic HAWK-I@VLT using images of seven different fields observed during commissioning in 2007. We computed a geometric-distortion solution for each chip of HAWK-I in three different broad band filters (J, H, K_S). Our dithered-observation strategy using the self-calibration technique allowed us to randomise the systematic errors and to compute the average stars' positions that provide an approximation of the true positions in the distortion-free master frame. A fifth-order polynomial solution highlighted a periodic pattern in the distortion residuals. We have demonstrated that this pattern is not a geometric effect (as it is the case for the WFPC2 or the WFC3/UVIS@*HST*) but it is a periodic lag introduced by alternating readout amplifiers. To remove it, we used a square-wave function and a 64-pixel step table of residuals. Finally we used four additional look-up tables (one per chip) to perform a bi-linear interpolation to take all uncorrected residuals into account and to further improve our solutions. Thanks to our 5-step distortion correction, we are able to reach a positional rms of $\sim$3.5 mas in each coordinate. Using a general 6-parameter linear transformations to match-up different images, the effects due to telescope+instrument and atmosphere are absorbed, and the σ(Radial residual) further decreases, reaching $\sim$2.8 mas under good seeing conditions. We emphasise that this is a relative positioning precision – i.e., it indicates how accurately we can measure the differential position of a star in multiple images of the same field.

We have also shown that the non-linear terms of our distortion solution can be transferred between observing runs at the 10 mas level. The astrometric accuracy contained in the pixel-coordinate system degrades moving toward the edges of the FoV because the stars' positions were obtained as the average of fewer images than in the centre of the field. Therefore, the average positions are more vulnerable to poorly-constrained transformations of the individual exposures into the master frame. The accuracy can decrease from $\sim$10 mas to $\sim$100 mas ($\sim$1 pixel) going from the centre to the edges of the FoV. For this reason, we advise to use the inner part of the detector for high-precision astrometry. To achieve a higher astrometric accuracy, we also advise to link the pixel-coordinate catalogue to a reference frame such as UCAC 4 to determine the linear terms of the distortion. Finally local transformations (as those used to compute the

proper motion in Sect. 2.9) should be used to minimise the effects of residuals in the geometric distortion corrections as described in Paper I.

In the second part of the Chapter, we showed the potential applications of our astrometric techniques and computed the *relative* proper motion of stars in the field of the globular clusters NGC 6656 and NGC 6121. With a time baseline of about 8 years, we have clearly separated cluster members from field stars. Accuracy of proper-motion measurements is limited by the depth and the precision of first-epoch data set. We note that the stellar positions in our catalogues have been derived from only a single epoch of HAWK-I data. A second-epoch HAWK-I (or another wide-field infrared camera) data set is needed to provide proper-motion solutions that allow these data to be extended with confidence to arbitrary future epochs. We exploit photometry and proper motions of stars in NGC 6656 to study its stellar populations. We find that the bi-modal SGB, previously discovered from visual and ultraviolet *HST* photometry (Piotto et al. 2012), is also visible in the $K_{\rm S}$ versus $(B-K_{\rm S})$ CMD. We combined information from HAWK-I observation of the outer part of NGC 6656 and from *HST* images of the innermost cluster region (Piotto et al. 2012) to study the radial distribution of the two SGBs. To do this, we calculated the number ratio of the faint SGB $\hat{\rm p}_{\rm fSGB}$ for stars at different radial distances from the cluster centre to $9'$ ($\sim$6.8 core radii). We found that the two SGBs have the same radial distribution within our uncertainty.

Table 2.9. Bulge#1 catalogue.

Column #	Name	Description
(1)	ID	ID number of the star
(2)	α	Right Ascension [°]
(3)	δ	Declination [°]
(4)	x	x-master frame position [pixel]
(5)	y	y-master frame position [pixel]
(6)	$\sigma_{\rm x}$	rms error in the x-position [pixel]
(7)	$\sigma_{\rm y}$	rms error in the y-position [pixel]
(8)	$\rm n_{pos}$	Number of images where the star was found in used to compute the master-frame position
(9)	J	Calibrated J magnitude in 2MASS system
(10)	H	Calibrated H magnitude in 2MASS system
(11)	$K_{\rm S}$	Calibrated $K_{\rm S}$ magnitude in 2MASS system
(12)	J	Calibrated J magnitude in MKO system
(13)	H	Calibrated H magnitude in MKO system
(14)	$K_{\rm S}$	Calibrated $K_{\rm S}$ magnitude in MKO system
(15)	σ_J	rms error in J photometry
(16)	σ_H	rms error in H photometry
(17)	$\sigma_{K_{\rm S}}$	rms error in $K_{\rm S}$ photometry
(18)	$\rm n_J$	Number of images where the star was found in used to compute the J magnitude
(19)	$\rm n_H$	Number of images where the star was found in used to compute the H magnitude
(20)	$\rm n_{K_S}$	Number of images where the star was found in used to compute the $K_{\rm S}$ magnitude
(21)	QFIT_J	Quality of J PSF-fit
(22)	QFIT_H	Quality of H PSF-fit
(23)	$\mathsf{QFIT}_{K_{\rm S}}$	Quality of $K_{\rm S}$ PSF-fit
(24)	$\rm weed_J$	J weed-out flag (1 = star, 0 = PSF-artefacts, -1 = star not found in J exposures)
(25)	$\rm weed_H$	H weed-out flag

Table 2.10. NGC 6822, NGC 6388, LMC and 47 Tuc catalogues.

Column #	Name	Description
(...)	(...)	(...)
(9)	J	Calibrated J magnitude in 2MASS system
(10)	$K_{\rm S}$	Calibrated $K_{\rm S}$ magnitude in 2MASS system
(11)	J	Calibrated J magnitude in MKO system
(12)	$K_{\rm S}$	Calibrated $K_{\rm S}$ magnitude in MKO system
(13)	σ_J	rms error in J photometry
(14)	$\sigma_{K_{\rm S}}$	rms error in $K_{\rm S}$ photometry
(15)	$\rm n_J$	Number of images where the star was found in used to compute the J magnitude
(16)	$\rm n_{K_S}$	Number of images where the star was found in used to compute the $K_{\rm S}$ magnitude
(17)	QFIT_J	Quality of J PSF-fit
(18)	$\mathsf{QFIT}_{K_{\rm S}}$	Quality of $K_{\rm S}$ PSF-fit
(19)	$\rm weed_J$	J weed-out flag (1 = star, 0 = PSF-artefacts, -1 = star not found in J exposures)
(20)	$\rm weed_{K_S}$	$K_{\rm S}$ weed-out flag

Table 2.11. Bulge#2 catalogue.

Column #	Name	Description
(...)	(...)	(...)
(9)	$K_{\rm S}$	Calibrated $K_{\rm S}$ magnitude in 2MASS system
(10)	$K_{\rm S}$	Calibrated $K_{\rm S}$ magnitude in MKO system
(11)	$\sigma_{K_{\rm S}}$	rms error in $K_{\rm S}$ photometry
(12)	$\rm n_{K_S}$	Number of images where the star was found in used to compute the $K_{\rm S}$ magnitude
(13)	$\mathsf{QFIT}_{K_{\rm S}}$	Quality of $K_{\rm S}$ PSF-fit
(14)	$\rm weed_{K_S}$	$K_{\rm S}$ weed-out flag (1 = star, 0 = PSF-artefacts, -1 = star not found in $K_{\rm S}$ exposures)

Table 2.12. NGC 6656 catalogue.

Column #	Name	Description
(...)	(...)	(...)
(9)	$K_{\rm S}$	Calibrated $K_{\rm S}$ magnitude in 2MASS system
(10)	$K_{\rm S}$	Calibrated $K_{\rm S}$ magnitude in MKO system
(11)	B	Calibrated B magnitude
(12)	V	Calibrated V magnitude
(13)	I	Calibrated I magnitude
(14)	$\sigma_{K_{\rm S}}$	rms error in $K_{\rm S}$ photometry
(15)	σ_B	rms error in B photometry
(16)	σ_V	rms error in V photometry
(17)	σ_I	rms error in I photometry
(18)	$\rm n_{K_S}$	Number of images where the star was found in used to compute the $K_{\rm S}$ magnitude
(19)	$\rm n_B$	Number of images where the star was found in used to compute the B magnitude
(20)	$\rm n_V$	Number of images where the star was found in used to compute the V magnitude
(21)	$\rm n_I$	Number of images where the star was found in used to compute the I magnitude
(22)	$\mathsf{QFIT}_{K_{\rm S}}$	Quality of $K_{\rm S}$ PSF-fit
(23)	QFIT_B	Quality of B PSF-fit
(24)	QFIT_V	Quality of V PSF-fit
(25)	QFIT_I	Quality of I PSF-fit
(26)	$\rm weed_{K_S}$	$K_{\rm S}$ weed-out flag (1 = star, 0 = PSF-artefacts, −1 = star not found in $K_{\rm S}$ exposures)
(27)	$\mu_\alpha \cos\delta$	Proper-motion value along $\mu_\alpha \cos\delta$ [mas yr^{-1}]
(28)	$\sigma_{\mu_\alpha \cos\delta}$	rms of $\mu_\alpha \cos\delta$ [mas yr^{-1}]
(29)	μ_δ	Proper-motion value along $\mu_\alpha \cos\delta$ [mas yr^{-1}]
(30)	σ_{μ_δ}	rms of μ_δ [mas yr^{-1}]
(31)	$\rm n_{pairs}$	Number of pairs of 1$^{\rm st}$-2$^{\rm nd}$ epoch images used to compute the proper motion of the star
(32)	$\rm P_\mu$	Membership probability

Table 2.13. NGC 6121 catalogue.

Column #	Name	Description
(...)	(...)	(...)
(9)	J	Calibrated J magnitude in 2MASS system
(10)	$K_{\rm S}$	Calibrated $K_{\rm S}$ magnitude in 2MASS system
(11)	J	Calibrated J magnitude in MKO system
(12)	$K_{\rm S}$	Calibrated $K_{\rm S}$ magnitude in MKO system
(13)	B	Calibrated B magnitude
(14)	V	Calibrated V magnitude
(15)	Rc	Calibrated Rc magnitude
(16)	σ_J	rms error in J photometry
(17)	$\sigma_{K_{\rm S}}$	rms error in $K_{\rm S}$ photometry
(18)	σ_B	rms error in B photometry
(19)	σ_V	rms error in V photometry
(20)	σ_{Rc}	rms error in Rc photometry
(21)	$\rm n_J$	Number of images where the star was found in used to compute the J magnitude
(22)	$\rm n_{K_S}$	Number of images where the star was found in used to compute the $K_{\rm S}$ magnitude
(23)	$\rm n_B$	Number of images where the star was found in used to compute the B magnitude
(24)	$\rm n_V$	Number of images where the star was found in used to compute the V magnitude
(25)	$\rm n_{Rc}$	Number of images where the star was found in used to compute the Rc magnitude
(26)	QFIT_J	Quality of J PSF-fit
(27)	$\mathsf{QFIT}_{K_{\rm S}}$	Quality of $K_{\rm S}$ PSF-fit
(28)	QFIT_B	Quality of B PSF-fit
(29)	QFIT_V	Quality of V PSF-fit
(30)	QFIT_{Rc}	Quality of Rc PSF-fit
(31)	$\rm weed_J$	J weed-out flag (1 = star, 0 = PSF-artefacts, −1 = star not found in J exposures)
(32)	$\rm weed_{K_S}$	$K_{\rm S}$ weed-out flag
(33)	$\mu_\alpha \cos\delta$	Proper-motion value along $\mu_\alpha \cos\delta$ [mas yr^{-1}]
(34)	$\sigma_{\mu_\alpha \cos\delta}$	rms of $\mu_\alpha \cos\delta$ [mas yr^{-1}]
(35)	μ_δ	Proper-motion value along $\mu_\alpha \cos\delta$ [mas yr^{-1}]
(36)	σ_{μ_δ}	rms of μ_δ [mas yr^{-1}]
(37)	$\rm n_{pairs}$	Number of pairs of 1$^{\rm st}$-2$^{\rm nd}$ epoch images used to compute the proper motion of the star
(38)	$\rm P_\mu$	Membership probability

Bibliography

Anderson J., King I. R., 1999, PASP, 111, 1095

Anderson J., King I. R., 2003, PASP, 115, 113

Anderson J., King I. R., 2004, acs..rept, 3

Anderson J., Bedin L. R., Piotto G., Yadav R. S., Bellini A., 2006, A&A, 454, 1029, Paper I

Anderson J., King I. R., 2006, acs..rept, 1

Anderson J., et al., 2008, AJ, 135, 2114

Arsenault R., et al. , 2006, Msngr, 123, 6

Bedin L. R., Piotto G., King I. R., Anderson J., 2003, AJ, 126, 247

Bellini A., Bedin L. R., 2009, PASP, 121, 1419

Bellini A., et al., 2009, A&A, 493, 959, Paper III

Bellini A., Bedin L. R., 2010, A&A, 517, A34, Paper IV

Bellini A., Anderson J., Bedin L. R., 2011, PASP, 123, 622

Golimowski D., Suchkov A., Loose M., Anderson J., Grogin N., 2012, acs..rept, 2

Hadjiyska E., et al. , 2012, IAUS, 285, 324

Han I., 1989, AJ, 97, 607

Harris W. E., 1996, AJ, 112, 1487

Kaiser N., et al. , 2010, SPIE, 7733, 77330E

Kaluzny J., Thompson I. B., 2001, A&A, 373, 899

Kissler-Patig M., et al. , 2008, A&A, 491, 941

Kozhurina-Platais V., Girard T. M., Platais I., van Altena W. F., Ianna P. A., Cannon R. D., 1995, AJ, 109, 672

Libralato M., Bellini A., Bedin L. R., Piotto G., Platais I., Kissler-Patig M., Milone A. P., 2014, A&A, 563, A80

Lindegren L., 1980, A&A, 89, 41

Madore B. F., Rigby J., Freedman W. L., Persson S. E., Sturch L., Mager V., 2009, ApJ, 693, 936

Milone A. P., Stetson P. B., Piotto G., Bedin L. R., Anderson J., Cassisi S., Salaris M., 2009, A&A, 503, 755

Milone A. P., et al., 2012, A&A, 540, A16

Minniti D., et al. , 2010, NewA, 15, 433

Piotto G., et al., 2012, ApJ, 760, 39

Platais I., et al. , 2002, AJ, 124, 601

Platais I., Wyse R. F. G., Zacharias N., 2006, PASP, 118, 107

Saito R. K., et al. , 2012, A&A, 537, A107

Shokin Y. A., Samus N. N., 1996, AstL, 22, 761

Skrutskie M. F., et al. , 2006, AJ, 131, 1163

Stetson P. B., 1987, PASP, 99, 191

Stetson P. B., 2000, PASP, 112, 925

Stetson P. B., 2005, PASP, 117, 563

van Altena W. F., 2013, asas.book

Yadav R. K. S., et al., 2008, A&A, 484, 609, Paper II

Zacharias N., Finch C. T., Girard T. M., Henden A., Bartlett J. L., Monet D. G., Zacharias M. I., 2013, AJ, 145, 44

Zloczewski K., Kaluzny J., Rozyczka M., Krzeminski W., Mazur B., 2012, AcA, 62, 357

3 Toward high-precision astrometry with deg^2 field of views: VIRCAM

Driven by the promising results obtained with HAWK-I, we moved to a larger ground-based, near-infrared instrument: VIRCAM. This detector has a 0.6-deg^2 field of view and it is mounted at the VISTA telescope. VIRCAM is scanning several regions across the Galaxy within different photometric surveys (Ultra-VISTA, VIKING, VMC, VVV, VHS, VIDEO). In this Chapter we show that we are able to push the astrometric capabilities of these surveys close to their limits. This is an important step not only in preparation for possible synergies with *GAIA* and/or JWST, but also toward another important goal of this thesis: the exploitation of the full potentialities of *Kepler* and *K2* missions (Chapter 5). The material discussed in this Chapter has been published in Monthly Notices of the Royal Astronomical Society (MNRAS)[1].

3.1 Introduction

The VISTA Variables in the Vía Láctea (VVV) variability campaign started in 2010. Thanks to the VISTA InfraRed Camera (VIRCAM; Dalton et al. 2006; Emerson, McPherson, & Sutherland 2006), mounted at the 4.1 m telescope VISTA (Visible and Infrared Survey Telescope for Astronomy), this ongoing survey is mapping the Galactic bulge and disc to create a 3-D map of the Milky Way (Minniti et al. 2010; Saito et al. 2012). As for many long-term variability surveys, the observing strategy is mainly focused on covering a portion of the sky as large as possible in a single night, scanning the full field of view (FoV) many times every few days. To this aim, the exposure time of each image has to be short enough in order to achieve the survey specifications. In the VVV survey, the typical exposure time for K_S-filter images is about 4 s, e.g. a factor of 7 smaller than the 30 s threshold set by Platais et al. (2002) and Platais, Wyse, & Zacharias (2006) as the

[1] Libralato et al. (2015, MNRAS, 450, 1664) - Received 2014 December 03 - Accepted 2015 March 25.

Table 3.1. List of the VIRCAM@VISTA data used for the astrometric calibration. Each observing block is made by $N_{\rm step}$ images, where 'step' is the dither spacing in arcmin between two consecutive exposures in an observing block. The single-image exposure time is given by the integration time (DIT) multiplied by the total number of individual integrations (NDIT).

Filter	$N_{\rm step}$	**Exposure time** (NDIT×DIT)	**Seeing** (arcsec)	**Airmass** (sec z)
Program ID: 488.L-0500(A) – PI: Bellini				
NGC 5139 – ω Cen				
2012 February 23–24				
J	$25_{1.2}$	(6×10 s)	0.97-1.42	1.026-1.107
J	$25_{8.5}$	(6×10 s)	0.74-1.08	1.134-1.198

minimum exposure time required to average out the large-scale semi-periodic and correlated atmospheric noise that harms ground-based astrometry. In spite of this, we chose to exploit the astrometric capabilities of this survey that will release to the community a data set with more than one hundred epochs over six years.

In this Chapter, we present our reduction pipeline for the VIRCAM detectors and the geometric-distortion correction. As an example, we also show a few applications made possible by the astrometric accuracy reached by the VVV data obtained between 2010 and 2014.

3.2 Instrument and observations

VIRCAM is a mosaic of 4×4 detectors mounted at the focus of the VISTA 4.1 m telescope. Each detector is a Raytheon VIRGO 2048×2048-pixel array and covers ∼694×694 arcsec^2 on the sky. The average pixel scale is 0.339 arcsec pixel^{-1} (Sutherland et al. 2015). The gaps between the detectors are quite large and correspond to 42.5 and 90 per cent of the detector size along the X and Y direction, respectively.

Dithered observations are recommended to self-calibrate the geometric distortion of a detector (e.g., Anderson et al. 2006, Bellini & Bedin 2010, or Libralato et al. 2014, hereafter Chapter 2). However, the standard dither pattern adopted by VVV is not adequate for this purpose. For this reason, a calibration programme (Program ID: 488.L-0500(A), PI: Bellini) was approved in 2012. The calibration field is centred on globular cluster NGC 5139 (ω Cen). This field was chosen due to its relatively high star density over more than one square degree.

The field was observed in the J filter in two runs of 25 images each (Table 3.1), both organised in an array of 5×5 pointings, but with a different dither spacing (Fig. 3.1). Large dithers were taken to cover the gap between the 16 chips and to allow us to construct a single reference system for all observations. The small dither pattern was obtained to allow independent modelling of the high-frequency residuals of the geometric distortion for each chip.

3.3 Data reduction

We developed a reduction package that makes use of the same tools described in Chapter 2 for the HAWK-I detector. Here, we briefly describe the software, and focus on the few differences between the two works.

One peculiarity of VIRCAM is the striped pattern that affects all the images, both calibration and scientific. These stripes are generated by the IRACE electronics (Sutherland et al. 2015) and change from one exposure to the next. To correct them, we made a FORTRAN routine based on the Cambridge Astronomy Survey Unit pipeline correction, that resembles the correction applied by Maybhate et al. (2008) for the WFPC2@*HST* background streaks. We computed in each image the clipped-median value of the counts in each row, then we took the median

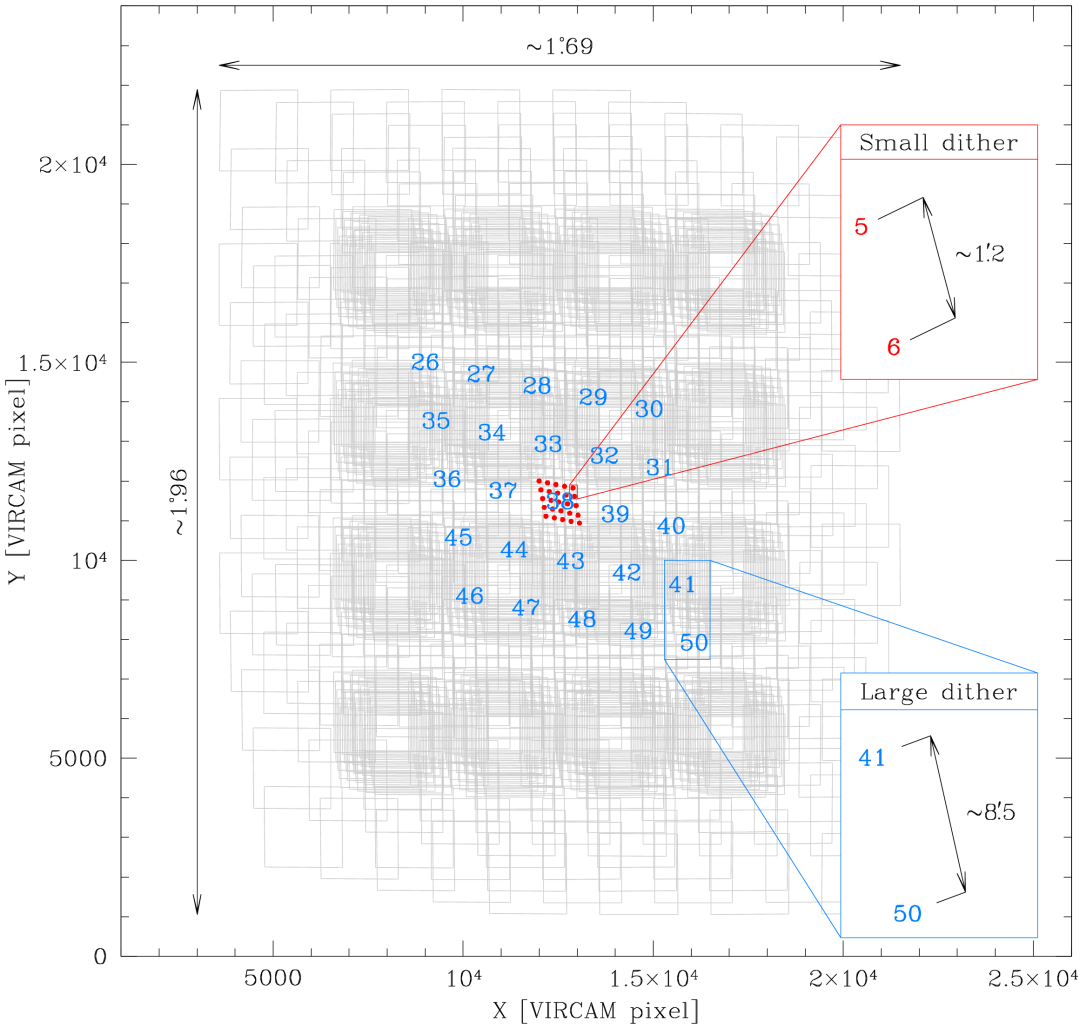

Figure 3.1. Outline of our adopted dither pattern used for *J*-filter data. Large- and small-dither images are organised in two 5×5 arrays. The pointings of the large-dither images are taken to cover the gap between the 16 detectors. The total FoV covered by our observations is about 1.°7×2.°0 on sky. The two zoomed-in panels show the dither spacing for large (azure panel) and small (red panel) dither pattern.

of these values and subtracted it from the clipped-median value of each row. These differences represent the corrections to be applied to each row. We did not include bad/warm/hot pixels while computing the median values.

Using archival flat-field images we were not able to completely correct for the pixel-to-pixel sensitivity variation of the detectors, in particular for chip [16] where the very high quantum-efficiency variation on short time-scales sometimes makes it impossible to properly apply the flat-field correction[2]. So, we constructed master flat-field frames using the scientific images

[2]http://casu.ast.cam.ac.uk/surveys-projects/vista/technical/known-issues

themselves, masking all bad/warm/hot pixels and those in close proximity of any significant source (stars and galaxies) and considered these purged images as on-sky flat-field images.

First, we applied dark and flat-field corrections to all images. Then, for each chip we computed the median sky value in a 5×5 grid and subtracted it according to the table. Then we made a 5×5 grid of fully empirical point-spread function (PSF) models for each detector of each exposure, following the prescription given in Anderson et al. (2006). Unlike the procedure given in the original IMG2PSF_WFI and IMG2PSF_HAWK-I programs, the finding criteria (minimum flux and minimum separation from brighter stars) to choose the stars that would be used to model the PSF are applied locally and are different in each cell of the grid. This way, we are able to find the most suitable combination of these criteria in each of the 5×5 regions of the chip (e.g., if the cluster centre is located in a corner of a chip, the minimum separation from the brighter stars in that corner is usually lower than in the opposite corner where the crowding is lower). With an array of PSF models, we are able to measure positions and fluxes for all sources on an image. The final catalogues (one for each chip) contain positions, instrumental magnitudes[3], and another quantity called quality-of-PSF-fit (QFIT) which represents the absolute fractional error in the PSF-model fit to the star (Anderson et al. 2008). The lower the QFIT, the better is the PSF fit. The QFIT parameter is a useful quantity to discriminate among well-measured and poorly-measured stars. Typically, in ω Cen catalogues we considered bright, unsaturated stars with a QFIT<0.05 to be well-measured stars. These selections allow us to always have at disposal over 100 stars per chip, with an average value of 350 well-measured stars for a corner chip and 1000 stars for a centremost chip.

3.4 Geometric-distortion correction

In the large FoV of VIRCAM, the tangential-plane projection effects are not negligible (at one degree from the tangent point this corresponds to more than 0.18 arcsec, ∼0.5 VIRCAM pixel). This means the farther from the centre, the larger is the difference between the true position and the projected position of a star.

We chose to perform an auto calibration. By using as a reference system 2MASS (Skrutskie et al. 2006) or UCAC4 (Zacharias et al. 2013), which are among the most accurate absolute systems, we would have unavoidably ended up limited by their accuracy (of the order of 0.2-0.3 arcsec for 2MASS). Not to mention the non-negligible contribution from the stellar motion between the reference system and our exposures. Furthermore, as stated in Bellini & Bedin (2010), it is difficult to find a distortion-free reference frame with a homogeneous stellar density and luminosity. Therefore we adopted the auto-calibration solution. The basis of the auto-calibration is to observe the same star in as many different locations on the detector as possible and to compute its average position once it is transformed on to a common reference frame. Thanks to the large number and varied spacing of our dither pattern, a given star will be observed in several different locations in the FoV and, as such, the systematic errors in its mean position should average out. This way, the average positions of the stars should provide a reasonable approximation of their true positions in a distortion-free frame (the master frame). We built the master frame by cross-identifying the stars in each single-detector catalogue of each exposure. We used conformal transformations (four-parameter linear transformations: rigid shifts in the two coordinates, one rotation, and one change of scale) to bring the stellar positions measured in each image into the reference system of the master frame. In the left-hand panels of Fig. 3.2 we show the effects of the projection on the master frame. The positional residuals along the X and Y axes show several bumps where two different chips overlap.

When we first examined plots like these, it was clear that the bumps at the boundaries of the chips could be due either to internal distortions within each chip or to errors in placing the chips properly with respect to each other. To ensure that the distortion within each chip was

[3]Defined as $-2.5 \times \log(\sum \text{counts})$, where $\sum$ counts is the sum of the total counts under the fitted PSF.

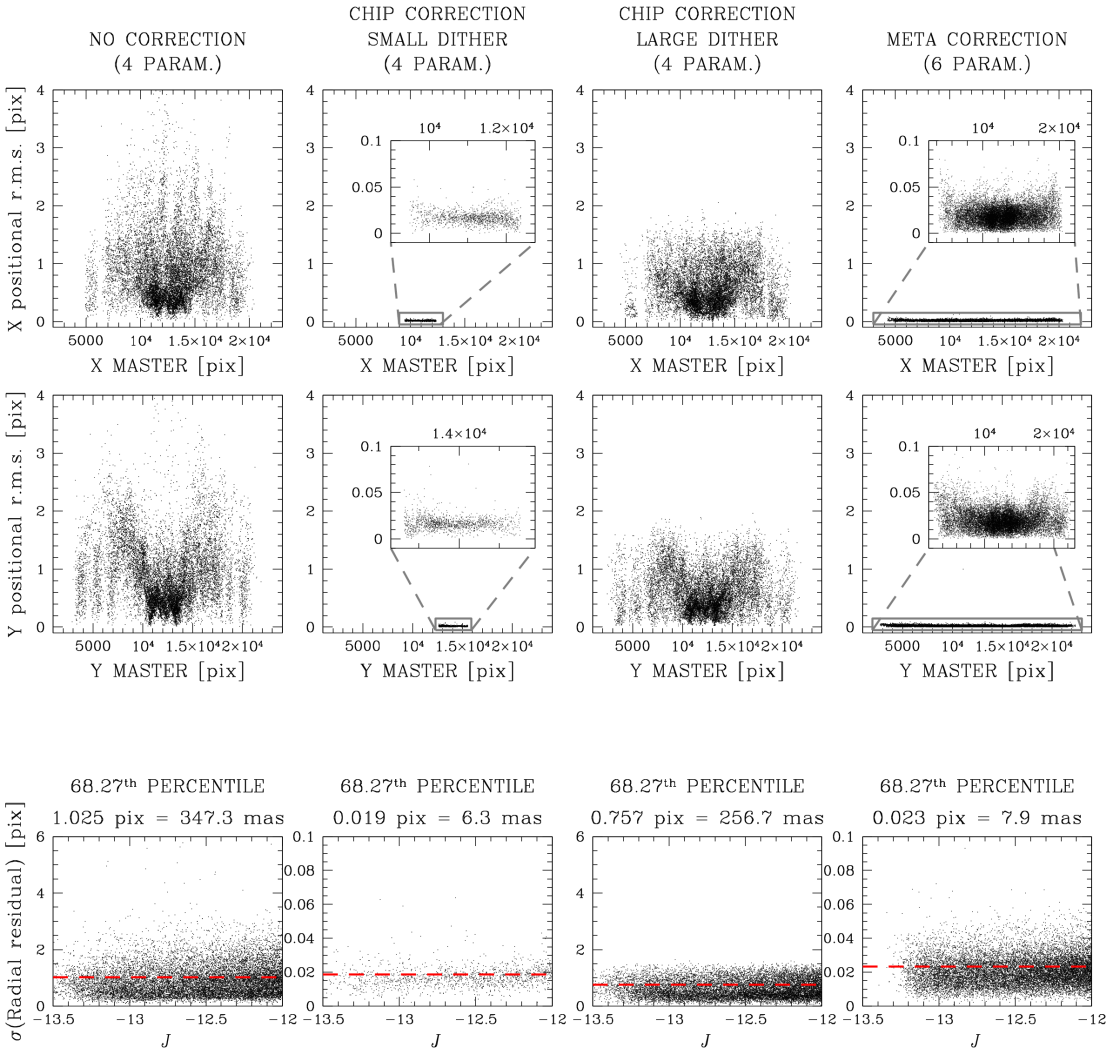

Figure 3.2. In each column of the figure we show the positional residuals for different master frames. Left: master frame based on single-chip, uncorrected catalogues and conformal transformations. Middle-left: chip #10 master frame based on single-chip correction, small dithers, and conformal transformations. Middle-right: master frame based on single-chip correction, large dithers, and conformal transformations. Even if there is an improvement with respect to the '`NO CORRECTION`' case, the bumps (caused by projection-induced effects) are still visible. Right: master frame based on our final distortion solution, six-parameter linear transformations and taking into account the projection effects. In the top (middle) row, we show the positional rms along the $X(Y)$ axis as a function of the $X(Y)$ position on the master frame. In the middle-left and right panel insets, we zoomed-in to better show the residuals. In the bottom panels, we plot the σ(Radial residuals) as a function of the J magnitude. The red dashed lines are set to the 3σ-clipped 68.27^{th}-percentile value of σ(Radial residuals). In all these panels, we show only bright, unsaturated and well-measured stars. See text for more details.

properly accounted for, we independently solve for the geometric distortion of each chip, as done in Chapter 2. For this specific purpose, we only used the small-dither images where the gaps between the chips are not covered (no detector overlaps with any other detector). The accuracy of the single-chip distortion solution was at the 0.02-pixel level ($\sim$7 mas). As an example, in the middle-left panels of Fig. 3.2 we show the residuals after we applied the single-chip correction to the catalogues and constructed a small-dither-based master frame using only chip #10. As shown in Fig. 3.1, the small dithers do not allow us to put all the 16 chips in the same reference system since the gaps are so large that the chips do not overlap each other. For this reason we selected one random chip (chip #10) to show that our single-chip distortion solution was good as we wrote above. Then, we applied our single-chip correction to all catalogues and used four-parameter linear transformations to create a new master frame based on large-dither images. Again, the positional-residual bumps were still visible (middle-right panels of Fig. 3.2). Therefore, these trends in the positional residuals are ascribable to projection effects, which have to be taken into account while cross-identifying the catalogues.

We chose to define a meta reference system in which to properly project all single-chip catalogues and, at the same time, solve for most of the geometric distortion that affects this detector. We proceeded as follows. We used the 2MASS catalogue as our initial reference frame. We projected the 2MASS catalogue on to a tangent plane centred on ω Cen and followed the prescriptions given in van de Ven et al. (2006) to convert R.A. and Dec. positions into pixel-based coordinates. This is an important step because we imposed the master-frame scale to be exactly equal to 0.339 arcsec pixel^{-1} for all chips. This value is the average pixel scale declared by Sutherland et al. (2015).

Initially, we cross-identified all stars of each single-chip raw frames with the 2MASS catalogue by using six-parameter linear transformations (which also include the deviation from orthogonality and the change of relative scale between the two axes). Then, we located the centre of each chip (x,y)=(1024,1024) on the 2MASS-based reference system. Without properly taking into account for the projection effects, the chip-centre positions on the 2MASS reference frame depend on their distances from the tangent point (ω Cen centre) and on the geometric distortion. To get rid of the first dependence and find the best position of the chip centres, we iteratively de-projected the 2MASS catalogue on to the celestial sphere, and then projected it again using as the tangent point the current chip-centre position on the 2MASS reference system, in order to compute new, improved transformations. For each chip of each exposure/image we iterated the whole process five times (after the fifth iteration the adjustments were negligible).

Once the chip centres in the 2MASS reference frame converged to fixed positions, in order to build the meta reference system, we had to impose additional constraints. First, the meta centre was defined as the average position of the four centremost chips. The second constraint we imposed is that the Y and X axes of our meta-frame system had to be oriented up and to the right, respectively. For each of the four centremost chips, we computed the angle between the expected meta-frame X axis and the segment that connects the centre of the meta frame to the chip centre. Then we rotated all chips by the average of the four angles.

For each image we de-projected the 2MASS frame on to the celestial sphere and projected it back on a tangent plane, but this time using as tangent point the meta centre computed as described above. Then, we rotated and shifted these 2MASS-based positions according to the other constraint. The final products of this effort are 2MASS-based positions projected on the meta-frame centre of each image, rotated and shifted to have the meta centre in (x,y)=(0,0). These positions represent the best approximation of the expected distortion-free meta positions.

For each star in common between our catalogues and the 2MASS-based catalogue, we have a pair of positional residuals that correspond to the difference between the raw-chip positions and the expected meta-frame positions (given by the stellar positions on the modified 2MASS reference frame). We used both saturated and unsaturated stars with magnitude $J<-12$ and QFIT$<$0.2. Since 2MASS is a shallow survey, we had to use saturated ($J\lesssim-13.4$) stars in order to have an adequate sample size. We divided each chip into a 3$\times$3-grid elements and, in each such

element, we defined the grid-point value as the average value of the residuals within. The cells have different sizes, with those close to the edges (for example 512×512 pixels on the corners) smaller than the central one (1024×1024 pixels), in order to better model the distortion close to the edges. As described in Chapter 2, for those cells adjoining the detector edges we shifted the grid points to the edge. We built a look-up table of correction for any location of the chip, using a bi-quadratic interpolation among the surrounding four grid points. To avoid extrapolation, our grid points extended to the corners, but this meant that we needed several iterations (each time applying 90% of the suggested correction to the raw positions and computing new residuals) before convergence could be achieved.

After this first part of the correction, we have star positions transformed into a meta reference frame and corrected for geometric distortion. All the stellar positions collected in one meta catalogue are those of the stars imaged in one exposure. Therefore, accordingly to the Table 3.1, we have 50 meta catalogues at our disposal (25 of which are based on large-dither exposures, while the other 25 are based on the small-dither exposures). The astrometric accuracy achieved is about 0.2–0.3 pixel, similar to that of 2MASS. The astrometric quality of our measurements should be ten times better than this, so to further improve our result, we applied an additional table-of-residuals correction to each chip by comparing the positions of the stars as measured in different meta catalogues, thus enabling a precision of ∼0.03 pixel per comparison, as follows. For each pair of meta catalogues (hereafter catalogues #1 and #2), we cross-identified all stars in common by using six-parameter linear transformations. We found the meta centre of catalogue #1 into the reference system of catalogue #2 and projected the stellar positions measured in catalogue #2 into the tangent plane centred at the centre of catalogue #1. Then we computed the positional residuals as the difference between the stellar positions in the meta #1 reference system and the positions in the meta #2 reference system, once projected and transformed into the meta #1 reference system. For those meta catalogues obtained from the large-dither images, we compared each of them to the other 49 catalogues, while small-dither catalogues were only compared to the large-dither ones. When we computed the distortion correction for each chip individually, we used only small-dither images. We then applied this correction to large-dither images and looked at the residuals computed by comparing our stellar positions with those of 2MASS. We noticed that the non-linear terms of the distortion over a very large scale were not completely accounted for. Therefore, we chose to compute the positional residuals by comparing only images far enough on the sky from each other. For each chip, we collected all these residuals together and divided them into an array of 11×11 square elements. We assigned to each array element the median value of the residuals within. For any location on the chip, the correction is computed as the bi-linear interpolation between the surroundings four grid points. We iterated five times, computing new residuals and adding the new correction to the previous one.

In summary, the distortion solution of each chip consists of two parts: a 3×3 look-up table of residuals (that is used to compute the correction at any inter-chip location via a bi-quadratic interpolation between the surrounding four grid points), and an additional fine-tuning 11×11 look-up table of residuals (this time using a bi-linear interpolation to compute the correction). The final stellar positions are distortion corrected and projected with respect to the centre of the meta catalogue. Therefore, each meta catalogue is projected into a different tangent plane. It is important to transform all the catalogues into the same tangent plane during the construction of the master frame. In the rightmost panels of Fig. 3.2 we show the result of our efforts. We applied our distortion correction to the stars in each meta catalogue. We used six-parameter linear transformations to bring these corrected positions on the master-frame reference system using the same tangent plane for each catalogue. This way, the σ(Radial residuals)[4] improves

[4]The σ(Radial residuals) is defined as

$$\sigma(\text{Radial residual})_i = \sqrt{(x_{i,j}^{T_j} - X_i^{\text{master}})^2 + (y_{i,j}^{T_j} - Y_i^{\text{master}})^2}/\sqrt{2} \ ,$$

where $(x_{i,j}^{T_j}, y_{i,j}^{T_j})$ is the position of the i-th star of the j-th image, distortion corrected and transformed into

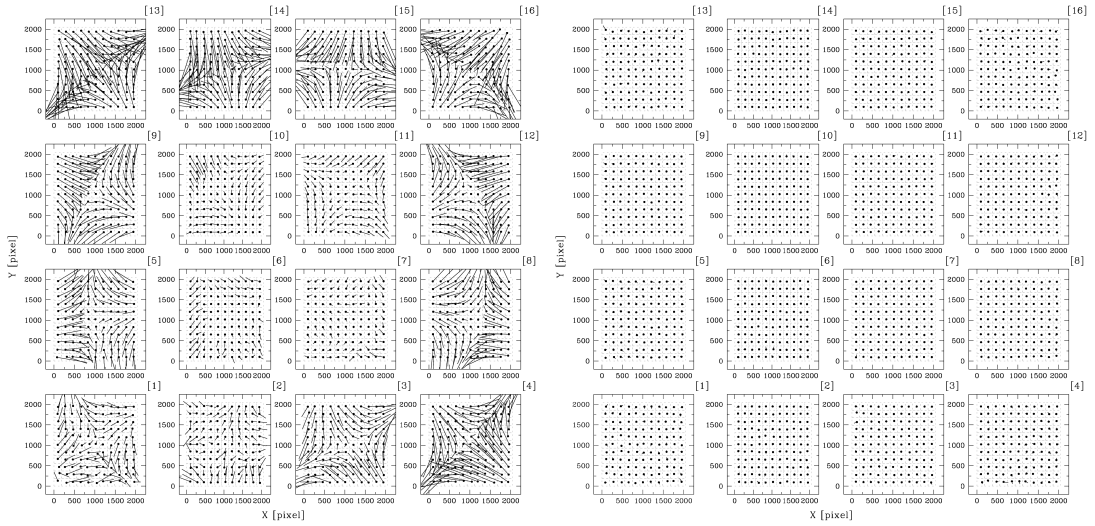

Figure 3.3. Left: residual trends for the 16 chips when we use uncorrected stellar positions. The labels on the top-right corner of each box represent the chip number. The size of the residual vectors is magnified by a factor of 250. Some degree of distortion is clearly visible in the outermost chips. Right: residuals after our distortion correction is applied. The size of the residual vectors is now magnified by a factor 5000.

from ∼1.025 pixels (347.3 mas) to 0.023 pixel (7.9 mas).

In Fig. 3.3 we show the distortion maps before and after the correction, for each of the 16 chips of VIRCAM. In Figs. 3.4 and 3.5 corresponding positional residuals along the X and Y axes, with and without applying our distortion correction, respectively.

We release a FORTRAN routine to correct the geometric distortion. It requires the single-chip raw coordinates ($x^{\rm raw}$,$y^{\rm raw}$) and the chip number. In output, the code computes ($x^{\rm corr}$,$y^{\rm corr}$) coordinates in the meta-frame reference system. The code is available at our group's web page[5].

3.5 Application: NGC 6656

To test our geometric-distortion correction we computed relative proper motions (PMs) of stars in the field of the globular cluster NGC 6656, $(\alpha,\delta)_{\rm J2000.0} = (18^{\rm h}36^{\rm m}23^{\rm s}.94, -23^\circ54'17''.1$, Harris 1996, 2010 edition), using VVV data. We chose this object for its closeness and relatively-high PM with respect to the field objects. We used images taken between 2010 and 2014. We have 12 images in each of the 45 epochs used (except for one epoch for which we have 14 images) in the $K_{\rm S}$ filter (from 2010 to 2014), while for the J filter there are only 12 images taken in 2010.

We obtained astro-photometric catalogues for each image of each epoch as described in Sect. 3.3, distortion corrected as described in Sect. 3.4. The VIRCAM photometry is calibrated by using stars in common with the 2MASS catalogue. We applied linear relations between the VVV instrumental magnitudes and the 2MASS magnitudes based on well-measured, unsaturated stars. We replaced the photometry of VVV saturated stars with that of 2MASS.

the master-frame reference system, T_j is the transformation of the j-th image into the master frame, and $(X_i^{\rm master}, Y_i^{\rm master})$ is the distortion-free (master-frame) position of the i-th star.

[5]http://groups.dfa.unipd.it/ESPG/NIR.html

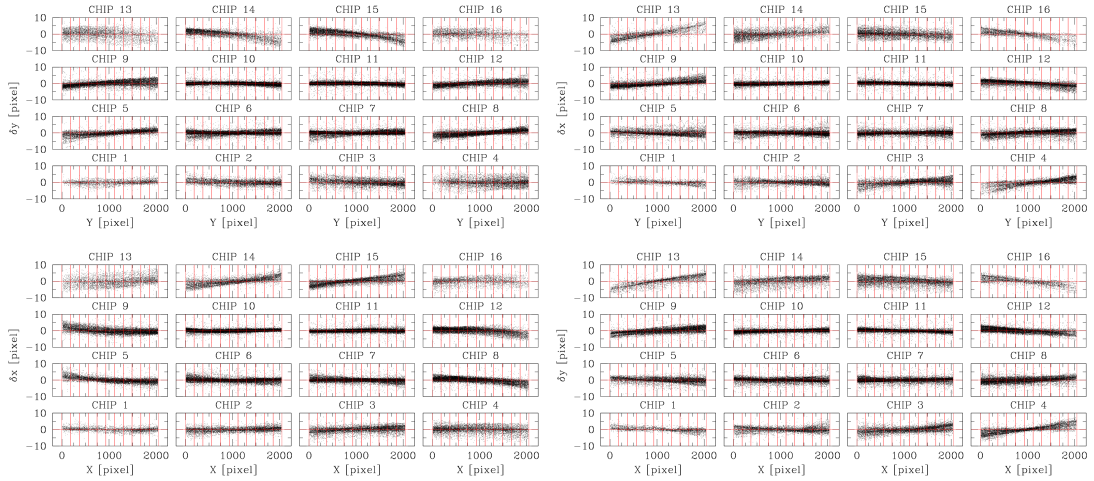

Figure 3.4. From the bottom-left panels, clockwise: δx versus X, δy versus Y, δx versus Y and δy versus X for each of the 16 VIRCAM chips before we applied the distortion correction.

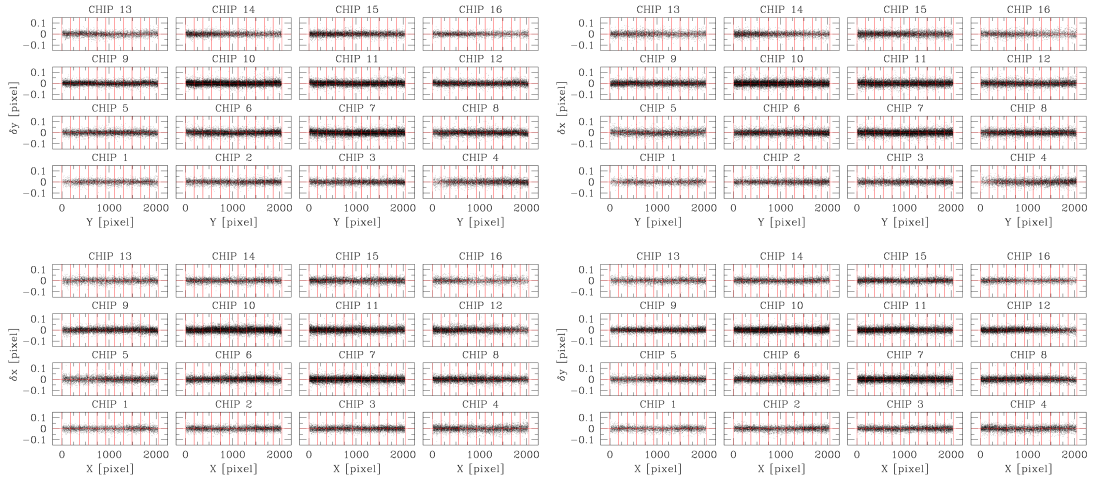

Figure 3.5. As in Fig. 3.4 but after the distortion correction is applied.

The adopted reference frame is based on images taken on 2012 August 16 (which have the best available seeing, are the closest to the zenith, and are taken halfway between 2010 and 2014). The covered FoV is about 1.°1×1.°5. We limited our PM analysis to the innermost region of the field, within a radius of 20 arcmin from the cluster centre, where there is a significant number of cluster members. We then computed the coefficients of the local transformations to transform the stars' positions of each image into the reference frame (Anderson et al. 2006). Local transformations reduce most of the uncorrected distortion residuals and other systematic effects that could harm our measurements. Indeed, the astrometric accuracy reached in our reference master frame is ∼0.08 pixel (27 mas), more than three times larger than that described in Sect. 3.4. The main reason for this larger uncertainty is that the VVV observations are not taken with an astrometric strategy in mind (see discussion in Sect. 3.1 and 3.2). Furthermore, our geometric-distortion correction is an *average* solution, suited for J-filter images and at a

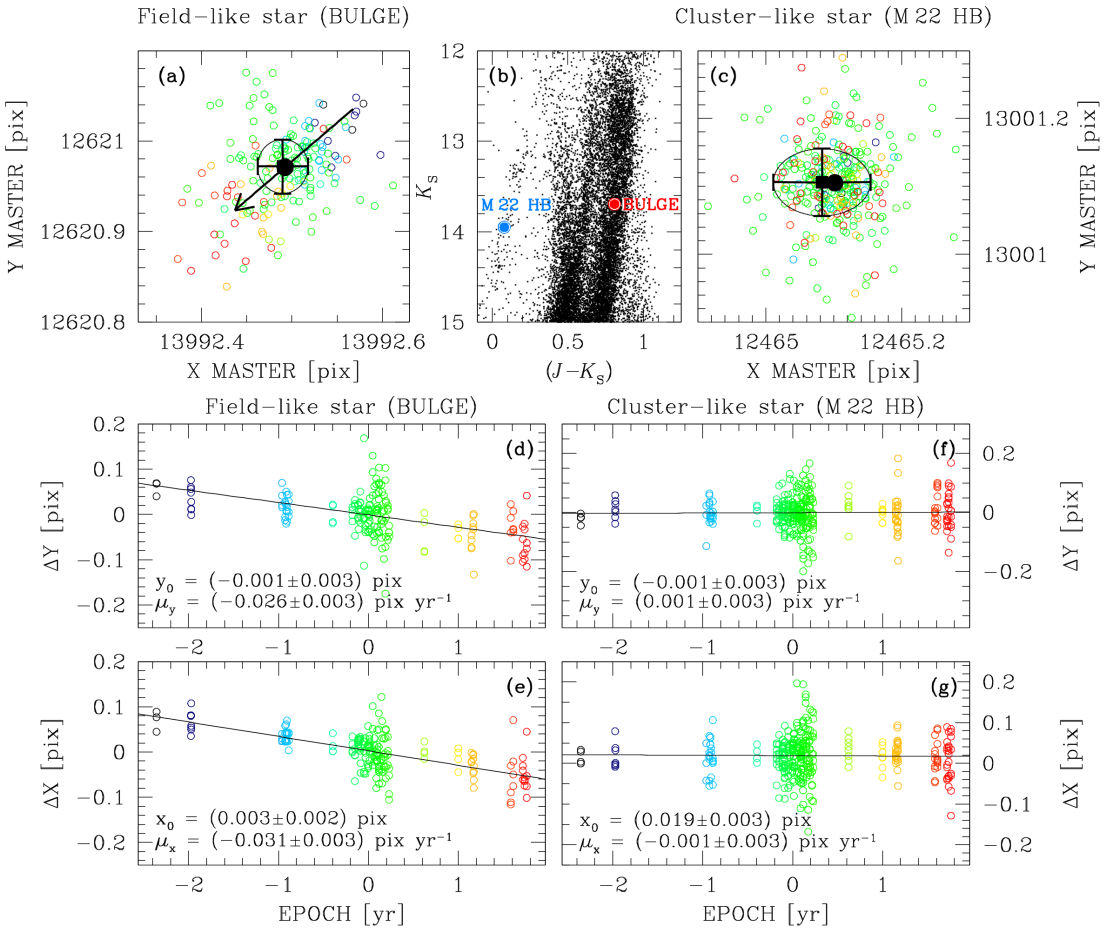

Figure 3.6. Multi-epoch fit of PMs for a field-like ('BULGE') and a cluster-like ('M 22 HB') star. Top: in panels (a) and (c), the open circles represent star's positions at different epochs transformed into the reference master frame, colour-coded (as defined in the bottom panels) depending on the time interval relative to the reference epoch (J2012.62423). The master-frame position is represented by the filled black square (surrounded by an ellipse with semi-axes equal to the positional rms along the X and Y direction); the filled black circle is the expected position of the star at the reference epoch based on the PM fit. In the panel (a), the black arrow shows the ∼4-yr displacement of the star. In panel (b) we show the position of the selected stars on the CMD. Bottom: motion in Y [panels (d) and (f)] and in X [panels (e) and (g)] as a function of the time from the reference epoch. The black line is the least-squares fit of the PM.

specific epoch. The fact that the positional residuals are three times larger also implies that the distortion correction is not stable over time-scales of six months. The local-transformation approach compensates for these issues.

In our local-transformation approach, we transformed the stellar positions as measured in each image into the reference-frame system using a subset of close-by, likely-cluster members (reference stars) to a given star to compute its linear-transformation coefficients. As such, our PMs are computed relative to the cluster mean motion, and cluster members will end up around the (0,0) location on the vector-point diagram (VPD). At the first iteration we selected the reference stars for the local transformation based on their position on the colour-magnitude diagram (CMD).

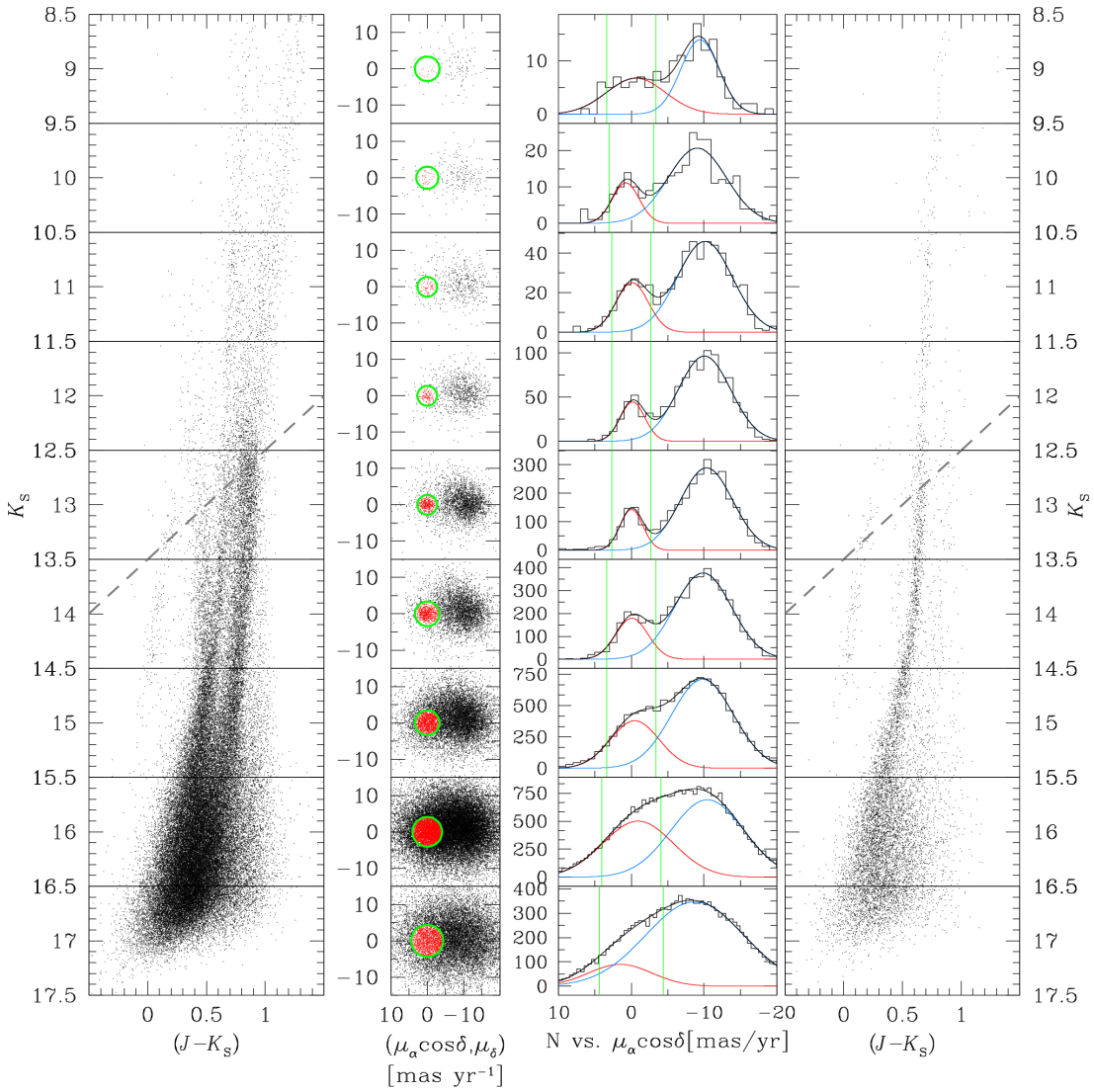

Figure 3.7. Left: K_S versus $(J-K_S)$ CMD of the NGC 6656 field. We show only well-measured-PM stars. We split the CMD in nine intervals of 1 mag each. The grey dashed line sets the average saturation threshold. The saturation level slightly varies within each VIRCAM chip. The variation becomes substantial across the total FoV, and of course from one exposure to the next (because of generally different seeing conditions). Middle-left: VPDs for each of the corresponding magnitude interval. The mean motion of cluster members is centred at (0,0) in the VPDs. We plotted with red dots the cluster-like stars. The radius for the cluster-member selection (green circle) ranges from ∼4.4 mas for stars with $16.5<K_S\leq17.5$ to ∼4.1 mas for those stars with $8.5<K_S\leq9.5$. Middle-right: histograms for the $\mu_\alpha \cos\delta$ PM distribution. The bin size changes depending on the total number of stars in each magnitude bin. Dual-Gaussian fit in black; individual Gaussians in red and azure are used for cluster and field $\mu_\alpha \cos\delta$ distributions respectively. The field distribution is wider than that of the cluster and contaminates the cluster-member sample in all magnitude bins. Right: CMD with only cluster-like-motion stars. It is clear that the fainter the magnitude bin, the higher is the field contamination in our sample. The PMs have been corrected for differential-chromatic refraction as described in the text.

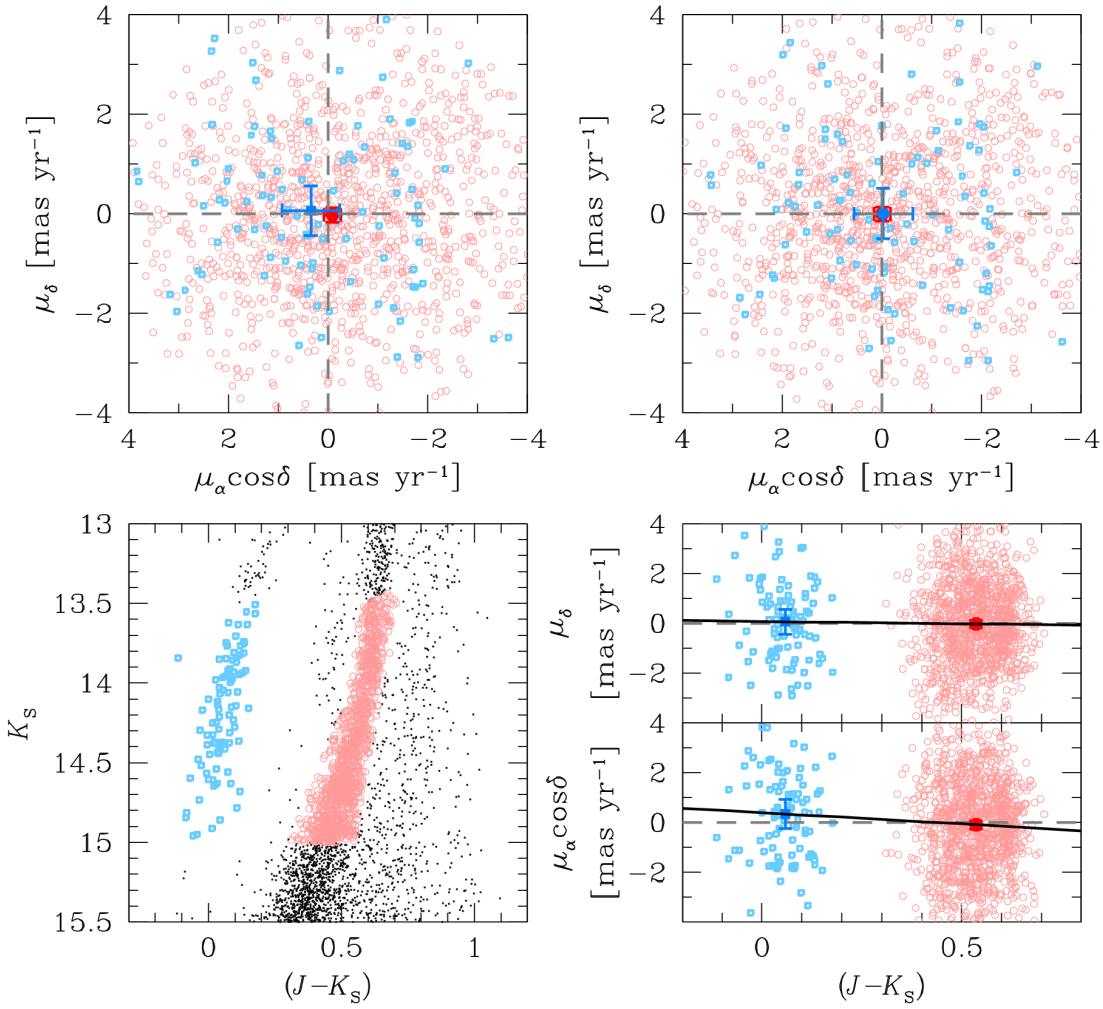

Figure 3.8. Bottom-left: K_S versus $(J-K_S)$ CMD of NGC 6656. We plotted the horizontal-branch stars with light blue open squares and red giant branch stars with light red open circles. We considered only stars with K_S between 13.5 and 15. Top-left: VPD with only the blue and red stars before the differential-chromatic-refraction correction. The azure filled square represents the mean motion of the blue stars, while the red filled circle that of the red stars. We also plot the 3σ error bar as reference. Bottom-right: $\mu_\alpha \cos\delta$ and μ_δ as function of the $(J-K_S)$ colour. A linear fit (solid black line) in each direction was used to model the correction. Top-right: VPD after the correction.

Once PMs were also estimated, we improved our reference-star list by removing all those stars which motion is not consistent with the cluster mean motion.

We computed the stellar displacements as the difference between the transformed single-exposure positions and the master-frame positions. In Fig. 3.6 we illustrate the multi-epoch PM fit for a Bulge star (left-hand panels) and for a cluster member (right-hand panels). In the top panels of the figure we show the stellar positions transformed into the reference frame, colour-coded according to their epoch. In the bottom panels, we show the displacements as a function of time (relative to the reference epoch). The black lines are the weighted least-

squares fit to the data, where the weight is defined as the square root of stars' QFIT (with poorly-measured stars' having less weight). The PM along the two directions (μ_x, μ_y) is the slope of the straight lines. The relative PM errors are the formal errors of the least-squares fit. The constant terms x_0 and y_0 indicate the corrections to be applied to our reference-frame positions at epoch J2012.62423. To exclude obvious outliers, for each star we iteratively removed one point at a time from the sample, fit the PM with the remaining points, and re-computed the vertical residual of the removed point. We rejected all those points for which vertical residuals were five times larger than the fit residual. A final fit to all the remaining points provides our PM estimate for the star.

In Fig. 3.7 we show the K_S versus $(J-K_S)$ CMDs and the VPDs for the stars in the NGC 6656 field. In the VPDs we show the $(\mu_\alpha \cos\delta, \mu_\delta)$ PMs. In the left-hand panel, we plotted the CMD of the entire sample of well-measured-PM stars[6] observed in the selected field, and split it into nine bins, one K_S-magnitude wide. In the middle-left panels, we show the corresponding VPD for each magnitude bin, in which we drew a circle to enclose cluster-like-PM stars. The radius is a compromise between including field stars with a cluster-like mean motion and excluding cluster members with larger PM uncertainties. Saturated and faint stars have poorly-measured PMs, so the selection radii are more generous. In the middle-right panels, we show the histograms of the motion along the $\mu_\alpha \cos\delta$ direction (where the difference between cluster and field stars in the PMs is more evident) to show the field contamination expected by our selections. The rightmost panel shows the CMD of NGC 6656 members. The horizontal branch, red giant branch, main sequence turn-off and upper main sequence are mostly cleaned by field stars and can be used for studies of the properties of these stars in the near-infrared. We also analysed the possible impact of differential-chromatic-refraction effects on our PMs (Fig. 3.8). We selected two samples of NGC 6656 stars with a K_S magnitude between 13.5 and 15, one on the horizontal branch (blue stars) and the other on the red giant branch (red stars). Even if the mean motion of both samples is the same within the error bars, we chose to remove the small contribution of this effect (clearly visible in the $\mu_\alpha \cos\delta$ direction). All PMs in Figs. 3.7, 3.9 and 3.10 have been corrected accordingly.

To evaluate our PM precision we proceeded as follow. By construction, our PMs are relative to the cluster mean motion. As such, the mean location of cluster members on the VPD is (0,0), and the observed dispersion of cluster members should in principle reflect the stellar internal-motion dispersion plus our measurement errors. The internal dispersion of NGC 6656 is about 0.5 mas yr^{-1} (assuming a distance of 3.2 kpc and a central velocity dispersion of 7.8 km s^{-1}; Harris 1996, 2010 edition). The 1D dispersion (defined as the 68.27$^{\rm th}$ percentile of the distribution around the median) of bright, unsaturated ($13 \leq K_S \leq 14$) cluster stars in the VPD is of about 1.5 mas yr^{-1}. By subtracting in quadrature the internal dispersion of 0.5 mas yr^{-1}, we end up with an external estimate of our PM precision, which is of about 1.4 mas yr^{-1}.

To further test of our astrometric accuracy, we measured the relative difference between the Bulge and the Disc bulk motion within the same selected VVV field of NGC 6656 (Fig. 3.9). To this aim, we selected two samples of stars, one from the Disc main sequence and one from the Bulge red giant branch. We considered only Disc (Bulge) stars that in the K_S versus $(J-K_S)$ CMD are bluer (redder) than the respective fiducial line of the sequence. Furthermore, we considered only those stars with PMs larger than 5 mas yr^{-1} with respect to the bulk motion of the cluster. We fit a single Gaussian to the histograms of the Bulge and Disc PMs along each direction, and found a relative displacement of $(\Delta\mu_\alpha \cos\delta, \Delta\mu_\delta) = (-2.13 \pm 0.22, -3.58 \pm 0.24)$ mas yr^{-1}. The absolute difference between Bulge and Disc bulk motions is therefore 4.18 ± 0.32 mas yr^{-1}.

To test this result, we measured the relative displacement between the Bulge and the Disc components using the motion of the same test stars as measured in the UCAC4 and the PP-

[6] We plot the PM errors as a function of the K_S magnitude and drew by hand a fiducial line to remove obvious outliers. The cut is more important for faint stars, where PMs are less accurate. We used the same purging method for the stellar QFIT. Furthermore, we kept only those stars measured in at least 50 exposures.

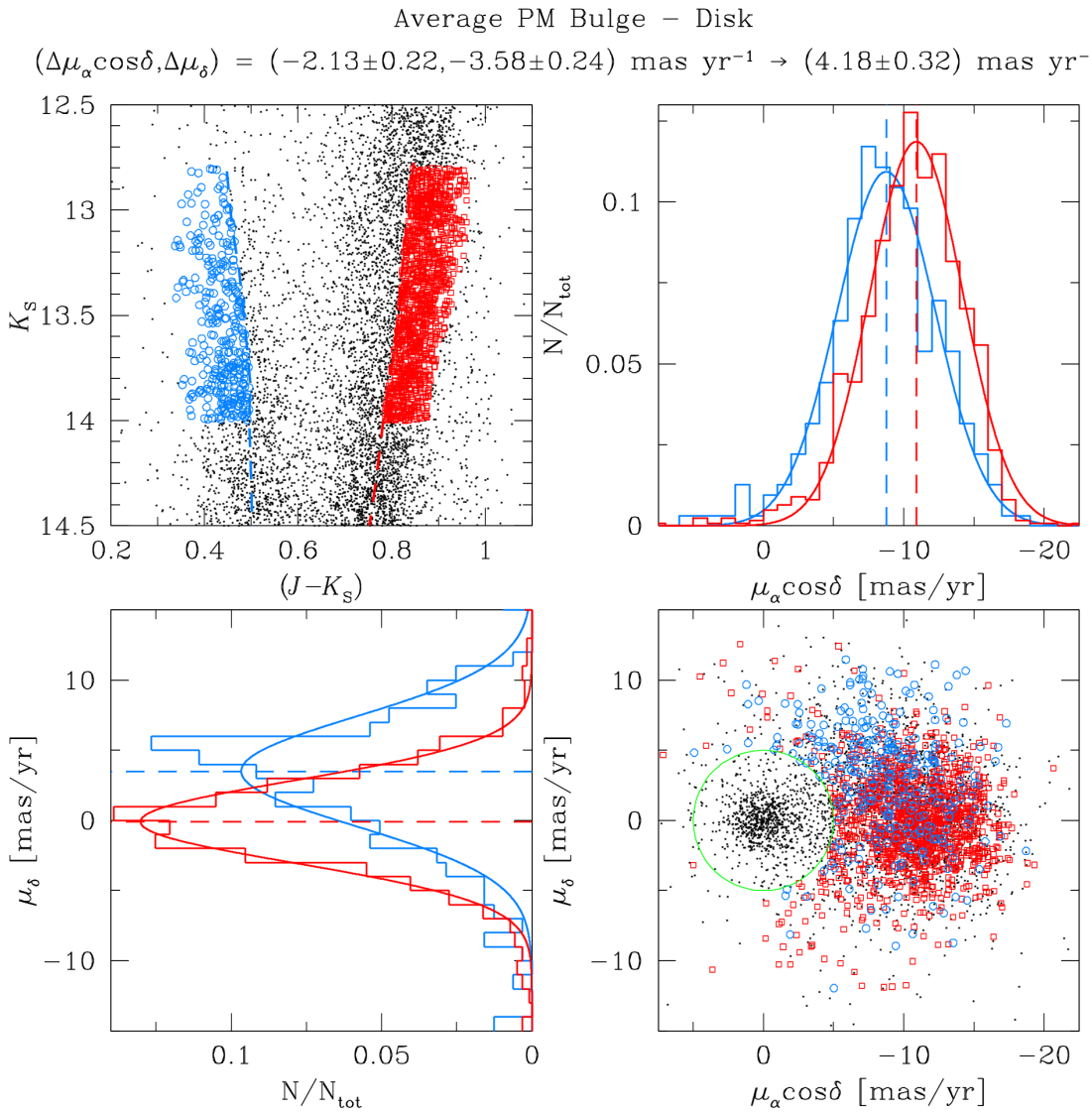

Figure 3.9. Top-left: K_S versus $(J-K_S)$ CMD. We plotted Disc main sequence stars with blue open circles and Bulge red giant branch stars with red open squares. We limited our samples to $12.8 \leq K_S \leq 14$ in order to use only well-measured bright stars. We did not plot all stars within 5 mas yr^{-1} from the centre of the VPD to exclude most of the NGC 6656 members. Bottom-right: VPD with stars within $12.8 \leq K_S \leq 14$. The green circle used to exclude cluster members has a radius of 5 mas yr^{-1}. Bottom-left: histograms of the μ_δ for the Bulge and Disc stars previously selected. We fitted each histogram with a single Gaussian. Top-right: as on bottom-left but for the $\mu_\alpha \cos\delta$.

MXL (Roeser, Demleitner, & Schilbach 2010) catalogues. We found a relative displacement of 3.79±0.98 mas yr^{-1} using UCAC4 and 2.93±1.3 mas yr^{-1} using PPMXL, which are in agreement with our estimate within the error bars, though our estimate has a smaller uncertainty. We also compared our measured difference between Bulge and Disc motion with that predicted by the

Besançon models (Robin et al. 2003). We simulated both populations in the same field covered by our application. We adopted an exponential trend for photometric and PM errors as function of the magnitude to create a model as close as possible to our data. The major challenge was to take into account for the correct absorption toward the Galactic plane. We used the 'Bulge Extinction And Metallicity' (see Gonzalez et al. 2012, 2013) calculator to compute the average extinction in our field. This value, divided by NGC 6656 distance, gives us the diffuse absorption of 0.15 mag kpc^{-1}. The difference between Bulge and Disc motion obtained this way is 1.38±0.12 mas yr^{-1}. This value is not consistent with our measurements. We performed different simulations varying the absorption coefficients to understand if the absorption law could somehow change the simulated kinematics, but we found the results were about the same. We attribute this significant difference to the difficulty of the Besançon model in simulating the reddening, Galaxy stellar densities and kinematics towards the Galactic plane where the extinction is high.

3.5.1 Future perspectives

The VVV survey will be completed in 2016 (Hempel et al. 2014), and the time baseline provided by the uniform VVV data will be about six years. As an example, we combined the VVV images of NGC 6656 and the HAWK-I data previously used in Chapter 2. Since the HAWK-I images were taken in 2007, we used only the VVV archival images between 2010 and 2013 in order to have approximately the six years of time baseline. We computed the PMs as described in the previous section and in Fig. 3.10 we show the resulting CMDs and VPDs. As expected, with a larger time baseline we are able to completely separate cluster and field stars. This example shows again the great astrometric potential of the full-baseline VVV data. Older epochs (both optical and near-infrared data) are available in the archives, and the PMs will be an invaluable resource to distinguish the different stellar populations in the Galaxy.

3.6 Conclusions

In this Chapter, we present our reduction pipeline for the VIRCAM detector and the geometric distortion solution based on the J filter. Thanks to our distortion correction and to the adopted dithered observing strategy, we are able to reach a positional residual of ∼8 mas in each coordinate in each exposure across the entire FoV of VIRCAM. Note that we are talking about relative astrometry. Our absolute astrometry is not as good as the relative one because the linear terms are constrained only with 2MASS.

We release a FORTRAN routine to correct the geometric distortion. For a given position in a single-chip raw frame ($x^{\rm raw}$,$y^{\rm raw}$) and the chip number, the code produces ($x^{\rm corr}$,$y^{\rm corr}$) coordinates in the meta-frame reference system. The code is available at our group's web page[7]. The use of this distortion solution is encouraged regardless of the specific method adopted to measure stellar positions. Each meta catalogue is projected into a plane tangential to its centre. This offers the best single-catalogue, distortion-free positions. Please note that, in order to construct a common reference frame, all meta catalogues should be instead projected into the same tangent plane (see Sect. 3.4).

As a test bed of the astrometric accuracy reached by our geometric-distortion correction, we applied our reduction pipeline to a set of VVV archival images. We chose a field centred on the globular cluster NGC 6656 and we computed the relative PM of the NGC 6656 and Galactic bulge and disc stars, as well as the individual motion of each star in the field. We noticed that our astrometric accuracy is worse (∼0.08 pixel) using VVV data. Our geometric-distortion correction is an average solution and the distortion is not entirely stable. However, by starting with a good average solution, local transformations (used to compute the PMs) can be used to efficiently achieve optimal precision even with this type of data. We demonstrate that we

[7] http://groups.dfa.unipd.it/ESPG/NIR.html

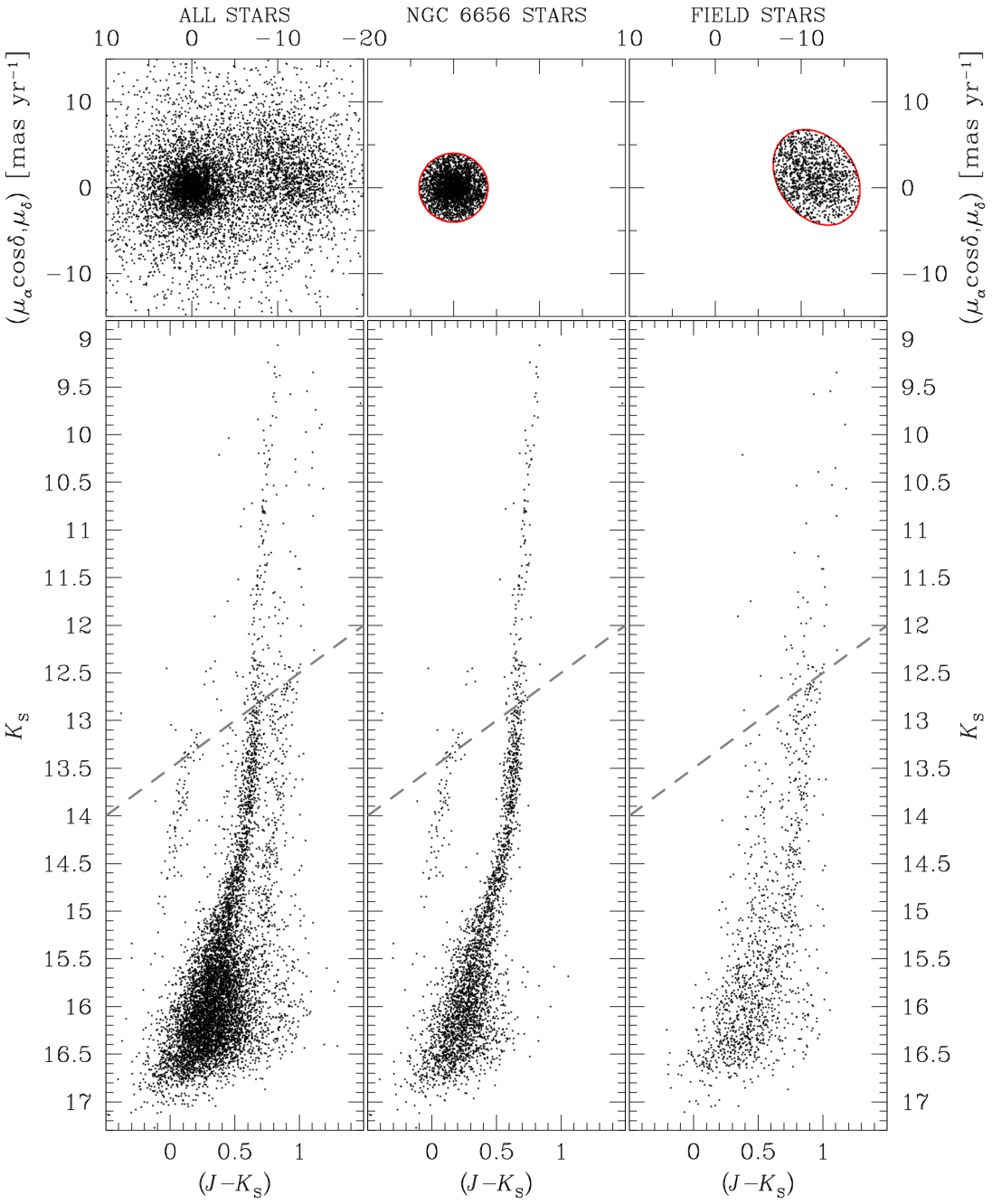

Figure 3.10. Top: VPDs with a time baseline of about six years obtained combining the HAWK-I and VVV data. Bottom: K_S versus $(J-K_S)$ CMDs of the stars in common between the HAWK-I and VVV fields. We plot only well-measured-PM stars. On the left-hand panels we plot the entire sample, while in the centre and right-hand panels we plot only cluster members and field stars respectively. We considered NGC 6656 stars those stars with a PM within 4 mas yr^{-1} around the cluster mean motion (red circle centred in (0,0) in the middle VPD); while the stars enclosed in the ellipse centred in (−11.5,1.2) mas yr^{-1} with major and minor axes of 12 and 9 mas yr^{-1} are probable field stars.

are able to separate cluster and background/foreground field stars with a time baseline of only four years. The cluster stars, in the cleaned CMD, can be used for the study of the stellar populations of NGC 6656. We also showed that the field stars, in the direction of NGC 6656, are of great use, e.g., to separate (and study) the PMs of the Galactic disc and bulge components. We demonstrated that our results are consistent with what can be obtained using UCAC4 and PPMXL catalogues, though our measurements have a much smaller error. Galactic models fail to reproduce the observations, likely because of the difficulties to reproduce the reddening and kinematics towards the Galactic bulge.

With the images analysed in this Chapter and a time baseline of about four years, we obtained a typical astrometric precision of 1.4 mas yr^{-1} for bright, unsaturated well-measured stars. This value corresponds to $\sigma_v \sim$21 km s^{-1} at the distance of NGC 6656 (3.2 kpc from Harris 1996, 2010 edition), or $\sim$53 km s^{-1} at 8 kpc (a reference distance for the Bulge). At the end of the VVV survey, the total time baseline will be of about six years, thus further increasing the final achievable PM accuracy. The use of older, archive, optical and near-infrared data will further enhance the PM capability of the VVV survey. The astrometric capability of this survey is complementary to *GAIA*, in particular in the most crowded and heavily-absorbed regions not reachable by *GAIA*, and to study objects below its magnitude limit ($G \sim$20).

Bibliography

Anderson J., Bedin L. R., Piotto G., Yadav R. S., Bellini A., 2006, A&A, 454, 1029

Anderson J., et al., 2008, AJ, 135, 2114

Bellini A., Bedin L. R., 2010, A&A, 517, A34

Dalton G. B., et al., 2006, Proc. SPIE, 6269, 62690X

Emerson J., McPherson A., Sutherland W., 2006, The Messenger, 126, 41

Gonzalez O. A., Rejkuba M., Zoccali M., Valenti E., Minniti D., Schultheis M., Tobar R., Chen B., 2012, A&A, 543, AA13

Gonzalez O. A., Rejkuba M., Zoccali M., Valent E., Minniti D., Tobar R., 2013, A&A, 552, AA110

Harris W. E., 1996, AJ, 112, 1487

Hempel M., et al., 2014, The Messenger, 155, 29

Libralato M., Bellini A., Bedin L. R., Piotto G., Platais I., Kissler-Patig M., Milone A. P., 2014, A&A, 563, A80

Libralato M., et al., 2015, MNRAS, 450, 1664

Maybhate A., Grumm D., McMaster M., Sirianni M., 2008, Instrument Science Report WFPC2 2008-03, Correcting Background Streaks in WFPC2 Data, STScI, Baltimore, MD, p. 3

Minniti D., et al., 2010, New Astron., 15, 433

Platais I., et al., 2002, AJ, 124, 601

Platais I., Wyse R. F. G., Zacharias N., 2006, PASP, 118, 107

Robin A. C., Reylé C., Derrière S., Picaud S., 2003, A&A, 409, 523

Roeser S., Demleitner M., Schilbach E., 2010, AJ, 139, 2440

Saito R. K., et al., 2012, A&A, 537, A107

Skrutskie M. F., et al., 2006, AJ, 131, 1163

Sutherland W., et al., 2015, A&A, 575, A25

van de Ven G., van den Bosch R. C. E., Verolme E. K., de Zeeuw P. T., 2006, A&A, 445, 513

Zacharias N., Finch C. T., Girard T. M., Henden A., Bartlett J. L., Monet D. G., Zacharias M. I., 2013, AJ, 145, 44

4 Astrometry and photometry with optical facilities

As discussed in the previous Chapters, the techniques introduced by Anderson et al. (2006) and that we extended are powerful tools for high-precision astrometry and photometry with wide-field imagers. In this Chapter, I give an overview of different applications, in particular focusing on the geometric-distortion-correction aspect. The material discussed in this Chapter is part of refereed papers published in Astronomy and Astrophysics (A&A)[1] and Monthly Notices of the Royal Astronomical Society (MNRAS)[2] to which I contributed to as coauthor.

4.1 Proper-motion decontamination of ultra-faint dwarf galaxies using LBC-red@LBT

Ultra-faint dwarfs (UFDs) are among the least luminous, most dark-matter dominated and most metal-poor galaxies. The study of their stellar populations and structure is mainly harmed by the difficulty to remove external sources that contaminate the colour-magnitude diagram. This is the case for the work of Fabrizio et al. (2014) on the UFD Hercules[3], a galaxy among the brightest UFDs of the Milky Way. To disentangle Hercules members from foreground Galactic stars, Fabrizio et al. mainly used proper motions computed from data obtained with the Large Binocular Telescope (LBT).

LBT is equipped with two wide-field cameras (Large Binocular Cameras or LBCs) placed at the prime foci of the blue (LBC-blue) and red (LBC-red) arms of the telescope. Each LBC is optimised for observations at different wavelength ranges, and it is made up by four 2048×4608 pixel^2 CCDs with a pixel scale of 0.2297 arcsec pixel^{-1}, for a total field of view of 24×25 arcmin^2 (Bellini & Bedin 2010). To compute Hercules' stellar proper motions, we used LBC-red images obtained through the $r_{\rm Sloan}$ filter in two epochs (2008 and 2013) for a total time baseline of $\sim$4.94 yr. To achieve the required astrometric accuracy, we solved for the geometric distortion

[1] Fabrizio et al. (2014, A&A, 570, A61) - Received 2014 March 11 / Accepted 2014 August 13.
[2] Nardiello et al. (2015, MNRAS, 447, 3536) - Received 2014 December 09 / Accepted 2014 December 17.
[3] $(\alpha,\delta)_{\rm J2000.0} = (16^{\rm h}31^{\rm m}02\overset{\rm s}{.}0, 12^\circ47'25\overset{''}{.}6)$.

using 25 properly-dithered images taken in the second epoch (INAF-DT no. 38, PI: Brocato), specifically designed to calibrate the geometric distortion of the LBC-red in the $r_{\rm Sloan}$ filter. The geometric-distortion correction was iteratively solved for in a similar way as done in Libralato et al. (2014, hereafter simply Chapter 2).

The data set was reduced using the procedures described in Bellini & Bedin (2010). In each pre-reduced exposure and independently for each CCD, we derived spatially-varying, empirical PSF models with which we measured positions and fluxes of all detectable stellar sources.

The blue and red LBT arms have the same optical design, and their cameras are constituted by the same detectors, arranged in the same way. This means that both the blue and the red LBCs have a similar geometric distortion to the 0-th order, and, therefore, the distortion solution found for the LBC-blue should also represent a good first-guess solution for the LBC-red. Hence, to derive the geometric-distortion solution for the $r_{\rm Sloan}$-filter exposures of the LBC-red, we started by correcting the stellar positions of the 2013 data set with the LBC-blue V-filter distortion correction of Bellini & Bedin (2010). Next, we cross-identified the stars in each catalogue and put them into the same reference frame system (master frame) by means of 4-parameter linear transformations (two rigid shifts, one rotation and one change of scale). We used only bright, unsaturated stars to compute the coefficients of the transformations. Our master frame was built with stars measured in at least 3 images. Even if the V-filter correction of the LBC-blue is not perfectly adequate to correct the $r_{\rm Sloan}$-filter LBC-red images, systematic errors have a random amplitude from one exposure to the other due to the adopted observing strategy (dither pattern). Therefore, the average stellar positions on the master frame provide a good first-guess approximation of their true positions in a distortion-free frame.

The distortion solution for the $r_{\rm Sloan}$-filter of the LBC-red is made up by three parts: (i) a linear transformation to put all images onto the master frame; (ii) a polynomial correction; and (iii) a table of residuals. We used a fifth-order polynomial for the polynomial correction and followed the prescriptions given in Bellini & Bedin (2010). At the first iteration, the cubic part of the polynomial was set to be the same of the V-filter third-order polynomial of Bellini & Bedin, while higher-order terms were set to zero. Then, we iterated the procedure to derive new polynomial coefficients and improved the master frame until the stellar positional residuals did not change significantly from one iteration to the next. The last part of our correction consisted of four look-up tables (one for each CCD) to minimise uncorrected polynomial residuals. We followed the methods described in Bellini, Anderson, & Bedin (2011) for the WFC3/UVIS detector of *Hubble Space Telescope* and in Chapter 2 for HAWK-I@VLT. We subdivided each chip of the 4-CCDs LBC mosaic into 11×25 elements. The table correction at a given location of the chip is obtained by bi-linearly interpolating the surrounding four grid points. We iterated this procedure by applying 75% of the suggested correction, building a new master frame, and computing new, improved grid points. The convergence was reached when the change in the suggested correction was negligible from one iteration to the next.

In Figs. 4.1 and 4.2, we show the distortion maps before and after applying the distortion corrections, respectively. Figure 4.3 shows the σ(Positional residuals), computed as in Chapter 2 (Sect. 2.5.5), after each step of our correction. In the bottom panel, we show the σ(Radial residual) for a master frame derived using more general 6-parameter linear transformations. By applying all corrections, the σ(Positional residuals) improves from $\sim$74.2 mas to $\sim$9.5 mas.

Thanks to this high-precision distortion correction, Fabrizio et al. (2014) were able to compute Hercules stars relative proper motions using a local-transformation approach as done by Anderson et al. (2006). Hercules members, selected using proper motions, were further constrained according to their location on a colour-colour diagram. The final sample of Hercules members consists of 357 stars; enough to study stellar-population metallicities and ages by comparing the observed Hercules colour-magnitude and colour-colour diagrams with synthetic diagrams and isochrones. The proper-motion-based approach of Fabrizio et al. (2014) is a promising and more efficient way to select the UFD members with respect to other kinematic measurements like, e.g., radial velocities.

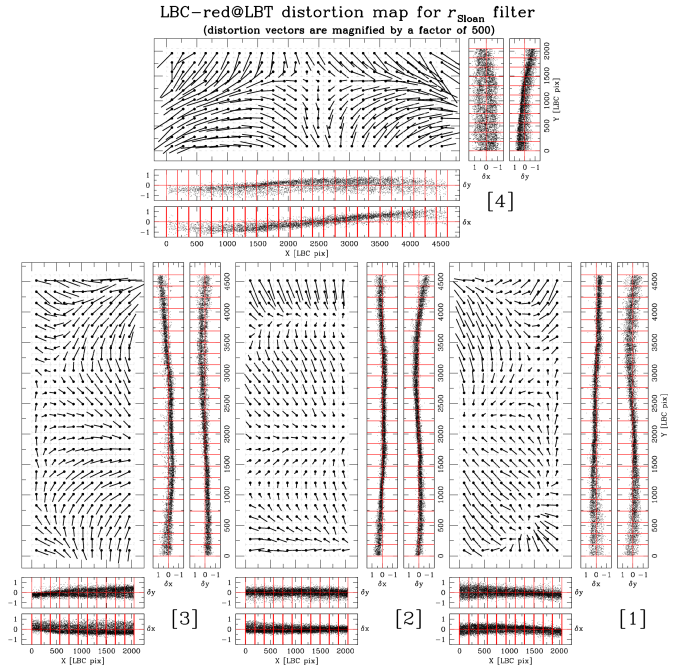

Figure 4.1. Residual trends for the four LBC-red chips when we use uncorrected stars' positions, and single positional residual trends along X and Y axes. The size of the residual vectors is magnified by a factor 500. Units are expressed in LBC-red raw pixel.

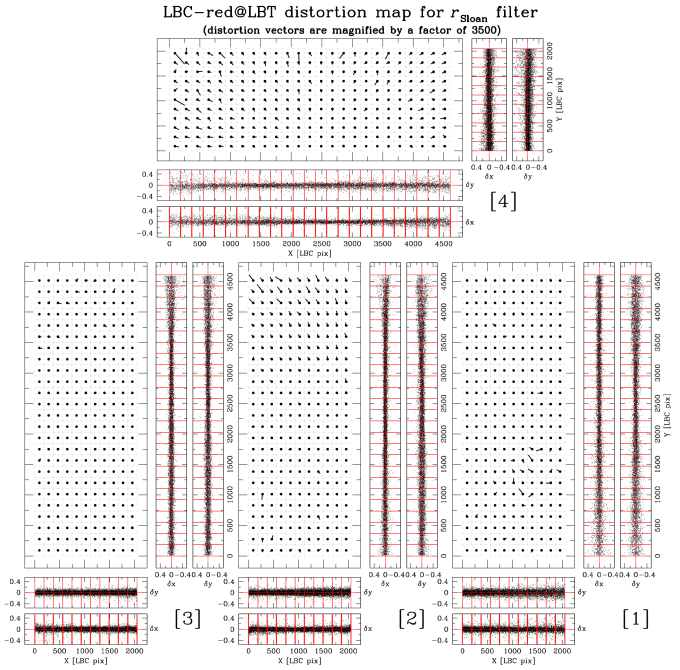

Figure 4.2. As in Fig. 4.1 but after all the corrections were applied. The size of the residual vectors is magnified by a factor 3500.

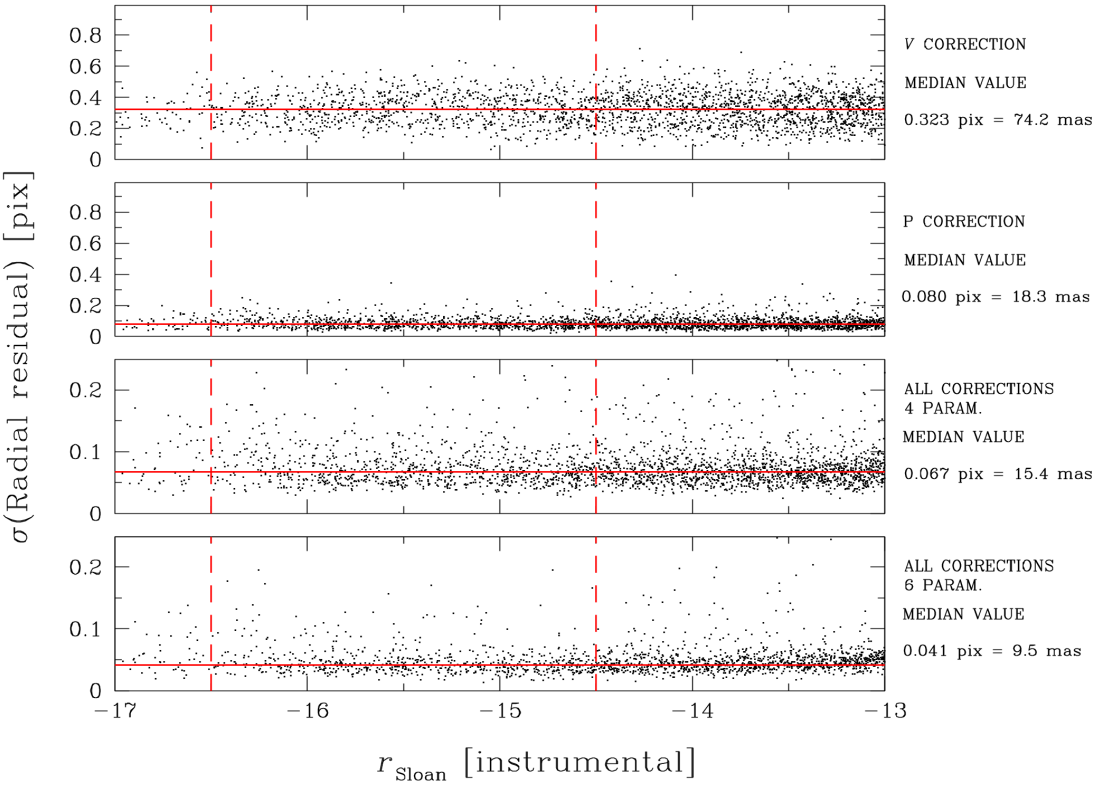

Figure 4.3. σ(Radial residual) versus instrumental $r_{\rm Sloan}$ magnitude after each step of our solution. The red solid horizontal line shows the median value of σ(Radial residual) for stars in the magnitude interval marked by the two red vertical dashed lines.

4.2 High-precision light curves in the *K2* fields with the Asiago Schmidt telescope

The multi-year, multi-wavelength photometric survey 'The Asiago Pathfinder for HARPS-N' (PI: Bedin) is characterising variable stars and searching for candidate transiting exoplanets in open clusters, to be then followed-up with HARPS-N@TNG. In the first paper of the series, Nardiello et al. (2015) focused on the open clusters M 35 and NGC 2158, observed in three different runs of ∼10 days each, and described the survey outline and the method used to extract high-precision light curves in these crowded environments.

The Asiago 67/92 cm Schmidt telescope used for this survey is equipped with a SBIG STL-11000M camera, that is made by a 4050×2672 pixel^2 Kodak KAI-11000M detector with a pixel scale of 0.862 arcsec pixel^{-1}, for a total FoV of 58×38 arcmin^2. In addition to different optical filters (B, V, R, I), there is the possibility to collect images in white light (no filter). The unfiltered setup is particularly suited to maximise the signal-to-noise ratio for the largest number of stars possible, although more vulnerable to atmospheric effects. The observing strategy of the first M 35/NGC 2158 campaign was designed as follows. During the first run, unfiltered images with an exposure time of 120 s were collected to observe as many stars as possible in the field. In the following runs, mainly long and short R-filter images, but also some in B and V filters, were collected, in order to use colour information to discover and characterise already-known and new

variable stars.

As for the LBC, the reduction software developed for the Asiago Schmidt detector directly derives from the one described in Anderson et al. (2006). Again, for each exposure we made a 9×5 grid of empirical PSFs and used them to measure positions and fluxes for all detectable stars. To achieve the astrometric accuracy needed for the light-curve-extraction phase, we computed geometric-distortion corrections for the B and R filters using 25 properly-dithered exposures. As in Chapter 2 and in Sect. 4.1 (Fabrizio et al. 2014), we auto-calibrated the geometric distortion and solved for it by using a fifth-order polynomial correction and a look-up table of residuals. In Figs. 4.4 and 4.5 we show the distortion maps before and after we applied our distortion solution to B- and R-filter images, respectively. The astrometric accuracy reached is of the order of 17 mas (less than 0.02 pixel) per coordinate for both filters (Fig. 4.6). This accuracy is good enough to constrain the location of a given star on the CCD grid during the entire time series and register the time-series photometry.

4.2.1 The neighbour-subtraction technique

Nardiello et al. (2015) extracted light curves for all stars in M 35 and NGC 2158 detected in the white-light exposures. The light-curve extraction is based on several steps. First, we cross-identified all stars in common between the single-exposures catalogues and built a common reference frame system, one for each filter. Second, for images taken through the R filter and the white light, we combined all exposures and made a stacked image. We then derived empirical PSF models and measured stellar positions and fluxes on the stacked image in the same way as previously done on the single images. The higher signal-to-noise ratio of the image stacks with respect to that of a single image allowed us to extract a more complete and deeper input list to use for the light-curve extraction. By combing the R-filter and the unfiltered input lists, we obtained a master list with more than 66 000 objects. For each star in the master list, we locally transformed its master-list position into that of each individual exposure by using 6-parameter, linear transformations. Local transformations are important to minimise uncorrected distortion residuals (see Chapter 1). We then performed aperture and PSF-fitting photometry on the original and on the neighbour-subtracted single exposures. In the latter case, we subtracted from the image all the close-by neighbours which light could pollute that of the target star. Neighbour-subtracted photometry works best in crowded environments; the aperture photometry offers better photometric rms for bright stars, while the PSF photometry is better suited for faint stars. With this method, Nardiello et al. (2015) discovered 519 new variables in these fields.

Many of the clusters observed during 'The Asiago Pathfinder for HARPS-N' survey have been or will be observed during the so-called *K2* mission (Howell et al. 2014). M 35 and NGC 2158 were already observed during the *K2* Campaign 0, and the light-curve-extraction method described by Nardiello et al. (2015), together with their high-angular-resolution master list, proved to be very useful to exploit the data coming from *K2*, as we will see in the next Chapter.

Bibliography

Anderson J., Bedin L. R., Piotto G., Yadav R. S., Bellini A., 2006, A&A, 454, 1029

Bellini A., Bedin L. R., 2010, A&A, 517, A34

Bellini A., Anderson J., Bedin L. R., 2011, PASP, 123, 622

Fabrizio M., et al., 2014, A&A, 570, A61

Howell S. B., et al., 2014, PASP, 126, 398

Libralato M., Bellini A., Bedin L. R., Piotto G., Platais I., Kissler-Patig M., Milone A. P., 2014, A&A, 563, A80

Nardiello D., et al., 2015, MNRAS, 447, 3536

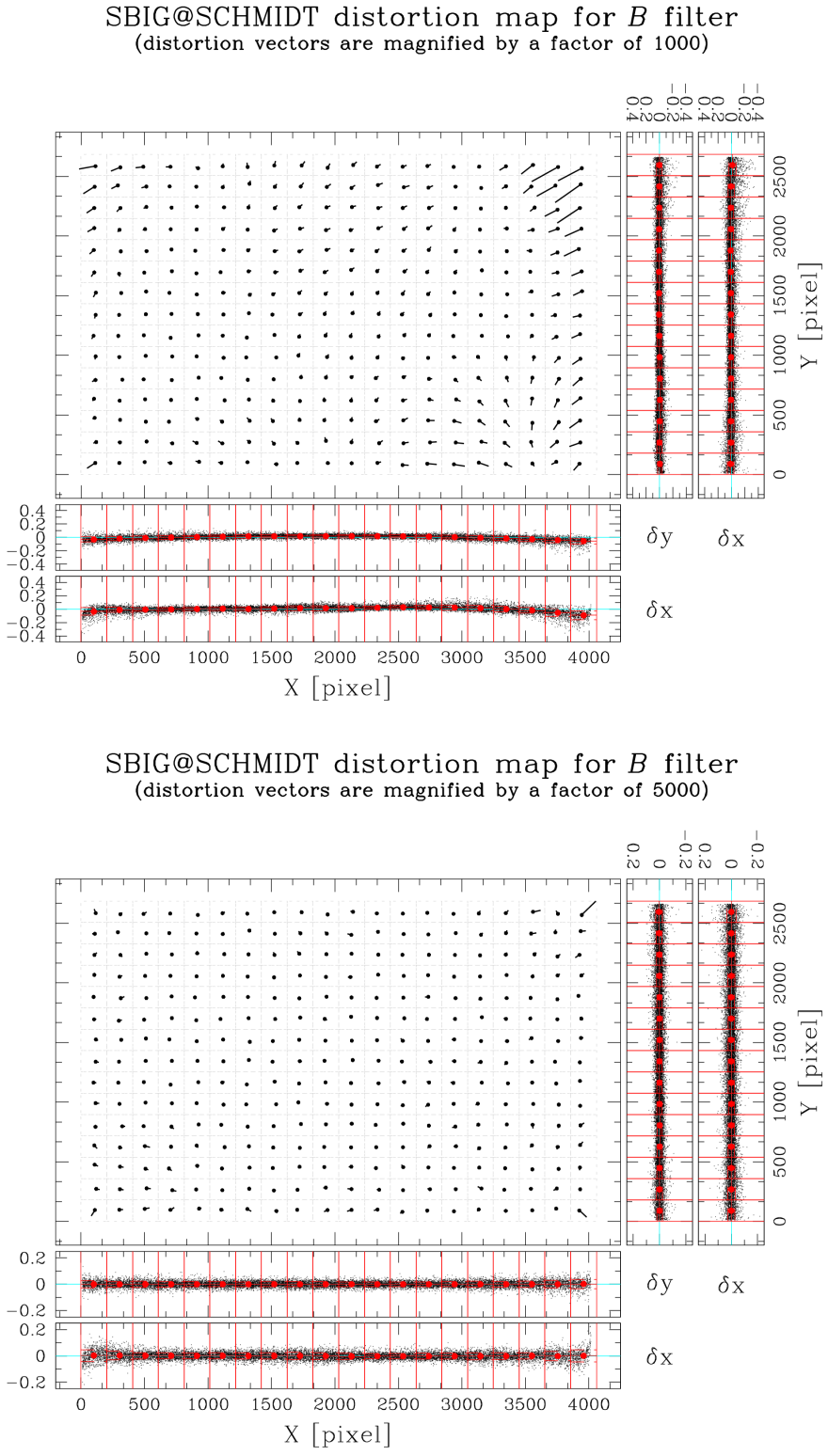

Figure 4.4. *B*-filter distortion maps of the SBIG CCD of the Asiago Schmidt telescope before (top panels) and after (bottom panels) we applied the geometric-distortion correction. The corresponding single residual trends along the X and Y axes are also shown around each map. The size of the distortion vectors is magnified by a factor 500 and 5000 on top and bottom panels, respectively. Units are expressed in SBIG raw pixel.

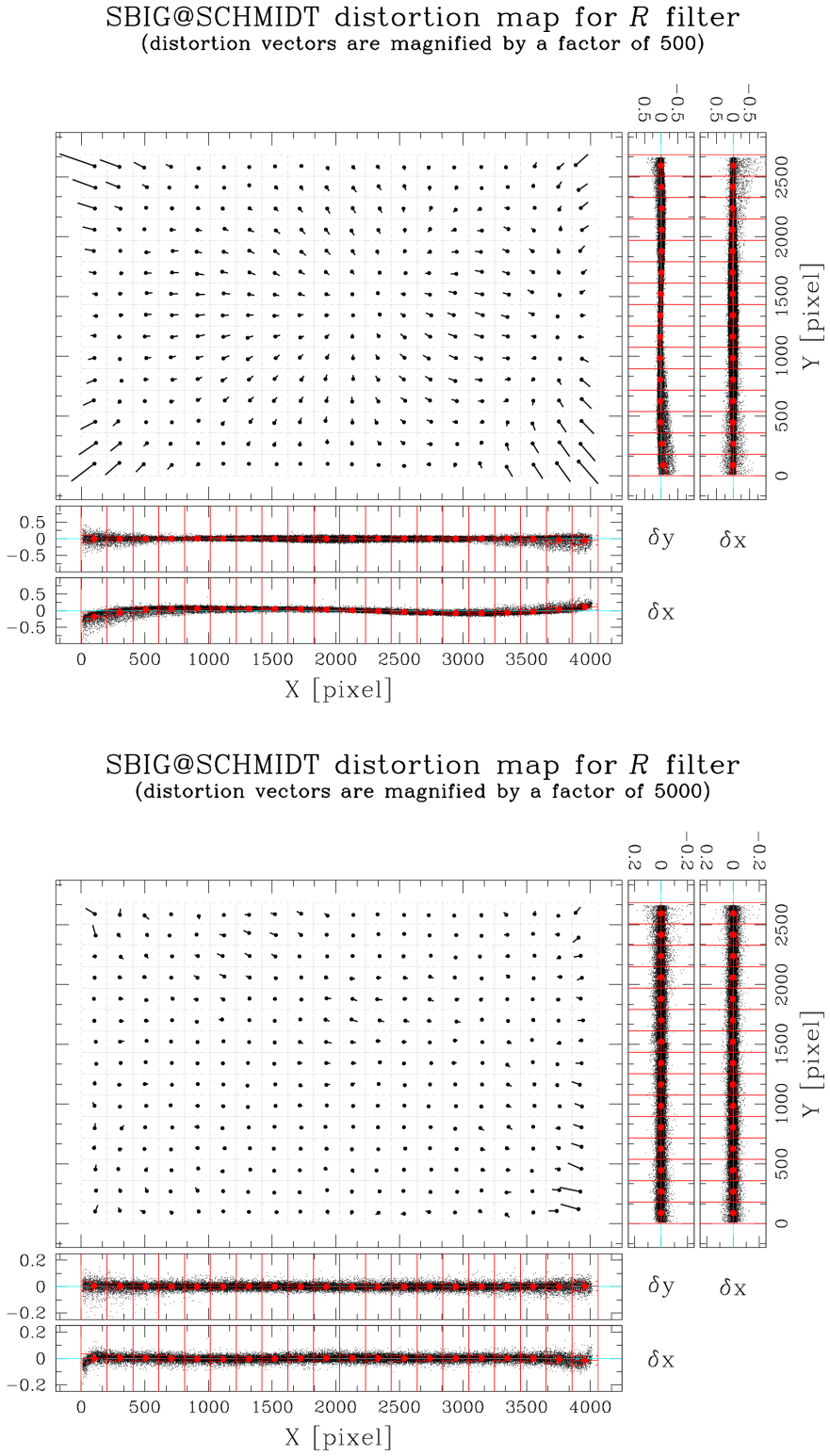

Figure 4.5. As in Fig. 4.4 but for the R filter.

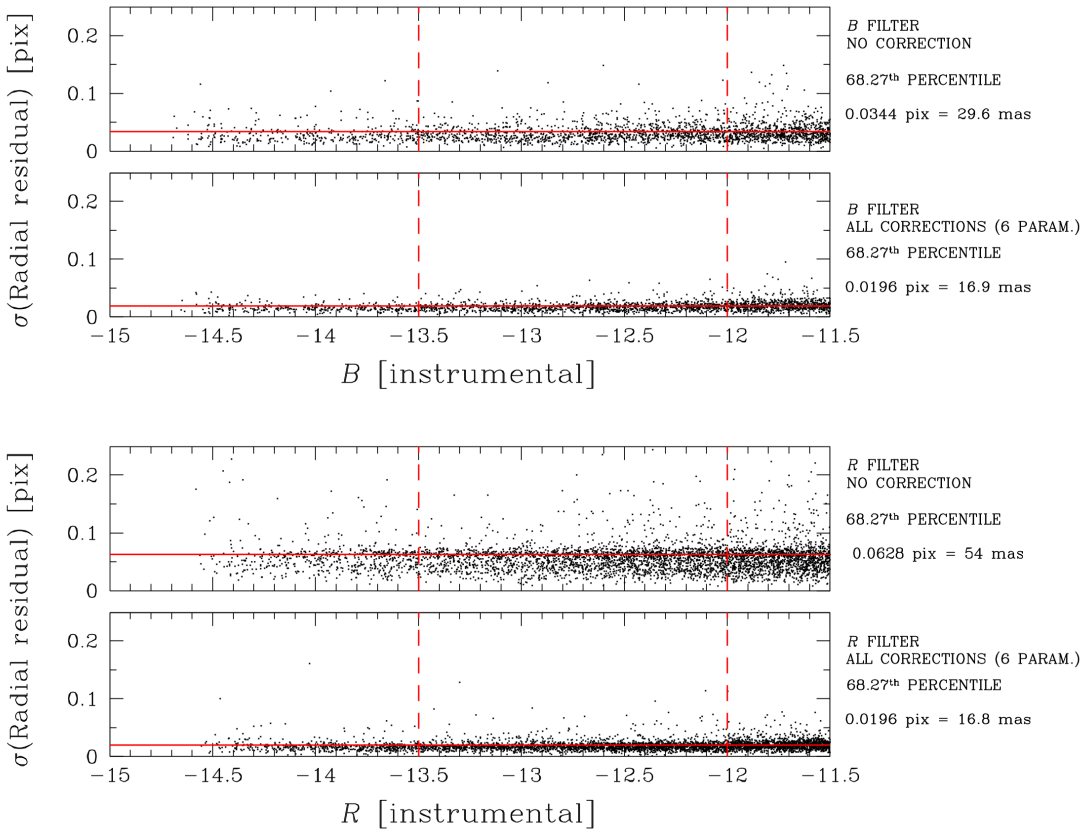

Figure 4.6. First and second panel from top: σ(Radial residual) versus instrumental B magnitude before and after the distortion correction was applied. Third and fourth panel from top: same as above but for the R filter. The red solid horizontal line shows the 68.27^{th} of the distribution of the σ(Radial residual) around the median value. The stars used to compute these reference values are those between the two red dashed vertical lines.

5 High-precision photometry with *K2*

The analysis of *Kepler* and *K2* data reported in the literature is mostly based on aperture photometry. Because of *Kepler*'s large pixels and undersampled images, aperture photometry is not always ideal to obtain high-precision photometry in crowded environments. For these reasons, some data set have not yet been fully exploited. In this Chapter, we present a new reduction method of *K2* data, which is based on our experience with undersampled *HST* images and ground-based, wide-field detectors (described in the previous Chapters). The method involves a point-spread-function, neighbour-subtraction technique, and is developed to exploit the huge potential offered by *Kepler* main-mission and *K2* 'super-stamps' covering the core of dense star clusters. The material discussed in this Chapter has been published in Monthly Notices of the Royal Astronomical Society (MNRAS)[1].

5.1 Introduction

The *Kepler* observatory began science operation in 2009 May 12, with the main scientific goal of discovering exoplanet candidates transiting their host stars. The *Kepler* Input Catalog (Brown et al. 2011) includes ∼150 000 targets. The *Kepler* telescope is essentially a defocused 0.95-m/1.4-m Schmidt camera with a field of view of about 100 deg^2.

For a detailed description of the *Kepler* mission and design, see the *Kepler* technical documents web page[2], Borucki et al. (2010), Koch et al. (2010), and references therein. Here we provide a brief review of the relevant characteristics. On the telescope focal plane there is an array of 21 modules, each of which is associated to two 2k×1k CCDs. Each CCD is read out in two 1k×1k channels, for a total of 84 independent channels over the whole focal plane. On 2010 January 12, one module failed (MOD-3) and a second one (MOD-7) failed in 2014 February. So, currently only 76 channels are operative.

The pixel scale is ∼4 arcsec pixel^{-1}, and the not-in-focus images causes the average point-spread function (PSF) to extend across several pixels (except in the area close to the centre of the field). Even so, many features of the PSF are undersampled, even in the outskirts of the field. Knowing the exact shape of the PSF is the key for high precision photometry in crowded fields. The determination of an appropriate PSF for the *Kepler* images represents the main effort of this work.

Due to limitation in telemetry, the scientific data were downloaded once a month using a maximum data-transfer rate of approximately 550 kB s^{-1}. For this reason the *Kepler* spacecraft conducts its own pre-reduction of the data, and sends only a small portion of the exposed pixels.

[1] Libralato et al. (2016, MNRAS, 456, 1137) - Received 2015 September 03 / Accepted 2015 November 05.
[2] https://archive.stsci.edu/kepler/documents.html

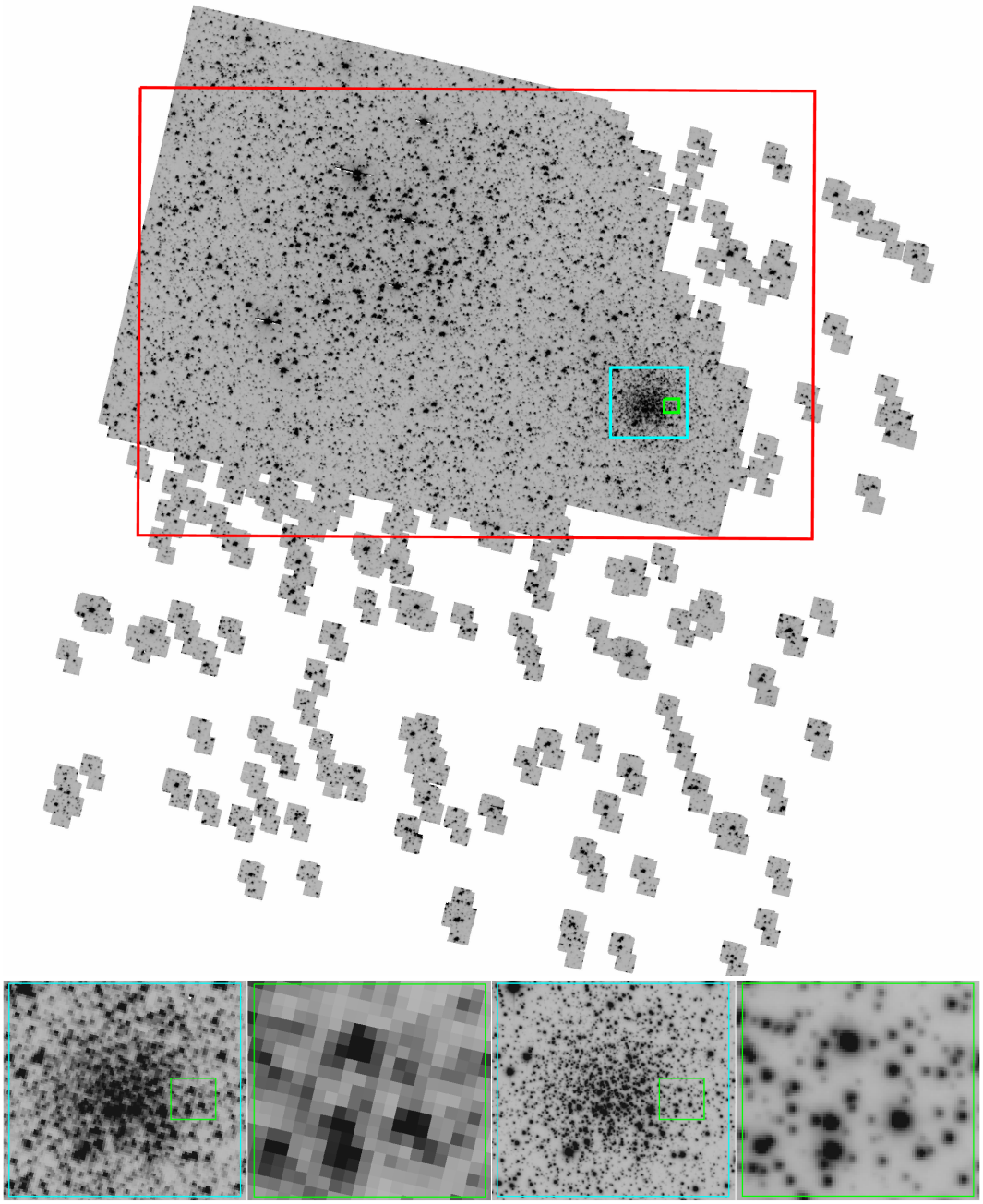

Figure 5.1. Field of view covered by all available *K2*/C0/channel-81 exposures used in our LC extraction (Sect. 5.4). On the top we show the *K2* stacked image obtained by combining 2422 exposures. The red rectangle represents the field of view of the Schmidt input list of Nardiello et al. (2015). The cyan and green boxes highlight two different zoomed-in regions around NGC 2158. In the bottom row we compare these two regions in the *K2* (left-hand and middle-left panels) and in the Schmidt stacked image from Nardiello et al. (2015, middle-right and right-hand panels). All these images are oriented with north up and east left. It is clear that the higher resolution of the Schmidt image allows us to measure more sources than in the *K2* image, as well as to better discern close-by stars.

Around each target, a small area (a 'stamp') of various dimensions (typically a few pixels square) is read out with an integration time of 6.02 s. Every 270 exposures, the stamps are co-added on board to create a long-cadence stamp of about 29 min of total integration time; short cadences involve adding nine exposures for a 1-minute integration time. A time series of such long- or short-cadence stamps is called a target-pixel file (TPF). When several targets of interest are in a relatively small patch of sky, multiple contiguous stamps are collected together to form a so-called super-stamp. In the original *Kepler* field, two such super-stamps were taken around the stellar clusters NGC 6791 and NGC 6819.

In 2012 and 2013, the failures of two reaction wheels that were used to maintain accurate, stable spacecraft pointing, forced NASA to re-design the mission. After a period of study and evaluation, NASA approved an extension to the mission (named *Kepler*-2.0, hereafter, *K2*, Howell et al. 2014), essentially for as long as the two remaining reaction wheels continue to operate or until the fuel is exhausted.

The mission was cleverly designed to use the radiation pressure from the Sun to balance the spacecraft drift, allowing it to observe four fields per year close to the Ecliptic. Each of these fields corresponds to a so called *K2* Campaign[3], and can be continuously observed for ∼75 d.

While the two functional reaction wheels control the pitch and yaw, the thruster needs to be fired every ∼6 h to control the roll angle of the field. This operation mode causes significantly larger jitter than in the original *Kepler* main mission. Therefore, although the *K2* data collection procedures are similar to those adopted for the original *Kepler* mission, the reduced pointing capabilities impose the adoption of 2–4 times larger target stamps. Because the *K2* stamps include 4–16 times more pixels, the number of observed targets is proportionally reduced from the ∼150 000 targets of the original *Kepler* field to ∼10 000–20 000 objects for the various *K2* fields. A new list of target objects is defined for each campaign: the Ecliptic Plane Input Catalog[4] (hereafter, EPIC).

Despite the changes introduced in *K2* mission, several notable results have been achieved, from exoplanet discovery and characterisation (e.g., Crossfield et al. 2015; Foreman-Mackey et al. 2015; Vanderburg et al. 2015) to asteroseismology (Hermes et al. 2015; Stello et al. 2015) and stellar astrophysics (Armstrong et al. 2015; Balona et al. 2015; Kraus et al. 2015; LaCourse et al. 2015).

5.1.1 The purpose of this study

In this study we apply our expertise on PSF photometry and astrometry on dithered and undersampled images in crowded fields (Anderson & King 2000, 2006) to extract high-precision photometry of stars in the two Galactic open clusters (OCs) M 35 and NGC 2158, which happened to lie within the *K2* Campaign 0 (C0) field.

The temporal sampling and coverage of *Kepler* and *K2* missions and their high photometric precision could be an invaluable resource for different stellar cluster fields, for example gyrochronology (Barnes 2007; Mamajek & Hillenbrand 2008; Meibom et al. 2011, 2013, 2015), stellar structure and evolution (e.g., age and Helium content from detached eclipsing binaries as done by Brogaard et al. 2011) or asteroseismology membership (Stello et al. 2011). Another interesting topic concerns exoplanets. We could improve our knowledge about the exoplanets in star clusters, in particular on how the environment (chemical composition, stellar density, dynamical interaction) can affect their formation, evolution and frequency (Adams et al. 2006; Brucalassi et al. 2014; Gilliland et al. 2000; Meibom et al. 2013; Mochejska et al. 2004, 2006; Nascimbeni et al. 2012; Quinn et al. 2012, 2014; Weldrake, Sackett, & Bridges 2008).

Until now, most of the published studies based on *Kepler* and *K2* data have focused on isolated, bright objects. Focusing on *K2* data, photometry on such bright objects is well described in the literature. The main difference between the methods concern the mask determination,

[3]http://keplerscience.arc.nasa.gov/k2-fields.html
[4]https://archive.stsci.edu/k2/epic/search.php

the stellar centroid measurement and the subsequent detrending algorithms to improve the photometric precision (for a review of the *K2* methods adopted by the different teams, see Huang et al. 2015). However, the potential scientific information on faint objects and on stars in the super-stamp crowded regions has not been completely exploited.

In this Chapter we intend to obtain the most accurate possible models for the *Kepler* PSFs and to use them to explore the light curves (LCs) of the sources in the densest regions that have been and will be imaged by *Kepler* and *K2*. The *Kepler* main mission includes four OCs (NGC 6791, NGC 6811, NGC 6819 and NGC 6866); many more clusters have been and will be observed during the *K2* campaigns, which will also include the Galactic Centre and the Bulge (Campaign 7 and 9, respectively).

Thanks to our PSF models, for the first time on *Kepler* images, it will be possible to obtain precise photometry for stars in crowded fields, and down to $K_{\rm P}{\sim}24$. Having access to accurate *Kepler* PSFs and comprehensive catalogues from high-angular-resolution ground-based imaging allows us to subtract neighbours before measuring the flux of target stars, thus giving us better corrections for dilution effects that might result in under-estimates of the true radius of transiting/eclipsing objects. Indeed, the combination of PSFs and catalogues allow *all* reasonably bright sources within the stamps to be measured accurately. Finally, even without ground-based imaging, accurate PSFs, combined with aperture photometry, will allow better identification of blends. We will illustrate a few examples of mismatched variables in the EPIC catalogue, showing that the real variable is a different, much fainter source (see Sect. 5.7.3).

5.2 Image reconstruction

This pilot work makes exclusively use of pixels within channel 81 and collected during *K2* C0, focusing on the OCs M 35 and NGC 2158. We downloaded all the *K2* TPFs, which contain the complete time series data, for both these clusters from the 'Mikulski Archive for Space Telescopes' (MAST). In our approach we find it more convenient to work with reconstructed images of the entire channel, putting all saved pixels into a common reference frame, rather than working with separate stamps. This gives us a better sense of the astronomical scene and enables us to work with all pixels collected at a same epoch in a more intuitive way. We assigned a flag value to all pixels in the CCD unsaved in any stamp.

We wrote a specialised PYTHON routine to construct an image for each cadence number of the TPFs and the corresponding *Kepler* Barycentric Julian Day (KBJD) was defined as the average KBJD of all the TPFs with the same cadence number. For C0 channel 81 we thus reconstructed a total of 2422 usable images. Each channel-81 image is a $1132{\times}1070$ pixel^2 array. The value assigned to each pixel in each image is given by the `FLUX` column of the corresponding TPF. To cross-check that the reconstructed images were correct, we compared them with full-frame images of the field (which were also available from the MAST).

Figure 5.1 gives an overview of our data set. We show the coverage and the resolution the *K2* stacked image obtained with 2422 images and the Schmidt stacked image from Nardiello et al. (2015, see Sect. 5.4.1 for the description of the catalogue and its usage).

5.3 Point-spread function modelling

Even taking into account the large defocusing of the *Kepler* camera, its PSFs are still undersampled. Indeed, *Kepler* PSFs are not simple two-dimensional Gaussians, and several of the PSF's fine-structure features are severely undersampled. If not correctly modelled, these substructures can introduce sources of systematic errors into the measurement of the positions and fluxes of the studied sources. Furthermore, if a PSF model is not sufficiently accurate, any attempted neighbour-subtraction results in spurious residuals and consequent systematic errors.

Anderson & King (2000), hereafter AK00, introduce a convenient formalism to model the PSF. Rather than model the *instrumental* PSF as it impacts the pixels, they model the *effective* pixel-convolved PSF (ePSF) in a purely empirical way using a simple look-up table formalism. Their PSF is similar to the *pixel response function* (PRF) described in Bryson et al. (2010). One of the issues that AK00 found in modelling the undersampled *Hubble Space Telescope* (*HST*) Wide-Field Planetary Camera 2 (WFPC2) PSF is that such PSFs suffer from a degeneracy between the positions and the fluxes of the point sources. An appropriate calibration data set where stars are observed in different pixels of the detector and map different sub regions of the pixels is required to solve for this issue.

The AK00 approach involves taking a dithered set of exposures and empirically constructing a self-consistent set of star positions and a well-sampled PSF model that describes the distribution of light in the pixels. Such a data set was taken for *Kepler* during *Kepler*'s early commissioning phase (see Bryson et al. 2010 for a description), but unfortunately it has not yet been made available to the public (though it may be within a few months according to Thomas Barclay, private communication).

Given the urgent need for PSFs to make optimal use of the *K2* data, we decided to do the next best thing to construct an accurate set of star positions, so that properly sampled PSFs can be extracted from *Kepler* images. The main-mission *Kepler* data are not suitable for this, since they have very little dither and each star provides only one sampling of the PSF. The *K2* data are actually better for PSF reconstruction purposes, since the loss of the reaction wheels means that the spacecraft is no longer able to keep a stable pointing. Every ∼6.5 h, a thruster jet is fired to re-centre the boresight position to its nominal position. As a consequence, the stellar positions continuously change during *K2* observations, with each star sampling a variety of locations within its central few pixels. Moreover, channel 81 contains the large super-stamp covering M 35 and NGC 2158 (our main targets) with a large number of high signal-to-noise ratio (SNR) point sources. We will see in the next sections that this mapping is not optimal, but it is the best available so far.

5.3.1 Initial assess of the dithered pointings

The complicated drift-and-repositioning process inherent in the *K2* data collection results in a very uneven sampling of each star in pixel phase[5]. There are many observations at the initial phase, and few at the latter phases. We note that even with the repeated drift, a star typically samples its pixels along a line, rather than evenly across the face of a pixel, so even the achieved dither is less than ideal. In order to make the dither sampling as even as possible, we selected a subset of images (out of the 2422 exposures described in the previous section) in order to evenly map the astronomical scene across pixel phases. To do this, we used the *empirical* approach of Anderson et al. (2006) to construct an initial PSF model that was spatially constant across each detector. Such a PSF is not ideal for our ultimate purposes, but it provides better positions than a crude centroid approach and will allow us to identify a subset of images that can be used to extract the best possible PSF.

For each exposure, we made one empirical-PSF model for the entire channel because most of the stars are located in the M 35/NGC 2158 super-stamp and the spatial variability is not significant for this initial purpose. With such PSFs, we were able to measure positions and fluxes for all sources. We then built a common reference system (hereafter master frame) by cross-identifying the stars in each image. We used six-parameter linear transformations to bring the stellar positions as measured in each exposure into the reference system of the master frame. At the first iteration, the master frame was chosen using as reference one of the exposures of our sample. We then adopted a clipped-average of the single-frame positions transformed into the master frame in order to improve the definition of the master frame itself, and re-derived

[5]The pixel phase of a star is its location with respect to the pixel boundaries and can be expressed as the fractional part of its position: $\mathrm{PIXEL\,PHASE} = x_i - \mathrm{int}(x_i + 0.5)$.

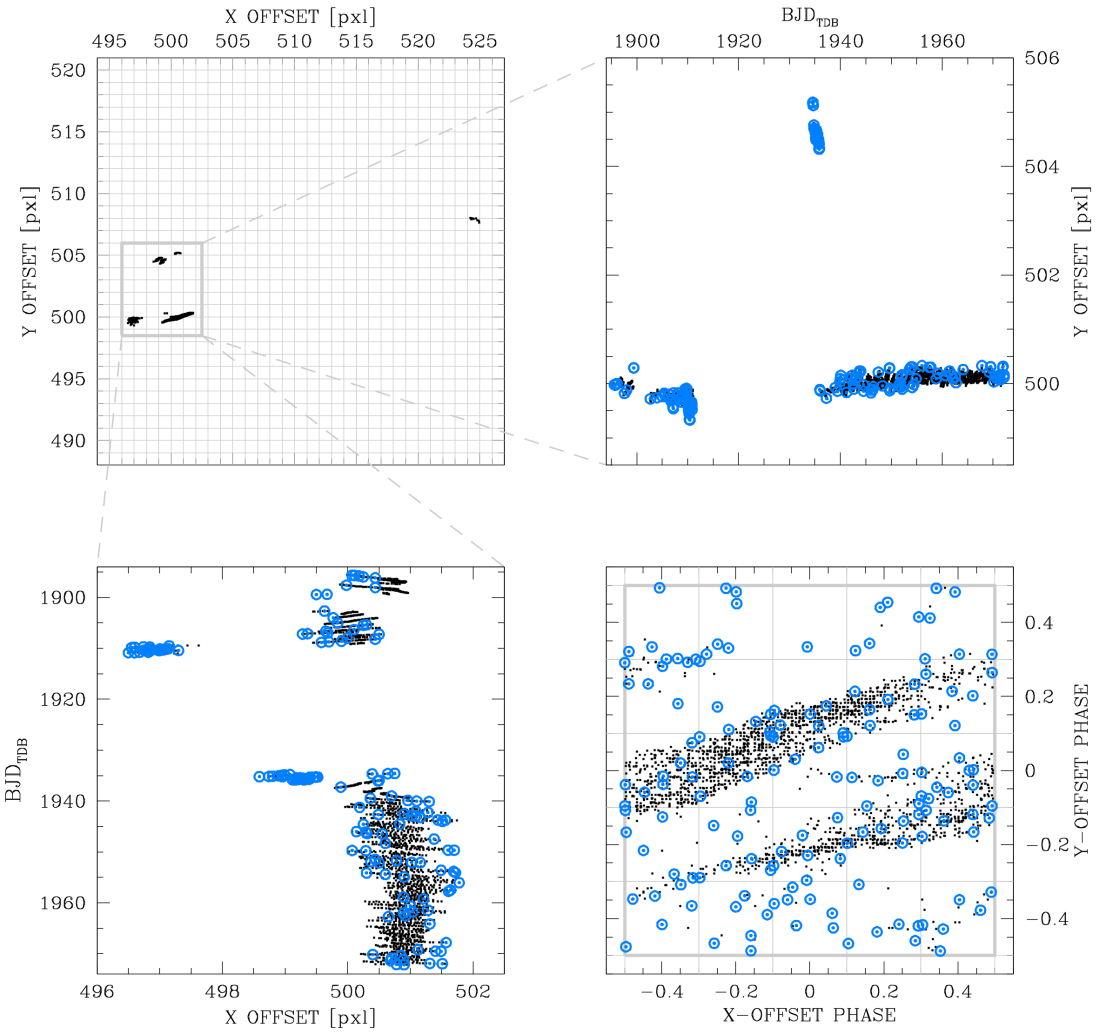

Figure 5.2. Top-left: dither-pattern outline of the 2422 images used in our analysis. The grey grid represents the pixel matrix in the master-frame reference system. The thick-line grey rectangle encloses the points plotted in the top-right and bottom-left panels. Top-right: y-offset variation during C0. We excluded the 10 points around (524,508) with the largest offset with respect to the average value to better show the time variation of the y-offset. The azure points are those images used for the ePSF modelling (see text). Bottom-left: as on top-right but for the x offsets. Bottom-right: dither-pattern pixel phase. The centre of the pixel (dark grey square) is located at (0,0). The pixel was divided into 5×5-grid (thin grey lines) elements and, in each such element, we selected six images (when possible) to map that sub pixel region as homogeneously as possible.

improved transformations. This process was iterated until the master-frame positions did not significantly change from one iteration to the next.

The transformations between each frame and the master frame allowed us to analyse the dither pattern. In Fig. 5.2 we show this pattern along with its time evolution. The dither pattern was made by transforming the same pixel in each exposure into the master-frame reference system. Since the behaviour of the geometric distortion is different along the detector, the dither-pattern outline can change using a different pixel. However, for our purpose, such representation allows us to understand it anyway. It is clear that the dithering places the same star at a range of locations in its central pixels. While the dither coverage along the x-axis is reasonably uniform, along the y-axis the bulk of the 2422 exposures is located in a narrow area. We constructed a homogeneous mapping of the pixel-phase space (bottom-right panel of Fig. 5.2) as follows. We divided the pixel-phase space in a 5×5-grid elements and, in each element, we selected by hand six exposures in order to include that sub pixel region in our PSF construction. This was possible in almost all the cells. We ended up with 154 images out of 2422. This is a compromise between the need to have an adequate number of samplings for the ePSF, and the necessity to map the entire pixel space homogeneously, avoiding over-weighting of any sub-pixel region (by using the whole data set which is very heterogeneous).

5.3.2 Building the *effective*-PSF

With this subset of images, we were finally able to construct a reliable PSF model. For all exposures, we assumed the PSF to be spatially constant within our super-stamps, and to have no temporal variations. For a given star of total flux z_* located at the position (x_*,y_*), the value of a given pixel $P_{i,j}$ close to such star is defined as

$$P_{i,j} = z_* \cdot \psi(i - x_*, j - y_*) + s_* \ ,$$

where s_* is the local sky background and $\psi(\Delta x, \Delta y)$ is the PSF, defined as the fraction of light that would be recorded by a pixel offset by $(\Delta x, \Delta y) = (i - x_*, j - y_*)$ from the centre of the star. By fitting the PSF to an array of pixels for each star in each exposure, we can estimate its x_*, y_* and z_* for each observation of each star. The equation to be used to solve for the PSF can be obtained by inverting the above equation:

$$\psi(\Delta x, \Delta y) = \frac{P_{i,j} - s_*}{z_*} \ .$$

With knowledge of the flux and position of each star in each exposure, each pixel in its vicinity constitutes a sampling of the PSF at one point in its two-dimensional domain. The many images of stars, each centred at a different location within its central pixel, give us a great number of point-samplings and enable us to construct a reliable ePSF model. This is described in detail in AK00. Here, we just provide a brief overview of the key points:

- We made a common master frame by cross-identifying bright, isolated[6] stars in each image and computing their clipped-averaged positions and flux. On average, we have 650 good stars per exposure to use.
- We transformed these average master-frame positions back into the frame of each image in order to place the samplings more accurately within the PSF domain (since each measure is an average of 154 images).
- We converted each pixel value in the vicinity of a given star in a given image into an ePSF sampling, and modelled the variation of the PSF across its two-dimensional domain. We have on average 650 reliable stars per exposure, for a total of 10^5 samplings.

[6]The adjective 'isolated' should be considered in a relative way. Within a 1×1-pixel square on a *K2* exposure there could be more than one star, as we will see in the Fig. 5.21. Therefore by 'isolated' we mean that, in the *K2* image, there are no other obvious stars close to the target.

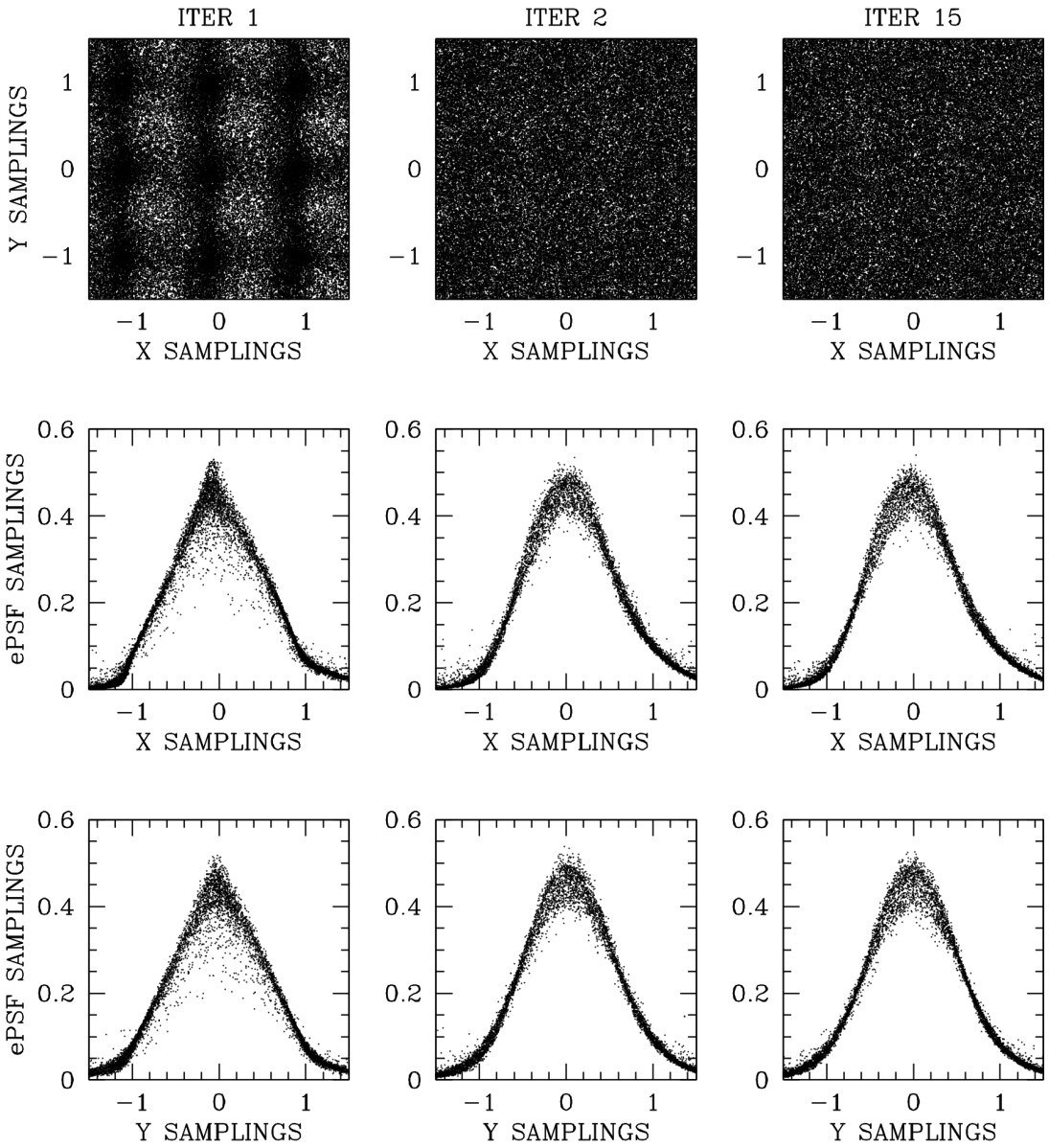

Figure 5.3. Effective-PSF samplings at the first (left-hand column), second (middle column) and last (right-hand column) iteration. On the top-row panels we show the location of the estimated value of the PSF with respect to the centre of the stars, placed at (0,0). At the beginning the star position was computed using the photocentre. From the second iteration, the sampling becomes more uniform. On the middle- and bottom-row panels we show the ePSF profile along the x and y axes for a thin slice with $|\ \Delta y\ |<0.01$ and $|\ \Delta x\ |<0.01$, respectively. In all panels we plotted only 10% of the available points, for clarity.

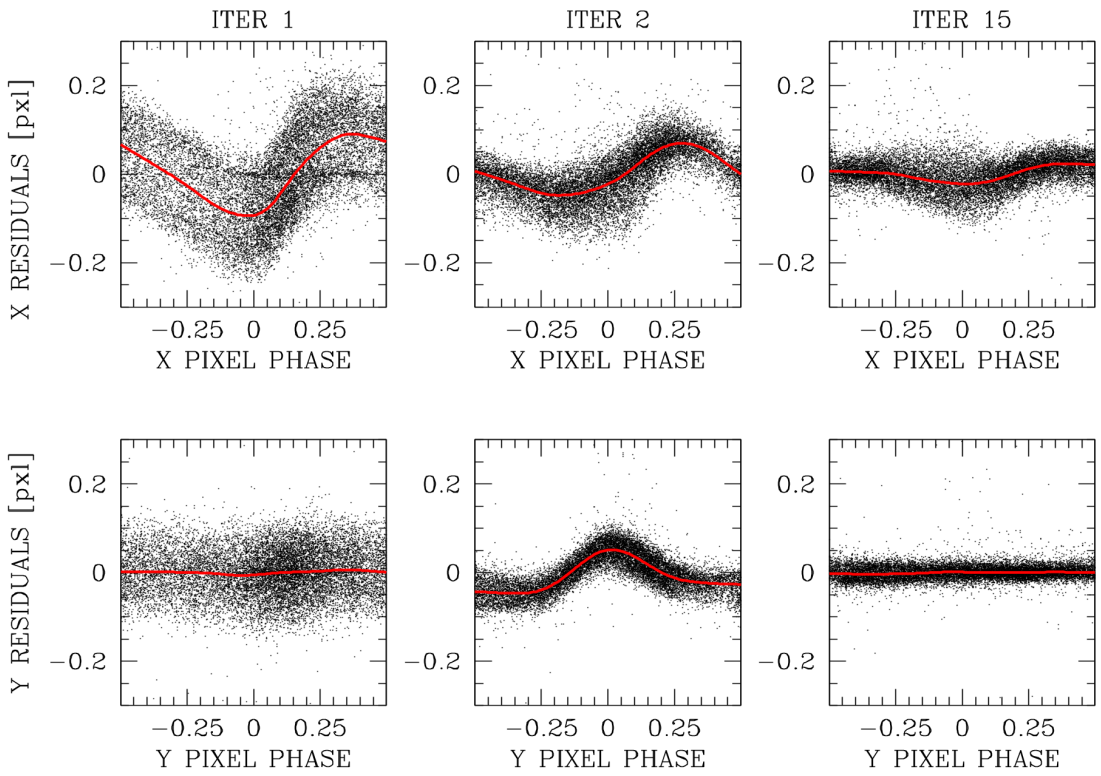

Figure 5.4. Pixel-phase errors progression. On the left-hand column we show the first, in the middle column the second and in the right-hand column the last iteration of the ePSF modelling. In the top row we show the pixel-phase errors along the x axes, in the bottom row the errors along the y axes. As in Fig. 5.3, we plotted only 10% of the points.

- The available ePSF was used to measure an improved position and flux for the stars in each image.

The whole procedure was iterated 15 times, after which we noticed that the overall improvements were negligible (i.e., the pixel-phase errors did not change from one iteration to the next). The final ePSF was a 21×21 array of points that maps the 5×5-pixel region around a star (as in AK00, our ePSF model was supersampled by a factor of 4).

In Fig. 5.3 and 5.4, we show the result of our procedure. At the beginning, the ePSF sampling is not homogeneous and the shape of the ePSF is not well constrained. Even in the second iteration, the sampling began to improve and the ePSF became smoother. The same behaviour can be seen in the pixel-phase errors. Note that the pixel-phase errors appear to be behaved along the y axes rather than the x axes. However, it is not clear whether the available pixel-phase sampling simply allows us to see the errors in x better than those in y. Again, when the *Kepler* PSF-characterisation data set becomes public, it will allow for a much better characterisation and verification of the PSF.

5.3.2.1 Comparison with *Kepler*-main-mission PRFs

We investigated whether our *K2*/C0 ePSF is broader than the *Kepler*-main-mission PRF (Bryson et al. 2010). The broadening is expected because of the *K2* pointing jitters larger than those in

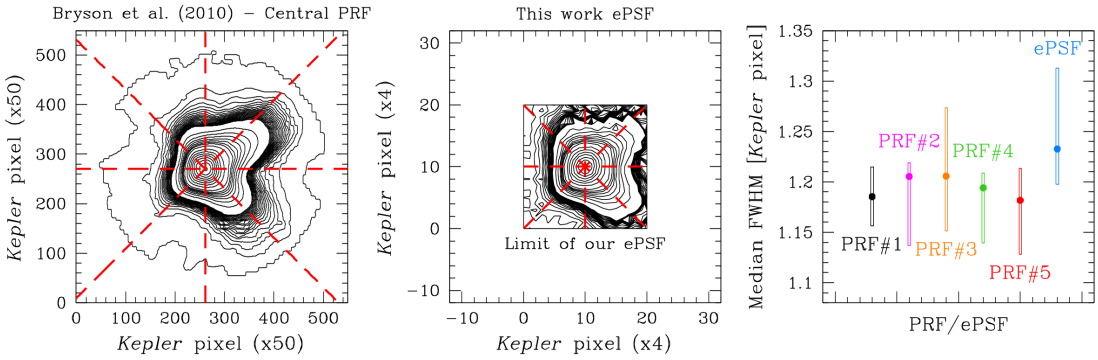

Figure 5.5. FWHM analysis. In the left-hand and middle panels, we show a contour representation of channel-81 central PRF and our average ePSF, respectively. The red dashed lines show the direction along which we measured the FWHM (−45, 0, 45 and 90 deg). The PRF and the ePSF are plotted with their original supersampling factor (50 and 4, respectively) but their size in the images are the same (in real *Kepler* pixels). It is clear that our ePSF is limited to the centre part, due to the data set used that was not designed to model it. In the right-hand panel, we show in different colours the median of these FWHM values for the five PRFs (black, magenta, orange, green and red) and for our *K2*/C0 ePSF (azure). The rectangle around each point shows the minimum-to-maximum range of the FWHM values along the considered directions.

the main mission.

We measured the full-width at half-maximum (FWHM) of the five channel-81 PRFs (one for each corner and one for the central region of the CCD) and that of our average ePSF along different directions. In Fig. 5.5, we show a contour representation of our ePSF and the central PRF of Bryson et al. (2010). The ePSF size in this representation is the same as for the PRF (in *Kepler* pixels). Our ePSF is limited to a small region around the centre and does not model the ePSF wings, as the crowding in the studied super-stamp does not allow the modelling of the ePSF wings. In the right-hand panel of Fig. 5.5 we show the median FWHM values for the PRFs/ePSF. We found that our *K2*/C0 ePSF is broader than the *Kepler*-main-mission PRFs.

5.3.3 Perturbed ePSF

The basic assumption of the original AK00 method is that the ePSF is constant in time and identical for all the images. This is of course an ideal condition and –at some level– it is never the case; surely not for the *HST* or for any other instrument we have used. There are also other subtle effects. The selection of a uniformly distributed subsample of images in pixel-phase space could have introduced some biases. For example, some of the dither pointings in the less-populated regions of the pixel-phase space could have been taken while the telescope was still in motion, resulting in a more 'trailed' ePSF than the average ePSF. In any case, as a working hypothesis, and having detected no obvious trailed images in the subsample that we selected for the ePSF determination, we proceeded under the approximation that these effects are not larger than the general, ePSF variations as a function of time. Indeed, the shape of the *Kepler* ePSF clearly changes over time, as one can infer in Fig. 5.3 from the vertical broadening of the ePSF around the centre (rightmost middle and bottom panels).

Figure 5.6 illustrates the temporal variation of the PSF. We colour coded the samplings of the final ePSF (top panels) according to the epoch of observation (see bottom panel). There are clear trends that are not simply monotonic.

In order to suppress as much as possible the impact of the temporal dependences of the

ePSF we introduced a perturbation of the average ePSF. This perturbation of the ePSF was first described in Anderson & King (2006), and can be summarised as follows. In each image, we fitted and subtracted the current ePSF model to high SNR stars. We then modelled (with a look-up table) the normalised residuals of these ePSF fits and added these tabulated residuals to the initial ePSF to obtain an improved ePSF model (for a more recent application and a detailed description of the method see Bellini et al. 2014).

In Fig. 5.7 we show an example of the time-variation adjustments of the average ePSF for two images. The improvements in position and flux of the perturbed ePSFs over a constant ePSF for all the 2422 images are quantified in Fig. 5.8. We measured position and flux of all sources in each exposure with and without perturbing the ePSF. The PSF-fit process (a least-squares fit) is achieved with a program similar to the IMG2XYM_WFI described in Anderson et al. (2006) that measure all sources, from the brightest to the faintest (up to a minimum-detection threshold set by the user) objects, in seven iterations. From the second iteration ahead, the fitting procedure is also performed on neighbour-subtracted images, in order to converge on reliable positions and fluxes for close-by objects. We then made two master frames, one for each of the two different approaches, by cross-identifying the stars in each of our 2422 images. We computed the 3σ-clipped median value of the following quantities: QFIT[7], the 1D positional rms, and the photometric rms. These values were calculated in 1-mag bins and, for an appropriate comparison, we used the same set of stars for the two samples. In most cases, we found that the difference between the use of perturbed or unperturbed ePSF is not negligible. Using the perturbed rather than the average ePSF to measure position and flux of a star in an image improves the PSF fit because the former is a representation of a star in that particular image, while the latter is the representation of a star averaged on the entire C0.

In the following, we assume that the spatial variation of the ePSF across the super-stamp region in channel-81 detector where NGC 2158 and M 35 are imaged is negligible; therefore, we will use only one ePSF model per image. A substantial improvement to the ePSF will be achieved when the PSF characterisation data are made available, so that we can properly account for the spatial variability.

5.4 Photometry in *K2* reconstructed images

The main purpose of this effort is to extract precise photometry from main-mission and *K2*-mission pixel data for sources in crowded fields and at the faintest end. These two issues are very closely related, since each 4 arcsec $\times$ 4 arcsec pixel includes many faint sources that we need to take into account. Because of this crowding, classical aperture photometry has major obvious limitations.

Different authors showed that photometry on neighbour-subtracted images leads, on average, to a better photometric precision than on the original images (see, e.g. Montalto et al. 2007 and reference therein). By subtracting a star's neighbours before measuring its flux, it is possible to avoid including (or at least to reduce the impact of) light that could contaminate the true flux of the target. The knowledge of positions and flux of all sources in the field is therefore fundamental to our approach.

In order to obtain the best photometric precision with *K2* data, we used the same method as described in Nardiello et al. (2015, see also Section 4.2) to which we refer for a more detailed description. This method makes use of accurate PSF models for each exposure and of a (ground-based) input list to disentangle from the flux of a given star the contribution of its close-by sources. The more complete the input list with all detectable objects in the field, the better will be the final result of the method. A corollary is also that the transformations of the input-list positions and fluxes into the individual-exposure reference system need to be known with high

[7]The QFIT represents the absolute fractional error in the PSF-model fit to the star (Anderson et al. 2008). The lower the QFIT, the better the PSF fit.

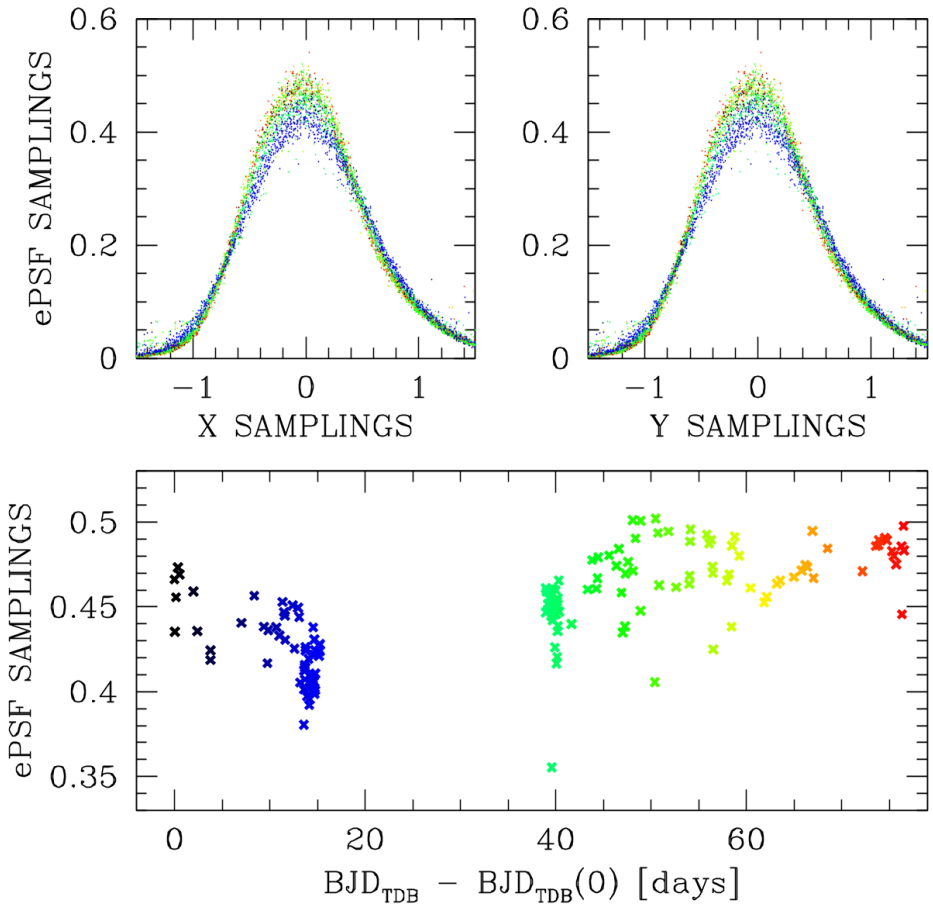

Figure 5.6. Time variation of the ePSF shape in the 154 images we used for the modelling. In the bottom panel, the central-peak value of the ePSF (interpolated from the samplings) as a function of the time interval relative to the first-image epoch. In the top-left and top-right panels we show the ePSF samplings as in the right-hand column of Fig. 5.3, using the same colour codes for the time of image acquisition.

accuracy, as well as the PSF, in order to subtract the neighbours as well as possible. In the following we provide the adopted key ingredients.

5.4.1 The Asiago Input Catalogue

Our input list is described in great detail in Nardiello et al. (2015). It comes from a set of white-light (i.e., filterless) observations collected at the Asiago Schmidt telescope. It includes 75 935 objects. At variance with Nardiello et al., we used all stars measured in white light, and not only those found in both white-light and *R*-filter lists (see section 3.5 of their paper). Hereafter, we will refer to this catalogue as the *Asiago Input Catalogue*, or AIC, which is available at the 'Exoplanet and Stellar Population Group' (ESPG) website[8].

The AIC was constructed by measuring the position and flux of each source found in the Schmidt stacked image via PSF fitting. This input list was then transformed into the photometric

[8]http://groups.dfa.unipd.it/ESPG/M35NGC2158.html

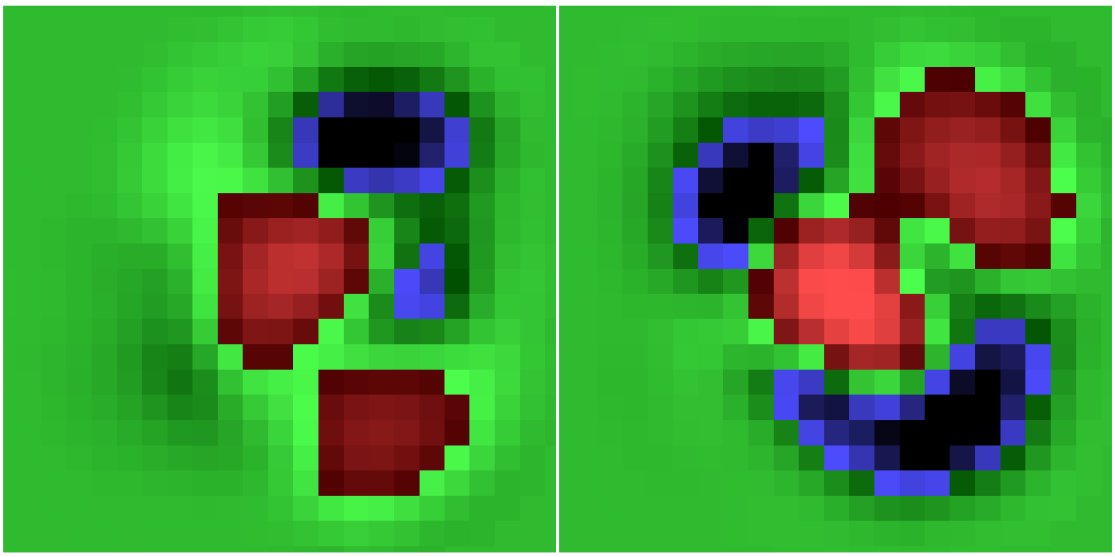

Figure 5.7. Difference between the average ePSF and the perturbed ePSF for an image at the beginning (left) and at the end (right) of C0. In these two examples, the variation ranges between ∼−0.5 per cent (blue colour) and ∼1.4 per cent (red colour) of the total flux.

system of a reference image (among those of the Schmidt data set). The catalogue was purged for various artefacts, such as PSF bumps and fake detections along the bleeding columns. The purging is not perfect and it is a compromise between excluding true, faint stars around bright objects, and including artefacts in the catalogue. Of the 75 935 sources included in the input list, ∼77% could be measured reasonably well with the *K2* data set.

The stacked Schmidt image has higher angular resolution than the *Kepler*/*K2* images, allowing us to locate faint sources whose flux could pollute the pixels of a nearby star. The relative astrometric accuracy of the AIC is also sufficiently accurate to allow us to pinpoint a star in any given *K2* image with an accuracy down to about 20 mas (0.005 *Kepler* pixel). Details about the absolute astrometry, the stacked images, and other information of the AIC can be found in Nardiello et al. (2015).

5.4.2 Photometry with and without neighbours

The procedure for LC extraction is the same as in Nardiello et al. (2015) and can be summarised as follows. For each star in the AIC, hereafter 'target star', we computed six-parameter, local linear transformations to transform the AIC position of the target into that of each individual *K2* image. In order to compute the coefficients of the transformations, we used only bright, unsaturated, well-measured target's neighbours within a radius of 100 pixels (target star excluded). If there were not at least 10 neighbour stars within such radius, we increased the searching area progressively, out to the whole field. Local transformations were used to minimise the effect of the geometric distortion, since it does not vary significantly on small spatial scales.

These reference stars were also used to transform the AIC white-light magnitude of the target into the corresponding instrumental *K2* magnitude in each given exposure. The AIC magnitudes in white light and our $K_{\rm P}$ instrumental magnitudes are obtained from instruments with a rather similar total-transmission curve and, as a first approximation, we can safely use a simple zero-point as photometric transformation between AIC and *K2* photometric systems.

We extracted the photometry from the original and from the neighbour-subtracted *K2* images.

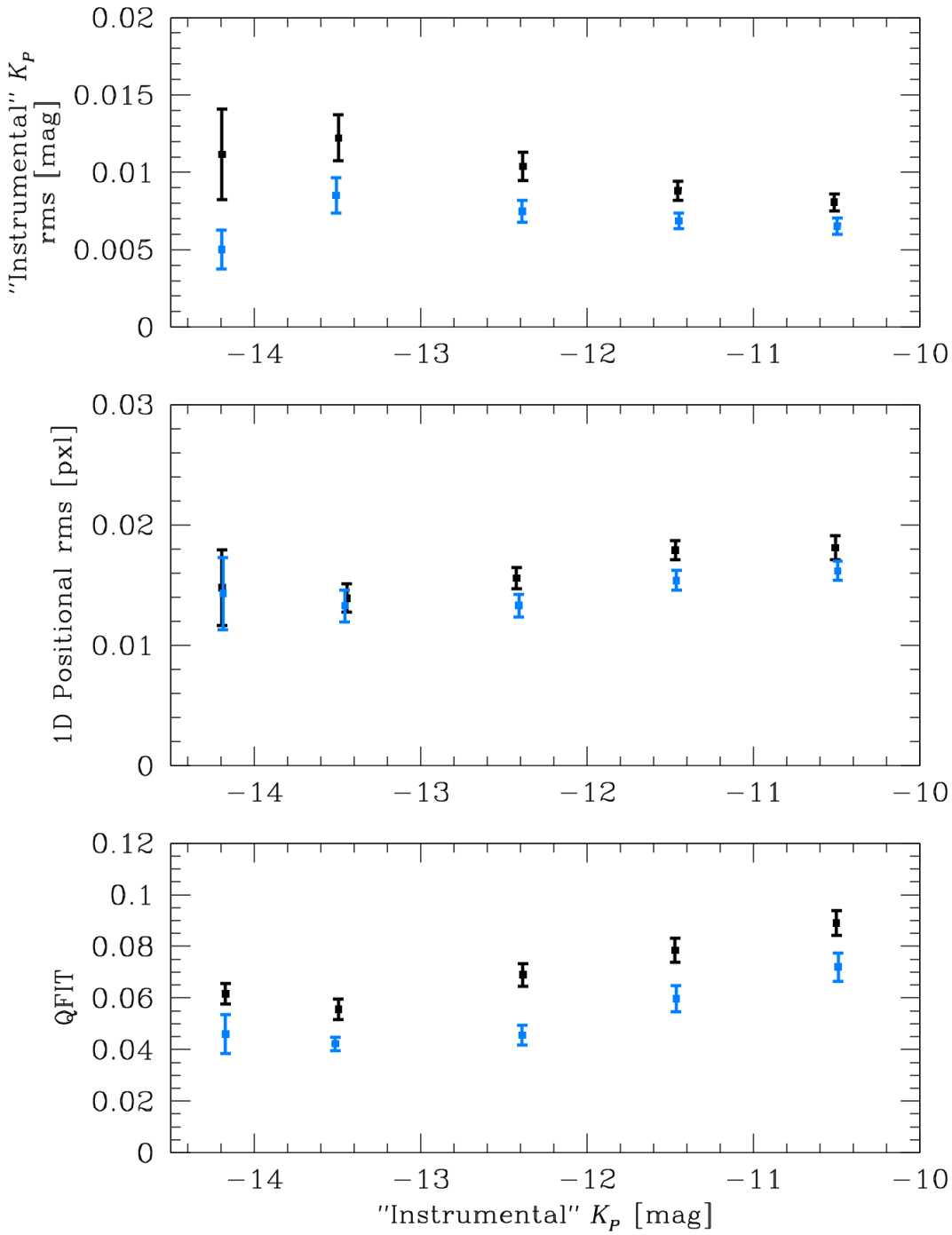

Figure 5.8. QFIT (bottom), 1D positional rms (middle) and photometric rms (top) as a function of the 'instrumental' magnitude of the master frame with (azure points) and without (black points) perturbing the average ePSF to account for the time-dependent variations. Each point represents the median value in 1-mag bins. The error bars represents the 68.27^{th} percentile of the distribution around the median value divided by $\sqrt{N}$, with N number of points. The instrumental magnitude in each single catalogue is defined as $-2.5 \times \log(\sum \text{counts})$, where $\sum$ counts is the sum of the total counts under the fitted PSF. Since we used the column `FLUX` while building the full-frame channel images, these counts are actually fluxes (for this reason we used the double quotes in the label). Hereafter, we will omit the double quotes in the text.

The neighbour-subtracted images were created by subtracting from the original images the flux-scaled perturbed ePSF of all AIC sources within a radius of 35 *Kepler* pixels (∼2.3 arcmin) from the target star. We postpone the discussion about the quantitative improvements in the photometry by using neighbour-subtracted images instead of the original images to Sect. 5.7.1.

On the neighbour-subtracted images, the target flux of each AIC object was measured using aperture photometry with four aperture sizes (1, 3, 5 and 10 pixels radius) and using ePSF-fit photometry. On the original images, we used only 3-pixel-aperture and ePSF-fit photometry. These fluxes were stored in a LC file, which also contains other information such as the KBJD.

5.5 Photometric calibration into the $K_{\rm P}$ System

In order to calibrate the instrumental magnitudes we extracted from the individual *K2* exposures to the *Kepler* Magnitude System ($K_{\rm P}$), we determined and applied a simple local zero-point. For each photometric approach (1, 3, 5, 10 pixels aperture and PSF), we made a catalogue with absolute positions from the AIC and with magnitudes obtained from 3σ-clipped median values of the *K2* instrumental magnitudes as measured in each LC (when available). We then cross-matched these catalogues with the EPIC obtained from the MAST archive. We computed the zero-points as the 3σ-clipped median value of the difference between our magnitudes and the EPIC $K_{\rm P}$ magnitudes. We used only those bright, unsaturated stars that in our catalogue are within 3 mag from the saturation and for which the $K_{\rm P}$ magnitude in the EPIC was obtained from '*gri*' photometry. We chose this specific photometric method among the different methods adopted to compute the $K_{\rm P}$ magnitude in the EPIC due to the larger number of sources in common between this EPIC subsample and our well-measured-star sample. As in Aigrain et al. (2015) and Lund et al. (2015), the zero-points of our photometric methods we found are between 24.7 (1-pixel aperture) and 25.3 (the other photometric methods).

5.6 Detrending of *K2* light curves

The unstable spacecraft pointing results in a well-defined motion of the stars across the pixel grid. A combination of intra- and inter-pixel sensitivity variation leads to a correlation between this motion and the 'raw' flux of each star that must be corrected in order to increase the *K2* photometric accuracy and precision. Different methods have been developed to correct such systematic effect, e.g., the self-flat-fielding approach of Vanderburg & Johnson (2014), the Gaussian process of Aigrain et al. (2015) or the simultaneous fit for all systematics of Foreman-Mackey et al. (2015).

In order to detrend the LCs from the drift-induced effects, we took into account all usable channel-81 exposures collected during the entirety of C0, including those taken during the first part of the campaign, when the fine guiding was still in progress (which caused the stars to be shifted by up to 20 pixels from their average position; see Fig. 5.2). This is important, since the number of points to be used for the detrending increases, and it could also be useful to detect variable stars with periods of ∼35 d (the duration of the C0 after the second safe mode). Briefly, our correction was performed by making a look-up table of corrections and applying it with simple bi-linear interpolation.

An overview of our detrending approach is shown in Fig. 5.9. For each target star, we made a model of the raw LC trend, normalised by its median flux (panel a), by applying a running-average filter with a window of ∼10 h. The model (panel b) was then subtracted from the raw LC with the aim of removing the intrinsic stellar variability. In this way, the model-subtracted LC (panel c) reflects the systematic effect originated from the motion of the spacecraft. The window size of the running-average filter was chosen as a compromise between our attempt of avoiding the removal of the positional trend and still being able to model short-period variables.

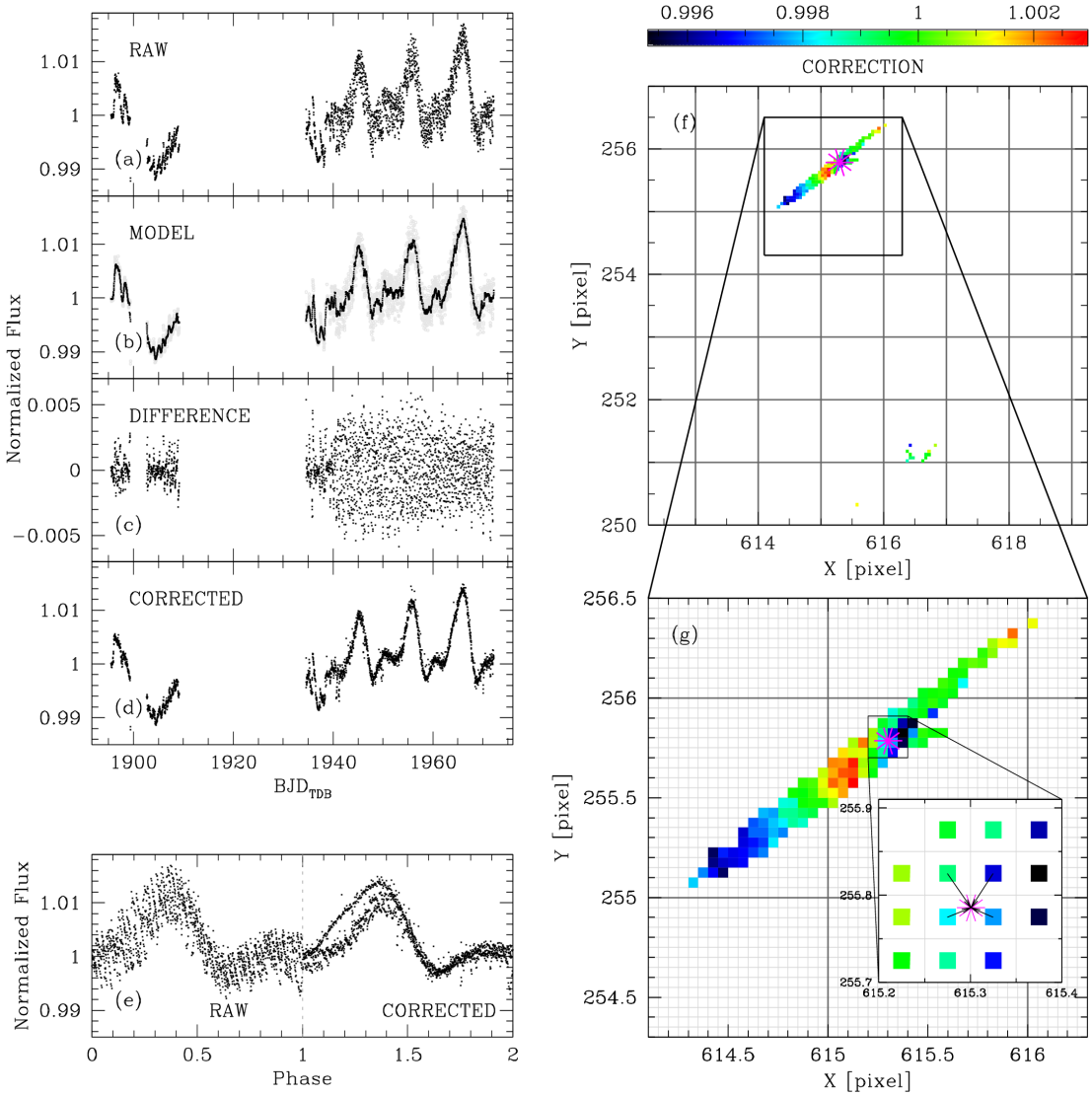

Figure 5.9. Left: 3-pixel-aperture LC of star no. 1881 (EPIC 209183478) after each step of our correction. From panel (a) to (d): raw LC normalised to its median flux; LC model (black points) put on top of the raw LC (light-grey points); model-subtracted LC; final detrended LC. In panel (e) we show the comparison between the phased (with a period of ∼10.6 d) LC before (left) and after (right) the correction. It is clear that the drift-induced scatter in the LC is reduced and more details arise, e.g., the LC amplitude of this object changed during the C0. Right: Outline of our correction. In panel (f) we show the cell and grid-point locations around the star no. 1881 loci on the channel 81 over the entire C0. The thick, dark-grey lines mark the pixel boundaries. The magenta ∗ marks the star location on the channel at a given time. The squares represent the median values of the model-subtracted flux in each of the 0.05×0.05-pixel-square bins in which each pixel is divided, colour-coded accordingly to the colour bar on top. In panel (g) we zoom-in around the bulk of the points to highlight the sub-pixel elements of the grid (thin, light-grey lines). For the star position at a given time, we used the four surrounding grid points to perform the bi-linear interpolation (sketched with the arrows) and compute the correction.

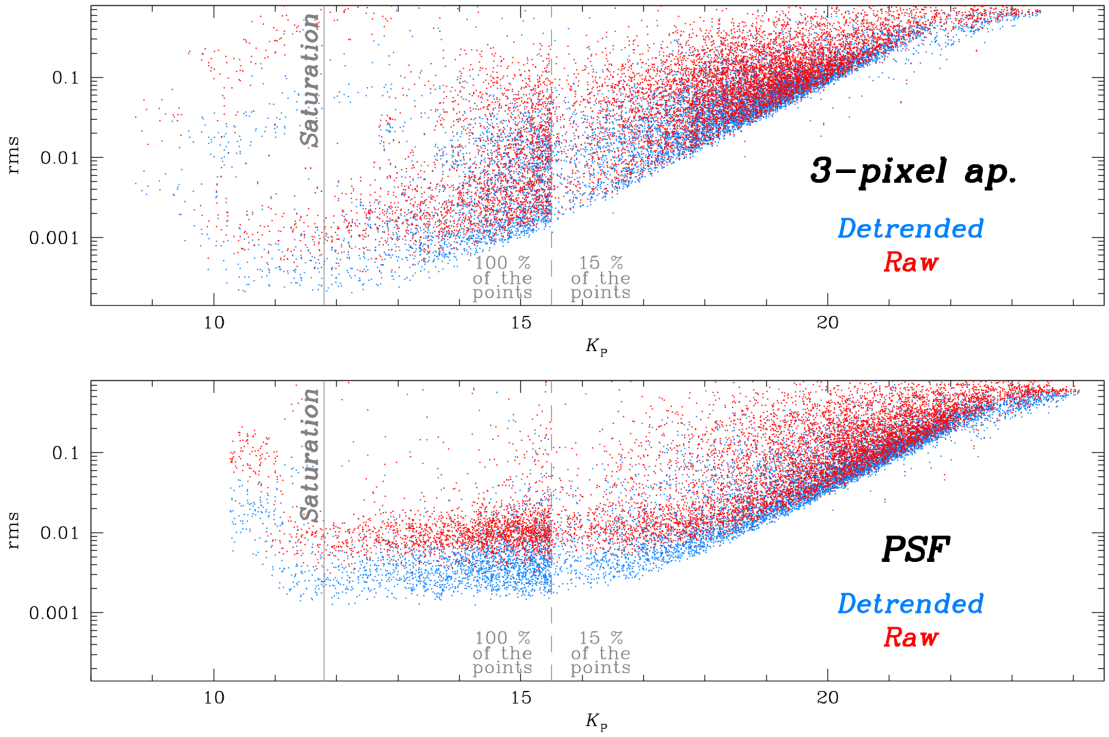

Figure 5.10. Photometric rms as a function of the K_P magnitude before (red points) and after (azure points) applying our detrending procedure. We plot only the neighbour-subtracted photometry from the two measurements that show the best rms in the bright (3 pixels aperture, top panel) and faint (PSF, bottom panel) regime. For K_P>15.5 (vertical, grey dashed line) we show only 15% of the points for clarity. The vertical, grey solid line is set at the saturation threshold K_P∼11.8.

Each pixel into which a given star fell during the motion was divided into an array of 20×20 square elements and, in each such element, we computed the 3.5σ-clipped median of the model-subtracted LC flux. The grid is sketched in panels (f) and (g) of Fig. 5.9. For any location on the CCD, the correction was performed by applying a bi-linear interpolation between the surrounding four grid points. The correction was not always available, because for some grid elements there are not enough points to compute the correction. In these cases, no correction was applied.

The whole procedure was iterated three times, each time making an improved LC model by using the LC corrected with the available detrending solution. In Fig. 5.9 we show the results of the final iteration of our procedure.

Panel (e) of Fig. 5.9 shows a direct comparison of the folded LC before (left) and after (right) the correction. The rms is improved and allows us to see more details in the LC.

One advantage of our LC-extraction method is a more robust position measurement. Indeed, as described in Sect. 5.4, we transformed the position of a target star as given in the AIC into the corresponding image reference system by using a subset of close-by stars, target excluded, to compute the coefficients of the six-parameter linear transformations. The local-transformation approach reduces (on average by a factor N^{-1}, where N is the number of stars used) most of the systematic effects that could harm the stellar positions (e.g., the uncorrected geometric distortion).

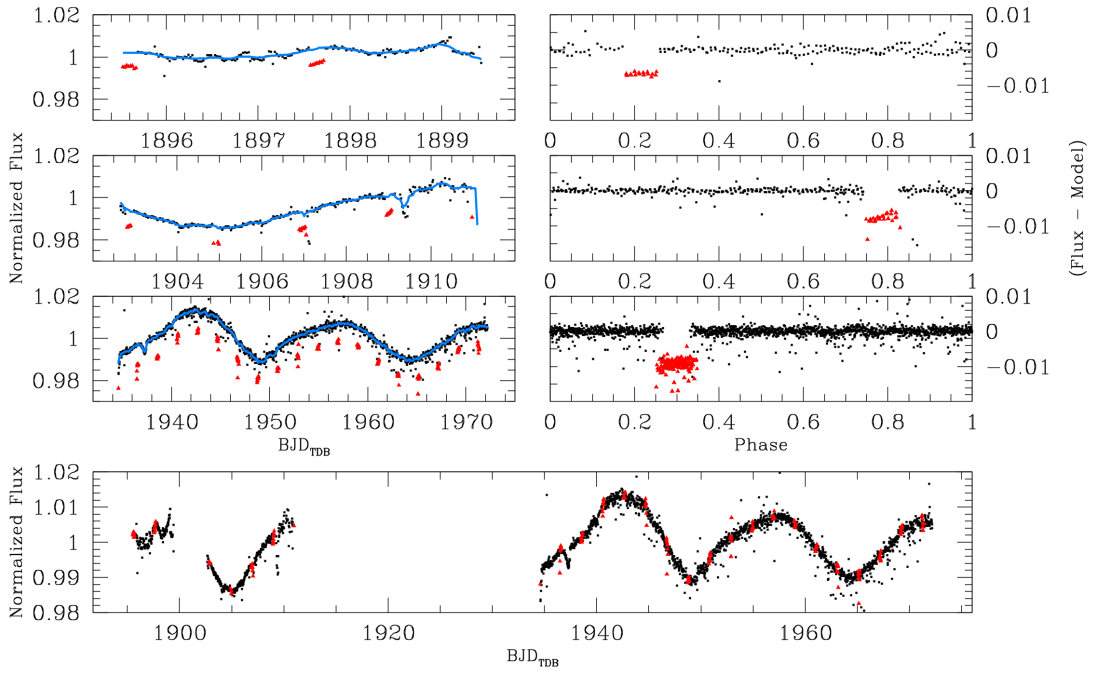

Figure 5.11. Example of an LC (AIC no. 8600, 5-pixel-aperture photometry) affected by the flux-drop effect described in Sect. 5.6.1. From top, in the first-row panels we show the first subseries (before the first safe mode) of points of the C0/channel-81 LC (left) and the corresponding phased LC with a period of 2.04 d (right). In the second and third rows we show the same as above but for the second (between the first and the second safe modes) and third (after the second safe mode) subseries of the LC and the phased LC. The black dots represent the unaffected points, the red triangles are the photometric points affected by the flux drop. The azure line is the LC model. Note that the phase at which the flux drop occurs is not the same in the different parts of the LC, meaning that this effect could be related to the instrumentation, and that it is reset after each break in the C0. Finally, in the bottom panel we plot the corrected LC.

The LC detrending is critical both to the removal of the spacecraft-related systematics that degrade the *K2* photometric precision and to pushing *K2* performance as close as possible to that of the original *Kepler* main mission. In Fig. 5.10 we show the rms (defined as the 3.5σ-clipped 68.27^{th}-percentile of the distribution about the median value of the points in the LC) improvement after the detrending process for the 3-pixel-aperture and PSF photometry on neighbour-subtracted images. The rms was calculated on the normalised LC, i.e. after the LC flux was divided by the 3.5σ-clipped median value of all the flux measurements. As we will see in subsection 5.7.2, these two photometric methods are the best-performing methods at the bright- and faint-end regime, respectively. The improvement is greater for bright stars, i.e. stars with high SNR and better-constrained positions; while for faint stars the effect is lost in the random noise.

5.6.1 A previously unknown 2.04-d periodic artefact

Several LCs turned out to exhibit a periodic drop in their fluxes that we have not seen described anywhere. These drops are rather sharp and resemble boxy transits; we illustrate them in Fig. 5.11. The period of this effect is ∼2.04 d, and the drops last for exactly six images, for each

of the non-interrupted subseries within C0. Not all the stars in the affected images show the drop feature.

We extensively investigated the affected and unaffected stars on individual *K2*/C0/channel-81 images and found that the effect could be column-related. The amount of drop in the flux is not always the same and it correlates with magnitude. We have not found any description of such an effect either in the *Kepler* manual or in the literature.

We suspect that it might be due to an overcorrection in correspondence of mis-behaving columns. This overcorrection might be the result of electronic activities related to the periodic momentum dump of the two remaining reaction wheels through thruster firings; which happens every two days (Howell et al. 2014; Lund et al. 2015). For example, it could be a change in the reading rate.

Another possibility is that this effect can be originated by a non-identical *Kepler*-pipeline processing of contiguous TPFs that can create some un-physical discontinuity. Such 2.04-d periodic effect could only be detected when dealing with more than one TPF at a time, as we did in our reconstructed-image approach.

Lacking more engineering data and detailed knowledge of the on-board pre-reduction pipeline, we have limited ourselves to simply describing and correcting these effects empirically. We first made a model of the LC trend (by applying a running-average filter with a window of ∼6 h) and computed the median value of the model-subtracted LC flux for affected and unaffected data points. If the difference between these median values was greater than the model-subtracted LC rms (computed using only the unaffected points), we marked the LC as flux-drop-affected, and corrected it. The correction to add is computed as the difference between the model of the LC with only the unaffected points and the model obtained using only the flux-drop-affected points (see Fig. 5.11).

The drawback of our correction is obviously that any true variable star with a significant flux drop every 2.04 d was considered as flux-drop affected and corrected accordingly. Of course, since this flux-drop is not periodic across safe-mode subseries, it is possible to distinguish these events from true eclipses.

5.6.2 The role of ePSFs in *Kepler*/*K2* images

The ePSF is not only more suitable to performing photometry in crowded regions and for faint stars, but it can also be used as an additional diagnostic tool to discern among exposures that are most affected by some systematic effects, such as the drift motion of the spacecraft. In the following we show that, by taking advantage of all the information that we have from the ePSFs adjusted for each exposure, we can also select the best exposures (that correspond to points in the LCs) to search for variability (Sect. 5.8.1).

In Fig. 5.12, we show an outline of our best-exposure selection for a variable-candidate LC (AIC star no. 9244). It is well known that *K2*/C0 data contain a periodic, systematic effect every ∼6 h, related to the thruster-jet firings used to keep the roll-angle in position. Indeed high SNR stars show a well-defined periodic effect every ∼0.2452 d (and at its harmonics). In the top-left panel of Fig. 5.12 we show the hand-selected points in the phased LC with a period of ∼0.2452 d, while in the top-right panel we show the corresponding location of such points during C0. By phasing different LCs with this period, we noticed that there is one group of points (red, solid triangles) that is more scattered than the others. These points are associated with the thruster-jet events. The remaining points, marked with different colours and shapes, represent different portions of the LC. The less populated groups (black, solid squares) were taken during the first part of the campaign; while the more populated clumps (green dots) were taken during the second part of the C0. The remaining outliers (azure, open circles) are those points obtained during the coarse pointing of the spacecraft, flagged in the TPFs accordingly. In practice, we discarded all points corresponding to the first part of C0, and the points collected during the thruster-jet events and coarse pointing.

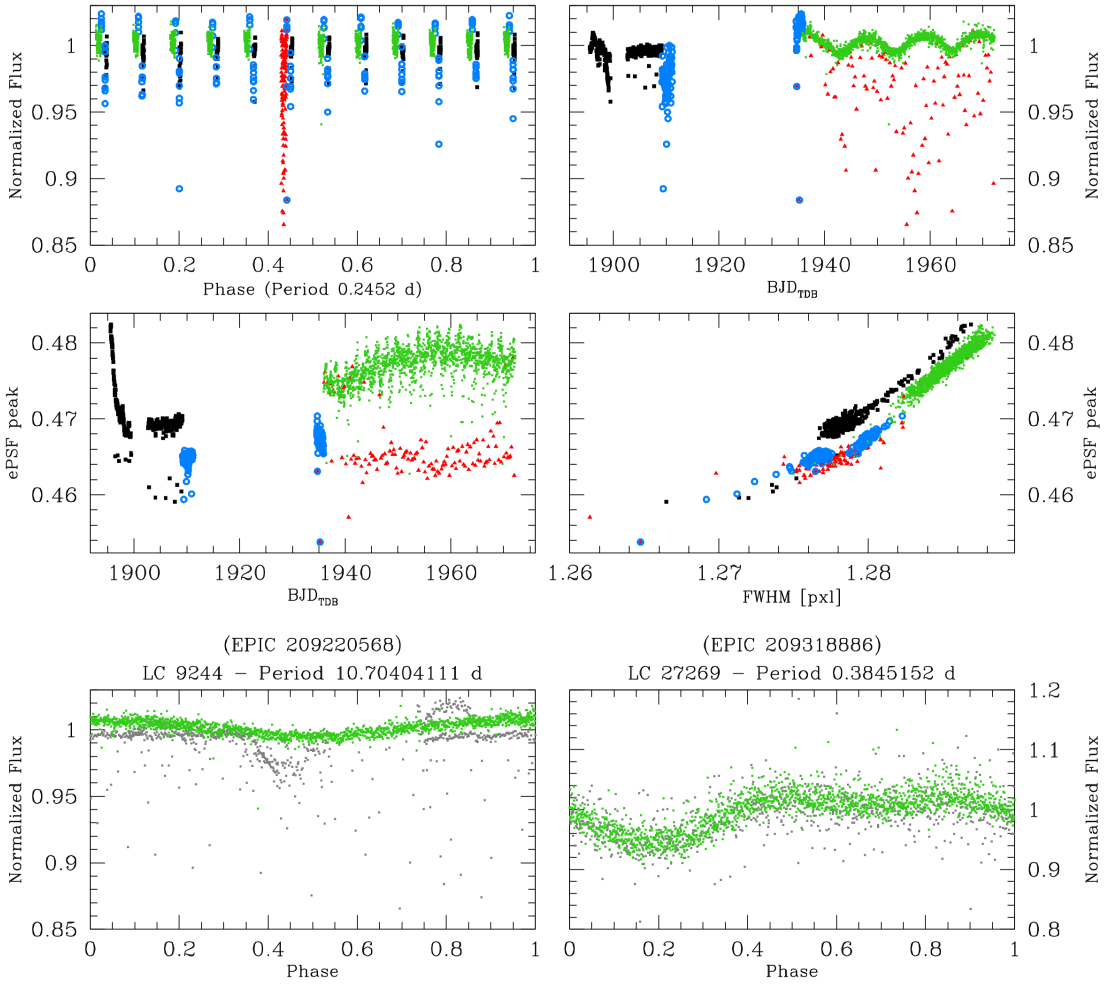

Figure 5.12. Clean LC definition. In the top-left panel, we show the phased LC with a period of 0.2452 d for the object no. 9244 in the AIC. We mark with black filled squares the points obtained before the second safe mode during the C0 observations and with azure, open circles the points corresponding to the 'coarse pointing' flag in the original TPFs. The red triangles highlight the exposures that are associated to a thruster-jet event. Finally, with green dots we show the best 1629 out of 2422 points (exposures) for the LC analysis. In the top-right we show the normalised flux as a function of the time for the same LC, with the points colour-coded as before. In the middle-left panel we plot the peak value of the perturbed ePSF of each exposure as a function of time. In the ePSF peak–FWHM plane (middle-right panel), it is also clear that there is a correlation between every effect that could harm the observations and the ePSF. This is a hint of the usefulness of the ePSF parameters as a diagnostic tool. Finally, in the bottom panels we show the LC for the bright object illustrated above (left) and for a fainter star (right, AIC no. 27269) in which we plot with green and grey dots the good and the bad points, respectively.

We found very good agreement between such point selection and the ePSF (middle-left panel) peak and FWHM (middle-right panel). For example, the exposures taken during a thruster-jet event have a less-peaked ePSF because the exposure is blurred during the long-cadence integration time. Hereafter, we use the adjective '*clean*' to define a LC based on the stable part on the second half of the Campaign (green points in Fig. 5.12). We run our variable star finding algorithms only on the clean LCs.

5.7 Photometric precision

We used three different parameters to help us to estimate the photometric precision:

- *rms* (defined as in Sect. 5.6);
- *p2p rms*: he point-to-point rms (p2p rms) is defined as the 3.5σ-clipped $68.27^{\rm th}$-percentile of the distribution around the median value of the scatter (the difference between two consecutive points);
- *6.5-hour rms*: the *6.5-hour rms* is defined as follows. We processed each available LC with a 6.5-h running-average filter, and then divided it in 13-point bins. For each bin, we computed the 3.5σ-clipped rms and divided it by $\sqrt{12}$ ($\sqrt{N-1}$, with N the number of points in each bin). The 6.5-hour rms is the median value of these rms measurements.

All three parameters have been calculated on the normalised LC.

Our PSF-based, neighbour-subtracted technique has been specifically developed to deal with crowded regions and faint stars. Therefore, we expect substantial improvements with respect to what is in the literature in these two specific regimes. In the following, we will demonstrate the effectiveness of our new approach.

5.7.1 Photometry on images with and without neighbours

By subtracting stellar neighbours before measuring the flux of a given star, we can obtain performance comparable with that achieved by others in the literature, but in more crowded regions. In general, within a single 4×4 arcsec^2 pixel, there can be more than one source that contribute to the total flux. Therefore, we expect the neighbour-subtraction method to be useful not only in stellar clusters or fields in the Galactic bulge, but also in relatively-lower-density regions.

To demonstrate this assertion, we selected two samples of stars: a 'crowded', sample centred on NGC 2158, and an 'isolated' sample, which comes from five different regions where the stellar density is lower. The two samples contain the same number of sources. We computed the LC rms for a 3 pixels aperture and for PSF photometry with and without subtracting stellar neighbours (Fig. 5.13).

Without removing stellar neighbours, the light of close-by stars that falls within the aperture increases the target flux, alters the faint-end tail of the rms trend (naturally, the problems becomes larger for larger apertures). The effect is more evident in crowded regions, in particular when using aperture photometry. For the 3-pixel aperture photometry, in the crowded region the limiting magnitude on the original images is $K_{\rm P}$ ∼18, to be compared with the $K_{\rm P}$ ∼22 limiting magnitude in neighbour-subtracted images of the same field (second-to-the-last panels in Fig. 5.13). In summary, in crowded regions, by using the neighbour-subtracted images, we obtained a more reliable stellar flux and gained about four $K_{\rm P}$ magnitudes for the 3-pixel-aperture photometry. Furthermore, for both aperture and PSF photometry, we have a lower rms for the LCs, and the bulk of the LC-rms distribution as a function of magnitude looks sharper. In conclusion, hereafter we will consider only neighbour-subtracted LCs.

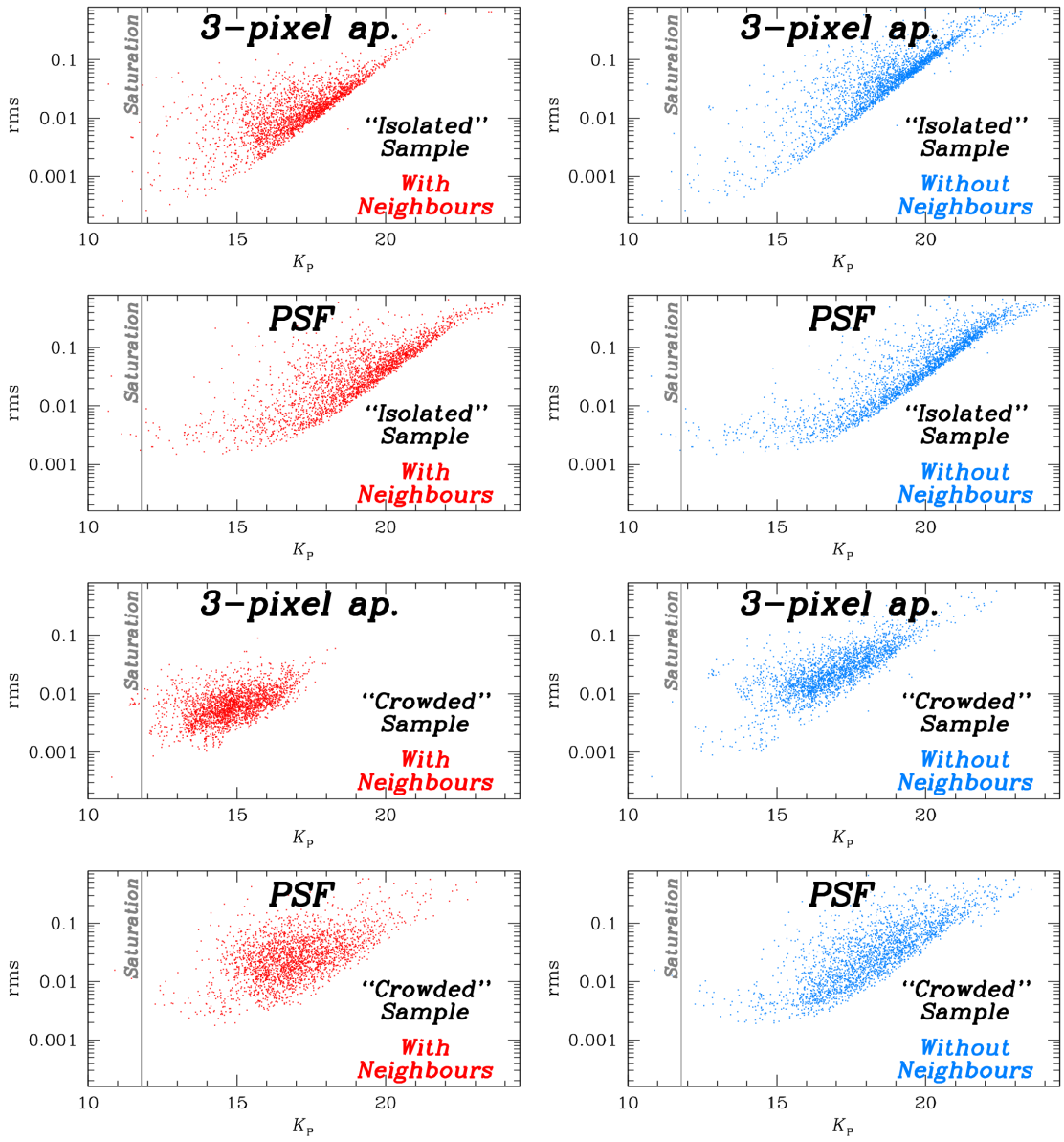

Figure 5.13. Photometric rms of LCs extracted from the original (red points in left panels), and the neighbour-subtracted (azure points in the right panels) images as a function of the K_P magnitude. We show the rms trend for the 'isolated' (the first and second rows from top) and the 'crowded' (the third and fourth rows) samples, defined as described in the text, for LCs obtained using a 3-pixel aperture and the PSF. The saturation threshold is set at $K_P \sim 11.8$ (vertical, grey solid line).

Table 5.1. Photometric precision of the 3-pixel-aperture- and PSF-based photometry evaluated as described in Sect. 5.7. The values are given in parts per million. We used the clean LCs to compute these quantities. When no stars were found in a given magnitude interval, we inserted a '/' in the corresponding cell.

K_P magnitude interval	3-pixel aperture			PSF		
	rms	p2p	6.5-h rms	rms	p2p	6.5-h rms
8 – 9	4365	1994	840	/	/	/
9 – 10	4550	1915	771	/	/	/
10 – 11	3083	433	101	18231	3918	2054
11 – 12	446	124	44	2636	949	424
12 – 13	744	168	62	3300	1068	459
13 – 14	926	276	97	3200	983	439
14 – 15	1977	585	196	3871	1085	489
15 – 16	5720	1882	633	3988	1274	528
16 – 17	10631	4731	1606	4822	1875	693
17 – 18	21219	9533	3176	7214	3518	1189
18 – 19	40885	19749	6564	14070	7936	2601
19 – 20	76625	41163	13534	32813	18376	6150
20 – 21	159131	89546	29876	71199	40570	13456
21 – 22	327174	179254	71173	153875	89963	30335
22 – 23	487721	282520	109300	309403	179357	73297
23 – 24	606784	412491	140349	468002	292661	114074

Table 5.2. As in Table 5.1, but for 1-, 5- and 10-pixel-aperture-based photometry.

K_P magnitude interval	1-pixel aperture			5-pixel aperture			10-pixel aperture		
	rms	p2p	6.5-h rms	rms	p2p	6.5-h rms	rms	p2p	6.5-h rms
7 – 8	/	/	/	/	/	/	5222	2032	917
8 – 9	/	/	/	3983	1758	802	3640	1230	582
9 – 10	/	/	/	8641	2982	1558	6083	2311	1152
10 – 11	9126	5411	1755	10449	4554	1745	18628	7103	3199
11 – 12	5625	3552	1122	451	116	43	1397	261	87
12 – 13	5594	3461	1098	1023	246	87	2972	1081	437
13 – 14	5589	3482	1113	3959	989	387	10915	3876	1350
14 – 15	5918	3484	1115	7777	2897	1043	15341	6028	2083
15 – 16	6108	3566	1141	13369	5306	1866	24145	10945	3738
16 – 17	6473	3743	1201	21162	8917	3056	44430	21238	7173
17 – 18	8003	4477	1439	39276	17885	6022	84555	43223	14664
18 – 19	13766	7833	2521	69978	36431	12105	170644	91746	34174
19 – 20	30515	17248	5557	141595	77484	26331	285471	134808	69279
20 – 21	66356	37814	12241	299378	158724	63791	404477	185638	87072
21 – 22	141837	83477	27306	432749	225126	97786	528062	289481	116628
22 – 23	301746	173745	66720	591510	359285	128364	587527	373223	138088
23 – 24	447170	287843	106035	687907	511448	147173	/	/	/

5.7.2 Photometry on bright and faint stars

As expected, and as shown by Nardiello et al. (2015) for ground-based data, aperture photometry performs, on average, better on isolated, bright stars, while the PSF photometry gives better results on faint stars. In Table 5.1 and 5.2 we list the rms values in parts per million (ppm) for each of the five photometric methods we adopted.

As can be inferred from these tables, for bright stars, 3-pixel-aperture photometry shows, on average, lower rms than 5- and 10-pixel aperture photometry. The 1-pixel-aperture- and the PSF-based photometry have almost the same trend in the faint star regime ($K_P \geq 15.5$), with the 1 pixel aperture showing a slightly smaller rms for K_P>19, while the PSF photometry performs 2–3 times better on brighter stars. In the following discussion, for faint stars, we prefer to use PSF rather than 1-pixel-aperture neighbour-subtracted photometry, although, on average, equivalent in terms of photometric scatter.

In Fig. 5.14 we show a comparison between the PSF and the 3-pixel aperture photometric methods. It is clear that for K_P>15.5 the PSF photometry performs better than the 3-pixel aperture. For bright stars, the 3-pixel-aperture 6.5-hour rms is below 100 ppm between 10<K_P<14, with a best value of about 30 ppm for stars with 11<K_P<12.5. For stars brighter than K_P∼10, the rms increases, mainly because we are working on heavily-saturated stars. In the faint-end regime, using PSF photometry we obtained 6.5-hour rms 2-3 times better than using a 3-pixel-

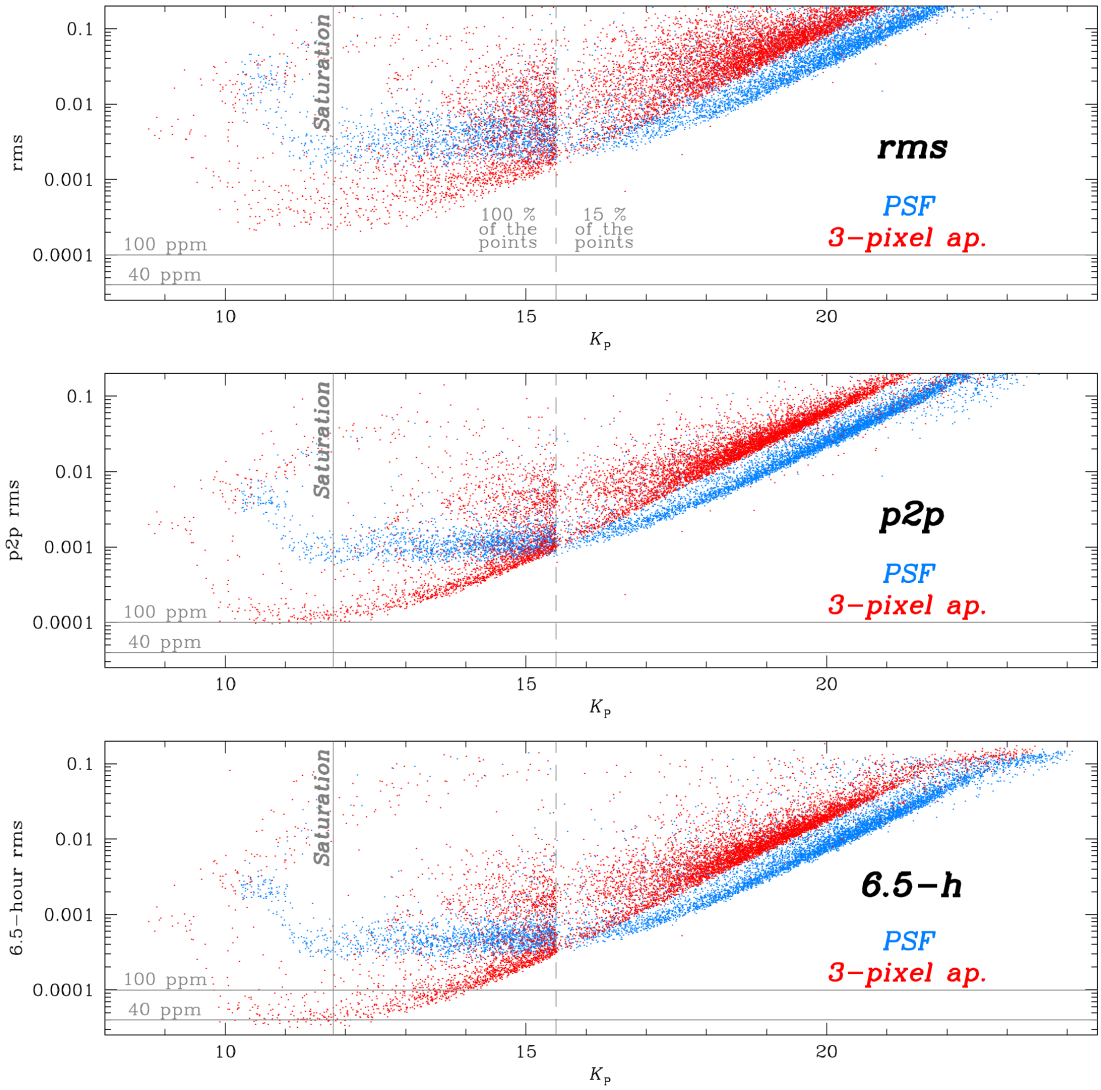

Figure 5.14. Photometric rms (top), p2p rms (middle) and 6.5-hour rms (bottom) as a function of the K_P magnitude derived from the 3-pixel-aperture- (red points) and PSF-based (azure points) neighbour-subtracted LCs. The vertical, grey dashed line is set at K_P=15.5. For stars fainter than K_P∼15.5 the PSF photometry has a lower rms. The vertical, grey solid line is set at the saturation threshold (K_P∼11.8). As a reference, we plot two horizontal, grey solid lines at 100 and 40 ppm, respectively. As in Fig. 5.12, for K_P>15.5 we show only the 15% of the points, for clarity.

aperture photometry. At 18<K_P<19 the 6.5-hour rms is about 2600 ppm. Such precision allows us to detect a flux drop of a few hundredths of magnitude, i.e., the LC dimming due to exoplanet candidate TR1 discovered by Mochejska et al. (2006). We will further discuss this object in Sect. 5.9.

In conclusion, we find that even at the bright end our neighbour-subtracted technique allows us to obtain performance that is comparable to those in the literature. This is the case even though we are dealing with a more crowded region than most previous studies.

5.7.3 Comparison with existing works on *K2* data

At present, there are a number of studies in literature that are focused on the C0 data of *K2*. Here, we provide a comparison, both using the LC rms and through a visual inspection of the LCs, for the objects in common with previous published studies.

Before making such a comparison, we warn the reader about some aspects that should be taken into account in the following. A fair comparison should be made by comparing the single LCs point by point. Unfortunately, thus far, no one has ever attempted to measure all stars in the entire super-stamps. Rather it is more common practice to restrict the analysis to the outer parts of dense stamps, where the crowding is less severe.

That said, we do have several LCs from stars in common with various studies; in the best case (Vanderburg & Johnson 2014), we have 40 stars. Furthermore, by simply comparing the rms given in the different papers, we could introduce some biases. For example, the rms in a given magnitude bin can be overestimated by the number of variable stars within that bin; the methods adopted to compute the rms can be different; there might be different calibration methods to transform 'raw' magnitudes into the *Kepler* photometric system. In the latter case, stars can fall in different magnitude bins in different papers. Finally, our neighbour-subtracted LCs are less affected by neighbour-light contamination. As noticed above, the light pollution would result in a brighter LC, which would move the star into a brighter magnitude bin, and decrease its rms (because of the higher number of counted photons).

5.7.3.1 Comparison with Vanderburg & Johnson (2014)

The first published study on *K2* photometry was that of Vanderburg & Johnson (2014), and was based on the Engineering data set. The C0 data set was subsequently reanalysed by Vanderburg (2014), who worked to improve the photometric performance for fainter stars.

We downloaded from the MAST archive all his LCs for the targets within channel 81, and found 40 objects in common with our catalogue. We computed the three rms as described above. The LCs from Vanderburg (2014) show, on average, a larger p2p and 6.5-hour rms than our LCs for the variable objects, but their p2p and 6.5-hour rms for non-variable stars was lower. While the former behaviour was predictable, (as reported by Vanderburg & Johnson (2014), their self-calibrated-flat-field approach works best on dwarfs rather than on highly-variable stars) the latter trend was unexpected. Therefore, we also visually inspected the location of all stars in common on the images and the regions covered by the adopted aperture masks[9].

For bright stars, Vanderburg (2014) used a circular aperture that included several neighbour sources. For faint stars, the ad hoc aperture that was designed to avoid light contamination works only partially, since the flux on the wings of the PSF can still fall inside it. Furthermore, for blended stars the adopted aperture mask included all of them and, finally, the EPIC catalogue seems not complete enough. In either cases, the total flux of the source is increased because of the contribution of the neighbours, resulting in a higher SNR for the source (with a consequent better Poisson rms), but this does not correspond to the true SNR of the individual target source. Of course, we cannot exclude that Vanderburg (2014) detrending algorithm works better, further improving the final rms. A larger sample of stars is required for a more conclusive comparison.

We also found that at least two variable objects identified by Vanderburg (2014) were mismatched/blended, difficult for him to identify due to the limitations introduced by the EPIC (bright, isolated objects) and the low resolution of the *K2* images (see next section).

It is worth to mention that Vanderburg (2014) releases for each LC a flag that marks the cadence number associated to a thruster-jet event. We compared their flag with our flag described in Sect. 5.6.2. Among the cadences in common between the two works, we found that we flagged (and do not used) a lower number of images. This is probably due to our perturbed-PSF approach

[9] https://www.cfa.harvard.edu/∼avanderb/k2.html

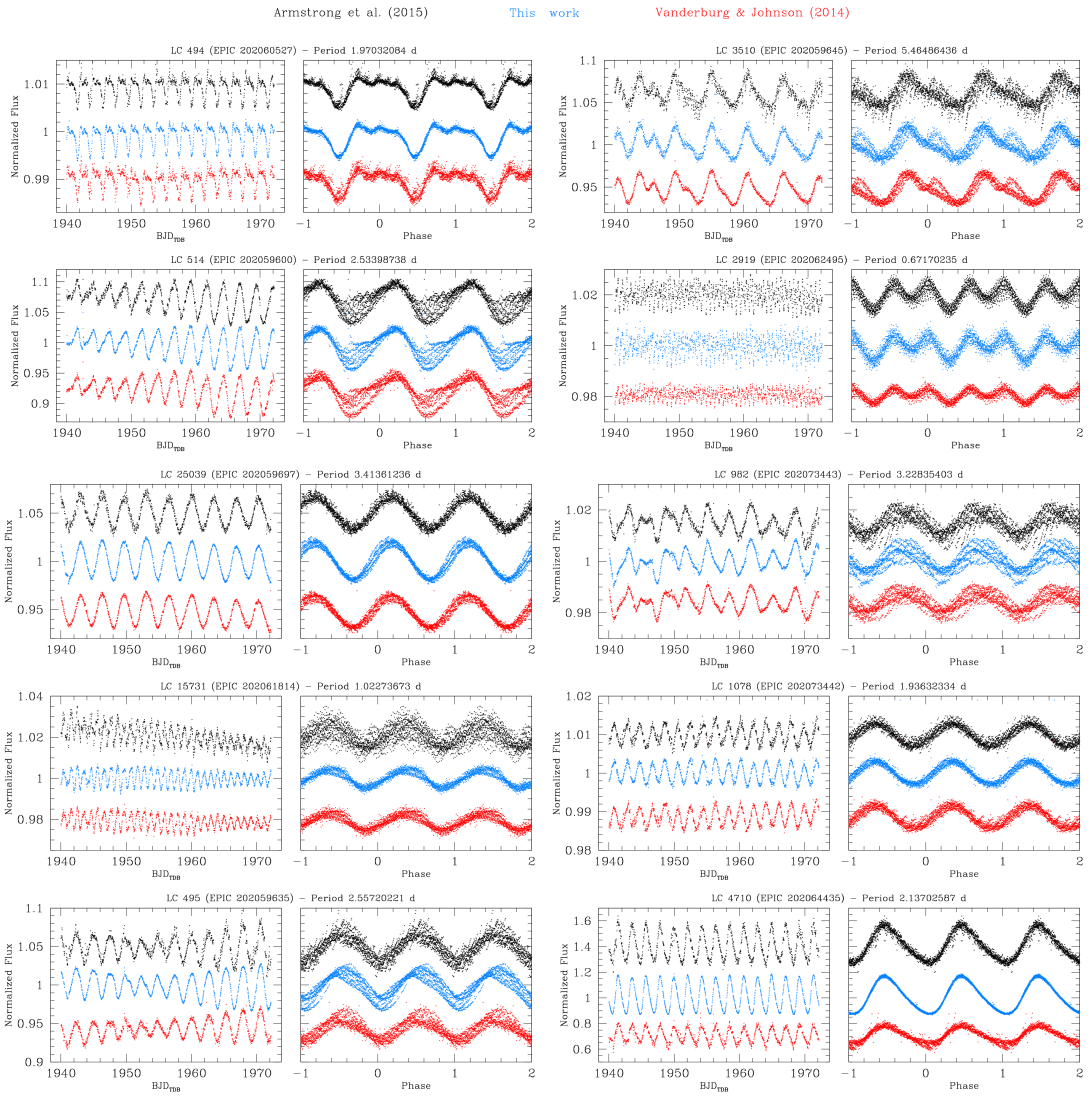

Figure 5.15. Point-by-point comparison between our LCs (azure points) and those from Vanderburg & Johnson (2014, red) and Armstrong et al. (2015, black). We show only the points imaged at the same $\mathrm{BJD_{TDB}}$ in common among the three works.

that is able to fit reasonably well objects imaged while the thruster-jet effect was not severe. However, we found a good agreement between the two thruster-jet-identification methods.

5.7.3.2 Comparison with Armstrong et al. (2015)

Armstrong et al. (2015) released C0 LCs obtained with a similar method and with comparable performance to those of Vanderburg & Johnson (2014). We downloaded the LCs from their archive[10] and computed the rms for the 12 objects we have in common. Again, we found that our photometry provides LCs with a lower rms for almost all these variable stars.

As the rms cannot give a direct measurement of the goodness of the photometry, we made a

[10] http://deneb.astro.warwick.ac.uk/phrlbj/k2varcat/

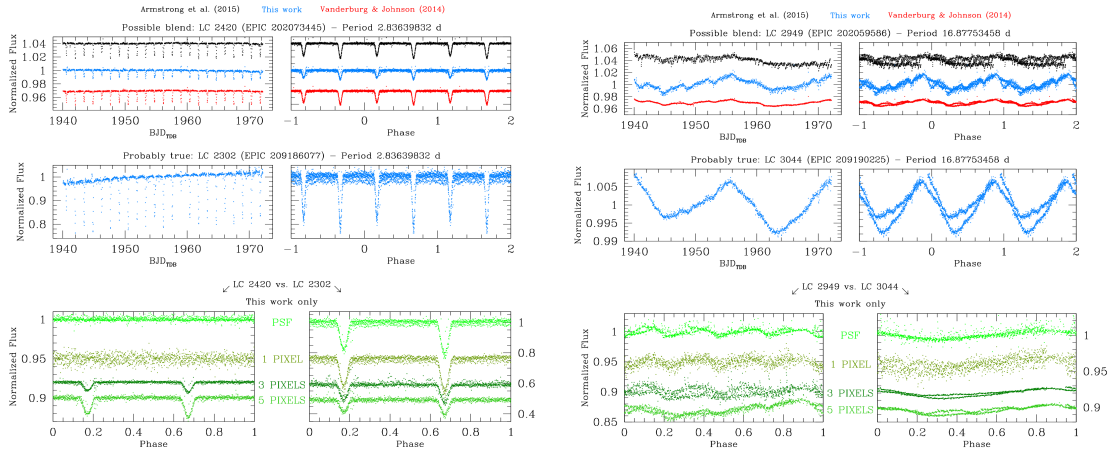

Figure 5.16. Left: LC comparison between EPIC 202073445 (LC no. 2420 in AIC) and EPIC 209186077 (LC no. 2302). On the top panels we compared our LC of the probable-blend object (EPIC 202073445) with those found in the literature as in Fig. 5.15. In the middle panels we show the LC of the object that we found to be the true variable (EPIC 209186077). We show only our LC since these objects are neither in Vanderburg & Johnson (2014) nor in Armstrong et al. (2015) data set. In the bottom panels we finally show our LCs colour-coded with different shades of green according to the photometric method (PSF, 1, 3 and 5 pixels aperture). Right: as in left-hand panels, but for the case of EPIC 202059586 (LC no. 2949) and EPIC 209190225 (LC no. 3044).

visual comparison of the 12 LCs in common between our data set and Armstrong et al. (2015) one. In Fig. 5.15 we show the LC comparison of 10 out of 12 objects in common. We also included the LCs of Vanderburg & Johnson (2014) since these objects are present in their sample too. We plotted the best photometry for all the LCs. On average, our LCs looks sharper (e.g., LC 4710).

Left-hand panels of Fig. 5.16 show the first of the remaining two objects we have in common. EPIC 202073445 is an eclipsing binary. The depth of our LC is smaller than in the two papers. However, Nardiello et al. (2015) found that the real eclipsing binary is another star (namely, EPIC 209186077), very close to EPIC 202073445. To further shed light on this ambiguity, we compared the LCs of both stars using different kinds of photometry. The mismatched eclipsing binary does not show any flux variation with the PSF and 1-pixel-aperture photometry. On the other hand, the larger the aperture, the deeper the eclipse. Instead, the 'real' eclipsing binary shows that the eclipses become dimmer and dimmer with increasing aperture radius, as expected since its flux is diluted by the remaining flux of the (un-)subtracted neighbours. We confirm that the true eclipsing binary is the one identified by Nardiello et al. (2015, EPIC 209186077). This mis-identification is also present in the eclipsing-binary catalogue of LaCourse et al. (2015).

There is a similar ambiguity between EPIC 202059586 and EPIC 209190225 (right-hand panels of Fig. 5.16). Again, comparing the PSF- and aperture-based LCs, we found that the first object is rather an aperiodic star that shows a flux modulation due to the latter object, while the second one is the real variable.

5.7.3.3 Comparison with Aigrain et al. (2015)

Aigrain et al. (2015) developed a different method, which is described in detail in their paper.

Their approach has some similarities with the effort here described, e.g., the image reconstruction and the adoption of an input list. Unfortunately, a proper comparison is not possible since they analysed only the Engineering data. C0 showed different problems and lasted longer. Anyway, for the sake of completeness, we compared their results with our LCs.

Due to its less-ambiguous definition, we compared the p2p rms. In the brightest magnitude intervals ($9<K_{\rm P}<11$), Aigrain et al. (2015) show a better p2p rms than we derived here. In the interval $11<K_{\rm P}<15$, our 3-pixel-aperture p2p rms ranges from 124 to 585 ppm; while their p2p rms varies between 238 and 867 ppm. For fainter magnitudes up to $K_{\rm P}\sim19$ our p2p rms is slightly better. On the other hand, our PSF-based photometry performs much better in the magnitude interval $15<K_{\rm P}<19$, with a minimum p2p-rms value of 1274 ppm and a maximum of 7936 ppm, to be compared with that of Aigrain et al. (2015) that increases from 1841 to 23673 ppm in the same magnitude range. It is worth to mention that we could measure objects up to 5 mag fainter than those measured by Aigrain et al. (2015).

5.8 Variable Candidates

5.8.1 Search for Variables

In order to detect candidate variable stars, we followed the procedure adopted by Nardiello et al. (2015); we describe the basics of the procedure below. We obtained the periodograms of all clean LCs using three different tools included in the VARTOOLS v1.32 package, written by Hartman et al. (2008) and publicly available[11]:

- The first tool is the Generalized Lomb-Scargle (GLS) periodogram (Press et al. 1992; Zechmeister & Kürster 2009), useful in detecting sinusoidal periodic signals. It provides the formal false alarm probability (FAP) that we used to select variable-star candidates.
- The second tool is the Analysis of Variance (AoV) periodogram (Schwarzenberg-Czerny 1989), suitable for all kind of variables. We used the associated AoV FAP metric (Θ) that is a good diagnostic useful to select stars that have a high probability to be variables.
- The third tool is the Box-fitting Least-Squares (BLS) periodogram (Kovács, Zucker, & Mazeh 2002), particularly effective when searching for box-like dips in an otherwise-flat or nearly-flat LC, such as those typical of detached eclipsing binaries and planetary transits. We used the diagnostic 'signal-to-pink noise' (Pont, Zucker, & Queloz 2006), as defined by Hartman et al. (2009), to select eclipsing-binary and planetary-transit candidates.

Figure 5.17 illustrates the procedure used to identify candidate variables resulting by the application of the AoV finding algorithm. The same procedure has been adopted for the GLS and BLS finding algorithms. First, we built the histogram of the periods (P) of all clean LCs, as shown in panel (a) of Fig. 5.17. For each period P_0 we computed the median of the histogram values in the bins within an interval centred at P_0 and extended by $50 \times \delta P$, where δP is the bin width chosen to build the histogram. We flagged as 'spike' the P_0 corresponding to a histogram value 5σ above that median, where σ is the $68.27^{\rm th}$ percentile of the sorted residuals from the median value itself. These spikes are associated with spurious signals due to systematic effects such as, e.g., the jet-firing every $\sim$5.88 h, the long cadence at $\sim$29 min ($\sim$0.02 d) and the periodicity of $\sim$2.04 d (described in Sect. 5.6.1) and their harmonics. Finally, we removed from the catalogue the stars having periods inside $P_0 \pm \delta P/2$, keeping only those with high Θ. We performed our searching to periods between 0.025 (slightly higher than the long-cadence sampling) and 36.5 d (clean-LC total time interval). GLS, AOV and BLS input parameters were chosen to optimise the variable finding and are not perfect. Indeed, we selected a sample of

[11] http://www.astro.princeton.edu/~jhartman/vartools.html

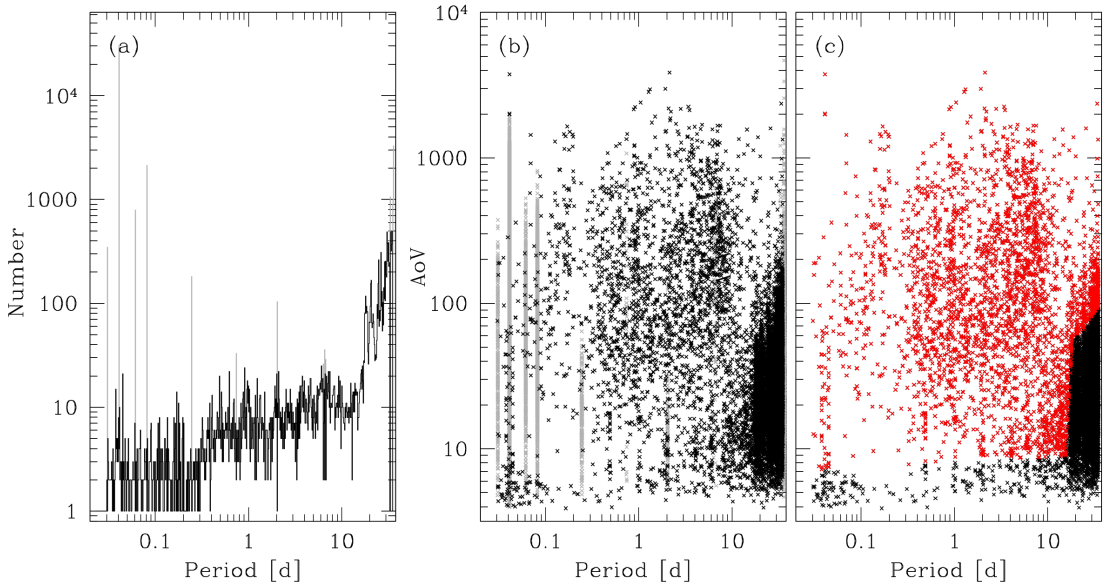

Figure 5.17. Example of candidate-variable selection using the AoV algorithm. Panel (a): the distribution of the periods; in black we show the distribution after removing the spikes, in grey the removed spikes. Panel (b): LC periods as a function of the AoV metric Θ for all the stars; the stars that have passed the first selection are plotted in black, the stars having periods corresponding to the removed spikes in grey. Panel (c): periods of LCs as a function of Θ after spikes suppression. Red dots represent variable candidates.

known variables and tuned the input parameters in order to maximise the SNR outputted by each of the three findings. This way, some variables could have been missed because the three tasks found the highest SNR with a wrong period, e.g., the 0.04-d alias.

In panel (b) of Fig. 5.17, for all clean LCs, we plot the Θ parameter as a function of the detected period, highlighting the objects removed because their period coincides with a spike. In panel (c) we selected by hand the stars that have high Θ.

We ran the VARTOOLS algorithms GLS, AoV, and BLS on a list of 52 596 LCs. We initially excluded all objects that in our input list were outside the *K2* TPFs. Then, for each star, we selected the photometry (1, 3, 5, 10 pixels aperture or PSF) that gives the best precision at a given magnitude, according to what was described in Section 5.7, Fig. 5.14, and Tables 5.1 and 5.2.

We combined the lists of candidate variables obtained by applying the three variable-detection algorithms and visually inspected each of them. We excluded all obvious blends by looking at the LC-shape and position of each star and of its neighbours within a radius of about 11 *K2* pixels ($\sim$43 arcsec).

We found a total of 2759 variables of which 1887 passed our visual inspection as candidates and 202 were flagged as blends. The remaining 670 LCs were difficult to visually judge. We included them into our final catalogue, but added a warning flag indicating that their variable nature is in doubt.

5.8.2 Comparison with the literature and sample improvement

In order to evaluate the completeness of our sample, we matched the Asiago Input Catalog with six catalogues found in the literature: Hu et al. (2005), Jeon & Lee (2010), Kim et al. (2004),

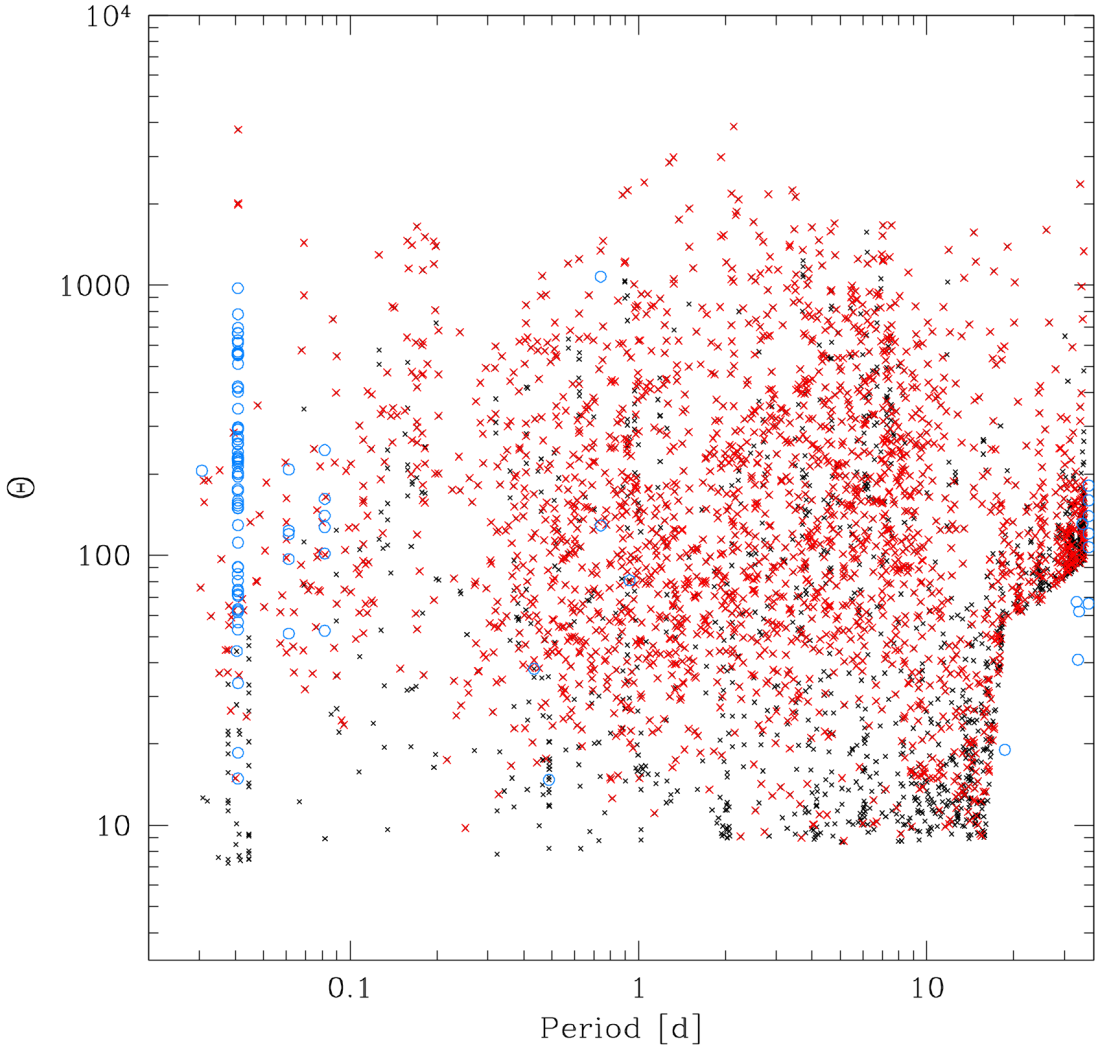

Figure 5.18. Periods of the LCs as a function of Θ for all the candidate variables. With red crosses we show all variables we found in our analysis of the *K2* data, with azure, open circles the variable stars from published catalogues and present in our AIC we failed to identify among our *K2* LCs. All these variables are included in our final catalogue of variable candidates, with different flags. Black crosses represent all variable sources that passes our first selection described in Fig. 5.17 but not our visual inspection (see text for detail).

Meibom, Mathieu, & Stassun (2009), Mochejska et al. (2004, 2006) and Nardiello et al. (2015). These studies, which all cover the M 35/NGC 2158 super-stamp region, analysed different aspects of stellar variability and made use of different observational instruments and detection techniques (e.g., Meibom, Mathieu, & Stassun 2009).

Cross-correlation of these catalogue results in 658 common entries. Of these, 555 sources are also present in our AIC. The remaining 103 objects are missing for various reasons. A small fraction (∼10%) of stars had a very-bright neighbour source that was badly subtracted because the PSF is still far from perfect or were just too close to the edge of our field of view. For the remaining missing known variables, we found that the periods given by the three VARTOOLS

algorithms were close to that of a spurious signal (spikes in the AoV versus period plot of Fig. 5.17) or lied below our selection threshold (panel c in Fig. 5.17). Therefore they were excluded before the visual check, even if their LCs showed a clear variable signature. As an example, we show in Fig. 5.18 the AoV parameter Θ as a function of LC period for all the candidate variables[12] in which we marked with a different colour the location of such missed objects. Since there is no reason to exclude them, we added such previously-discovered variables to our catalogue.

The variable stars found in the literature were also useful to refine our sample and remove some blends and fake detection left after the visual inspection of the LCs. Indeed, previously published studies have made use of images with a higher resolution than that of *K2*, and therefore we chose to rely on the former in ambiguous cases.

After this second refinement of our catalogue, we have 2133 candidate variables, 444 sources with possible blends or dominated by systematic effects, and 272 objects for which the LC is difficult to interpret. In the final catalogue that we release, we properly flag all these different sources (see Sect. 5.10). In any case, we release all LCs extracted from the *K2*/C0/channel-81 data, which are available to anyone for any further investigation. In Fig. 5.19 we show ten of such LCs as example.

5.8.3 Variable location on the M35 and NGC 2158 colour-magnitude diagrams

We also used the $BVRJ_{\rm 2MASS}H_{\rm 2MASS}K_{\rm 2MASS}$ and white-light-magnitude catalogue of Nardiello et al. (2015) to find the location of our variables in the colour-magnitude diagrams (CMDs). In Fig. 5.20, we show the B versus $(B-R)$ CMDs of the star sample used to search for variable candidates (Sect. 5.8.1) that have a B- and R-magnitude entry in the catalogue. We plot candidate variables, difficult-interpretation objects and blends in different boxes in order to better illustrate the three samples (panels a, b and c).

5.9 TR1 as a procedure benchmark

Mochejska et al. (2004, 2006) made an extensive ground-based campaign search for transiting exoplanets in NGC 2158 and, among the discovered variable sources, they found an exoplanet candidate with a transit depth of ∼0.037 mag (TR1, following their nomenclature). Mochejska et al. (2006) suggested that TR1 could be a hot-Jupiter with a period of 2.3629 d. The hosting star is a NGC 2158 member, $V_{\rm max}\simeq$19.218, $R_{\rm max}\simeq$18.544, $(\alpha,\delta)_{\rm J2000.0}\sim(06^{\rm h}07^{\rm m}35\overset{\rm s}{.}4,+24^\circ05'40\overset{''}{.}8)$.

This object represents an ideal test-bed for our independent pipeline reduction of *Kepler*/*K2* data in crowded regions. Figure 5.21 shows the region of sky around TR1 in images collected with three different instruments and completely different resolutions. The light pollution of target neighbours is evident. In the left-hand panel, we show an ∼10×10 arcmin^2 region (north up and east left) around TR1 from the *K2* stacked image of channel 81. A green circle of radius 3 *Kepler* pixels and a red square of 1 *Kepler* pixel per side centred on TR1 are barely visible in this panel. In the middle-left panel, a zoomed-in image of about 25×28 arcsec^2 centred on TR1 is visible. The yellow grid represents the *Kepler* CCD pixels. The red square shows the location of TR1. It is clear that, without knowing the positions of the target, TR1 identification would be hard if not impossible. The middle-right panel shows the same region, but from the Schmidt filterless stacked image of Nardiello et al. (2015). In this image the pixel scale is ∼0.862 arcsec pixel^{-1}. The higher spatial resolution of this instrument allows us to better identify TR1. We can identify at least 11 TR1 neighbours within the 3-*Kepler*-pixel aperture. These stars badly pollute the target LC, dimming the transit, and therefore leading to an underestimated radius if

[12]Irregular and long-period objects, such as the cataclysmic variable V57 found by Mochejska et al. (2004, period ∼48 d) for which we can see only one peak in the clean LC, are plotted with an arbitrary period ∼36.5 d.

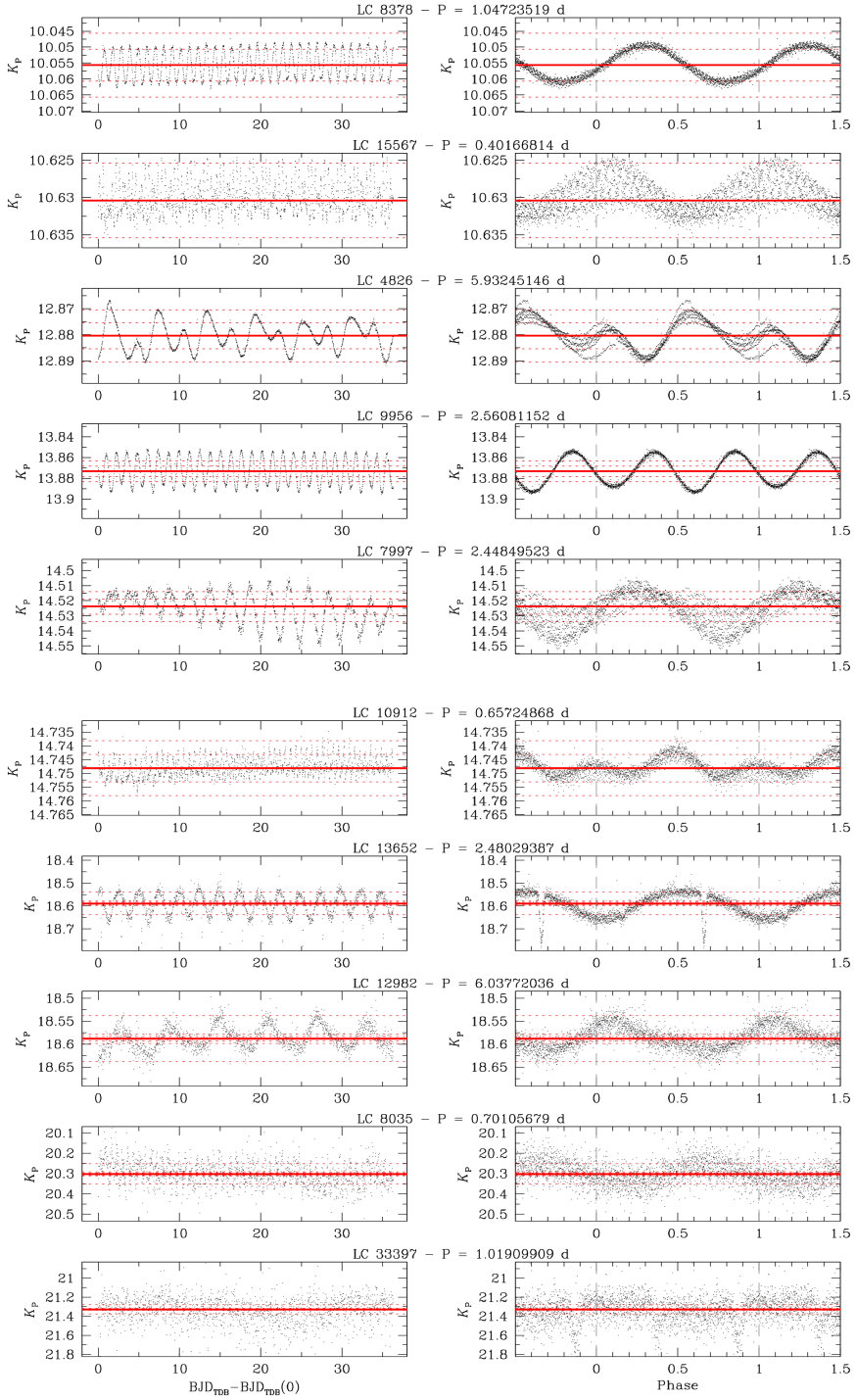

Figure 5.19. Example of variable LCs in our sample. We plot on the left and on the right the entire and the folded detrended clean LC of each object. The red solid line is set at the median magnitude of the LC, while the red dashed lines are set at ±0.005, ±0.01 and ±0.05 K_P from the median value. The vertical, grey dashed lines in the right-hand panels are set at phase 0 and 1. The LCs are plotted in order of decreasing magnitude from the top to the bottom.

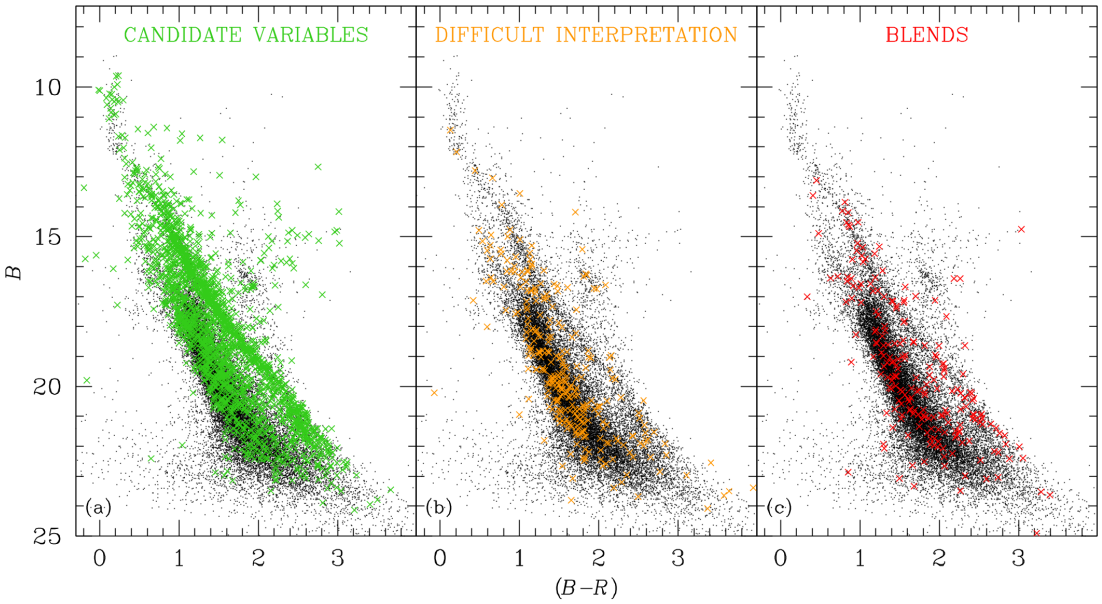

Figure 5.20. Distribution of our 2849 candidate variables in the B versus $(B-R)$ CMD. In the three panels we separately show the likely-variable stars (green crosses in panel a), the objects of which the LC was of difficult interpretation (orange crosses in panel b) and the blends (red crosses in panel c).

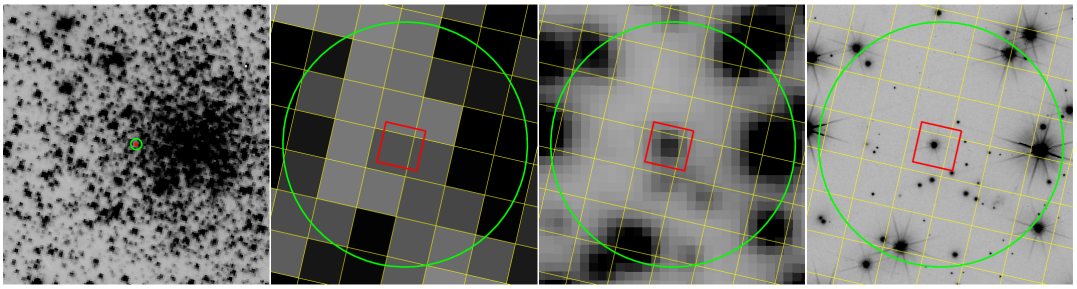

Figure 5.21. Left: 10×10 arcmin^2 region around TR1 in the *K2* stacked image. A green circle of radius 3 *Kepler* pixels and a red square with 1 *Kepler* pixel side are centred on TR1. Middle-left: zoom-in of the *K2* stacked image around TR1. The covered area is about 6.5×6.8 pixel^2 (about 25×28 arcsec^2). The yellow grid represents the *Kepler* CCD pixel grid. Middle-right: as in the middle-left panel, but for the Schmidt filterless stacked image of Nardiello et al. (2015). Right: ACS/WFC@*HST* F606W-filter stacked image (from Bedin et al. 2010). In all these panels, north is up and east to the left. It is clear that the higher the image resolution, the higher the number of detectable polluting sources within the aperture.

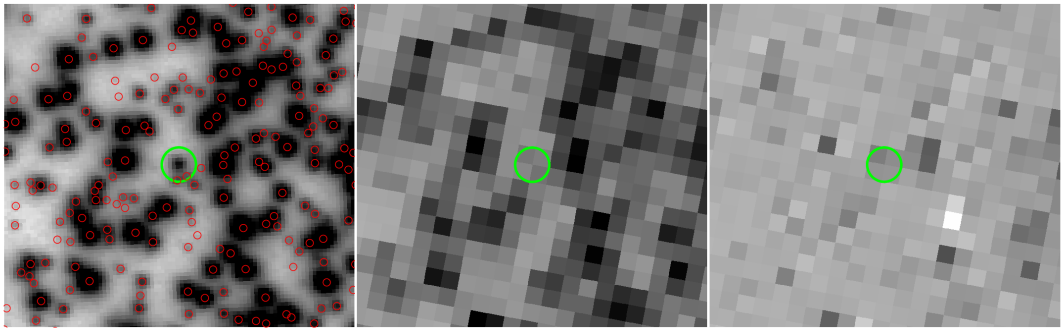

Figure 5.22. PSF-subtraction of the stellar neighbours (red circles) around TR1 (green circle). In the left-hand panel, we show all identified sources in the AIC that must be subtracted before measuring the TR1 magnitude. The image is the Schmidt stacked image from which the AIC was extracted. In the middle and right-hand panels we show a single *K2* image before and after the neighbour subtraction, respectively. Even if the PSF-based subtraction is not perfect due to the unavailable PSF calibration data (see Sect. 5.3), the light pollution is less severe.

we do not properly account for their contribution. Finally, in the right-most panel, we show the same region as seen in an ACS/WFC@*HST* F606W-filter stacked image described in Bedin et al. (2010, from GO-10500, PI: Bedin). In this case, the pixel scale is about 25 mas pixel^{-1} and the image shows that, within a single *Kepler* pixel, there can be more than one star. Figure 5.22 shows an individual *K2* exposure before and after subtraction of neighbour sources present in the input list.

The *Kepler* magnitude of TR1 is $K_{\rm P,max}\simeq$18.35. Therefore, this object is at the faint end of most of the previous studies. With the photometric technique developed in this work, TR1 becomes a well-measurable object, as we can push our photometry almost 5 mag fainter and measure stars in crowded environments. In this magnitude interval and at this level of crowding the 1-pixel-aperture and the PSF-based photometry are the only two photometric approaches that allow us to measure the light dimming in TR1 LC.

Despite the *Kepler* pixel size, and consequent neighbour contamination, the detrended LC from *K2* data is significantly more complete and precise than that of Mochejska et al. (2006). Figure 5.23 shows the phased and detrended clean LCs. In the top panel, we plot the original detrended LC. In the other panels we show the same LC after we applied a running-average filter of 24-h window to remove any systematic trend and/or long-period LC variability in order to better highlight TR1 transits. The period we found using the BLS algorithm is of 2.36489338 d. In Fig. 5.23 we phased the LC with double the period.

In the phased LC, both eclipses have more a 'V'-like than a 'U'-like shape[13]. If we also consider the location of TR1 in the CMD (right-hand panel of Fig. 5.23), it appears more likely to be a binary with a grazing eclipse rather than a transiting exoplanet candidate. In a future work we will make use of the input list from *HST* data to better characterise TR1. We will also better determine the LCs for the subsample of stars that fall within the ACS/WFC footprint of the *HST* programme GO-10500 field.

An important by-product of our method is that we can much-better measure the depth of the eclipses, since our transits are less diluted by the light coming from neighbour sources than other approaches. Figure 5.24 shows a comparison between the detrended clean TR1 LCs with (black points) and without (azure points) TR1 neighbours. The uppermost LCs were those obtained

[13]Using EXOFAST tool (Eastman, Gaudi, & Agol 2013) we found an impact parameter of 0.764114 and a 'planet' (star in TR1 case) to star radius ratio of 0.184497, confirming our qualitative classification.

with 3-pixel-aperture photometry, while those in the middle and in the bottom were extracted using the PSF photometry. We phased these LCs with a period of ∼4.73 d as in Fig. 5.23. In the right-hand panel we also binned the LCs with bins of 0.01 phase each and computed, within such each bin, the median and the $68.27^{\rm th}$ percentile of the distribution around the median values.

The 3-pixel-aperture-based LCs do not show any significant flux variation. The median magnitude is 3 mag brighter and the rms is smaller than in the PSF-based LCs; all evidences of neighbour-light contamination as discussed in Sect. 5.7. This LC represents the result of a classic approach found in the literature.

On the other hand, the remaining PSF-based LCs with (hereafter wLC) and without (w/oLC) neighbours clearly present at least one flux drop. First of all, TR1 in the wLC is about 0.25 mag brighter than in the w/oLC. The w/oLC does not only show a smaller rms and fewer outliers, but it shows two distinct eclipses; while the wLC exhibits only the eclipse around phase ∼0.2.

Using VARTOOLS BLS and EXOFAST suit (Eastman, Gaudi, & Agol 2013, assuming TR1 is a transiting exoplanet), we estimated a TR1 eclipse depth on the w/oLC (assuming the original BLS period of ∼2.36 d) of about 3.2 and 3.4 per cent, respectively. Taking into account (1) that our LC and that of Mochejska et al. (2006) are obtained from different pass-bands, (2) the measurement errors, (3) the *K2* integration time lasts half an hour, and (4) the incompleteness of the AIC, we conclude that the two values are in rather good agreement. Therefore, we confirm that our PSF-based approach is effective in disentangling blended sources in crowded regions.

We conclude this section remarking that it would have been simply impossible to extract the LC of TR1 from *Kepler*/*K2* data without using a input list from a higher resolution data set and subtracting the stellar neighbours. The approach of our method allows us to reach a 6.5-h photometric precision of ∼2700 ppm in a heavily crowded environment for sources as faint as TR1.

5.10 Electronic material[14]

For each source in the AIC that falls in a *K2*/C0/channel-81 TPF, we release raw and detrended LCs from the 1-, 3-, 5-, 10-pixel aperture and PSF photometry on the neighbour-subtracted images. We also make publicly available the AIC (with each star flagged as in/out any TPF) and the *K2* stacked image.

For the 2849 candidate variables we release a catalogue made as follows. Column (1) contains the ID of the star in the AIC. Columns (2) and (3) give J2000.0 equatorial coordinates in decimal degrees; columns (4) and (5) contain the pixel coordinates x and y from the AIC, respectively. In columns (6) and (7) we release the instrumental Schmidt filterless and the $K_{\rm P}$ magnitudes of the stars. The $K_{\rm p}$ magnitude is computed as the 3σ-clipped median value of the magnitude in the LC, calibrated using a photometric zero-point as described in Sect. 5.5. In column (8) we write the photometric method with which we extracted the LC of the object and searched for variability.

Column (9) contains a flag corresponding to our by-eye classification of the LC (Sect. 5.8.1 and 5.8.2):

- 0: high probability that it is a blend;
- 1: candidate variable;
- 2: difficult to classify;
- 30: star marked as 'difficult to classify' and that, by comparison with the literature, could be a possible blend;

[14] http://groups.dfa.unipd.it/ESPG/Kepler-K2.html

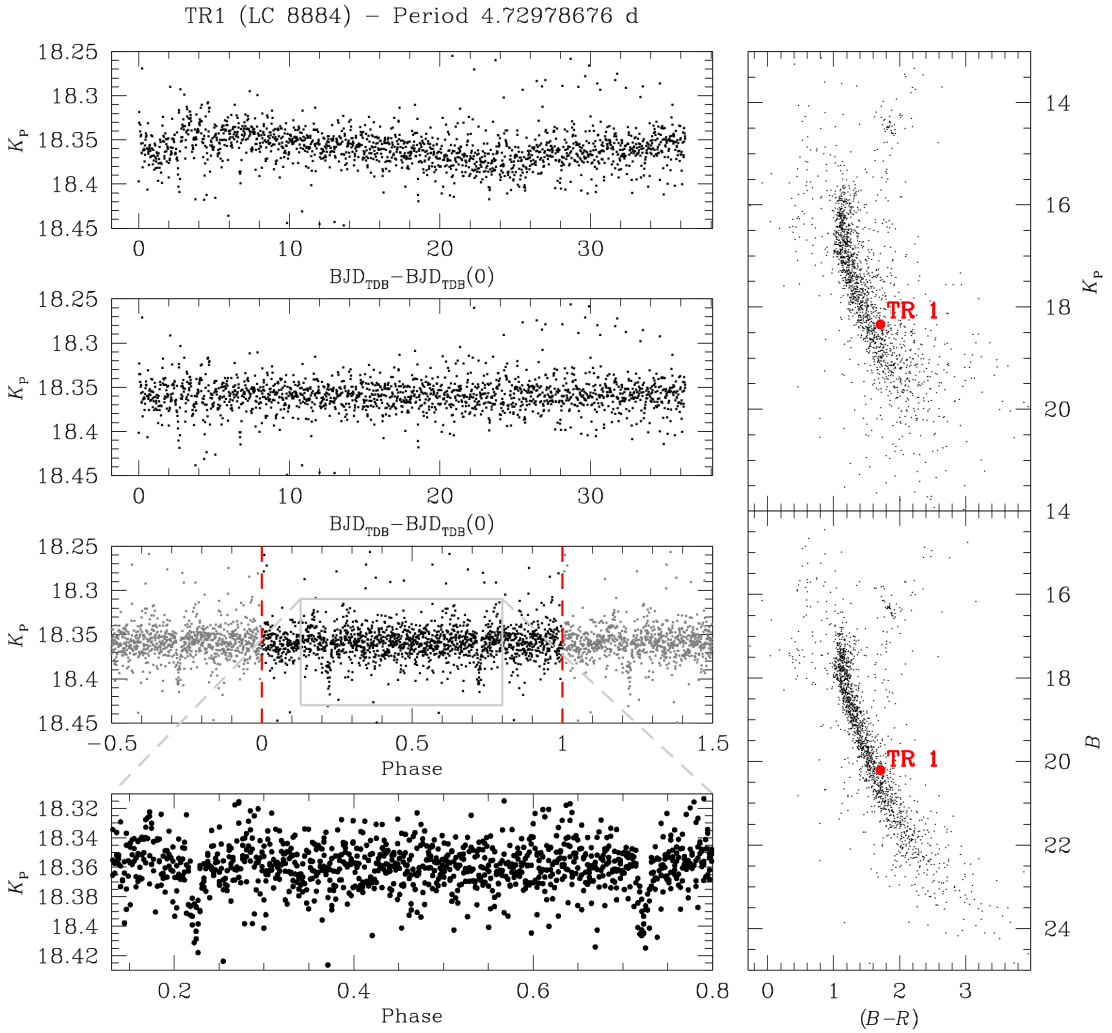

Figure 5.23. TR1 clean LCs and CMD location. Left, from top to bottom: detrendend LC, flattened LC (see text for details), phased LC with a period of 4.72978676 d and zoom-in on the phased LC to highlight the two minimums. In the one-to-the-last panel, the red, vertical dashed lines are set at phase 0 and 1. Right: K_P versus $(B-R)$ (top panel) and B versus $(B-R)$ (bottom panel) CMDs of NGC 2158. We considered as cluster members those stars that are within a radius of ∼3 arcmin from NGC 2158 centre. The red filled point marks the location of TR1. The K_P magnitude was computed as the 3σ-clipped median value of the PSF-based LC magnitude, calibrated into the *Kepler* photometric system (Sect. 5.5).

- 31: star marked as 'difficult to classify', but for which we found a correspondence in the literature;
- 32: star we classified as candidate variable but it is close to a variable star from the literature and that seems a possible blend.

Column (10) gives the period, when available. From column (11) to (16) we give the ID used in other published catalogues, namely Nardiello et al. (2015), Hu et al. (2005), Jeon & Lee (2010), Kim et al. (2004), Meibom, Mathieu, & Stassun (2009) and Mochejska et al. (2004,

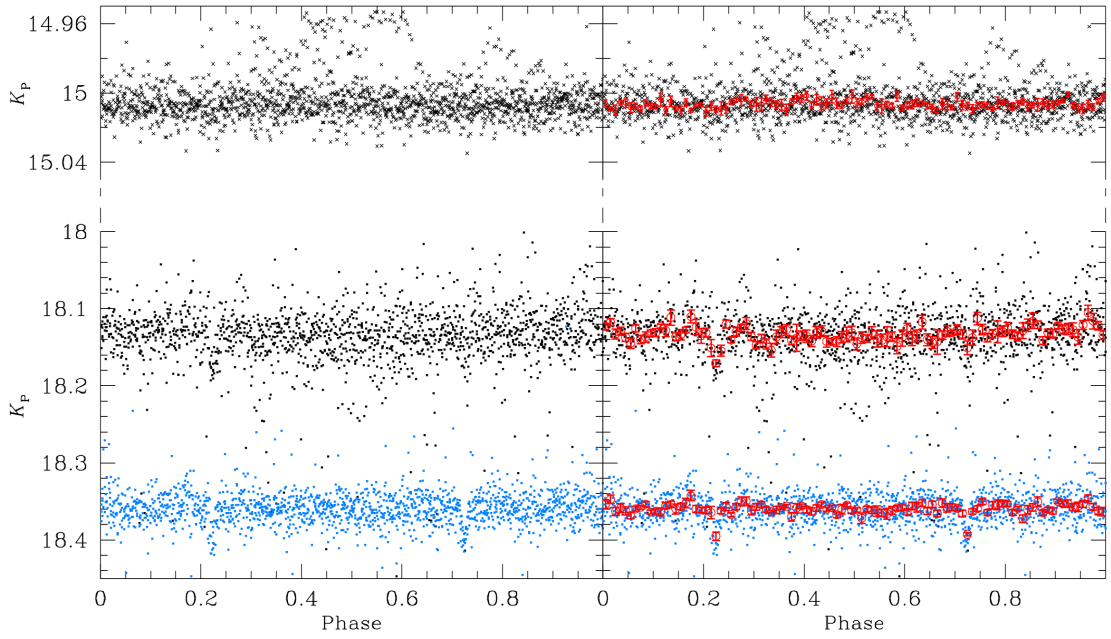

Figure 5.24. TR1 clean LCs with and without TR1 neighbours. From top to bottom: 3-pixel-aperture LC with neighbours (black crosses), PSF-based LC with (black dots) and without (azure dots) neighbours. The LCs are phased with a period of 4.72978676 d. In the right-hand panels we also plot the binned LCs. The red points are the median value in 0.01-phase bin, while the error bars are the 68.27^{th} percentile of the distribution around the median value divided by $\sqrt{N}$, where N is the number of points in each bin.

2006), respectively. Finally, we provide (columns from 17 to 22) the $BVRJ_{\rm 2MASS}H_{\rm 2MASS}K_{\rm 2MASS}$ calibrated magnitudes from Nardiello et al. (2015) catalogue, when available.

5.11 Conclusions and future planned works

In this Chapter we have presented our first analysis of *K2* data, focusing our effort on crowded images and faint stars. The test-beds for our method were super-stamps covering the OCs M 35 and NGC 2158.

Though the lack of *Kepler* calibration data – not made available yet to the community – prevented us to optimise our algorithm, based on a technique we have developed in the last 20 years on *HST* undersampled images, we nevertheless succeeded in implementing a photometric procedure based on the ePSF concept (Anderson & King 2000). We have shown that by using a crude PSF that is spatially constant across the channel and allowing for simple temporal variations, we were able to properly fit stellar objects. Future efforts will be devoted to further improve the PSF model, possibly with a better data set at our disposal.

In the second part of the Chapter, we focused our attention on the LC-extraction method and on the consequent detrending algorithms. The LC extraction is based on the methods we started to develop in Nardiello et al. (2015) and makes use of both PSF fitting and of a high-angular-resolution input list to subtract stellar neighbours before measuring the stellar flux of any given target. By subtracting the light of the close-by stars, we are able to decrease the dilution effects that significantly impact the photometry in crowded regions.

We compared aperture- and PSF-based photometric methods and found that aperture photometry performs better on isolated, bright stars (6.5-hour-rms best value of ∼30 ppm), while PSF photometry shows a considerable improvement with respect to the classical aperture photometry on faint stars and in crowded regions. The extension of the capability to exploit *Kepler* as well as *K2* data set to fainter (up to 5 mag fainter than what has been done up to now in the literature) stars and crowded environments is the main and original contribution of our efforts.

We release our raw and detrended LCs with the purpose of stimulating the improvement of variable- and transit-search algorithms, as well as of the detrending methods.

We are currently working on other clusters imaged during other *K2* Campaigns, and plan to work on the densest Galactic-bulge regions. We also plan to go back to OCs within the *Kepler* field, i.e. NGC 6791 and NGC 6819.

Bibliography

Adams F. C., Proszkow E. M., Fatuzzo M., Myers P. C., 2006, ApJ, 641, 504

Aigrain S., Hodgkin S. T., Irwin M. J., Lewis J. R., Roberts S. J., 2015, MNRAS, 447, 2880

Anderson, J., & King, I. R. 2000, PASP, 112, 1360

Anderson J., King I. R., 2006, acs..rept, 1

Anderson J., Bedin L. R., Piotto G., Yadav R. S., Bellini A., 2006, A&A, 454, 1029

Anderson J., et al., 2008, AJ, 135, 2114

Armstrong D. J., et al., 2015, A&A, 579, A19

Balona L. A., Baran A. S., Daszyńska-Daszkiewicz J., De Cat P., 2015, MNRAS, 451, 1445

Barnes S. A., 2007, ApJ, 669, 1167

Bedin L. R., Salaris M., King I. R., Piotto G., Anderson J., Cassisi S., 2010, ApJ, 708, L32

Bellini A., et al., 2014, ApJ, 797, 115

Borucki W. J., et al., 2010, Sci, 327, 977

Brogaard K., Bruntt H., Grundahl F., Clausen J. V., Frandsen S., Vandenberg D. A., Bedin L. R., 2011, A&A, 525, A2

Brown T. M., Latham D. W., Everett M. E., Esquerdo G. A., 2011, AJ, 142, 112

Brucalassi A., et al., 2014, A&A, 561, L9

Bryson S. T., et al., 2010, ApJ, 713, L97

Crossfield I. J. M., et al., 2015, ApJ, 804, 10

Eastman J., Gaudi B. S., Agol E., 2013, PASP, 125, 83

Foreman-Mackey D., Montet B. T., Hogg D. W., Morton T. D., Wang D., Schölkopf B., 2015, ApJ, 806, 215

Gilliland R. L., et al., 2000, ApJ, 545, L47

Hartman J. D., Gaudi B. S., Holman M. J., McLeod B. A., Stanek K. Z., Barranco J. A., Pinsonneault M. H., Kalirai J. S., 2008, ApJ, 675, 1254

Hartman J. D., et al., 2009, ApJ, 695, 336

Hermes J. J., et al., 2015, MNRAS, 451, 1701

Howell S. B., et al., 2014, PASP, 126, 398

Hu J.-H., Ip W.-H., Zhang X.-B., Jiang Z.-J., Ma J., Zhou X., 2005, ChJAA, 5, 356

Huang C. X., Penev K., Hartman J. D., Bakos G. Á., Bhatti W., Domsa I., de Val-Borro M., 2015, MNRAS, 454, 4159

Jeon Y.-B., 2010, PKAS, 25, 31

Kim H.-J., Park H.-S., Kim S.-L., Jeon Y.-B., Lee H., 2004, IBVS, 5558, 1

Koch D. G., et al., 2010, ApJ, 713, L79

Kovács G., Zucker S., Mazeh T., 2002, A&A, 391, 369

Kraus A. L., Cody A. M., Covey K. R., Rizzuto A. C., Mann A. W., Ireland M. J., 2015, ApJ, 807, 3

LaCourse D. M., et al., 2015, MNRAS, 452, 3561

Libralato M., Bedin L. R., Nardiello D., Piotto G., 2016, MNRAS, 456, 1137

Lund M. N., Handberg R., Davies G. R., Chaplin W. J., Jones C. D., 2015, ApJ, 806, 30

Mamajek E. E., Hillenbrand L. A., 2008, ApJ, 687, 1264

Meibom S., Mathieu R. D., Stassun K. G., 2009, ApJ, 695, 679

Meibom S., et al., 2011, ApJ, 733, L9

Meibom S., et al., 2013, Nature, 499, 55

Meibom S., Barnes S. A., Platais I., Gilliland R. L., Latham D. W., Mathieu R. D., 2015, Nature, 517, 589

Mochejska B. J., Stanek K. Z., Sasselov D. D., Szentgyorgyi A. H., Westover M., Winn J. N., 2004, AJ, 128, 312

Mochejska B. J., et al., 2006, AJ, 131, 1090

Montalto M., et al., 2007, A&A, 470, 1137

Nardiello D., et al., 2015, MNRAS, 447, 3536

Nascimbeni V., Bedin L. R., Piotto G., De Marchi F., Rich R. M., 2012, A&A, 541, A144

Pont F., Zucker S., Queloz D., 2006, MNRAS, 373, 231

Press W. H., Teukolsky S. A., Vetterling W. T., Flannery B. P., 1992, nrca.book

Quinn S. N., et al., 2012, ApJ, 756, L33

Quinn S. N., et al., 2014, ApJ, 787, 27

Schwarzenberg-Czerny A., 1989, MNRAS, 241, 153

Stello D., et al., 2011, ApJ, 739, 13

Stello D., et al., 2015, ApJ, 809, L3

Vanderburg A., 2014, arXiv, arXiv:1412.1827

Vanderburg A., Johnson J. A., 2014, PASP, 126, 948

Vanderburg A., et al., 2015, ApJ, 800, 59

Weldrake D. T. F., Sackett P. D., Bridges T. J., 2008, ApJ, 674, 1117

Zechmeister M., Kürster M., 2009, A&A, 496, 577

6 Conclusions

In this thesis we have analysed data obtained with both ground- and space-based facilities, and highlighted a possible synergy among them in order to overcome those technical issues (e.g., geometric distortion, detector undersampling, stellar crowding) that usually harm the feasibility of some high-precision-demanding studies. In this last Chapter, I summarise the main results of my work, and highlight the already-begun and future applications and projects.

6.1 Summary

We focused on wide-field imagers and showed that, with a careful analysis based on an accurate point-spread-function (PSF) modelling and geometric-distortion correction, it is possible to obtain high astrometric and photometric precision and accuracy with their data. However, the prescriptions discussed in the thesis can be easily extended to the most of the existing detectors placed at ground and space observatories.

In the first part of the thesis, we mainly utilised detectors that work in the near-infrared (NIR) regime, due to the increasing interest of the astronomical community for this particular kind of imagers in preparation for JWST, but in the second part of the thesis we also showed a couple of examples of studies performed with optical CCDs (LBC@LBT and the CCD mounted at the Asiago Schmidt telescope).

We started by investigating the astrometric and photometric performances of the NIR wide-field imager HAWK-I@VLT. We adapted to HAWK-I the techniques originally developed for the *Hubble Space Telescope* (*HST*) imagers to obtain high-precision astrometry and photometry, and then applied to the wide-field imager mounted at the 2.2-m MPI/ESO telescope. We accurately modelled its PSFs and solved for the geometric distortion of the detector. With this careful data reduction, we were able to reach an astrometric accuracy of a few mas over the entire field of view (FoV) of the instrument. Together with the distortion-correction routines, we also created astro-photometric catalogues of seven fields. Furthermore, to test the astrometric accuracy reached, we computed relative proper motions for stars in two globular clusters (M 22 and M 4) and successfully separated cluster members from background/foreground objects. Proper-motion-selected colour-magnitude diagrams of the globular cluster M 22 allowed us to study its multiple stellar populations, finding that the two stellar populations hosted in the sub-giant branches of M 22 have the same radial distribution from the cluster centre up to 9 arcmin, within our uncertainty.

We then moved to the wide-field imager VIRCAM@VISTA. Again, we exported the tools made for HAWK-I to this imager and solved for the distortion of the detector. The geometric-distortion correction of VIRCAM was quite challenging because the tangential-plane projection effects are not negligible anymore over a FoV larger than 1 deg^2 on the sky. We started by using the 2MASS (Skrutskie et al. 2006) catalogue as reference frame, and then we auto-calibrated the geometric distortion as done for the HAWK-I detector. This way, we were able to correct the geometric distortion of VIRCAM to an astrometric accuracy of about 8 mas. Finally, we

used the 'VISTA Variables in the Vía Láctea' (VVV, Minniti et al. 2010) data to compute M 22 globular-cluster relative proper motions. VVV observations were not designed to such high-astrometric-accuracy purposes, but with our tools we were able to separate cluster and field stars, as well as to measure the motion difference between Galactic bulge and disc stars toward the direction of M 22.

In the last part of the thesis we described our new project focused to exploit the data coming from the planet-hunting *K2* (Howell et al. 2014), the re-designed mission of the more famous *Kepler* (Borucki et al. 2010), after the problems that occurred to its spacecraft. The analysis of crowded environments using *K2* data can be very complex with classical photometric approaches. Our method is instead specifically developed to deal with these particular regions (stellar clusters and toward the Galactic centre) and its key ingredients are PSF astrometry and photometry, high-angular-resolution input catalogues and PSF-based neighbour subtraction.

We first addressed the problem of the *K2* undersampled PSFs which fine structures, if not properly modelled, can introduce systematic errors that worsen both astrometry and photometry. To this aim, we followed the iterative method made to model *HST* undersampled PSFs. We then used a high-angular-resolution, ground-based catalogue to analyse all the detectable objects in the field and, for each of them, we measured their flux after we subtracted all close-by neighbours. This way, we increased the number of sources studied in the field and obtained a more reliable estimate of their flux. But more importantly, for variable stars, eclipsing binaries and exoplanet candidates, this method led to a more reliable value of the true amplitude or eclipse/transit depth of their light curves because we reduced light-dilution effects. This is particularly interesting for exoplanets, because the true radius of the transiting objects would be otherwise under-estimated.

We applied this method to the first *K2* data release that observed two open clusters (M 35 and NGC 2158) and extracted about 50 000 light curves from one channel out of the 76 still working on *Kepler*'s focal plane. This number is more than two times the total number of sources usually analysed over the entire FoV of a given *K2* Campaign. For bright stars, we reached a photometric precision of ∼30 parts per million, comparable with other works in the literature focused on fields sparser than that of these two open clusters. At the faint end, we measured objects up to 5 magnitudes fainter than in the already-published works with *K2* data, and showed that the PSF photometry performs better than aperture photometry in this magnitude regime. The improvement was more significant in crowded regions. Within the field of these two clusters we also found more than 2000 variable stars.

6.2 Future works on ground-based imaging

We plan to continue to work with NIR detectors. High-precision astro-photometric NIR catalogues of crowded and/or heavily-absorbed regions can be very useful for a large variety of scientific investigations out of *GAIA*'s reach (e.g., globular clusters, Bulge and Galactic plane). We will mainly focus on different astrometric projects doable with the VVV data, by taking advantage of the ∼6-yr temporal baseline at disposal. In particular, we will search for high-proper-motion objects (e.g., close dwarfs that show a parallax signature) and compute stellar proper motions of globular clusters in the Bulge and Disc, with which we can separate cluster from field stars and look for any evidence of the presence of tidal tails in the outskirt of the clusters.

VVV will also be useful to exploit *K2* Campaigns 9 and 11. As we will see in next Section, these two *K2* Campaigns will cover the Galactic centre. In this extremely-crowded region, VVV will provide the required input list with all detectable sources in the field, crucial for our PSF-based neighbour-subtraction technique (Chapter 5).

Besides VVV projects, we are adapting our software and exporting our expertise to other wide-field detectors. For instance, we can use archival material of old detectors as first-epoch data for proper-motion studies. New detectors can be used to create accurate, deep and complete

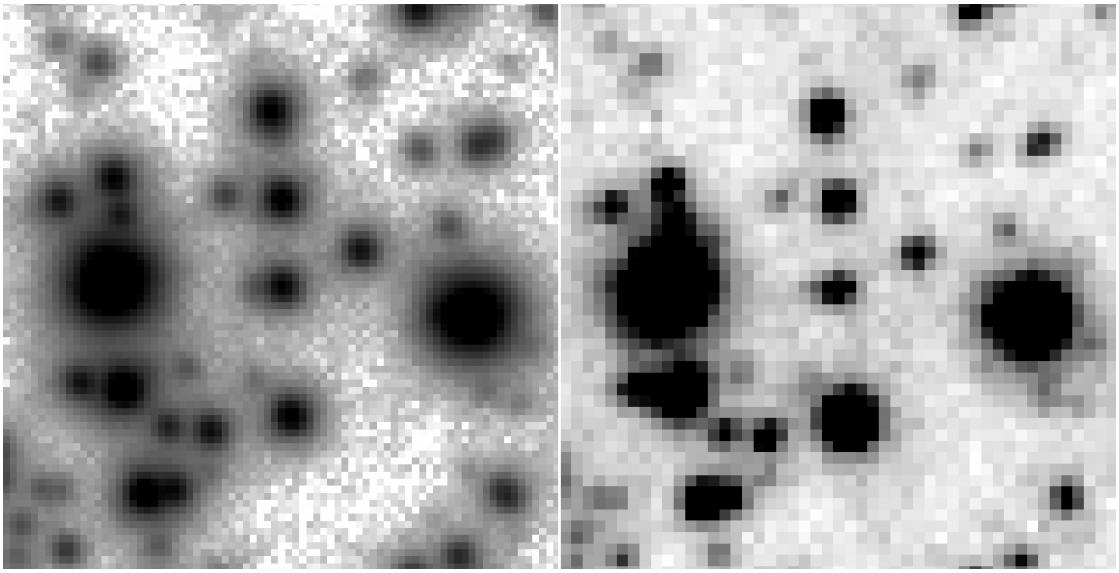

Figure 6.1. Comparison between a 691-s $g_{\rm Sloan}$-filter OmegaCAM exposure (left-hand panel) and a 60-s J-filter VIRCAM exposure (right-hand panel). The difference in the pixel scale between the two instruments is clear. The field is located ∼10 arcmin from ω Cen centre. Both images are in logarithmic grey scale.

astro-photometric catalogues. An example of these applications is our work with the wide-field imager OmegaCAM mounted at the VLT Survey Telescope (VST).

6.2.1 OmegaCAM@VST

OmegaCAM[1] is a wide-field imager mounted at the 2.6-m telescope VST. It is a mosaic of 32 CCDs with a pixel scale of ∼0.21 arcsec pixel^{-1} that covers a FoV of 1 deg^2 on the sky. Such FoV is more than 60 times larger than that of HAWK-I@VLT, about 1.5 times that of VIRCAM@VISTA or ∼3 times the FoV covered by the WFI@2.2-m MPI/ESO telescope. In Fig. 6.1 we show a comparison between an OmegaCAM and a VIRCAM exposure which illustrates the better pixel scale of OmegaCAM with respect to that of VIRCAM.

We have already started to adapt our reduction software to this instrument and to improve the quality of the image pre-reduction (Fig. 6.2). We have at our disposal two dithered data sets ($g_{\rm Sloan}$ and $i_{\rm Sloan}$ filters) centred around the globular cluster ω Cen (GTO time, PI: Piotto) with which to fine-tune our tools. These data sets will also be used to solve for the geometric distortion of the OmegaCAM detector. From the scientific point of view, these images fully cover ω Cen up to its tidal radius and beyond, allowing us to investigate the disputed presence of tidal tails and to study the cluster's multiple-stellar-populations radial distribution far from the cluster centre (e.g., Bellini et al. 2009). We already collected the first-epoch data. The second epoch is scheduled 10 yr after the first one, in order to maximise the cluster-field separation.

6.3 *Kepler* and *K2*: present and future

Our pilot project on *K2* Campaign 0 described in Chapter 5 showed very promising applications of our method, and we are now working to subsequent *K2* Campaigns (as of January 2016, 13

[1] https://www.eso.org/sci/facilities/paranal/instruments/omegacam.html

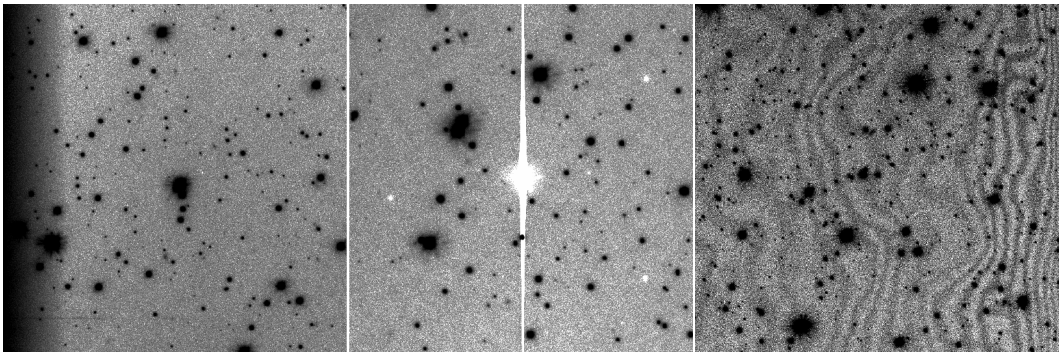

Figure 6.2. Left-hand and middle panels: example of vignetting and cross-talk in a OmegaCAM $g_{\rm Sloan}$-filter exposure. Right-hand panel: fringing in a $i_{\rm Sloan}$-filter exposure. All images are in logarithmic grey scale.

already approved and 5 proposed). In addition to this, we are re-reducing part of the *Kepler* main-mission data, focusing on the open clusters: NGC 6791, NGC 6811, NGC 6819 and NGC 6866. Our methodology is completely empirical, therefore it must be fine-tuned to each field, in order to improve the existing tools and find new solutions for high-precision photometry in other crowded environments. In the following I describe some of the projects in which I am involved.

6.3.1 ePSF modelling

In Chapter 5 we focused on the *K2* super-stamp covering M 35 and NGC 2158 regions. To model the effective PSF (ePSF), we took advantage of several aspects typical of Campaign 0. Even if crowded, the super-stamp is large enough to allow us to select moderately-isolated stars for the ePSF modelling far from NGC 2158 centre. Furthermore, the spacecraft average jitter was of the order of 2-3 *Kepler* pixels, with a maximum displacement of 20 *Kepler* pixels. All these features increased the probability to have an homogeneous pixel-phase-space coverage.

During the successive Campaigns, the spacecraft jitter decreased to $\sim$1 *Kepler* pixel, and consequently the super-stamps were set to be smaller, with only the most crowded stellar-clusters regions imaged in them. This is the case of NGC 6121 (M 4) and M 80 in Campaign 2. Therefore, using the same solutions and criteria as for the pilot project based on Campaign-0 data would result in a less optimal ePSF modelling.

Starting from Campaign 2, we chose to implement the ePSF neighbour subtraction at the ePSF-modelling stage (Libralato et al., in preparation). The new procedure can be summarised as follows. First, we iteratively make an ePSF model as described in Chapter 5. Ten iterations are enough to converge to a reliable ePSF model (at least more reliable than a fully-empirical PSF). We then iterate ten more times using the neighbour-subtraction technique before to collect the ePSF samplings, considerably improving our ePSF models. The list with all detectable stars in the field can be either obtained by using the *K2* images themselves or by using a higher-angular-resolution input list, as done in the light-curve extraction (Sect. 5.4, Chapter 5). Once the final average ePSF model is achieved, we also perturb the ePSF to take into account for its temporal variation. This neighbour-subtraction phase is also introduced at the ePSF perturbation stage.

By reducing the impact of crowding in the sample selection, we can naturally increase the number of stars at our disposal, and map the phase space more homogeneously, taking advantage of the random distribution of the stars on the pixel grid. The ePSF models can be further improved because, with this method, we can decrease the dilution effects, that produce a shallower ePSF, and model the ePSF wings, one of the missing features in the application described Chapter 5, even in a dense field as that of M 4.

Table 6.1. List of open (OC) and globular (GC) clusters observed or planned during *Kepler* and *K2* missions. For *K2*/C9 we added only stellar clusters listed in the *Kepler*/*K2*-field web page (see Note 1).

Cluster Name	R.A.	Dec.	Cluster type	Campaign
NGC 6791	$19^h20^m53^s$	$+37°46'18''$	OC	*Kepler*
NGC 6811	$19^h37^m17^s$	$+46°23'18''$	OC	*Kepler*
NGC 6819	$19^h41^m18^s$	$+40°11'12''$	OC	*Kepler*
NGC 6866	$20^h03^m55^s$	$+44°09'30''$	OC	*Kepler*
M 45 (Pleiades)	$03^h47^m00^s$	$+24°07'00''$	OC	*K2*/C4
Hyades	$04^h26^m54^s$	$+15°52'00''$	OC	*K2*/C4
NGC 2158	$06^h07^m25^s$	$+24°05'48''$	OC	*K2*/C0
NGC 2168 (M 35)	$06^h09^m00^s$	$+24°21'00''$	OC	*K2*/C0
NGC 2632 (M 44)	$08^h40^m24^s$	$+19°40'00''$	OC	*K2*/C5
NGC 2682 (M 67)	$08^h51^m18^s$	$+11°48'00''$	OC	*K2*/C5
NGC 6093 (M 80)	$16^h17^m03^s$	$-22°58'34''$	GC	*K2*/C2
NGC 6121 (M 4)	$16^h23^m35^s$	$-26°31'33''$	GC	*K2*/C2
NGC 6531 (M 21)	$18^h04^m13^s$	$-22°29'24''$	OC	*K2*/C9
NGC 6530 (M 8)	$18^h04^m31^s$	$-24°21'30''$	OC	*K2*/C9
NGC 6613 (M 18)	$18^h19^m58^s$	$-17°06'06''$	OC	*K2*/C9
IC 4725 (M 25)	$18^h31^m47^s$	$-19°07'00''$	OC	*K2*/C9
NGC 6717 (Pal 9)	$18^h55^m06^s$	$-22°42'05''$	GC	*K2*/C7
NGC 6774 (Rup 147)	$19^h16^m40^s$	$-16°17'59''$	OC	*K2*/C7

1. http://keplerscience.arc.nasa.gov/k2-fields.html

Unfortunately, even this new ePSF modelling is still not an optimal solution. We are still limited by the spacecraft jitter during a given Campaign, as well as by the strong assumptions about the ePSF stability over time baselines of a few months. A large room for improvement is expected when the *Kepler* pixel-response-function characterisation data will be made publicly available (see Sect. 5.3, Chapter 5, for the detailed discussion).

6.3.2 Crowded fields in *K2*

A list of the observed/planned open and globular clusters is shown in Table 6.1. Another interesting field will be the Galactic centre, whose observations are planned in Campaigns 9 and 11. Either in super-stamps or isolated stamps, our neighbour-subtraction method will be perfectly suitable in these very crowded regions, where more than one source is expected per *Kepler* pixel. We are committed to analyse stellar clusters and Bulge regions observed during *Kepler* and *K2* missions. In the following paragraphs, an introduction to our planned works is given.

6.3.2.1 NGC 2158

We are further analysing the most crowded regions close to the centre of NGC 2158 to search for variable stars, mainly focusing on eclipsing binaries (EBs) such as as TR1 (see Sect 5.9, Chapter 5). Differently from what described in Libralato et al. (2016, or Chapter 5), we are using an input list obtained from ACS/WFC@*HST* images in F606W and F814W filters, originally collected under the GO-10500 program (PI: Bedin) to study the white-dwarf cooling sequence of NGC 2158 (Bedin et al. 2010). With this data set, designed to reach very faint magnitudes, we can derive the deepest and most complete high-angular-resolution input list to exploit the *K2* data in this region.

This work is similar to what is described in Chapter 5, but with two main differences. In the original work, we used the white-light input list made with the Asiago Schmidt telescope by Nardiello et al. (2015). The total transmission curve of the Asiago Schmidt instrumentation with the unfiltered solution is, in first approximation, similar to that of *Kepler*, and a simple zero-point registration was enough to link the Asiago Input Catalog (AIC) and the *K2* photometric systems. In this further development, we used *HST* data. The ACS/WFC-filter transmission

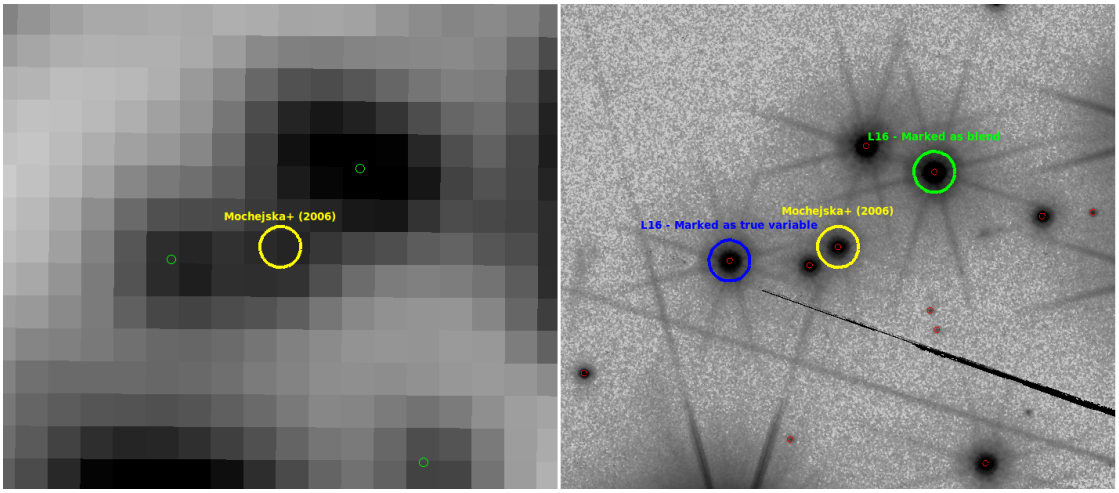

Figure 6.3. Left: Asiago Schmidt unfiltered stacked image around the location of the variable star (yellow circle) described in Mochejska et al. (2006). The green circles show the stars found in the AIC. Right: the same region as seen on the *HST* F606W-filter stacked image. Stars in the *HST* input list are marked with red circles. In Chapter 5 (Libralato et al. 2016), the star highlighted with a blue circle on the left was wrongly identified as that of Mochejska et al. (2006), while the star marked in green was classified as its blend. However, thanks to *HST* higher angular resolution, the identification becomes obvious. In both panels, the covered FoV is 14×12 arcsec^2, north is up and east to the left. Both images are in logarithmic grey scale.

curves are significantly different from that of *Kepler*, therefore we had to transform the F606W- and F814W-filter magnitudes and colour into the K_P photometric system. Second, the completely different angular resolution, the different FoV and the different photometric depth between *HST* and *K2* exposures resulted in a challenging astrometric registration between the two. Therefore, we underwent through an intermediate step, and transform stellar positions from the *HST* to the AIC reference system. This way, we can then easily compute transformations between the AIC and each *K2* image as done in Sect. 5.4.2.

The usage of the *HST* input list led to several improvements. Indeed, for each star we were able to find all significantly-bright neighbours, thus improving the neighbour-subtraction phase, the measurement of the true flux of the target and the true depth of possible eclipses/transits. Furthermore, we were able to remove blends and better identify the true variable stars, a task particularly difficult from ground due to the seeing-limited observations and lower angular resolutions. An example of these improvements is shown in Fig. 6.3. In Chapter 5, we found two variable stars very close to the variable V10 discovered by Mochejska et al. (2006) and, since all of them showed the same period, we marked the closest variable in the AIC as V10 and the other star as its blend. However, by using the *HST* images, a completely different scenario appears. First, none of the two stars in the AIC is V10. Variable V10 is missing from the AIC probably because a combination of crowding, seeing variation and its faintness made us to loose it during the AIC creation. Second, within a 10×10 arcsec^2 (∼2.5×2.5 *Kepler* pixel^2) there are six sources around V10 (and not only one as in the AIC) that we properly subtracted during the light-curve-extraction phase. However, looking at the new light curves extracted using the *HST* input list, it is not clear yet which star is the true variable among the small group imaged in Fig. 6.3. We will continue to investigate this issue.

Part of the work is focused on EBs. In Fig. 6.4 we show a preliminary result of our work on the NGC 2158 EB TR1 (see Sect. 5.9, Chapter 5). We used the BaSTI solar-scaled isochrones

(Pietrinferni et al. 2004) from Bedin et al. (2010, [Fe/H]=−0.03, E($B-V$)=0.42, $(m-M)_0$=12.98) to disentangle the two components of TR1 and estimate their masses and radii. For TR1, we find $q^{\rm TR1} = M_2^{\rm TR1}/M_1^{\rm TR1} = 0.69^{+0.11}_{-0.10}$, with $M_1^{\rm TR1} = 1.04^{+0.01}_{-0.03}$ $M_\odot$, $M_2^{\rm TR1} = 0.71^{+0.09}_{-0.09}$ $M_\odot$, $R_1^{\rm TR1} = 0.98^{+0.02}_{-0.04}$ $R_\odot$ and $R_2^{\rm TR1} = 0.65^{+0.07}_{-0.09}$ $R_\odot$. The quoted errors are just formal errors, they do not take into account for the uncertainties in the models. We are working to find and characterise new EBs in this field. By using *K2* light curves, *HST* photometry and high-resolution spectroscopy, we expect to measure NGC 2158 age and Helium content with an accuracy better than 1%, as done for NGC 6791 by Brogaard et al. (2011, 2012).

6.3.2.2 NGC 6121

M 4 is the geometrically-closest globular cluster to the Sun. It was observed by *K2* during Campaign 2. Unfortunately, only a half of the cluster (centre excluded) was imaged in a super-stamp. Nevertheless, the *K2* data still represents a treasure of information.

We have started to study the stellar variability. We can use different input lists, obtained with high-angular-resolution instruments (WFI@2.2-m MPI/ESO, FORS2@VLT, HAWK-I@VLT and *HST*). We begun with the public-available[2] catalogue made by Stetson et al. (2014), since it covers the entire super-stamp region. We extracted light curves with different photometric methods for all the 17 210 stars in this input list that fall on the *K2* M 4 region. As an example, in Fig. 6.5 we show the comparison between an original and its neighbour-subtracted *K2* image, centred on the EB V65 described in Kaluzny et al. (2013); in Fig. 6.6 we show the corresponding PSF-based light curves. Again, it appears clear that the neighbour-subtracted light curve has a smaller photometric rms and a more-reliable depth.

Besides stellar variability, M 4 is particularly interesting for many other reasons. For example, one exoplanet has been found in this cluster (Thorsett et al. 1999, Sigurdsson et al. 2003). Recently, within 'The M4 Core Project with *Hubble Space Telescope*' (PI: Bedin), Nascimbeni et al. (2014) also searched for exoplanets in this cluster. However, the *HST* data was not designed for this purpose (e.g., large dithers and sparse temporal sampling) and their result is a null detection. With *K2* we will be able to investigate more in depth the possible presence of other exoplanets in this cluster. Another very intriguing topic concerns multiple stellar populations. M 4 is known to host multiple stellar populations, and we plan to use *K2* data to learn more about them. We will use the data coming from 'The M4 Core Project' to create a deep, high-angular-resolution input list to fully exploit the overlapping regions between *HST* and *K2* observations (Fig. 6.7). *HST*'s high-precision photometry will allow us to select different samples of stars belonging to different stellar populations, extract their light curves and analyse them (focusing both on detached EBs to constrain their chemical composition, and on asteroseismological analysis) to characterise the different populations of stars hosted in M 4, with the hope of shedding some light on their formation and evolution.

6.3.2.3 Galactic centre

Campaign 9 (C9) is probably one of the most eagerly-awaited Campaigns, as it will observe the Galactic centre. During C9, the Bulge can be simultaneously observed from ground-based facilities. A peculiar class of exoplanets that will be targeted during C9 is made up by the so-called free-floating planets, that can be discovered using microlensing.

Because of the time-critical nature of microlensing events and their unpredictability, the observing strategy of C9 will be rather different from those of the previous Campaigns. The C9 field will be centred at $(\alpha, \delta)_{\rm J2000.0}$=($18^{\rm h}01^{\rm m}25^{\rm s}, -21°46'47''$). Accordingly to Henderson et al. (2015), a minimum of 3.4 deg^2 of the entire *K2*-C9 FoV should be dedicated to this microlensing survey. Therefore, to cover such large FoV, a super-stamp spanning across a couple of channels is suggested. Due to the size of this super-stamp, the C9 data would be split in two halves, at

[2] http://www.cadc-ccda.hia-iha.nrc-cnrc.gc.ca/en/community/STETSON/homogeneous/

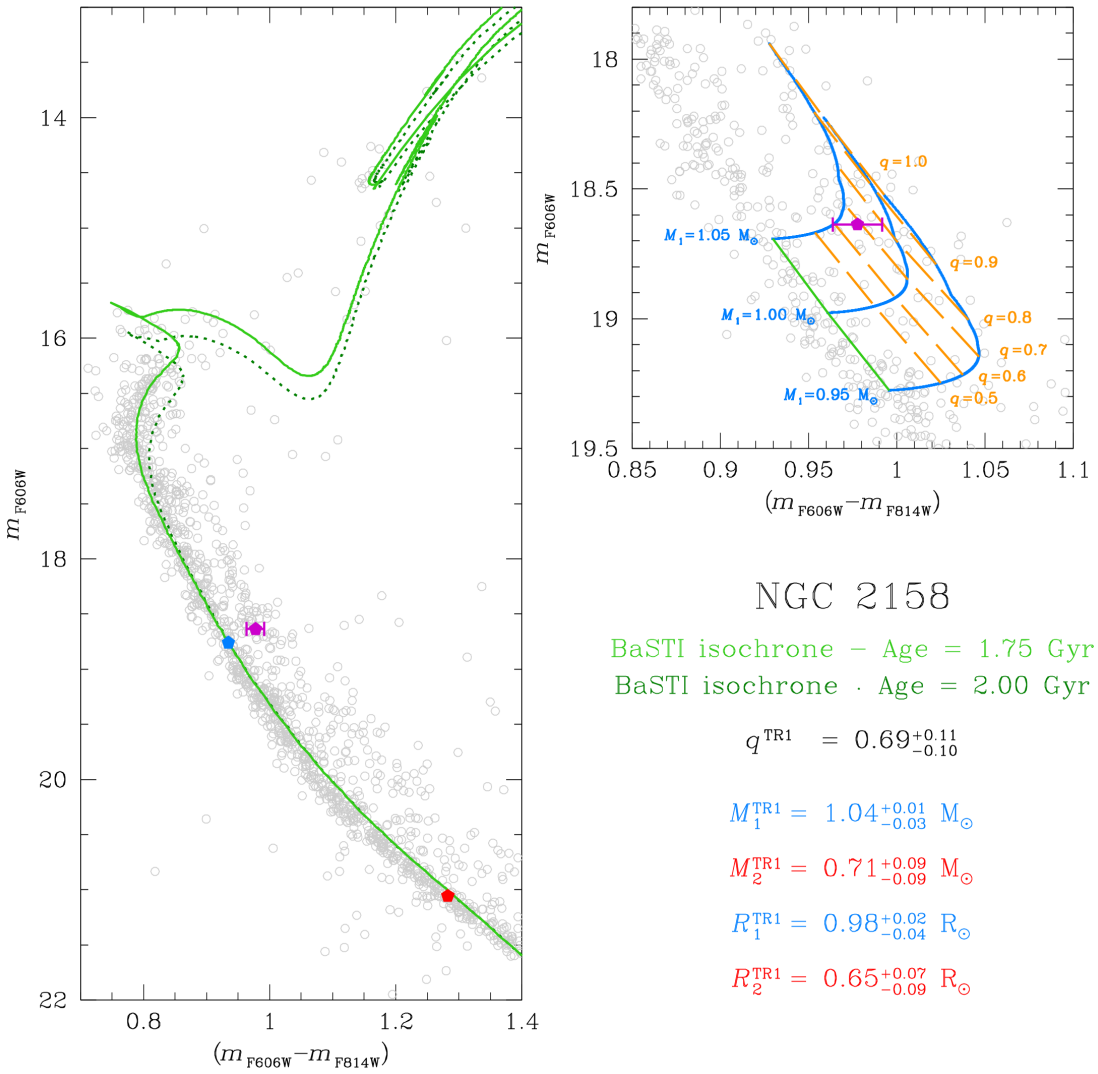

Figure 6.4. Left: m_{F606W} versus (m_{F606W}-m_{F814W}) colour-magnitude diagram of NGC 2158. The light-green solid line represents a BaSTI isochrone for 1.75 Gyr; the dark-green dashed line is for a BaSTI isochrone for 2.0 Gyr. The purple point (the error bar is the main-sequence width at the TR1 magnitude-level) shows the TR1 location in the colour-magnitude diagram. The azure and red points mark the location of the two components of the TR1 binary system. Right: model of two-main-sequence-star binary sequences with different mass ratios. The light-green solid line represents a BaSTI 1.75-Gyr isochrone track for a primary mass between 0.95 and 1.05 $M_\odot$. The azure lines mark the sequences of constant mass M_1; the yellow, dashed lines are the sequences of constant q.

the end of which the data would be downloaded to the ground. Depending on the number of additional isolated postage stamps (of 100 *Kepler* pixels each side, Henderson et al. 2015), C9 halves could be shorten by the amount of time requested to download the additional data. Only long-cadence data will be achieved, and the raw files will be publicly available after one week from the download.

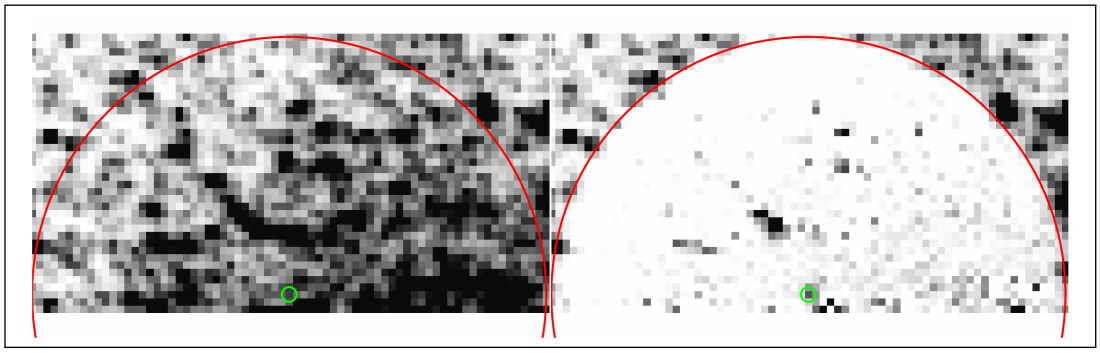

Figure 6.5. Neighbour-subtraction example in M 4 *K2* super-stamp. The field is centred around the variable star V65 (green circle) of Kaluzny et al. (2013). In the left- and right-hand panels we show the original and the neighbour-subtracted image, respectively. The red circle highlights the region within which we subtracted V65 close-by stars. All images are in logarithmic grey scale.

In the Galactic centre the crowding is severe and within a *Kepler* pixel there will be more than one source. Therefore, our PSF-based neighbour-subtraction technique, together with an adequate input list, will be very effective to extract high-precision photometry in this region. The required input list will come from the VVV data, with which we proved to be able to make astro-photometric and proper-motion catalogues of a high accuracy, as described in Chapter 3. In Fig. 6.8, we show the planned *K2* FoV of C9 (black squares) and the VVV-survey coverage (blue rectangles). Note that toward the Galactic centre several open and globular clusters could also be observed (right-hand panel of Fig. 6.8), increasing the scientific return of C9.

The Campaign-11 field will also be focused on the Galactic centre, but covering a region offset with respect to that of C9. In Fig. 6.9 we show an outline the proposed field. Unfortunately, VVV should only partially cover Campaign-11 regions.

6.4 Long-term perspectives after *K2*: TESS & PLATO

After *Kepler*/*K2*, the exoplanet hunting will continue, mainly with two space-based missions: TESS and PLATO. They will be two almost-consecutive missions focused on transiting-exoplanet discovery.

TESS (Transiting Exoplanet Survey Satellite, Ricker et al. 2014) is an Explorer-class NASA mission for a full-sky search of Earths and super-Earths transiting around bright, nearby stars, possibly within their habitable zone. TESS launch is scheduled for late 2017, with the all-sky survey starting in 2018 and lasting for two years. After 6 months from its launch, the first data release will be publicly available, followed by other releases with a 4-month cadence.

TESS will be made up by four lenses, each of them will have a diameter of 10.5 cm and will be equipped with a mosaic of four 2048×2048 pixel^2 CCDs. With a pixel scale of 21 arcsec pixel^{-1}, one lens will cover a field of view of 24×24 deg^2 on the sky. The four lenses will allow TESS to observe in one shot a total FoV of 24×96 deg^2, from the Ecliptic Pole down to 6 deg from the Ecliptic Plane. Each sector of each hemisphere will be observed continuously for ∼27.4 d (two spacecraft orbits). The stars will be imaged similarly to *Kepler*/*K2*. A small stamp of 10×10 pixel^2 around 200 000 pre-selected stars will be imaged with a 2-min cadence (60 2-s read outs summed on-board). Additional full-frame exposures will be obtained with a 30-min cadence, increasing the number of observed objects to more than 30 millions. Each object, depending

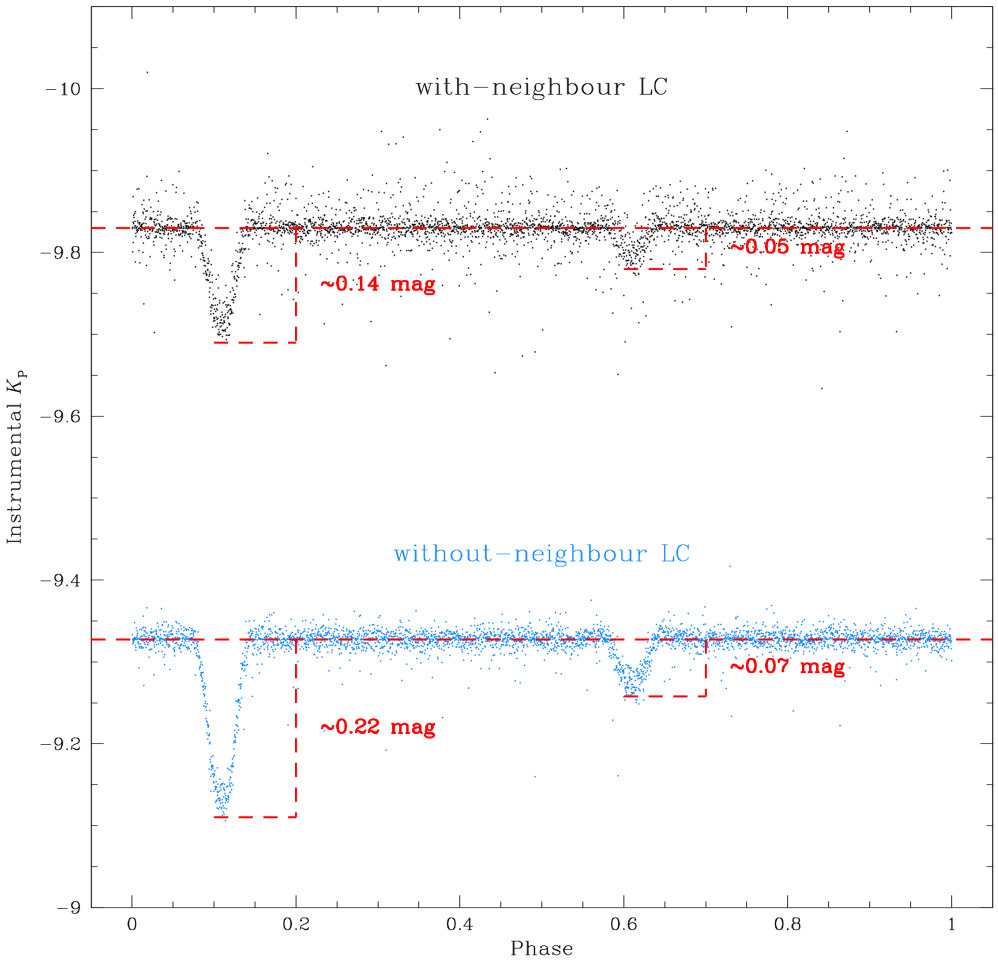

Figure 6.6. V65 PSF-based detrended light curves obtained from the original (black dots on top) and neighbour-subtracted (azure dots on bottom) *K2* images, phased with a period of ∼2.2930 d as in Kaluzny et al. (2013). We also removed the residual long-term systematics and intrinsic variability from both light curves. The red, dashed lines are set at the out-of-eclipse, primary-eclipse-depth and secondary-eclipse-depth levels. The star measured without removing the close-by neighbours is brighter and shows dimmer eclipses, evidence of light contamination.

on its Ecliptic latitude, will be observed from 27 d to about one year. Based on Monte Carlo simulations, Sullivan et al. (2015) predicted that about 1700 transiting exoplanets will be found within the 200 000 bright stars observed with a 2-min cadence. Only 48±7 of these discovered exoplanets should have a radius $<2R_{\oplus}$, and lie within or near the habitable zone of their host star. Using full-frame images, the number of detected exoplanets is expected to increase up to about 20 000.

PLATO (PLAnetary Transits and stellar Oscillations, Rauer et al. 2014) is a M3-class ESA mission, selected to be launched in early 2024. PLATO will cover half of the sky, searching for exoplanets, including Earth analogues, within the habitable zone.

PLATO instrumentation will be made up by 34 12-cm telescopes, 32 of which equipped with

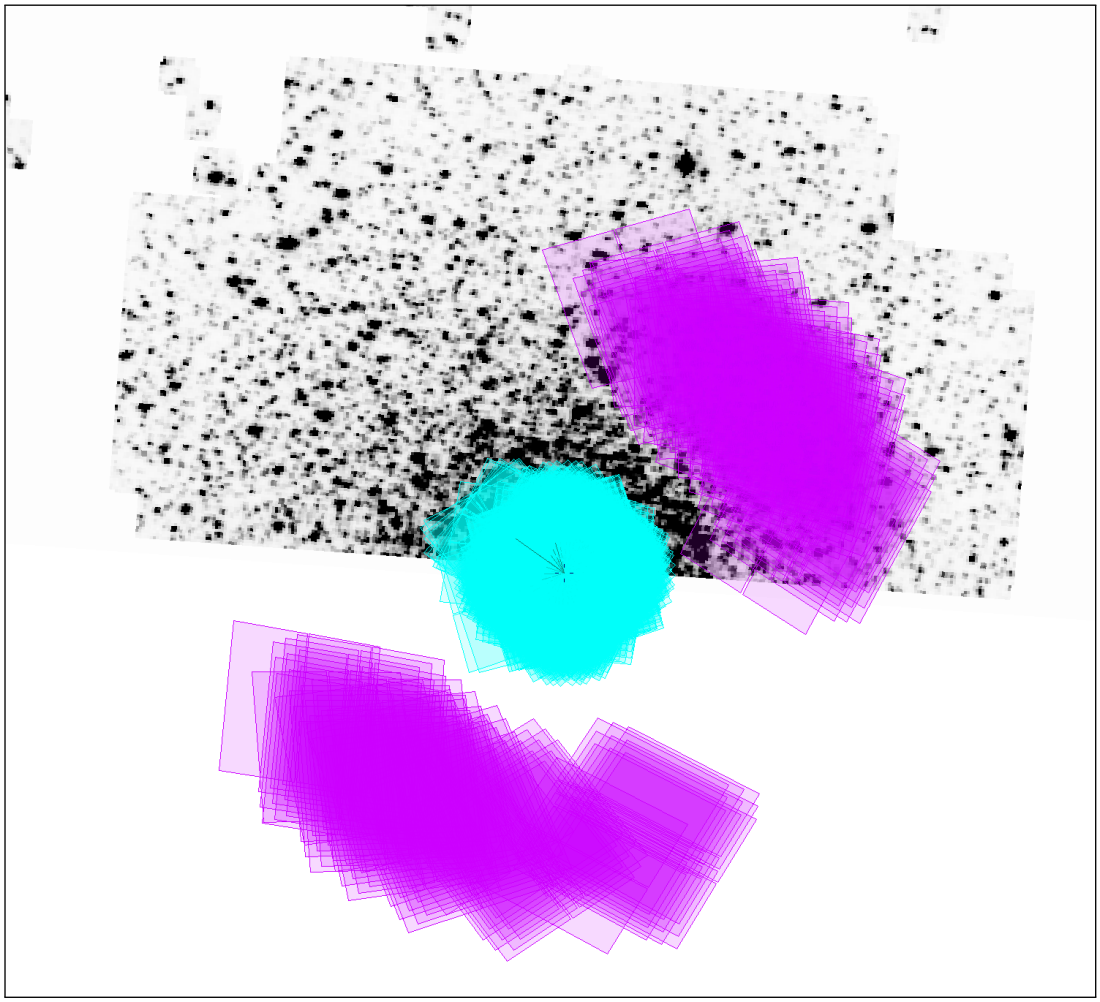

Figure 6.7. M 4 super-stamp region in the *K2* stacked image (in logarithmic grey scale). In cyan and magenta we show the *HST* WFC3 and ACS (parallel) fields, respectively, covered by 'The M4 Core Project' large program.

'normal' cameras and the remaining two with 'fast' cameras. A normal camera is a mosaic of four 4519×4510 pixel^2 CCDs with a pixel scale of 15 arcsec pixel^{-1}, for a FoV of about 1100 deg^2 on the sky. This camera is equipped with a wide broadband filter. Fast cameras cover half of a normal-camera (4519×2255 pixels^2) FoV, have a different read-out mode and are equipped with two filters to provide colour information for the observed stars. Normal cameras will be used to observe stars fainter than $V\sim$8 mag (with a 25-s cadence, exposure time of 22 s), while fast cameras will monitor bright stars (with a 2.5-s cadence, exposure time 2.3 s). The FoV coverage of PLATO is complex. The 32 normal cameras are set in groups of 8 telescopes each, that will observe the same portion of sky. The central pointing of each group is offset by ∼9.2 deg, increasing the total FoV to ∼48.5×48.5 deg^2. In this setup, the coverage is not uniform, with the centre of the FoV covered by all 32 normal cameras and the outskirts by only 8 cameras. The limited data storage and telemetry will force PLATO to download to the ground already-processed light curves for pre-selected targets and, for a limited number of stars (a few thousands, to be confirmed), small stamps of pixels as in *Kepler*/*K2*. PLATO will observe the

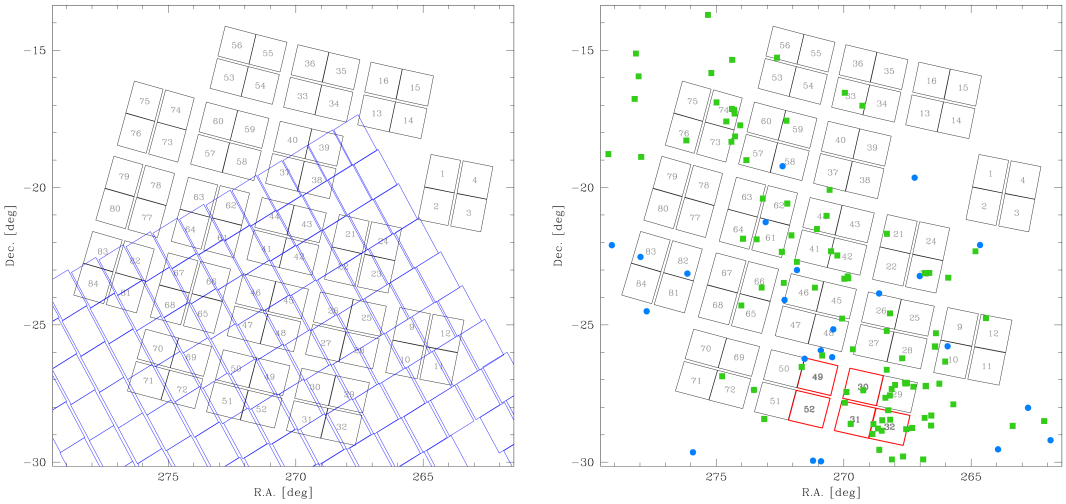

Figure 6.8. *K2*'s C9 FoV. The black squares represent *K2* channels. In the left-hand panel, VVV tiles are shown in blue. In the right-hand panel, we marked the location of globular (azure dots) and open (green squares) clusters in this region. The red squares in the right-hand panel are the channels that, according to Henderson et al. (2015), should be entirely or partially covered by a super-stamp. The *K2*'s FoV could change after the approval of the proposals.

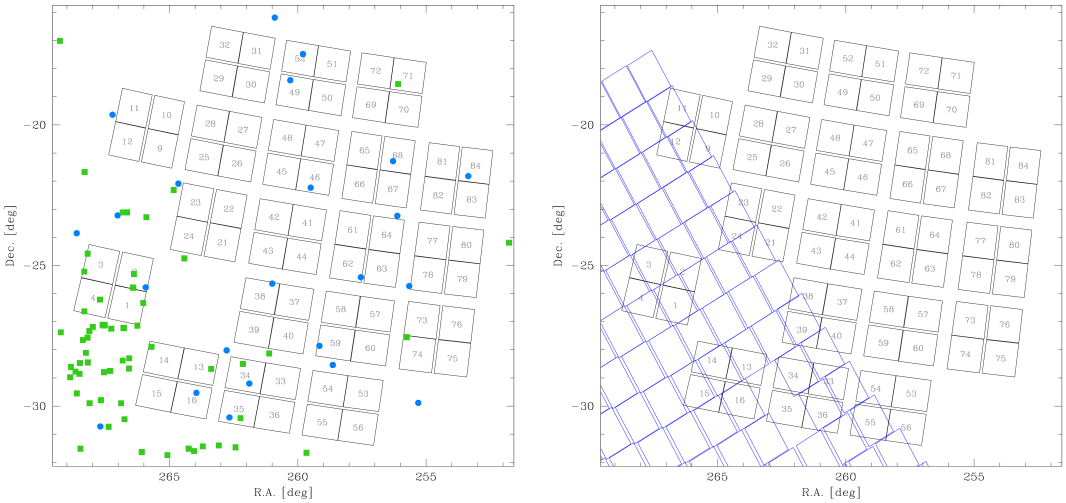

Figure 6.9. Same as in Fig. 6.8, but for Campaign 11. As for C9, the *K2* FoV could change after the approval of the proposals.

sky in two ways. Two long continuous pointings, of 2/3 yr and 2 yr respectively, will cover two fields to mainly search for (Earth-like) exoplanets in the habitable zone of Sun-like stars. Several pointings that will last for a shorter period (from a minimum of 2 months to a maximum of 5) will observe additional fields, increasing the number of transiting exoplanets and covering other scientific topics of the mission.

As described above, there are several characteristics that make TESS and PLATO very similar to *Kepler/K2* and, therefore, perfectly suitable for the high-precision analysis we are developing. TESS full-frame exposures and PLATO pixel stamps (it is not clear yet if PLATO will also deliver super-stamp regions as in *Kepler/K2* case) covering crowded regions, in particular stellar clusters, will be very important to shed light on the different formation and evolution scenarios of exoplanets, as well as to increase our knowledge in other stellar astrophysics fields, e.g., gyrochronology and asteroseismology.

Bibliography

Bedin L. R., Salaris M., King I. R., Piotto G., Anderson J., Cassisi S., 2010, ApJ, 708, L32

Bellini A., Piotto G., Bedin L. R., King I. R., Anderson J., Milone A. P., Momany Y., 2009, A&A, 507, 1393

Borucki W. J., et al., 2010, Sci, 327, 977

Brogaard K., Bruntt H., Grundahl F., Clausen J. V., Frandsen S., Vandenberg D. A., Bedin L. R., 2011, A&A, 525, A2

Brogaard K., et al., 2012, A&A, 543, A106

Henderson, C. B., Penny, M., Street, R. A., et al. 2015, arXiv:1512.09142

Howell S. B., et al., 2014, PASP, 126, 398

Kaluzny J., Thompson I. B., Rozyczka M., Krzeminski W., 2013, AcA, 63, 181

Libralato M., Bedin L. R., Nardiello D., Piotto G., 2016, MNRAS, 456, 1137

Minniti D., et al., 2010, New Astron., 15, 433

Mochejska B. J., et al., 2006, AJ, 131, 1090

Nardiello D., et al., 2015, MNRAS, 447, 3536

Nascimbeni V., et al., 2014, MNRAS, 442, 2381

Pietrinferni, A., Cassisi, S., Salaris, M., & Castelli, F. 2004, ApJ, 612, 168

Rauer H., et al., 2014, ExA, 38, 249

Ricker G. R., et al., 2014, SPIE, 9143, 914320

Sigurdsson S., Richer H. B., Hansen B. M., Stairs I. H., Thorsett S. E., 2003, Sci, 301, 193

Skrutskie, M. F., Cutri, R. M., Stiening, R., et al. 2006, AJ, 131, 1163

Stetson P. B., et al., 2014, PASP, 126, 521

Sullivan P. W., et al., 2015, ApJ, 809, 77

Thorsett S. E., Arzoumanian Z., Camilo F., Lyne A. G., 1999, ApJ, 523, 763